Laser Spectroscopy of Antiprotonic Helium Atomcules

— Collisional Shift and Broadening of Resonance Lines —

Hiroyuki A. Torii

Department of Physics
Graduate School of Science
University of Tokyo
7-3-1 Hongo, Bunkyo-ku, Tokyo 113-0033, JAPAN

Dissertatio Doctoralis

December 1997

dixitque Deus fiat lux et facta est lux

Abstract

The surprising existence of long-living metastable states in neutral antiprotonic helium "atom-molecule", or "atomcule" ($\overline{p}\mathrm{He}^+$) was first demonstrated in 1991 at an experiment at KEK. Since then this metastability has been studied in further experiments by the KEK group with additional European collaboration at CERN. We have so far found 13 resonant transitions among high-n, high-l metastable states of the $\overline{p}\mathrm{He}^+$ atomcule by the method of laser-induced annihilation spectroscopy. The observed transition energies showed excellent agreement with theoretical calculations, and thus established the level structures of this exotic atomcule.

In the meantime we observed that the central frequency of the resonances shifted and broadened with density, and systematically studied this phenomenon. High-resolution laser spectroscopy was performed in helium media of 0.2–8.0 bar at 5.8–6.3 K and 15.2 K, for two of the discovered transitions $(n, l) = (39, 35) \Rightarrow (38, 34)$ and $(37, 34) \Rightarrow (36, 33)$. We have measured the density dependence and observed linear red shifts of 0.61 ± 0.01 GHz and 0.22 ± 0.02 GHz per 1 g/ℓ, for the respective transitions at 597 nm and 470 nm. These results are qualitatively explained by a theoretical calculation based on the impact approximation with a van der Waals type collisional interaction between the atomcule and a helium atom, but certainly more elaborate theoretical work is needed for quantitative discussion.

With the shift parameters above, the transition vacuum wavelengths were extrapolated to zero-density limit, and these values were compared with recent theoretical calculations on the energy of the Coulombic three-body system, including relativistic corrections and the Lamb shift. The agreements between our experimental values and the calculations are now as good as 2×10^{-6}. This already surpasses the currently known precision of $\overline{p}$ Rydberg constant, and thus we have opened a new possibility of measuring fundamental constants of the antiproton.

Contents

Chapter 1

Introduction and Overview

1.1 History of Research on Long-living Exotic Helium Atoms

It was a long-held belief that antiprotons, and more generally negative hadrons, would annihilate by nuclear absorption with picosecond-scale lifetime when stopped in matter [1, 2]. This belief came into question when our former group fortuitously found in 1989 [3] in the course of their experiments at KEK* for a search of ${}^{4}_{\Sigma}$He hypernuclei [4], that a fraction of negative kaons (K^-) stopped in liquid helium target decayed freely with a lifetime of 10.2 ns, which was very close to the intrinsic kaon lifetime of 12.4 ns. From this measurement, they deduced that $3.5 \pm 0.7\%$ of the K^-'s escaped prompt annihilation by being captured in a metastable state with a mean lifetime of 59 ± 3 ns. Encouraged by the discovery, they made a similar experiment for negative pions (π^-) at TRIUMF† and observed that $2.30 \pm 0.07\%$ of them had a metastable lifetime of 10.1 ± 0.2 ns [5].

It was natural, that the group then tried antiprotons ($\overline{p}$), expecting a similar phenomenon with this hadronic antiparticle. The antiproton was more suited for the lifetime measurements of the metastable states, since it is a stable particle and thus there is no limitation in the observation time, in contrast to the case of the K^- and π^- in which the measurement period was restricted by their decay lifetimes. They found in 1991 at KEK, in favor of their expectation, that 3% of antiprotons stopped in helium survive with an average lifetime of about 3 μs‡ [6, 7].

*KEK stands for the Japanese National Laboratory for High Energy Physics in Tsukuba. *Kou-Enerugī butsurigaku Kenkyuujo* in Japanese.

†TRIUMF stands for the Canadian Tri-university Meson Factory located in Vancouver.

‡In recent experiments an average lifetime of 4 μs has been achieved in pure gaseous helium target, as shown in Figure **1.2**, p. 4.

This metastability was attributed to the formation of highly excited exotic helium atoms — specifically antiprotonic helium atoms ($\overline{p}$–He–$e^- \equiv \overline{p}\mathrm{He}^+$) in the case of the antiproton — where the antiproton (or negative meson) has no overlap with the nucleus and cannot therefore annihilate. This idea was already 30 years ago proposed by Condo [8] and theoretically studied by Russell [9]. Actually, exotic atoms in themselves were well known and many studies on the x-rays emitted from the $2p$, $3p$, $3d$, etc. states of deeply bound exotic atoms had been reported. There had however been no direct measurements which proved the existence of such highly excited exotic atoms nor any concrete indication of metastability.

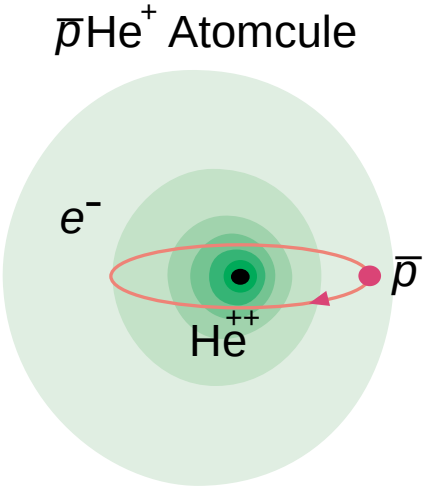

Figure 1.1: A schematic picture of a $\overline{p}\mathrm{He}^+$ atomcule, consisting of a helium nucleus (He^{++}), an antiproton ($\overline{p}$) and an electron (e^-). The $\overline{p}$ in a highly excited state moves round the helium nucleus along a classical orbit while the electron is in its $1s$ state, which is however slightly polarized by the repulsion of the $\overline{p}$ to the opposite side of the helium nucleus.

The formation of the $\overline{p}\mathrm{He}^+$ atom takes place after the incident antiproton has reduced its energy by ionizing surrounding atoms down to the ionization potential $I_0 = 24.6$ eV of a helium atom. The slow antiproton will then be captured[§] by the helium atom and replace one of the bound electrons, forming a neutral three-body system consisting of a helium nucleus, an antiproton, and the other electron (see Figure **1.1** and Color figure I). The cross section for this atomic capture process is largest when the energy of the bound electron and the antiproton match best, or in other words, when the wavefunction of the electron overlaps most closely the orbital of the antiproton in the new system. This condition gives a large principal quantum number $n \sim n_0 \equiv \sqrt{M^*/m_e} \approx 38$[¶] for the antiproton [10], where M^* denotes the reduced mass between the antiproton and the helium nucleus, and m_e the electron mass. On the other hand, the electron is in the $1s$ ground state with a small polarization in the opposite direction to the antiproton due to the $\overline{p}$–e^- repulsion. Among excited $\overline{p}\mathrm{He}^+$ atoms thus formed, those with a large angular

[§]Refer to Appendix **A.1** for a more detailed explanation on the formation and thermalization of $\overline{p}\mathrm{He}^+$ atoms.

[¶]$n_0 \approx 38$ for $\overline{p}\,^4\mathrm{He}^+$ atomcule while 37 for $\overline{p}\,^3\mathrm{He}^+$.

momentum $l \lesssim n-1$ ($v \equiv n-l-1 = 0, 1, 2, \ldots$) in which the antiproton is trapped in a nearly "circular" state, have been theoretically predicted to have long lifetimes of a few microseconds, as will be explained in detail in Section **2.1**.

This three-body system can be treated both as an atom and a molecule. If we pay attention to the negative charge of the antiproton, the system is regarded as an atom in which two negative particles orbit round the positive helium nucleus. On the other hand, if we emphasize on the large mass of the antiproton and regard it as another core, then the system is well described as a molecule where the electron cloud is distributed around the two nuclei. Both these pictures describe different aspects of the antiprotonic helium, therefore a new terminology "atomcule", a compound word of atom[‖] and molecule[**], was created for this three-body system.

1.2 Delayed Annihilation of Antiprotonic Helium Atomcules

In our successive experiments in 1992, the metastability of this atom was systematically studied. Figure **1.2** shows a typical "delayed annihilation time spectrum" (DATS) of the antiproton.[††] Most (97%) of the antiprotons annihilated promptly, but 3% survived for an average lifetime of 4 μs. An important point is the shape of the DATS which is bent downward when plotted in a semi-logarithmic scale. If the longevity were due to only one metastable state, then the spectrum would decrease linearly on this scale. If several states with different lifetimes contributed to the delayed annihilation independently of each other, then the spectrum would be bent toward the opposite side. The observed downward-bent shape can be explained in a cascade model, in which the $\overline{p}$'s are transferred through several metastable states in one or more decay chain(s) before they annihilate; an analogy to the decay of radioactive isotopes in nuclear physics.

The observation of these DATS reported in [11–13] thus supported the cascade mechanism, but the inclusive information of the longevity alone was not yet firm evidence for the formation of the metastable antiprotonic helium atomcules. The pursuit of more direct and conclusive information tempted us to attempt laser spectroscopy of this atomcule in 1993, in order to clarify not only its level structures but also its formation and the cascade mechanisms.

[‖]The word "atom" derives from a Greek word "$\acute{\alpha}\tau o\mu o\varsigma$" < a- + témnein + -os, meaning something which can not be cut or divided.

[**]The word "molecule" derives from a Latin word "mole" plus a suffix "-cule", meaning a small lump.

[††]The spectrum presented in Figure **1.2** was actually obtained in 1994.

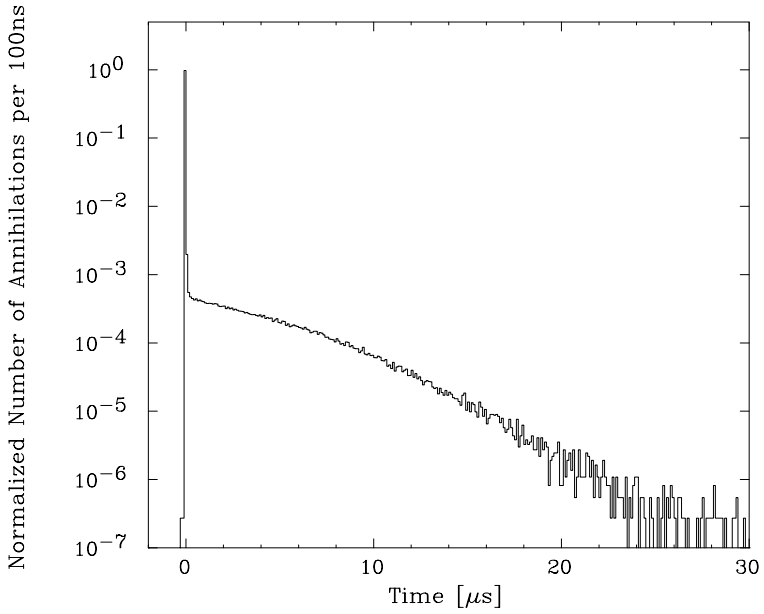

Figure 1.2: A time spectrum of the $\overline{p}$ annihilation in pure helium gas at 4 K and 400 mb shows that 3% of the antiprotons live for a mean lifetime of 4 μs. This long life is ascribed to the formation of high-n, high-l metastable states of $\overline{p}\mathrm{He}^+$ atomcules. The total number of incident $\overline{p}$ is normalized to unity.

1.3 Achievements by Laser Spectroscopy

A series of laser spectroscopy experiments in 1993–1996 turned out to be a great success. In 1993 we celebrated our first discovery of a theoretically expected resonant transition after a long search, and the second resonance was found in the following year. In 1995, a new theoretical calculation provided an accurate prediction of the transition energies and helped us to find 5 more lines. These discoveries undoubtedly confirmed the formation of the highly excited exotic atomcules, and identification of so many metastable states proved the theoretical description of both the $\overline{p}\mathrm{He}^+$ level structures and its cascade mechanisms.

The discovery not only clarified the transition energies to be compared with the theoretical calculations but also made it possible for the first time to measure the lifetimes and populations of individual states. We also found that certain levels were quenched by a high density of the helium or by a small amount of foreign gases, and studied systematically these phenomena. Moreover, we observed that the transition energies shifted as well as broadened in a high-density environment. These observations are interesting from the view point of atomic physics or chemical reactions, since they contain useful information

on the collisional dynamics of the $\overline{p}\mathrm{He}^+$ atomcule with other atoms and molecules.

In the meantime, there has been considerable progress on the theoretical side. The lifetime calculation of both radiative and Auger transitions have been refined, and doublet splittings of "hyperfine" substructures were predicted and experimentally confirmed afterwards. And especially, the energy calculations of the three-body system have become very accurate, and with recently calculated relativistic corrections and the Lamb shift included, now the agreement of values between experiment and theory is at a 10^{-6} level. This precision is already better than the known uncertainty of the Rydberg constant of antiproton, and therefore our current work would give the best limit on the $\overline{p}$ charge, or equivalently, on the mass.

For that comparison, the observed small shift as a result of collisional effects had to be corrected to give the transition energies at the isolated atomcule limit. In this thesis, our fruitful achievements in the series of laser-spectroscopy experiments of $\overline{p}\mathrm{He}^+$ atomcule will be reviewed (in Chapter **4** and Appendix **B**), with a special emphasis on the collisional interactions observed as shifts and broadenings of the laser resonances (in Chapter **5**). We will discuss how high-precision spectroscopy was performed, and how we determined the transition wavelength to be compared with the theoretical calculations with a ppm (part par million) accuracy. Also, the shifts and widths themselves are an interesting subject, because they contain useful information on the collisional dynamics between $\overline{p}\mathrm{He}^+$ and helium atoms. These will be the main subject of this thesis.

Before going into the experimental results, let us first present some theoretical background of the studies of the $\overline{p}\mathrm{He}^+$ atomcule in the next chapter, and our unique experimental method and instrumentation in Chapter **3**. Readers are referred, whenever necessary, for a brief explanation of special terms and notation used in this thesis, to Appendix **F** and indices at the end of this thesis.

Chapter 2

Theoretical Background and Strategy of Laser Experiments

2.1 Metastability of Antiprotonic Helium Atomcules

In this section the $\overline{p}\mathrm{He}^+$ atomcule is described and the reason is explained why some of them can long survive instead of annihilating promptly.

Figure **2.1** (▷ Color figure II) shows theoretically calculated level structure of $(\overline{p}\mathrm{He}^+)^0$ atomcule and $(\overline{p}\mathrm{He}^{++})^+$ ion,* together with a typical scheme of the key processes [14]. Antiprotons with an energy less than the ionization potential $I_0 = 24.6$ eV of a helium atom† are captured in a highly excited orbit with $n \sim 38$. Among many states of $\overline{p}\mathrm{He}^+$ atomcules, those with a large angular momentum $l \lesssim n-1$ have long lifetimes of typically a microsecond. These states are so-called "circular", and have a $\overline{p}$ wavefunction quite localized at a distance of nearly one Bohr radius‡, so that the antiproton can be treated as a classical particle in a circular (not elliptic) orbit. Since the $\overline{p}$ wavefunction never overlaps with the helium nucleus, direct annihilation from these states is not possible.

Some people may expect a fast decay of the states, but looking at the scheme, it is convincing that the internal Auger process, *i.e.* transitions to any $\overline{p}\mathrm{He}^{++}$ states, are strongly suppressed because it requires a large reduction of angular momentum $|\Delta l| > 3$ (explained later) which the outgoing electron must carry away. The fact that no underlying ionic states exist with matched angular momenta, is a key to the prohibited Auger transition, as discussed once more in Appendix **A.2**. This atom is also robust against frequent collisions with surrounding helium atoms. External Auger transitions are sup-

*The figure is shown for the ^{4}He isotope, but note that the metastability was observed also for ^{3}He targets [13].

†The value is for the center-of-mass (CM) system between the $\overline{p}\mathrm{He}^+$ and He. Refer to Appendix **A.1** for a more detail.

‡Here I mean the Bohr radius a_0 of normal hydrogen atoms, and not the mean radius $a_{\overline{p}}$ of $\overline{p}$ in a deeply bound $1s$ orbit.

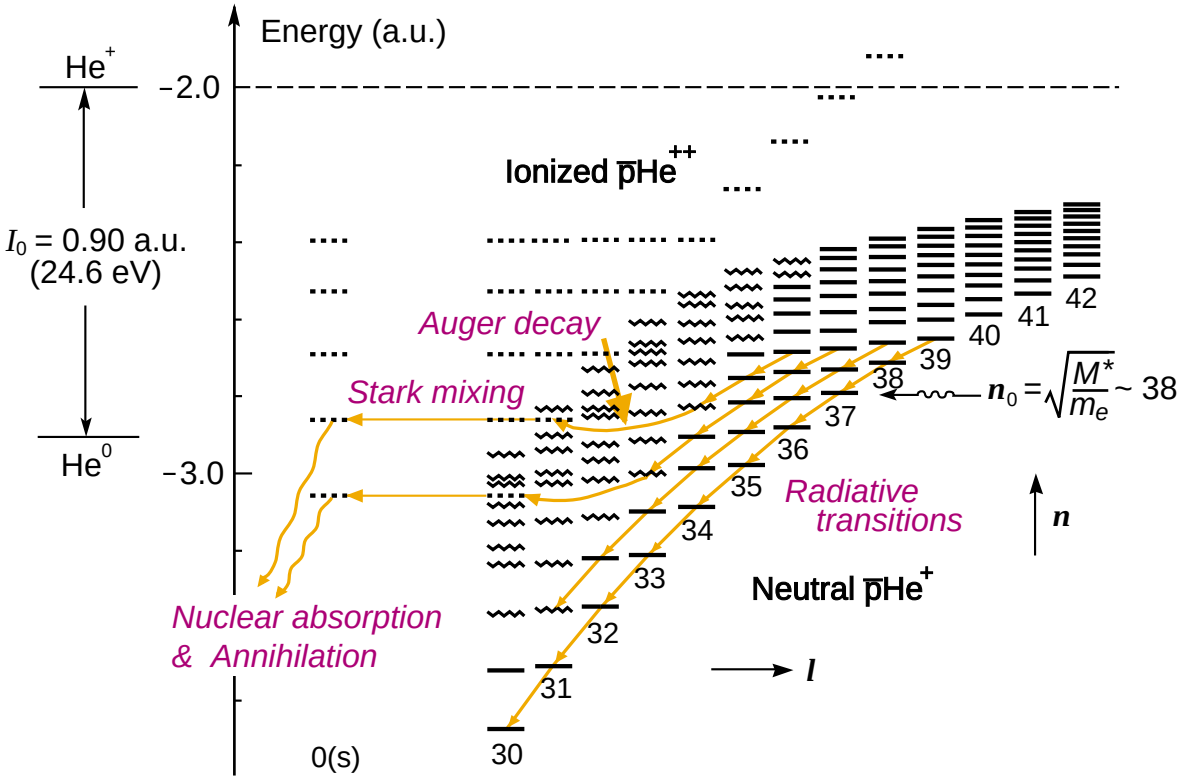

Figure 2.1: In the calculated $(\overline{p}\,^4\mathrm{He}^+)^0$ level scheme the straight lines denote metastable states with lifetimes in the microsecond region. The zigzagged lines stand for short-lived levels, where the Auger transition rates are much faster than the radiative transition rates. The arrows illustrate the typical fate of the antiproton which has a propensity to make radiative transitions along the $(\Delta n = -1,\ \Delta \ell = -1)$ lines until it reaches a short-lived state from which the $(\overline{p}\,^4\mathrm{He}^+)^0$ atomcule decays into a $(\overline{p}\,^4\mathrm{He}^{++})^+$ ion via a fast Auger transition. The antiproton is then absorbed by the helium nucleus from the s state $(l = 0)$ after Stark mixing caused by the weak field experienced during collision with ordinary helium atoms, and immediately annihilates. An analogous level diagram can be drawn for the $(\overline{p}\,^3\mathrm{He}^+)^0$ atomcule and the $(\overline{p}\,^3\mathrm{He}^{++})^+$ ion, with quantum numbers n, l smaller by 1 [13], and with the same deexcitation mechanism preceding the $\overline{p}$ annihilation.

pressed because of the large ionization potential (= 24.6 eV) of a helium atom compared with the small level spacing ($\sim$ 2 eV) of the highly excited exotic atom [9, (b)]. Stark mixing is also very weak, because the existence of an electron (i) keeps this exotic atom away from other helium atoms due to the Pauli principle and (ii) removes the degeneracy between the levels with different angular momentum l.

The only possible process is then a slow radiative transition, by which the exotic atom cascades, emitting photons in the visible-light range. The transition obeys a propensity rule $\Delta l = -1$ and $\Delta n = -1$ which keeps the radial node number $v = n - l - 1$ constant (see Section **2.3.1**). This means it is a good approximation to regard the radiative transitions as following one of the parallel cascade chains, as illustrated by the arrows in the Figure **2.1**.

Thus the formed metastable $\overline{p}\mathrm{He}^+$ atom will cascade down radiatively, staying at each state for about 1–2 μs [15], until it reaches a short-lived state. It will then emit an electron via the fast Auger transition, leaving a positive $\overline{p}\mathrm{He}^{++}$ ion. Since this ion is subject to strong Stark mixing[§] [9, 16], the antiproton is absorbed by the helium nucleus immediately from the s (or sometimes from p) state with a high n.

Note that anomalous longevity of antiproton in matter has been observed only in helium medium. See Appendix **A.3**.

2.2 Theoretical Descriptions and Calculations of Energy Levels

Up to now, many atomic theorists have calculated in various methods the energy levels and transition rates of $\overline{p}\mathrm{He}^+$ atomcules. Many of them had originally worked on the calculation of muonic atoms in connection with the muon catalyzed fusion [17] and showed interest in $\overline{p}\mathrm{He}^+$, as basically the same codes could be used for these similar three-body systems. In these few years, our experimental results and their theoretical work have stimulated each other in improving the accuracy, and by now the calculations have come to a state where the comparison with our experimental values on the transition energies agrees to a 10^{-6} level.

2.2.1 Atomic picture

[§]In the case of the ion, Stark mixing has a strong effect because this two-body hydrogen-like system penetrates into surrounding helium atoms (because it no more has an electron which produces Pauli repulsion) where it feels strong electric field, which mixes the l-degenerate levels of the $\overline{p}\mathrm{He}^{++}$ ion strongly enough.

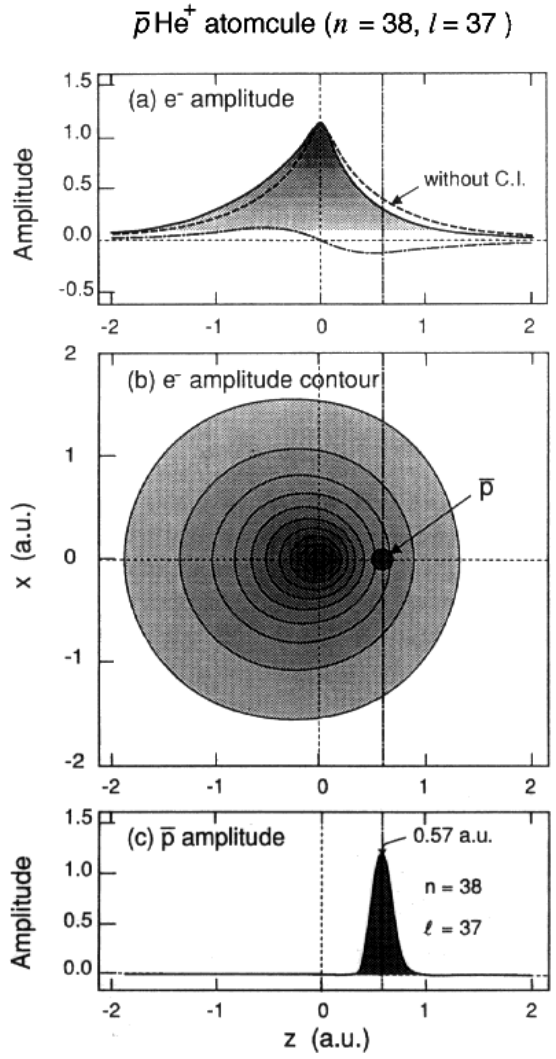

Figure 2.2: Calculated wavefunction for an $(n, l) = (38, 37)$ "circular" state. The electron is polarized away from the antiproton due to its Coulomb repulsion (which is included in the CI calculation in the atomic picture), and this reduces the dipole moment of the atomcule. The antiproton is localized at a radius of 0.6 a.u. from the position of the helium nucleus and moves along a circular orbit. Its large mass (and hence its low velocity) allows classical treatment of the $\overline{p}$ and adiabatic approaches in the molecular picture.

The antiprotonic helium is considered as a helium-like exotic atom with two negative $(-e)$ particles orbiting around the positive $(+2e)$ helium nucleus. The antiproton is captured in a high-n ($n \sim 38$), high-l ($l_{\overline{p}} \lesssim n - 1$) orbit and thus sometimes can be treated as a classical particle, while the electron is mostly in its ground $1s$ state, but its wavefunction is slightly polarized by the mixing of p states (mainly $2p$ state) due to the Coulomb repulsion against the antiproton. Thus most of the large total angular momentum l is carried by the antiproton and hence $l \approx l_{\overline{p}}$. Ohtsuki calculated [14, 18] the energy levels of this three-body system in this atomic picture using the configuration-interaction (CI) method. The total wavefunction $\Psi(n, l)$ was expressed as a sum of each configuration:

$$\Psi(n,l) = \sum_k c_k \phi_k(\boldsymbol{r}, l_e) \Phi_k(\boldsymbol{R}, l_{\overline{p}}) \,, \quad (|\, l_e - l_{\overline{p}} \,| \le l \le l_e + l_{\overline{p}}) \,, \tag{2.1}$$

where the wavefunctions ϕ_k and Φ_k for the two particles were expanded each by 15–30 Slater-type orbits (STO) and the eigen-functions for the total Hamiltonian were solved.

The result of his calculation is outlined in Figure **2.1**. In the case of the $\overline{p}\mathrm{He}^{++}$ ion (a two-body system), the energies are degenerate among the states with different angular momentum l. In the neutral $\overline{p}\mathrm{He}^{+}$, however, it is shown that the degeneracy is removed by the existence of the electron and the energy increases slightly for larger l, which suppresses Stark mixing between different-l states, thus contributing to the metastability. Also, the dipole moment of the $\overline{p}\mathrm{He}^{+}$ is reduced due to the anti-correlation between the antiproton and the electron; *i.e.* the electron cloud is always polarized away from the $\overline{p}$ across the helium nucleus because of the repulsive interaction, and quickly adjusts itself to the $\overline{p}$ motion (as illustrated in Figure **2.2**), which contributes coherently to the reduction of electric dipole transition rates.

Ohtsuki's calculation of the energy levels turned out to be accurate to a 10^{-3} order when it was compared with our experimentally determined transition energies (see Figure **4.3**, p. 44).

2.2.2 Molecular picture

The antiprotonic atomcule can also be described as a peculiar molecule. It has two heavy particles — a helium nucleus (α particle or a ^{3}He nucleus) and an antiproton — and an electron orbiting around them. Since the electron is much lighter than the heavy cores by a factor 1800 and more, it is reasonable to regard the system as a diatomic molecule with a single electron. In fact, the well-known Born-Oppenheimer (BO) approximation for normal molecules can be applied to this three-body system and has yielded several good results on the calculation of the energy levels. The validity of the BO approximation, or more generally, adiabatic approaches, is assured by the much slower motion of the nuclei than that of the lighter electron. Here the nuclear motion can be separated from the fast electron motion, and the effective electronic potential can be obtained by plotting the eigen-energies of the electronic Schrödinger equation calculated for different values of the nuclear distance. The electron is reasonably assumed to be in the ground $1s\sigma$ state. Figure 2.3 illustrates this effective potential as a function of the nuclear distance R, comparing the cases for the antiprotonic helium atomcule and normal molecules. The rough shapes of the potential curves are similar: the force is strongly repulsive for smaller R and weakly attractive for larger R, so that a potential minimum exists at an equilibrium nuclear distance, while the attractive force diminishes at very large distances ($R \to \infty$). This similarity allows the same theoretical treatments in calculating the nuclear motion.

However, the origins of the forces are quite different. For ordinary molecules, nuclear repulsion is the source of the repulsive force while the attraction originates from the chemical electron bond: the negative electron cloud has a higher probability between the positive nuclei and thus increases Coulomb attraction and buffers the repulsive forces. On

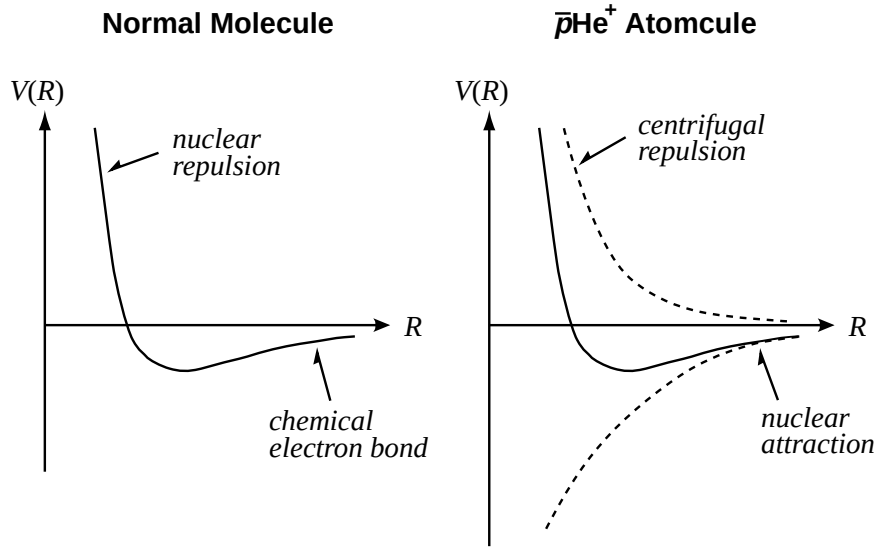

Figure 2.3: The electron energies, or the effective potentials, are compared. In normal molecules, nuclear repulsion is the source of the repulsive potential at a small internuclear distance R while the attraction at large R originates from the chemical electron bond. In the case of the $\bar{p}\mathrm{He}^+$ atomcule, however, the attraction is mainly due to the internuclear Coulomb force, while the repulsion arises from the centrifugal force. Although their origins are quite different, the similar shape of the potential allows the same theoretical treatment.

the other hand, in the case of the antiprotonic helium atomcules, the attraction is mainly due to the Coulomb force between the nuclei with opposite charge, while the repulsion arises from the centrifugal force due to the large angular momentum.

In this molecular picture, the states are denoted in terms of the vibrational quantum number v and the rotational quantum number L.[¶] Noting that v corresponds to the radial node number in the antiproton wavefunction in the case of the atomic picture, the quantum numbers in both pictures are related by the equations

$$L = l \quad \text{and} \quad v = n - l - 1\,. \tag{2.2}$$

An interesting comment is that for normal molecules the energy separations ΔE_L between the states with different L are usually much smaller than the separations ΔE_v for different

[¶] Usually a symbol J is used for the rotational quantum number. In this paper, however, the letter J is kept aside for the total angular momentum (Appendix **B.5**).

v. This is not true for the metastable $\overline{p}\mathrm{He}^+$ atomcule, because ΔE_L is proportional[‖] to L and the angular momentum $L = l$ is very large. Actually, $\Delta E_v \approx \Delta E_L$ for the "circular" states with $l \lesssim n - 1$.

Shimamura [19] and others [20–22] have calculated the energy levels of $\overline{p}\mathrm{He}^+$ atomcule using the BO approximation (or another adiabatic approximation method) based on this molecular picture, and yielded results which agreed with the experiment to a 10^{-3} order (see Figure **4.3**, p. 44).

2.2.3 Other treatments and finer calculations

There are yet other computational methods in the calculation of $\overline{p}\mathrm{He}^+$ energy levels. Kino [23–25] has included the correlation between all possible combinations of the three particles by taking into account the wavefunctions described in three different sets of Jacobian coordinates. In principle, this non-adiabatic "coupled rearrangement channel" (CR) calculation could have given more accurate values, but his first result in 1993 was not so prominent (see Figure **4.3**, p. 44), due to an unlucky computational mistreatment, as it turned out later.

Kartavtsev [26] used the variational method (VM) with a large configuration space and also yielded results with comparable accuracy to other calculations so far mentioned (Figure **4.3**). Tolstikhin *et al.* expressed the wavefunctions in hyperspherical elliptic coordinates [27] and calculated the energy levels [28]. There are yet other calculations as in Ref. [29].

In 1995 Korobov calculated the transition energies [30], in a molecular picture but beyond the adiabatic approximations, which showed agreements with our experimental values to 50–100 ppm levels (see Figure **4.5** in Section **4.2**, p. 47). He included excitation of the electron by taking into account σ, π and δ states ($\Lambda = 0$, 1, and 2, respectively), and calculated the eigen-energies and eigen-functions that were expanded with 2364 basis functions expressed in the spheroidal coordinates. The mixing coefficients between different basis functions were determined by the variational method.

In the following year, his calculation was augmented by including the relativistic correction for the motion of the 1s electron [31], and the agreement became as good as several ppm, as shown in the Figure **4.5**, *loc. cit.*

Very recently, Kino *et al.* [24, 25] and Elander *et al.* [32–34] have come up with new calculations including relativistic corrections and Lamb shifts. Elander *et al.* have used a three-dimensional finite-element method [33]. Korobov has also revised his calculation [35]. All their values showed agreement with each other to a several-ppm precision, and

[‖]Proportionality holds exactly for a rigid rotor but only approximately for a real molecule which changes its moment of inertia with different L.

with all effects taken into account, the discrepancies with our experimental values are only a few ppm! This agreement will be further discussed in Section **5.2**.

2.3 Transitions between the States

2.3.1 Radiative transitions

Calculation of the radiative dipole transitions is straightforward once the wavefunction of the system is obtained. The spontaneous transition rate $\lambda = \tau^{-1}$ is given by the equation

$$\tau^{-1} = \frac{4}{3}\frac{\omega^3 {\mu_{if}}^2}{\hbar c^3}\,, \quad \mu_{if} = |\,\langle f\,|\boldsymbol{\mu}\,|i\rangle\,|\,, \tag{2.3}$$

where $\boldsymbol{\mu}$ is the dipole operator of the $\overline{p}\mathrm{He}^+$ atomcule (defined in Eq. (D.33b)**, p. 123), so the rate is proportional to the dipole moment (μ_{if}) squared.†† The statement in Section **2.2.1** must be recalled that the (anti-)correlation between the electron cloud and the antiproton is important in the calculation of the transition rates [14, 19].

Figure **2.4** shows the transition rates for some of the allowed dipole transitions. It indicates that the transition with $\Delta n = \Delta l = -1$ dominates over the other side branches. This is because the overlap of the antiproton wavefunction between the two states is largest due to the same radial node number $n - l - 1$, or in the molecular point of view, the vibrational quantum number v is constant. We call this type of transition "favored", and use a term "propensity rule" to mean that the main transition occurs along the v-constant series. The calculated size of the dipole moments are 0.2–0.3 debye♯♭ for the "favored" transitions and 0.02–0.03 debye♯♭ for the "unfavored" (see the caption of Figure **2.4**) transitions.

2.3.2 Auger transitions

Apart from an early estimate by Russell [9, (c)], the calculation of Auger transition rates were performed first by Ohtsuki [36] in the atomic picture. To give a reliable calculation for Auger processes is in general not so easy because it involves treatment of unbound continuum states. Especially, the $\overline{p}\mathrm{He}^+$ atomcules are in highly excited autoionizing states coupled to a number of different continuum states. Ohtsuki's result (and

**Note the implicit factor e in the equation written in the atomic units.

††Precisely speaking, the dipole moment μ in this equation corresponds to μ_{tot} in Eq. (D.53b), p. 127.

♯ 1 debye $\approx 0.4\ ea_0$, see Appendix **F.1**

♭The value is for an average of μ for a specific transition ($\sigma^{\pm}, \pi$) between a certain m states, and not the μ_{tot} in Eq. (D.53b), *loc. cit.*

also Russell's estimation) indicated that the transition rate dropped drastically with an increasing "multipolarity" or the jump in the angular momentum ($|\Delta l|$); actually it changed by 3 orders of magnitude for a $|\Delta l|$ difference of unity. For transitions in $\overline{p}\,^4\mathrm{He}^+$ with $|\Delta l| = 2$, 3, 4 and 5, the rates clustered around $10^{11}, 10^8, 10^5$ and 10^2 s^{-1}, respectively, so that the Auger rates and the radiative rates of the order 10^6 s^{-1} are reversed at a border between $|\Delta l| = 3$ and 4. This "$|\Delta l| \leq 3$ Auger dominance rule" set a clear border in the level diagram between the metastable radiative-cascade region and the Auger-fast short-lived region, and was the key in the determination of targeted laser resonances.

In the molecular picture, Auger processes require high-order calculations which the Born-Oppenheimer approximation does not allow. Because of this reason, the Auger rates were calculated in this picture only recently. Those calculations using a variety of methods are published in Refs. [37–40], and their results are in accordance with the dominance rule above.

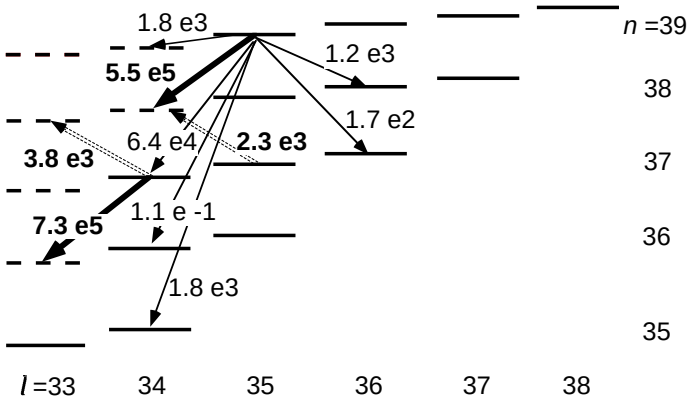

Figure 2.4: A diagram showing the theoretically calculated radiative rates indicates a propensity rule that the "favored" transition, which keeps the vibrational quantum number $v = n - l - 1$ constant, dominates over the other allowed transitions with the selection rule $\Delta l = \pm 1$. The rates are expressed in the form $x\,\mathrm{e}y \equiv x \times 10^y$. The "unfavored" transitions with $\Delta v = 2$ shown in dotted double lines have fairly large rates which are nevertheless about two orders of magnitude smaller than that of the "favored" ones.

2.4 Principle of Laser-Induced Annihilation Spectroscopy

In the planning of our laser spectroscopy experiments, the problem of detecting resonant transitions in the $\overline{p}\mathrm{He}^+$ exotic atomcules was not a trivial question. So far, in the spectroscopy of exotic systems such as muonium (μ^+e^-) and positronium (e^+e^-) [42], those atoms were dissociated by the laser light and the constituent particles were detected. For instance, for a fine measurement of $1S$–$2S$ transition of muonium, the transition from the ground $1S$ to the excited $2S$ state by two-photon absorption was detected via photoionization of the excited atom by photons of the same laser light pulse [43, 44]. In our case, however, ionization of the atomcule required an energy of ca. 20 eV, which is not accessible by the current laser technique, even though the transitions between highly excited states have a typical energy of 2 eV and are suited for laser studies. Furthermore, the muonium technique involved production of thermal (muonium) atoms in vacuum, which was not at all realistic in our case of a gas target and a low-intensity $\overline{p}$ beam.

Another possible way of spectroscopy would be to observe directly the visible light of the cascade transitions. This has been tried by our group, but in vain so far due to very small solid angle and an infinitesimal acceptance of the monochromator, together with relatively large background from the scintillation of helium atoms or excimer molecules and from the noise of the photon detectors.

How, then, can we detect resonant transitions? The antiproton has a feature which neither μ^+ nor e^+ has — it will annihilate by strong interaction into mesons after getting absorbed by the nucleus. If somehow the transition can be related with the annihilation, the resonant transitions can be traced by the detection of $\overline{p}$ annihilation. We took advantage of the fact that there is a distinct border between the metastable states and the short-lived states. For the metastable states as illustrated by straight lines in Figure **2.1**, p. 7, the Auger transition is much slower than the radiative transition which has a typical lifetime of 1–2 μs. For the other states with smaller angular momentum l (illustrated by wavy lines in the figure), the Auger transition is by orders of magnitude faster and dominates over the slow radiative transition, resulting typically in 10 ns lifetimes for those states at the border.

Our method was to use a high-power dye-laser pulse to stimulate a resonant dipole transition between a metastable state and a short-lived state.[♮] Fast Auger deexcitation of

[♮]Note that it is very difficult to detect resonant transitions between metastable states in this method because they will result in a slight difference in the DATS spectrum and no distinct peak will appear in that case. Such transitions could be observed by intentionally shortening lifetimes of certain metastable levels by admixing a small amount of hydrogen gases in the helium target as described in Appendix **B.4.3**.

the newly populated short-lived state to a $\overline{p}\mathrm{He}^{++}$ ion should be followed by annihilation within picoseconds via Stark mixing, and produce a sharp peak in the delayed annihilation time spectrum (DATS) at the time of application of the laser light pulse [45].

A distinct feature of our new technique is that the laser transition ($\sim$ 2 eV) in an atom is probed by annihilation of the composite particle itself ($\sim$ 2 GeV), which can be detected with practically 100% efficiency with a widely used technique in high-energy physics. The spectroscopy of single atoms was thus possible with this sensitive detection of the resonance.

Chapter 3

Experimental Setup

We used a continuous antiproton beam with 200 MeV/c momentum and an intensity of a few 10^4 s^{-1} extracted in parasitic mode to the C1 beamline from the low-energy antiproton ring (LEAR) at CERN* (see Figure **3.1** and Color figure III). The metastable atoms were produced by stopping antiprotons ($\overline{p}$) in a helium gas target cooled down to 4.5–10 K in order to freeze out impurity gases and produce a suitably small stopping volume. Each incident $\overline{p}$ was detected by a thin plastic scintillation counter (B) before it entered the gas target. Its subsequent annihilation was signaled by the passage of the annihilation products through a set of lead-scintillator sandwich counters ("shower" counters; S) placed around the target. These counters were designed so as to achieve a very high (99.7%) overall detection efficiency for $\overline{p}$ annihilation for the reason stated later. The $\overline{p}$ annihilation time was measured as the time difference between the signals from B and S. See Figure **3.2**.

We irradiated each metastable atom with a laser light pulse, which was introduced collinear to the $\overline{p}$ beam axis so that these overlap each other. Since the stopping region of $\overline{p}$ was 1.5 cm in diameter, the laser beam was expanded to the same size. A laser power density of nearly 1 MW/cm^2 was required to completely induce "favored" (conserving quantum number v) transitions on the target metastable states [45]. We employed two identical laser systems, each consisting of a tunable dye laser pumped by a XeCl-excimer laser at a wavelength of 308 nm. The typical output energy of the dye laser was 2–5 mJ per 40 ns pulse, thus the intensity was almost as high as required. The dual laser system played an essential role by permitting irradiation of the metastable atoms at two successive timings to obtain the information on the feeding and decay of the metastable states [48, 49].

The laser had a maximum repetition rate of 400 Hz, but not more than 200 laser pulses

*CERN: Organisation Européenne pour la Recherche Nucléaire, — European Laboratory for Particle Physics — , Geneva, Switzerland.

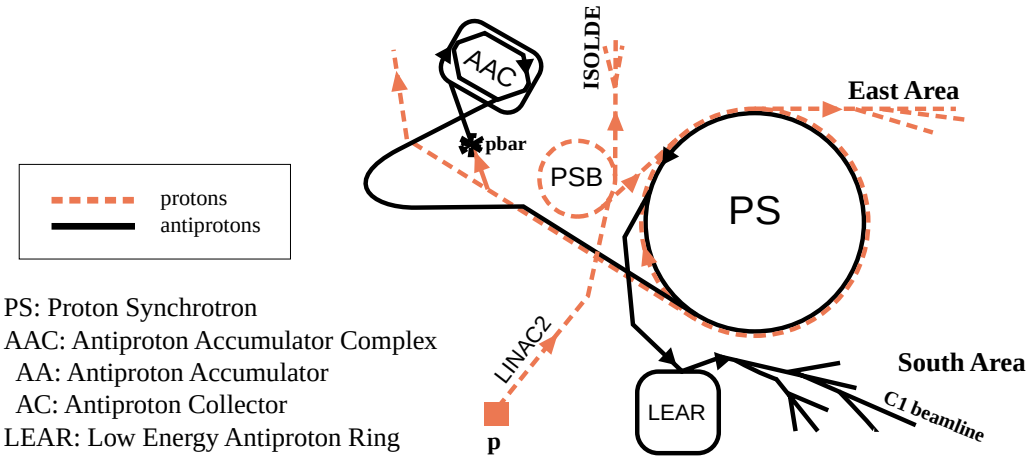

Figure 3.1: A drawing of the PS, AAC and LEAR accelerator complex at CERN. Antiprotons stored in the AA-AC complex at 3 GeV were decelerated in the PS to 600 MeV/c, cooled by Stochastic and electron cooling methods in LEAR down to 200 MeV/c, and then extracted continuously during a typically 80-minute spill.

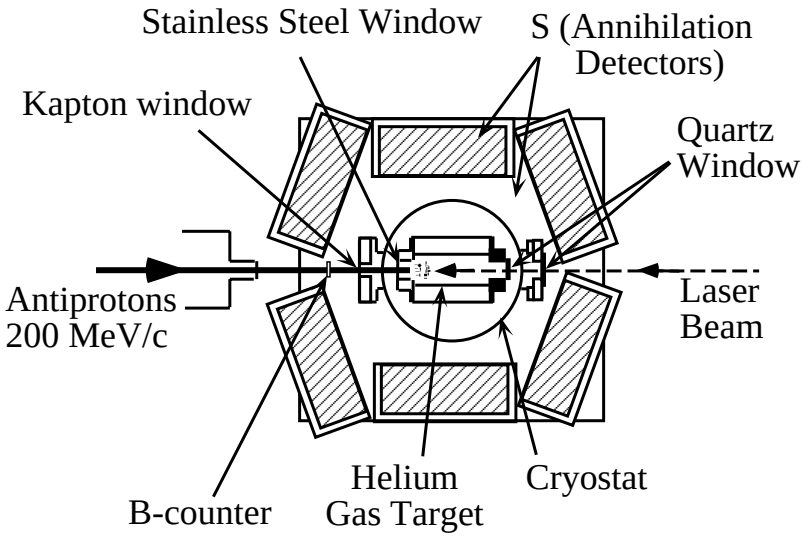

Figure 3.2: A schematic of the apparatus for our laser studies of the $\overline{p}\mathrm{He}^+$ atomcule.

per second were available for randomly arriving antiprotons. In order to apply this limited number of laser pulses selectively to the metastable atoms, we generated a laser trigger for every incident antiproton (B signal) which was not followed by a prompt annihilation (prompt S signal). Since misidentification of metastable antiprotons ($B \wedge \overline{S}$) had to be much less than the metastable fraction, an extremely high efficiency for the detection of antiproton annihilation was required. In the following sections, let us start with particle-detection system (Section **3.1**) and explain our target gas system (Section **3.2**) and the laser system (Section **3.3**). Then follows the analysis method in Section **3.4**, and a summary is given together with an introduction to a modified experimental method in the last section.

3.1 Particle Detection System

3.1.1 Antiproton beam monitoring

Antiprotons of 200 MeV/c momentum (21.1 MeV of kinetic energy) were extracted from LEAR. The beam traversed a 100 μm beryllium window of the C1 beamline before passing through the 0.55 mm thick plastic beam scintillator (B). The $\overline{p}$ beam path is

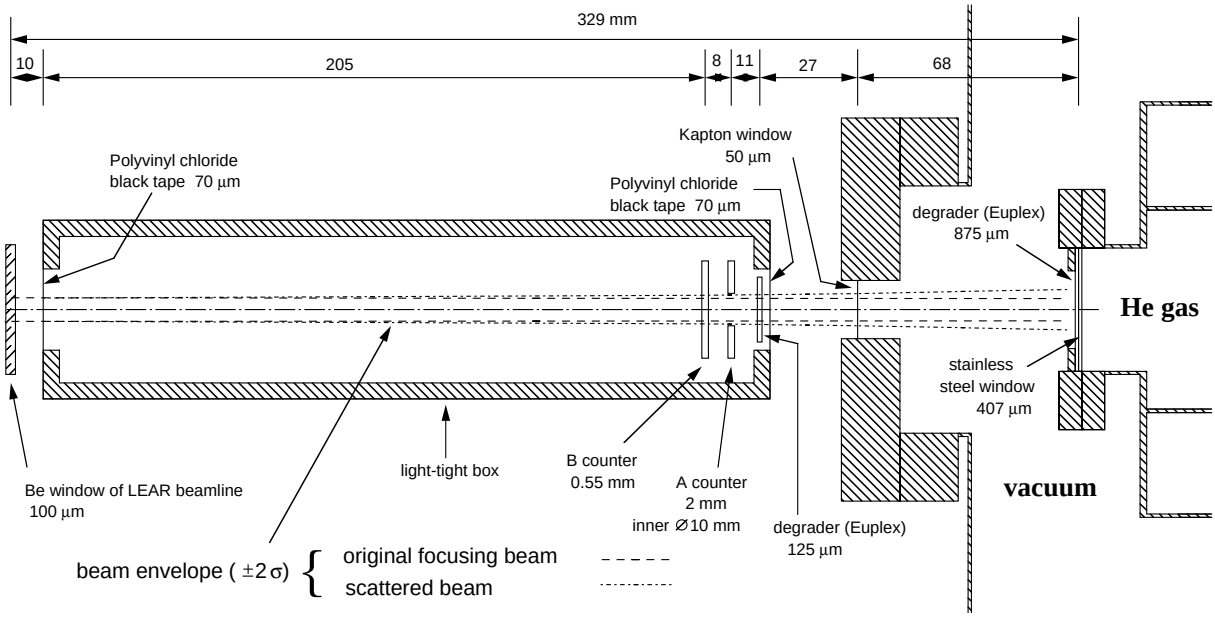

Figure 3.3: A schematic of the $\overline{p}$ beam path. The envelope of the original focusing beam provided from LEAR and the calculated beam scattering are shown in dashed lines.

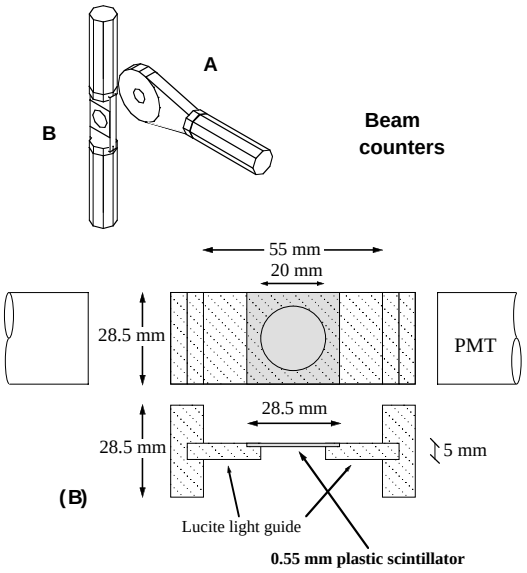

Figure 3.4: The $\overline{p}$ beam counters. The B counter is a 0.55 mm thick plastic scintillation counter in optical contact with a thicker Lucite lightguide and is viewed by two PMT's (*B1* and *B2*). The A counter was used to veto $\overline{p}$ the beam halo.

shown in Figure **3.3**. The scintillation light was detected by two photomultiplier tubes (PMT's: H3171, Hamamatsu Photonics; *B1* and *B2*) mounted on both edges of a Lucite lightguide (see Figure **3.4**). The B counter detected antiprotons with better than 99.9 % efficiency, which was necessary to prevent spurious delayed events [11]. Beam tuning was done beforehand by inserting a multi-wire chamber upstream of our setup. During the experiment we removed this chamber and imaged the dim scintillation light emerging from the surface of the B counter onto a CCD camera mounted in an angle of 45 degrees to the beam axis [60]. By integrating for the exposure time of one second and intensifying the image, we could directly observe the $\overline{p}$ beam as a luminous spot at $\overline{p}$ intensities greater than ~ 5000 per second. A ring-shaped veto counter (A) was placed just downstream of B and vetoed beam halo events. The counting rate of A compared with B was monitored to check the beam size and location, and when needed the beam tuning was done so as to minimize this ratio. After passing through a light-tight box containing the A and B counters and the CCD camera, the $\overline{p}$ traversed a 50 μm Kapton window of the cryostat and a 407 μm stainless-steel window of the target chamber, which was a horizontal cylinder, 21.8 cm long and 6.2 cm in diameter.

The $\overline{p}$ stopping position was tuned by inserting degrader foils made of "Euplex" (same composition as Kapton). It was extremely important that antiprotons stop in the helium target within the area covered by the laser beam, as this area has an upper limit fixed by the light intensity required to stimulate the transition. As degrading a beam's energy unavoidably increases its divergence, this also meant that the stopping volume had to be as close as possible to the stainless-steel entrance window of the target. We estimated the optimum foil thicknesses and positions using a Monte Carlo simulation program [61], which took into account the Barkas effect, energy straggling (Vavilov's formula) and mul-

tiple scattering (Molière's formula) which are essential at low energy region (< MeV) [11]. As a result, we put an 875 μm degrader inside the cryostat (in contact with the stainless-steel window) and an adjustable thin degrader outside (just in front of the Kapton window), whose thickness was optimized experimentally to be 125 μm. Figure **3.5** shows the calculated stopping distribution for 5 K and 600 mb helium gas target for this arrangement of the degraders. The incident $\overline{p}$'s stop in the gas with a radial distribution of 1.5 cm FWHM. Experimentally, the longitudinal stopping distribution could be roughly estimated from the time profile of the prompt annihilation: antiprotons stopping in the stainless-steel window resulted in a sharp peak in the annihilation time spectrum which showed up several nanosecond earlier than the broader peak from the ones stopped downstream inside the gas. From this information, we could check the simulated results and make a small correction in optimizing the degrader thicknesses. With the chosen condition, roughly 10% of the $\overline{p}$'s stopped in the window the rest being distributed close to it, thereby minimizing the divergence of the stopping distribution.

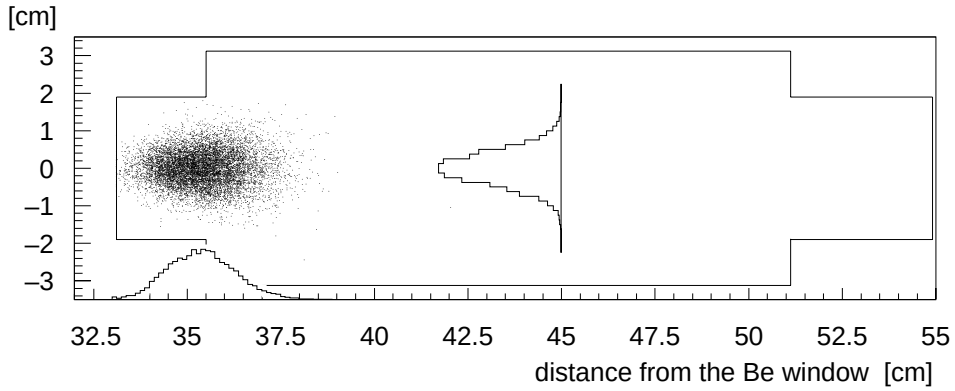

Figure 3.5: Calculated stopping distribution of 10 000 $\overline{p}$ in 5 K and 600 mb helium gas target is shown as a projection to a plane including the $\overline{p}$ beam axis. The polygonal frame illustrates the target chamber (see Figure **3.9**). The distance from the beryllium window (see Figure **3.3**) is taken as the horizontal axis. The radial width of 1.5 cm (FWHM) of the stopping distribution overlaps with the laser light beam.

3.1.2 Annihilation detection system

The absence of a signal in the annihilation counters (S) in the 70 ns period following entry of an antiproton into the gas as signaled by the B counter was taken to indicate the

presence of a metastable atom in the gas, and was used to trigger the laser system. As we knew from previous experimental data, the fraction of antiprotons forming metastable atoms is $\approx 3\%$. Inefficiency in the detection of the numerous (97%) prompt annihilations by S therefore had to be reduced to much less than this figure in order to keep the spurious laser firing rate to a small fraction of the genuine ones. Apparently, our formerly used arrangement of simple scintillation counters [11, 12] did not meet this requirement.

It is known [62, 63] that about 4% of $\overline{p}$-He annihilation products are neutral, producing π^0's which decay within 10^{-16} s into two photons each. To detect these gamma rays as well as charged particles with a large solid angle at reasonable cost, we employed the commonly used technique of "sandwiching" high-Z material, namely lead, between scintillator plates so as to convert photons into electromagnetic showers. We needed only the timing information, so a single PMT per each counter module sufficed for the read-out.

The sizes and arrangement of the counters were almost automatically determined by the geometrical constraints. The top of the cryostat had to be kept free to accommodate the cooling and the gas systems, so we chose an arrangement of six counters in a barrel shape around and an additional one below the cylindrical cryostat containing the gas target. Each "barrel" counter (*S1...S6*) measured 25×60 cm^2 and was about 25 cm distant from the center of the target vessel, while the "bottom" counter (*S0*) was 60×60 cm^2 in size and was placed 50 cm below the target (see Figure **3.6**). Thus the total solid angle coverage was 78% of 4π.

In order to design the "shower" counters and estimate their efficiency, we performed Monte Carlo simulations using the GEANT program library [64]. We required the overall detection efficiency, defined by the probability that any one of the counters detects at least one of the annihilation products, to be as high as 99.7% (0.3% missed prompt annihilation versus 3% metastable atoms).

We simulated $\overline{p}$ annihilation with a simple model in which an antiproton, practically at rest, annihilated directly into 3–7 pions whose momenta were distributed according to the relativistic phase space [65, 66]. Here we neglected kaonic modes and took the branching ratios for the pion final states of $\overline{p}p$ annihilation quoted in [67], since no complete list was available for $\overline{p}$-He annihilation to our knowledge. The calculated momentum distribution (see Figure **3.14**, p. 36) has a maximum at 250 MeV/c, which agreed well with the experimental data [67, 68] in spite of this simple model.

The energy loss, tracking and decay of annihilation products and their subsequent particles were traced by GEANT routines. With the seven sandwich counters in the mentioned geometry, we calculated the detection efficiency for varied parameters of the thickness and the number of layers. The simulations showed that for a fixed total amount of lead the overall efficiency was higher for finer sampling (*i.e.* larger number of thinner plates) until it saturated for thinner layers than 6 mm. This thickness is reasonably com-

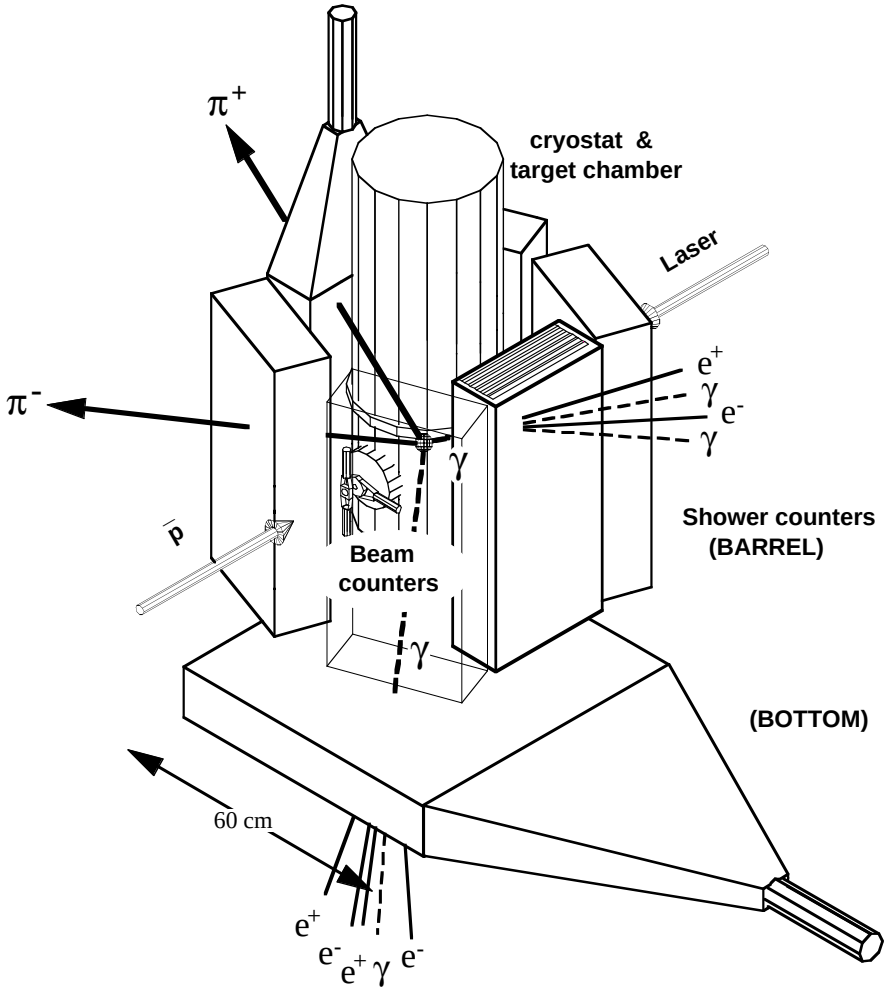

Figure 3.6: The setup of the particle detectors. The beam counters (B and A) detect the incident $\overline{p}$ while its annihilation products ($\pi^{\pm}$, $\pi^0 \rightarrow \gamma\gamma$) are detected by seven lead/scintillator sandwich counters (shower counters, S) surrounding the target. An example of an annihilation pattern is shown for one of the several annihilation modes. The shower counters cover 78% of the total solid angle and $\overline{p}$ annihilation events are detected with 99.7±0.1% efficiency.

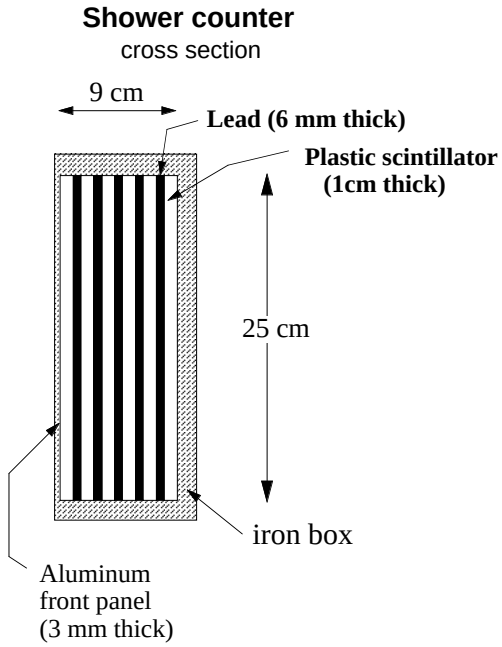

Figure 3.7: A cross section of the shower counter. As a result of the simulation each counter was built of five sheets of 6 mm thick lead interleaved between six plastic scintillator plates. It effectively converts γ rays from π^0 decay into electromagnetic showers.

parable with the radiation length of lead (5.6 mm) or the photon attenuation length (1 cm at a typical photon energy of 100 MeV : see Figure **3.14**). The calculations demonstrated that 5 lead layers of 6 mm thickness were sufficient. The scintillator thickness affected the efficiency only slightly, and we chose 1 cm for each layer to be thick enough for effective propagation of the scintillation light. The front layer of each shower counter was made of scintillator to detect charged particles, so that the five lead sheets were sandwiched between six layers of scintillator, as drawn in Figure **3.7**.

With this setup the simulation demonstrated that the overall efficiency would be 99.8%. The inefficiency of 0.2% was no longer attributed to neutral annihilation but mainly to annihilation into two charged pions. When more than three particles were emitted, a very high efficiency well over 99.9% was expected. Although the solid angle coverage was not very high, the multiplicity of the emitted particles enhanced the detection efficiency.

After a satisfactory performance test of its response to gamma rays using electron-tagged photon beam at INS, Tokyo, our shower counter system achieved 99.7 ± 0.1 % overall detection efficiency for $\overline{p}$ annihilation at CERN [69]. Figure **3.8** shows a histogram of the number (multiplicity M) of "hit" shower counters per $\overline{p}$ annihilation event. The experimental data are compared with the simulation, and they agree reasonably well except for a slightly lower mean value for the experiment ($\overline{M} = 3.80$ versus 3.99).

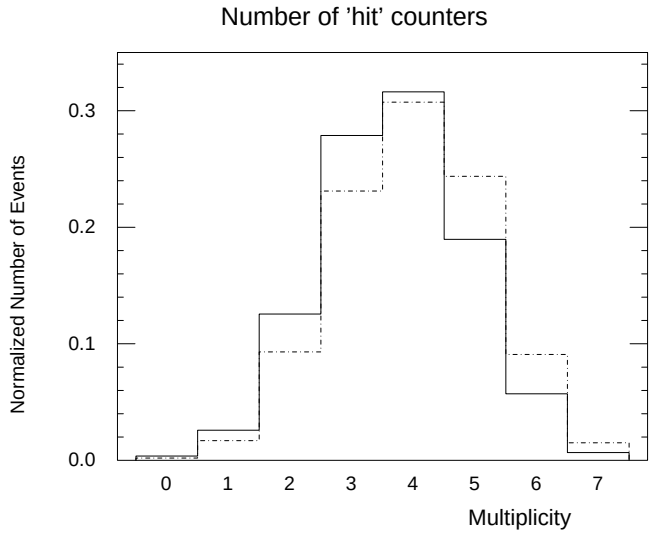

Figure 3.8: Multiplicity (M) distribution obtained as the number of shower counters which detected any annihilation products. Solid line: experimental data ($\overline{M} = 3.80$), dotdash line: result of simulation ($\overline{M} = 3.99$).

3.2 Target Gas System and the Cryostat

The helium gas target was cooled in a cryostat to temperatures between 4.5 K and 10 K at typical pressures between 0.3 bar and 1.0 bar. Although low gas temperature is not an essential condition for the metastability of antiprotonic helium atoms, two reasons required us to cool down the target. One was to ensure as small a stopping volume as possible of incident antiprotons by the high density of the helium gas at low temperatures. The other was to eliminate impurities from the helium gas target. Although we were careful about our vacuum system, traces of impurity gases such as hydrogen, oxygen, nitrogen or water were unavoidable. These gases work strongly as active quenchers of antiprotonic helium atoms, and even a few ppm (parts per million) of them would distort the spectrum [46, 54]. In cryogenic temperatures below 10 K, vapor pressures of these gases drop well below one ppm [70], and their quenching effect can be neglected.

We have observed longevity of antiprotons in the liquid and solid phases as well. However, their spectra showed a fast exponential component at early times [12] which was not explained by the theoretical simulation [14]. This component, absent in the low-pressure, low-temperature gas target, is due to interactions with neighboring helium atoms because of the high density. For all these reasons we chose low temperature gas as the target condition which was expected to approach the isolated atom condition most

closely.

3.2.1 Cryostat

Figure **3.9** shows our cryostat schematically. The target vessel, a cooling chamber, a liquid helium reservoir and a liquid nitrogen reservoir were all enclosed in a cylindrical evacuated outer vessel. Liquid helium which flowed from the bottom of the reservoir through a capillary was evaporated at the entrance to the cooling chamber, taking heat away from the inner target vessel. The flow rate which determined the cooling power could be adjusted by a needle valve at the entrance of the capillary. A heating wire and two sensors were attached to the end of the capillary and to the vessel, and the temperature of the gas target was stabilized at a chosen value by a controller which regulated the current of the heating wire.

The temperature was measured by the thermoelectric voltage of the thermocouple-type sensors. The calibration of the sensors used was checked in a test experiment which also aimed to verify the uniformity of the temperature of the target gas and the vessel; *i.e.* whether the temperature of the wall of the vessel at which the sensor was attached really reflected the temperature of the helium gas inside. For that, we inserted a thin and long bar with a calibrated thermocouple at its tip, through the gas tube from the top of the cryostat down into the target vessel. The real temperature $T_{\rm cal}$ of the gas (measured by the calibrated sensor) was compared with the temperatures $T_{\rm A}, T_{\rm B}, T_{\rm C}$ at a few points on the outer side of the walls. Thus the difference at ca. 6 K was $T_{\rm cal} - T_{\rm C} = -0.15$ K at 6.1 K and -0.21 K at 5.3 K for the target system in 1993–1995, and $T_{\rm cal} - T_{\rm A} = 0.0$ K for the modified setup in 1996, with an intrinsic error of ± 0.1 K of the sensors.

3.2.2 Target gas system

Figure **3.10** shows a diagram of the vacuum and the target gas system. The parts were connected by copper (1993) / stainless-steel (1994–1996) tubes and stainless-steel bellows. All lines connected to the target vessel were baked once before the experiments and were evacuated from time to time by a combination of a turbo-molecular pump and a rotary roughing pump to 10^{-6} Torr ($\sim 10^{-4}$ Pa). We measured the residual gas contamination with a mass spectrometer before filling with 99.9999% purity helium gas, and found the total contaminant pressure to be less than one ppm for temperatures below 30 K. The pressure of the target gas was monitored by a Baratron pressure gauge. The maximum pressure allowed for the target gas in the 1993–1995 experiments was 1.5 bar because of the tolerance of the quartz window. In 1996 we improved the target system which bore up to 10 bar. A 5 ℓ gas chamber was connected in the line both as a buffer for sudden

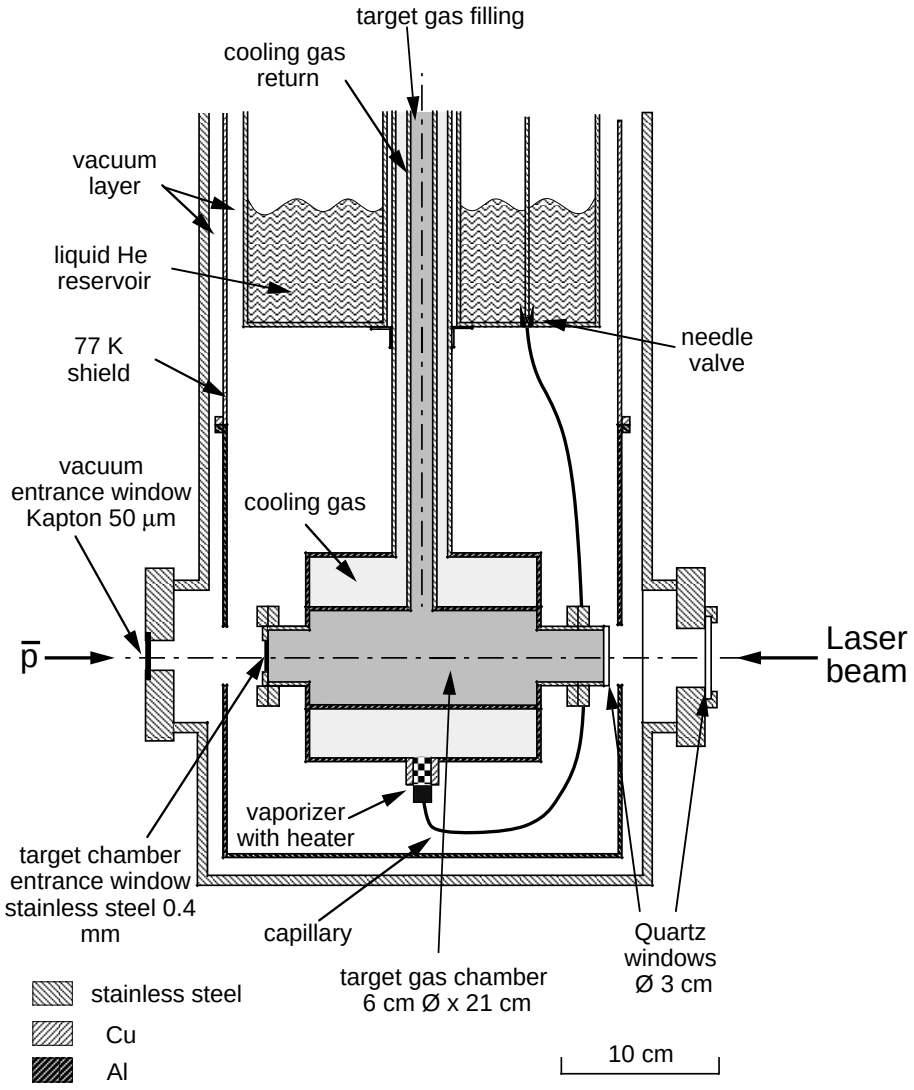

Figure 3.9: A diagram of the cryostat. The helium gas target was kept at a typical temperature of 4.5–10 K and pressure of 0.3–1.0 bar. By regulating the flow rate of liquid helium through the capillary into the cooling chamber and the current of the heating wire, the temperature could be stabilized to any cryogenic temperature.

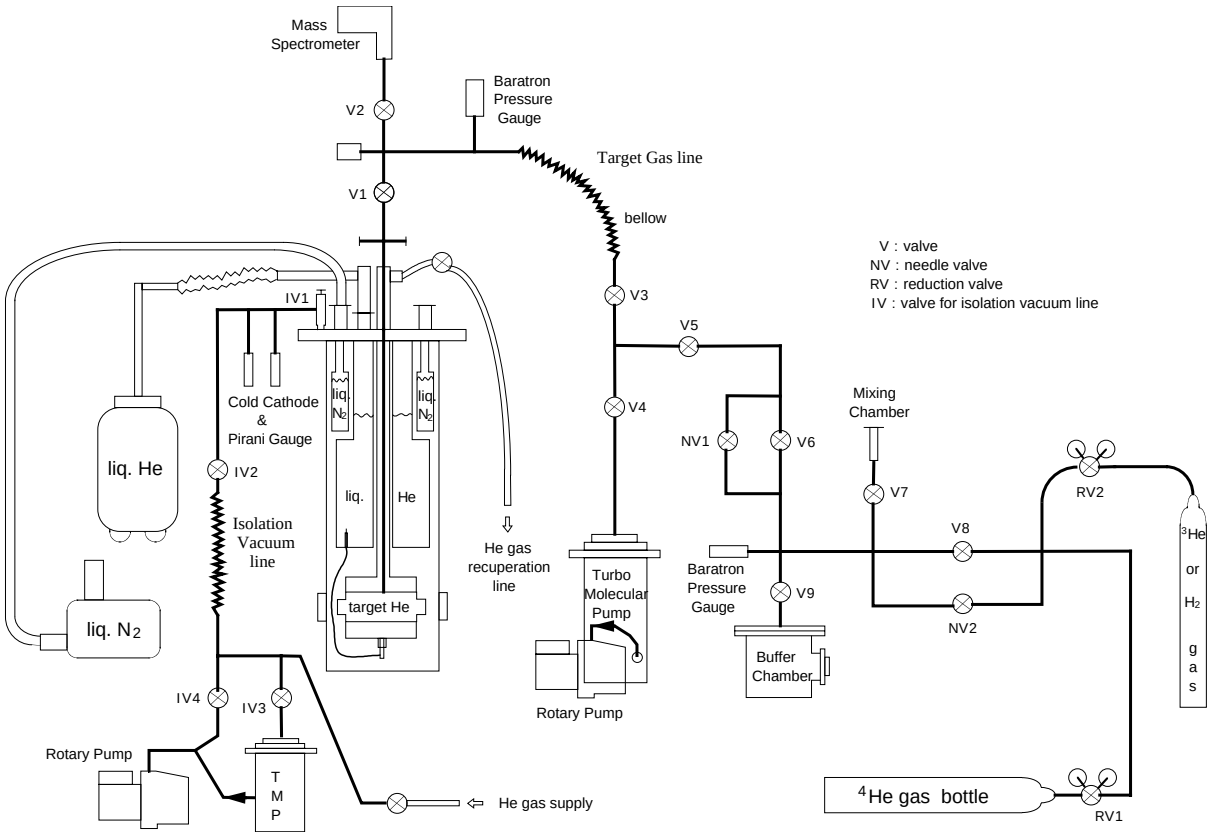

Figure 3.10: A diagram of the vacuum and the target gas systems.

pressure changes and for mixing additives to the target gas when investigating the effect of foreign gases on the metastability. A smaller cylindrical vessel of 50 cm^3 was used in parallel to this when preparing admixture at impurity (ppm) levels.

3.3 Laser System

3.3.1 Lasers

The level spacings of the metastable $\overline{p}He^+$ states we are interested in are about 2 eV [14, 15, 19, 20] and the wavelengths of the major transitions fall in the visible light range, so a tunable dye laser could be used. High power was required for the laser, due to the following reason: our strategy for observing the resonant transitions was to induce forced annihilation of antiprotons by the laser, and it had to occur within a relatively short time (less than tens of nanoseconds) compared with the lifetime ($\sim$ 3–4 μs) of the $\overline{p}He^+$ so that the resonance should appear as a visible sharp peak in the time spectrum. In order to fully deexcite the population from the metastable state in this short period, the Rabi

frequency Ω needed to be nearly of the order of a gigahertz. Theoretically calculated dipole moments μ for the "favored" transitions were typically 0.2–0.3 debye, and from the relation[†]

$$\frac{\Omega}{2\pi} = \frac{\mu E}{h} = 0.437 \times \mu\,[\text{debye}] \times \sqrt{P\,[\text{kW/cm}^2]}\ \ [\text{GHz}] \tag{3.1}$$

it was deduced that a laser power density (P) of nearly 1 MW/cm^2 was needed [45]. This requirement excluded the possibility of using continuous-wave lasers, and then the pulsed lasers had to be triggered by external signals produced when prompt annihilation of randomly arriving antiprotons did not occur. A high ignition rate was also required for reasonably fast data acquisition.

As a solution to these requirements, we used two identical and independent dye laser (Lambda Physik LPD3002) systems pumped each by a XeCl-excimer laser (LPX240i) at $\lambda = 308$ nm (see Figure **3.11** and Color figure IV). The excimer lasers had a maximum repetition rate of 400 Hz, *i.e.* they had a dead time of 2.5 ms after each shot for recharging their high voltage supplies. The lasers accepted external random triggers as well, with about 1 μs delay time before ignition. The duplication of the laser system not only halved the search time for the resonances, but also enabled the studies using two successive laser pulses with different timings mentioned in Appendix **B.2** [48, 49], permitted two laser beams to be applied simultaneously at different wavelengths to stimulate "double" resonant deexcitation (Appendix **B.1.2**) [51].

The first candidate resonance line was expected around $\lambda \sim 597$ nm, so we used Rhodamine 6G[‡] as a laser dye (which has a 40 nm scan range around 581 nm wavelength) dissolved in spectroscopy-grade methanol[§]. Another dye Coumarin 102[¶] was used for the observation of the second resonance line at 470 nm. For the search of resonances and the studies of lifetimes and population, the dye lasers were used in a broadband mode so that about 10 resonator modes were oscillating, yielding a bandwidth of 4–7 GHz (0.007 nm at 597 nm). For the measurements of the shift and width of the order of 1 GHz as mentioned in Chapter **5**, a higher resolution of the laser frequency and a more precise determination of the transition wavelengths were required. Thus, the bandwidth was narrowed to typically 1 GHz by using an intracavity etalon (dye laser model LPD3002E) and aligning the lasers carefully; especially we took care to suppress amplified spontaneous emission (ASE). Under these conditions, the best achievable resolution was 1.0 GHz. The

[†]Refer to equations in Appendix **F.1.2** for derivation of Eq. (3.1)

[‡]Rhodamine 6G: Benzoic Acid, 2-[6-(ethylamino)-3-(ethylimino)-2,7-dimethyl-3H-xanthen-9-yl]-ethyl ester, monohydrochloride. See Figure 3.12.

[§]For cleaning of the tube for the circulation of the dye solution, less flammable liquid "propylene carbonate" was also used. See Figure 3.12.

[¶]Coumarin 102: 2,3,4,6-1H,4H-Tetrahydro-8-methylquinolizino-[9,9a,1-gh]-coumarin. See Figure 3.12.

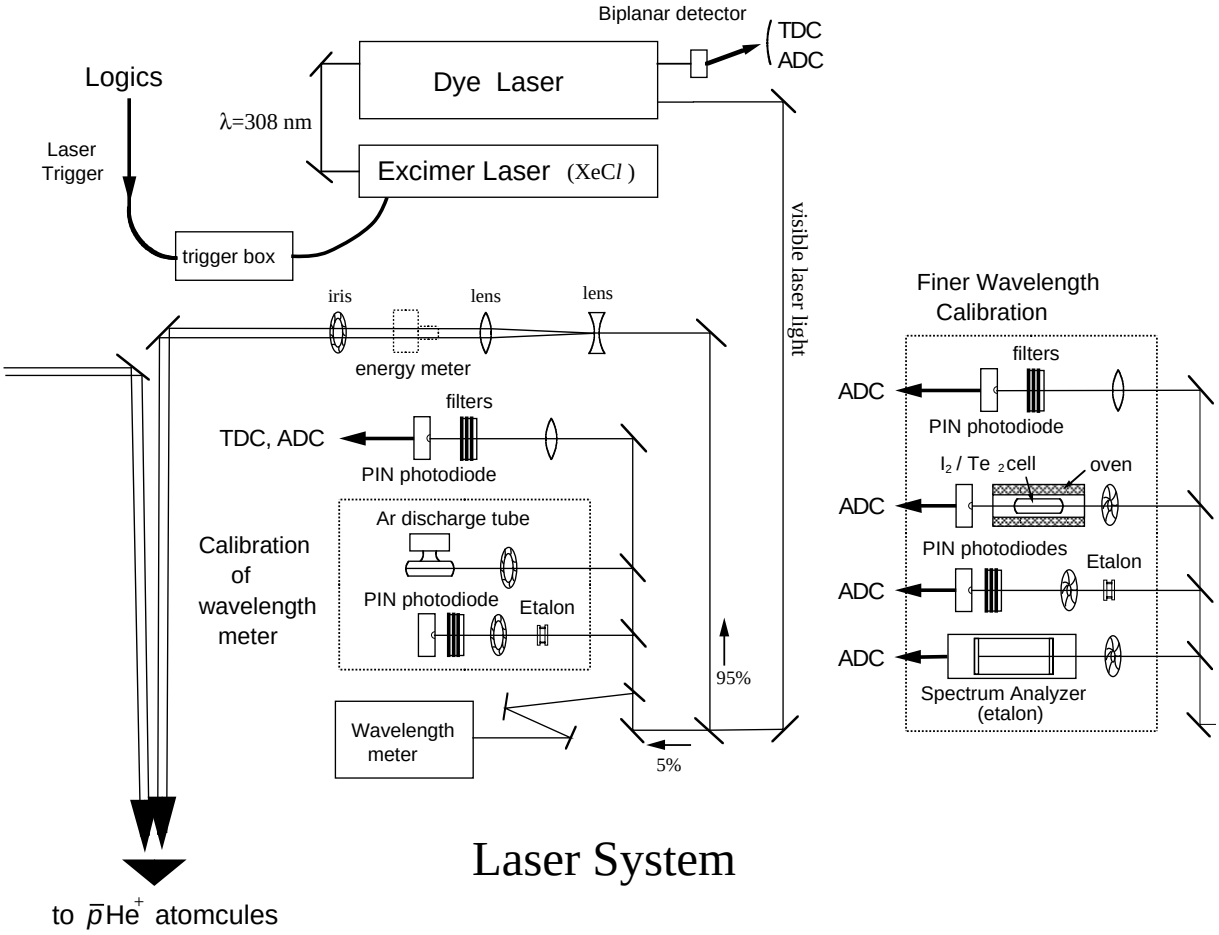

Figure 3.11: A schematic diagram of the laser system. We used two identical tunable dye laser systems pumped by XeC*l*-excimer lasers. The power of each dye laser beam was measured by a *p-i-n* photodiode and a thermopile-type energy meter, while the wavelength was monitored by a wavelength meter calibrated against standard argon atomic lines, or against iodine or tellurium molecular lines. The beams were expanded to about 15 mm diameter in the target in order to cover the stopping distribution of the antiprotons.

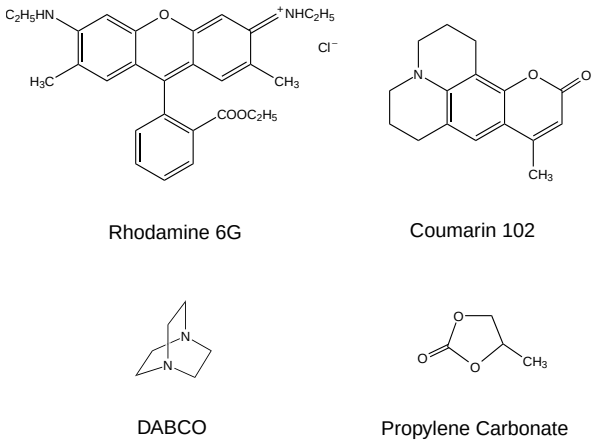

Figure 3.12: Dyes and other chemicals used for the dye lasers. Rhodamine 6G was used for the orange 597 nm resonance, Coumarin 102 for the blue 470 nm one. Triplet-quenching chemical "DABCO" was added to the solution to prolong the lifetime of the dye molecules. The dyes were dissolved in a spectroscopy-grade methanol, while propylene carbonate was also used for flushing the tube in which the dye solution circulated.

typical output energy in each excimer laser pulse was 80–140 mJ, and resulted in a dye laser pulse of 2–5 mJ. The excimer-laser pulses had disordered temporal profiles with decreasing three peaks, due to the characteristics of the discharge of the high voltage in a thyratron, and accordingly the dye-laser pulse had typically two peaks. Most of the dye-laser power was concentrated in the first 10 ns of the typical pulse duration of 40 ns. Refer to Figure **5.11-a**, p. 68.

Continuous workload of the lasers at high repetition required frequent maintenance. The normal lifetime at low ignition rate of dye solution of Rhodamine 6G is specified as 300 W h/ℓ. At 300 Hz and with the pulse energies above, we found that the dye deteriorated within one hour, corresponding to only 5–10 W h/ℓ input energy. This was probably because at our high ignition rate, dye molecules excited in one light pulse have a high probability of dissociation by further photon absorption in subsequent pulses. By adding triplet-quenching agent "DABCO"[‖] to the dye solution at a level of 1 g/ℓ, we were able to prolong the lifetime to 280 W h/ℓ. This still meant that we had to change the dye solution once a day, causing about two hours of interruption of our precious $\overline{p}$ beamtime and waste of a lot of solvents. Also the end mirrors of our excimer lasers needed cleaning in order to remove the deposits which accumulated on their surfaces and intercepted the

[‖]DABCO: 1,4-diazabicyclo[2,2,2]octane. See Figure 3.12.

light path. The whole process for cleaning took about three hours per laser, including flushing of the gas reservoir and realignment of the laser beam.

3.3.2 Light transport

The two dye laser pulses were merged about 8 m before the gas target after expansion in a telescope to a diameter of about 1.5 cm, large enough to cover the antiproton stopping distribution. After traversing the two quartz windows (see Figure **3.9**) and the target gas, the laser beam was retroreflected at the upstream stainless-steel window. The 20% reflection inefficiency of this put an additional heat load to the cryostat refrigerator. A PMT monitored light reflected and scattered from the quartz windows and allowed us to measure the time interval between the passage of the antiproton through the B counter and the arrival of the light pulse. The minimum time interval was typically 1.8 μs, and an additional delay could be added to the trigger signal when we studied the time dependence of the resonance peak intensity at later times [48, 49]. The minimum delay consisted mainly of electronic signal processing time (200 ns), response time of the excimer laser** ($\sim$ 1 μs), and propagation time of signals and laser light (300 ns). Short-term jitter of the ignition timing was only a few nanoseconds while the long-term drift was suppressed by a special trigger box to several nanoseconds. This trigger box measured for each pulse the time difference between the trigger signal and the ignition of the laser beam and adjusted its associated short delay time for the subsequent shots. Thus the ignition timing was stabilized over a long time. We note that for the 470 nm search we could reduce the minimum interval to 1.3 μs by improving the electronic logic processing and by bypassing the trigger box, at the cost of possible large ($\sim$ 100 ns) drift in the timing which could be eliminated or corrected for in the analysis program.††

3.3.3 Laser beam diagnosis

We measured the dye laser output power by inserting a thermopile-type energy meter (Scientech AC2501) into the main beam during the intervals of the LEAR spills. In addition, a p-i-n photodiode was used to monitor the timing and the energy of a small fraction of the separated beam for every pulse. The excimer pulse energies were also monitored pulse by pulse by biplanar detectors and were calibrated against another calorimeter (Scientech AC50UV). These data were sent to CAMAC TDC and ADC units‡‡ and added to the event record tapes.

**The response time of the thyratron until the discharge occurs.

††We could further reduce this interval down to 900 ns in 1996 by simply shortening the signal cable length.

‡‡TDC: time-to-digital converter, ADC: analog-to-digital converter

The vacuum wavelength of each dye laser was constantly monitored by a pulse-mode wavelength meter (Burleigh WA4500), the average value over about 40 laser light pulses being calculated in an auxiliary computer from the fringes of light transmitted through Fabry-Pérot interferometers. The wavelength meter itself was calibrated against standard absorption lines observed in an argon discharge-tube [71] using the opto-galvanic effect. The spacing between argon lines was measured by comparing them with the transmission curve through an interferometer (an etalon) with a fixed-space air gap. In the case of the narrow-band mode, the wavelength was calibrated instead with respect to standard iodine and tellurium lines [72, 73]. The absolute error of the wavelength meter was specified as 600 MHz, but the relative error was found to be better from the reproducibility of the central wavelength of the $\overline{p}\mathrm{He}^+$ resonance itself. The (systematic) error in relative frequency was thus 300 MHz for the narrow-band mode. Aiming at a more precise determination of the transition wavelengths, we also took the $\overline{p}\mathrm{He}^+$ resonance data simultaneously with the signals of the calibration standard, together with the interference pattern in a spectrum analyzer with a 3 GHz free spectral range. This so-called "on-line calibration" method will be explained in more detail in Chapter **5** and in Appendix **E.1**.

3.4 Data Acquisition and Analysis Method

3.4.1 Data acquisition

For each event the PM tube signals were standardized to NIM form for subsequent processing. The following discussion refers to the electronic logic diagram of Figure **3.13**.

A $\langle\!\langle$ good $\overline{p}\,\rangle\!\rangle$ is recognized as a coincidence between the two beam counter (B) PMT's with no corresponding signal in the ring counter (A) PMT ($\equiv B1 \wedge B2 \wedge \overline{A}$). When it has arrived and no prompt S signals are detected within 70 ns ("prompt veto"), we assume that a metastable $\overline{p}\mathrm{He}^+$ atom has been formed ($\langle\!\langle$ delayed event $\rangle\!\rangle$) in the target. If, however, any preceding $\overline{p}$ has been detected, confusion may occur in identifying which $\overline{p}$ has caused annihilation signals. To avoid this, only events with no preceding $\overline{p}$ within a period w are taken ("pre-pile-up rejection" by hardware [11]) as a $\langle\!\langle$ good delayed event $\rangle\!\rangle$, which opens a beam gate and starts the TDC's. A later signal from each shower counter will stop each channel of the TDC (LeCroy 4208) and gives the time delay of the $\overline{p}$ annihilation with 1 ns resolution. The $\langle\!\langle$ all $\overline{p}\,\rangle\!\rangle$ signal ($\equiv B1 \vee B2 \vee A$) enters a double-hit channel of the TDC which can record timings of the first two signals. The first pulse gives the arrival time of the $\overline{p}$, while the events with the second $\overline{p}$ signals are rejected in the analysis software ("post-pile-up rejection" [11]). At the end of the beam gate, the existence of a delayed $\langle\!\langle$ shower-counter hit $\rangle\!\rangle$ triggers the computer CES-J11 (Starburst: PDP-11 compatible CAMAC Auxiliary Crate Controller) and all the TDC and ADC data

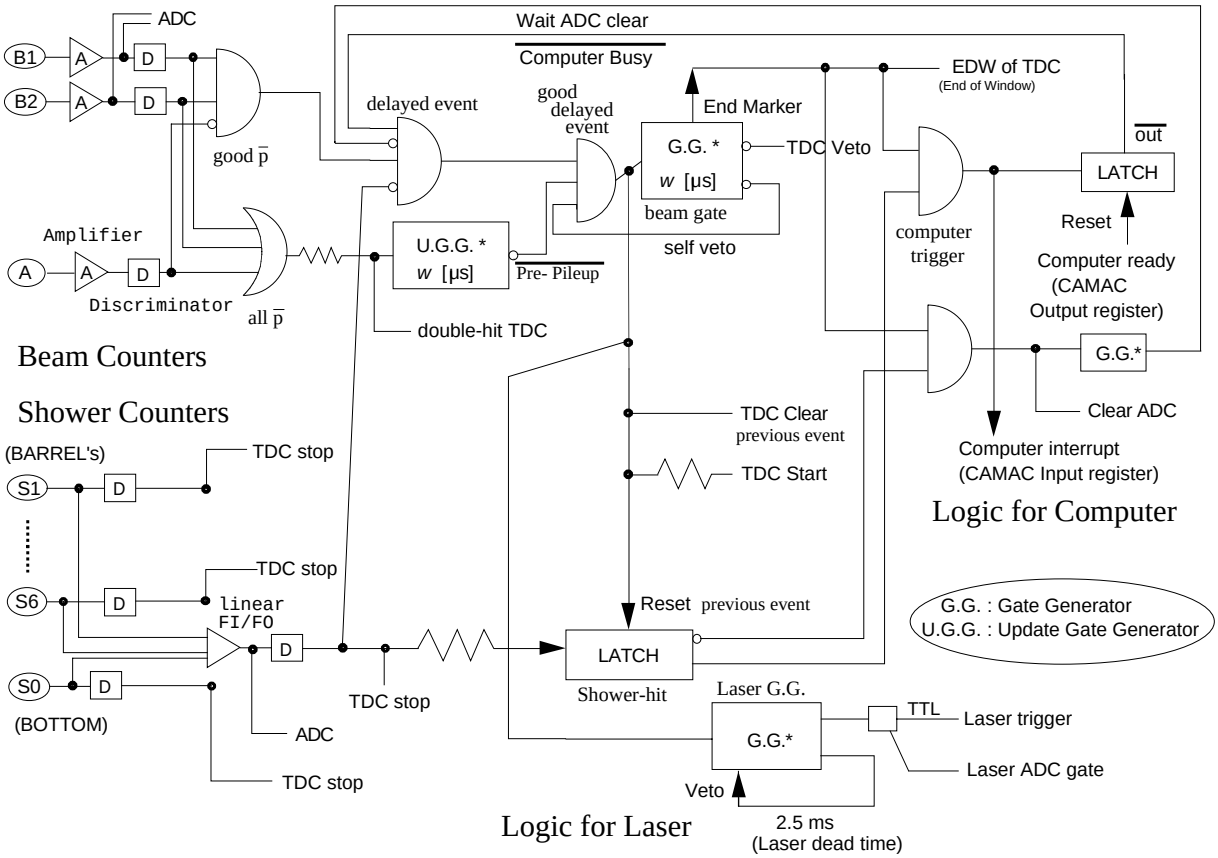

Figure 3.13: A simplified logic diagram for the detection system. When a "good $\overline{p}$" ($\equiv B \wedge \overline{A}$) has arrived and no prompt S signals are detected, we assume that a metastable $\overline{p}\mathrm{He}^+$ atom has been formed and generate a laser trigger unless the event is pre-pile-up rejected. At the same time the TDC gate is opened and the annihilation-time spectrum is taken for the period w (= 5,10,15 or 50 ns) of the beam gate. Any S signal during this period sets the latch module named "shower-hit", which then triggers the computer at the end of the gate and the event data are read out (or cleared if the latch is off).

a re read out and stored in its memory. When this memory has become full, the main VAX computer station is interrupted, the data are block-transferred and written down on the VCR tape. A large fraction of these are analyzed online. While the computers are busy by reading or transferring the data, data acquisition is blocked by hardware at the coincidence $\langle\langle$ delayed event $\rangle\rangle$.

If the lasers are to be fired and are in the ready state, they are triggered by a TTL pulse derived from the coincidence $\langle\langle$ good delayed event $\rangle\rangle$. A small fraction of the light beam diverted for laser diagnostic purposes to p-i-n photodiodes was also used to distinguish events with laser light from control events without laser light. For studies of metastable state lifetimes and the time dependence of their populations, we varied the laser trigger timing via a CAMAC programmable delay unit.

CAMAC scalers counted event rates of various coincidences and they were read out every two seconds. The temperature and the pressure of the target gas were converted into voltages and read out through ADC's. The wavelengths of the lasers were transferred via a GPIB interface, and were also recorded on the tape.

3.4.2 Data analysis and background elimination

The first action of the analysis program after discarding "post-pile-up" events in the B counter was to evaluate the time difference between the B signal and the corresponding S stop. We determined the absolute annihilation time of $\overline{p}$ after atomic capture by setting the $t = 0$ point at the center of the prompt peak for each (ith) shower counter, *i.e.* the annihilation time is given by $t_i = S_i - B - pedestal_i$. The error on this time interval comes from variation in particle flight times between the B counter and the stopping point and between the annihilation point and the S counters.

The time spectra were obtained by filling a histogram with the annihilation events according to the obtained annihilation time t_i. The spectra for single shower counters contained clear exponential background with about a 2.2 μs lifetime, which was ascribed to the decay of muons originating from positive pions that stopped in material surrounding the target, especially inside the heavy shower counters (see Figure **3.14**) [74]. In order to evaluate this background, we took data with an empty target (see Figure **3.15**), in which case all the incident antiprotons stopped at the walls or windows of the target vessel and annihilated promptly. The delayed signals attributed to the muon decay summed up to 1.6% of the number of incident antiprotons, as was also expected from the Monte Carlo simulations discussed in Section **3.1.2**.

It was essential to eliminate this π-μ-e background as its characteristic lifetime and the intensity were comparable to the one being studied. We did this by requiring that at least two of the seven shower counters were hit ($M \geq 2$ cut) and that the RMS deviation of

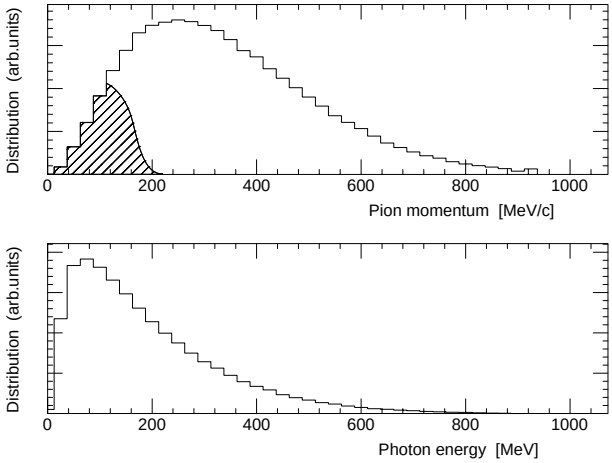

Figure 3.14: Top: The distribution of $\pi^{\pm}$ momenta calculated according to the phase space for several multi-pion final states. The hatched area indicates the low momentum region where positive pions stop inside the shower counters and show $\pi^+ \to \mu^+ \to e^+$ decay (see Section **3.4.2**). Bottom: The calculated distribution of the photon energy from $\pi^0 \to \gamma\gamma$ decay has a maximum around 100 MeV.

these hits from their mean be less than $\sqrt{10} = 3.16$ ns, *i.e.* $\sum_i^M (t_i - \overline{t})^2 / (M-1) < 10$ ns^2 (Δt cut), based on the fact that the decay of a positive muon gives only one positron out of time position whereas antiproton annihilation produces many particles simultaneously. These $M \geq 2$ and Δt cuts reduced the total background to less than 10^{-5} of the prompt peak, which meant a suppression by three orders of magnitude. In spite of this severe cut, it was only a quarter of the annihilation events that were lost, thanks to the high multiplicity of emitted pions and the high solid angle coverage of the shower counters. This excellent performance of the present detection system enabled us to obtain many background-free time spectra of the long-lived antiprotons [13].

3.4.3 Optimization of the event rates

For the laser spectroscopy experiments, we expected resonant enhancement in the $\overline{p}$ annihilation rate, which would appear as a sharp peak in the time spectra, and that this peak should be synchronized with irradiation of the laser light pulse some microseconds after the injection of the antiproton. The beam gate (annihilation time window) and the width of pile-up rejections were set to 5, 10 or 15 μs depending on the timing of the laser irradiation. In order to maximize data-acquisition effectivity, we calculated the event rate

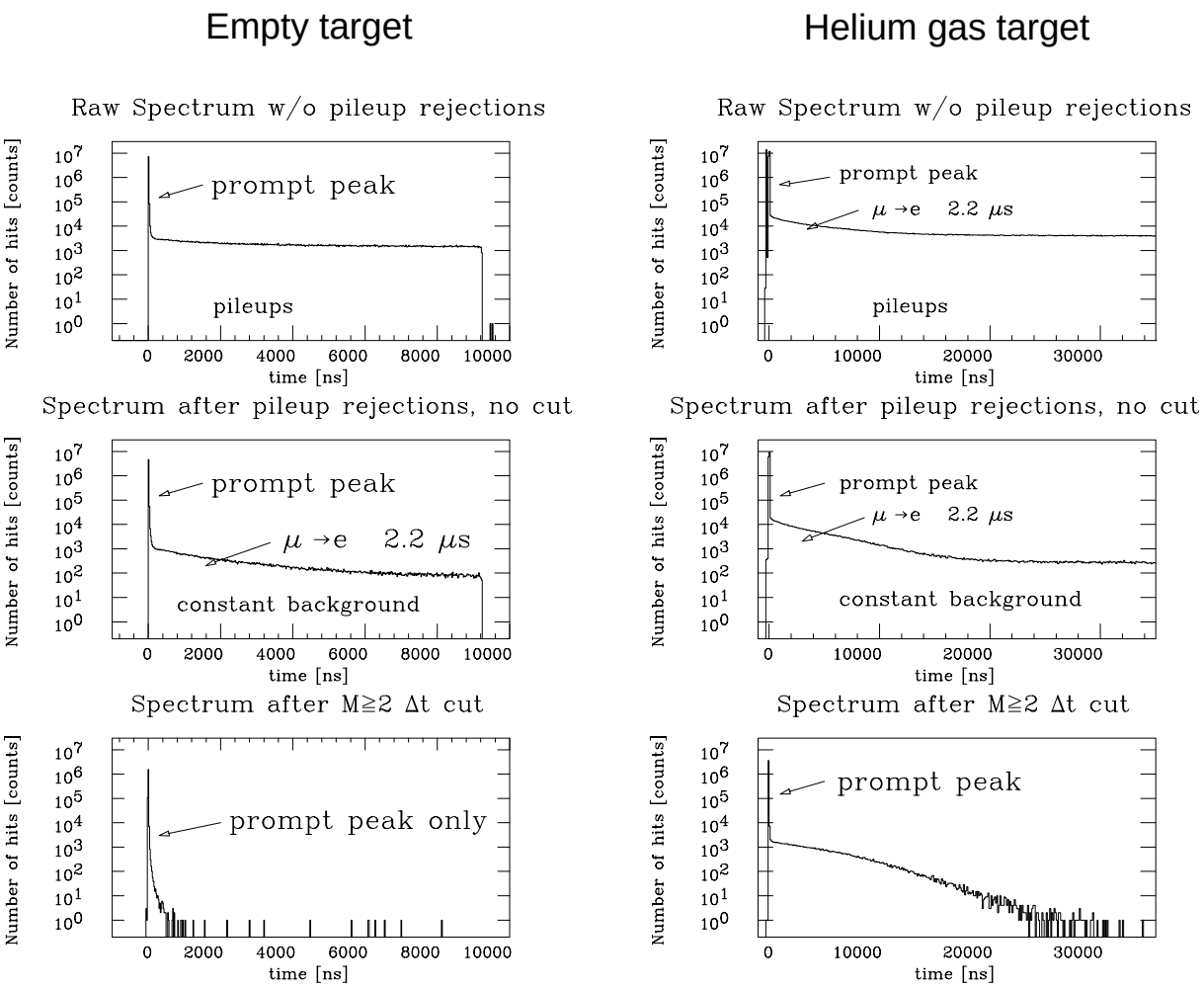

Figure 3.15: Top: The raw annihilation time spectra ($t_i = S_i - B - pedestal_i$) are filled with fake delayed annihilation associated with second antiprotons (post-pile-up). Middle: The spectrum for the empty-target data (left) after post-pile-up rejection by software contains a large exponentially decaying background from muons. Bottom: With the requirement of $M \geq 2$ and $\Delta t \leq \sqrt{10}$ ns a prompt peak remains solitary for the empty target (left) and a background-free DATS is obtained with the helium gas target (right). Note the different time scale among the figures on the left and right sides.

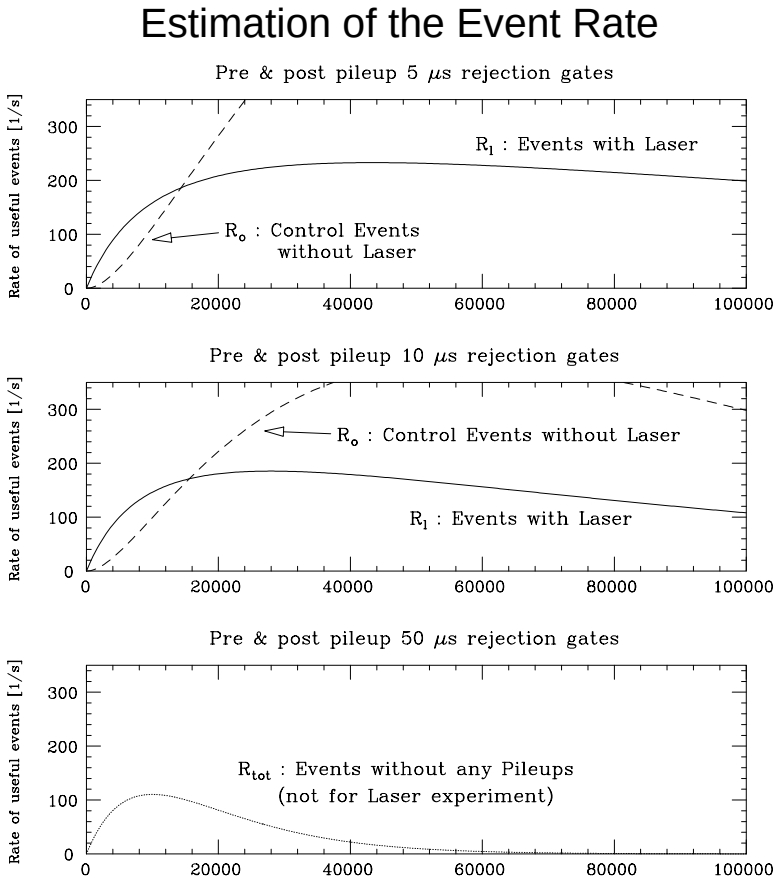

Figure 3.16: The estimated number of useful delayed events per second after pile-up rejection as a function of the rate r of incident antiprotons. Solid line: laser-triggered events (R_l), dashed line: control events without laser (R_o). The typical widths w of the beam gate and pile-up rejection gates were 5 μs (top) and 10 μs (middle). The experimental condition takes advantage of the flat plateau around the maximum of R_l : $20\,000 \leq r \leq 50\,000\ \mathrm{s}^{-1}$. When we studied the full lifetime spectra of $\overline{p}\mathrm{He}^+$ atoms without using lasers, a 50 μs beam gate was used (bottom).

as a function of the $\overline{p}$ beam intensity. Let us here define the following parameters:

r	: rate of incident $\overline{p}$ beam	$\sim 10^4$ s^{-1}
f	: fraction of delayed annihilation	$\sim 3\%$
$p \equiv rf$	: rate of delayed annihilation	$\sim 10^2 - 10^3$ s^{-1}
w	: width of the beam gate and the pre- and post-pile-up veto signals	~ 10 μs.
$p' \equiv p\,\mathrm{e}^{-wr}$	: rate of delayed annihilation free from pre-pile-up	
d	: dead time of the laser	~ 2.5 ms

The excimer laser had a $d = 2.5$ ms dead time after each shot. Delayed annihilation events which occurred during this period, however, were effectively accumulated as control data without laser. Once the laser is ready again, the next laser trigger will occur after an average time $1/p'$, so the rate of events with laser is given as $1/(d + 1/p')$. The post-pile-up rejection reduces the number of useful events by the factor e^{-wr} (the probability that no second $\overline{p}$ arrives within the window w). The rates R_l and R_o of useful delayed events with and without laser are then:

$$R_\mathrm{l} = \frac{\mathrm{e}^{-wr}}{d + 1/p'} \quad \text{and} \quad R_\mathrm{o} = p'dR_\mathrm{l} = \frac{p'd\,\mathrm{e}^{-wr}}{d + 1/p'}, \qquad R_\mathrm{tot} \equiv R_\mathrm{l} + R_\mathrm{o} = p\,\mathrm{e}^{-2wr}. \tag{3.2}$$

Figure **3.16** shows the calculated value of R_l as a function of the $\overline{p}$ rate r. The top and the middle graphs show flat plateaux around their maxima ($R_\mathrm{l} = 180$ – 230 s^{-1}) so that high event rates can be achieved over a wide range of the $\overline{p}$ beam intensity ($r = 20\,000$ – $50\,000$ s^{-1}) we were provided with during a LEAR spill. For finer intensity tuning we manipulated the opening of a collimator upstream in our beamline.

When we studied the full lifetime spectra (delayed annihilation time spectra, DATS) of the antiprotonic helium atoms without using lasers, a 50 μs beam gate was opened, and accordingly the gates for the pile-up rejections were increased to 50 μs. In this case the event rate was given by R_tot, as is shown in the bottom figure.

The computer deadtime was negligible because of the small event rate, except during runs in which prompt annihilations were included in the trigger in order to estimate the fraction of the delayed annihilation [13], in which case the computer deadtime was up to 80% and the equation above no more holds.

3.5 Analog Data Acquisition Method

Our unique technique of laser-induced annihilation so far explained was widely used for most of the experiments which brought about fruitful results to be presented in the later chapters. This digital counting method worked excellently, enabling spectroscopy of single atomcules [69] and was especially suited for precise measurements, some improvements

can nevertheless be made. Especially the inefficient use of laser pulses (each fired at one single atom) meant an enormous number of laser shots per measured point, relatively long measurement times and hard work of frequent maintenance. In order to overcome these deficiencies, we have also developed a modified experimental technique ("an analog method") [75] utilizing bunched $\overline{p}$ beams, which is more powerful for new resonance searches and lifetime measurements. Instead of digital-counting each $\overline{p}$ and accumulating millions of events with the same number of laser shots, a pulsed beam with 10^{8-9} $\overline{p}$'s were extracted at once and the consequent annihilations were recorded as an analog signal into a digital oscilloscope. Resonance spike was observed with a single laser shot irradiating the whole bunch of metastable $\overline{p}\mathrm{He}^+$ atomcules in the target chamber, which helped to save otherwise enormous number of laser shots.

This method had another merit when we studied the lifetimes of the metastable states. In the digital counting method, the laser trigger was created after a $\overline{p}$ has already stopped in the target, and due to the excimer laser which had a delay of ca. 1 μs until the ignition, The earliest possible laser timing was ca. 1.3 μs as mentioned in Section **3.3.2**. On the contrary, with the pulsed $\overline{p}$ beam, the arrival time of the $\overline{p}$ bunch was foreseen by the signal from the kicker magnet of the LEAR ring, so that the laser could be triggered in advance of the $\overline{p}\mathrm{He}^+$ formation. We could investigate the state populations at as early as 500 ns[♯] after the formation. The readers are referred to Ref. [75] for details of the experimental setup for this analog method.

With both these complementary modes, digital and analog, of "laser-induced annihilation spectroscopy" techniques, we have so far clarified many unique properties of antiprotonic helium atoms.

[♯]Here the earliest possible timing was limited by the response time of the switching gate for a PMT we used for this analog counting method. This PMT was specially made, with less number of dinodes and the ability of gating off the huge signals by the prompt annihilation of numerous antiprotons.

Chapter 4

Observation of Laser Resonances

In the series of our laser spectroscopy experiments we have so far found 13 resonance lines of $\overline{p}\mathrm{He}^+$ atomcules including 3 for $\overline{p}\,{}^3\mathrm{He}^+$. The observed transition energies all agreed with those of the theoretical calculations, and thus proved the theoretically predicted level structure of the $\overline{p}\mathrm{He}^+$ atomcule.

4.1 Discovery of the First Resonances

For searching resonant transition lines, the wavelengths of the dye lasers were scanned step by step. To gain enough statistics, about half a million delayed-annihilation events were taken (with the same number of laser shots fired) for each wavelength. This took 20–30 minutes. The scanning region was chosen according to theoretical calculations, available at that time, on the level scheme and the transition rates of the states [14, 19, 20]. Their predictions for the transition wavelength varied from 594 nm to 600 nm for the first candidate transitions (see Figure **4.3**) while the laser bandwidth was narrow (~ 0.007 nm), so that we had to scan for a few hundred steps until we found the resonance.

The signals of the first two successful observations of laser-induced resonant transitions in a $\overline{p}\mathrm{He}^+$ atom, discovered in 1993 and 1994, respectively, are shown in Figure **4.1** and in Figure **4.2**. The laser induced a transition from a metastable state to an Auger-dominated short-lived state followed by immediate annihilation, resulting in a sharp peak in the spectrum at $t = 1.8$ or $t = 1.3$ μs (arrival time of the laser beam) after the injection of the antiproton. The distinct depletion in the annihilation rate after the peak (clearly visible in Figure **4.2**) is also evidence for the depopulation of the metastable state.

In order to determine the central resonance wavelength, the DATS spectra were taken for a range of wavelengths around the resonance line, and the area of the resonance peak,

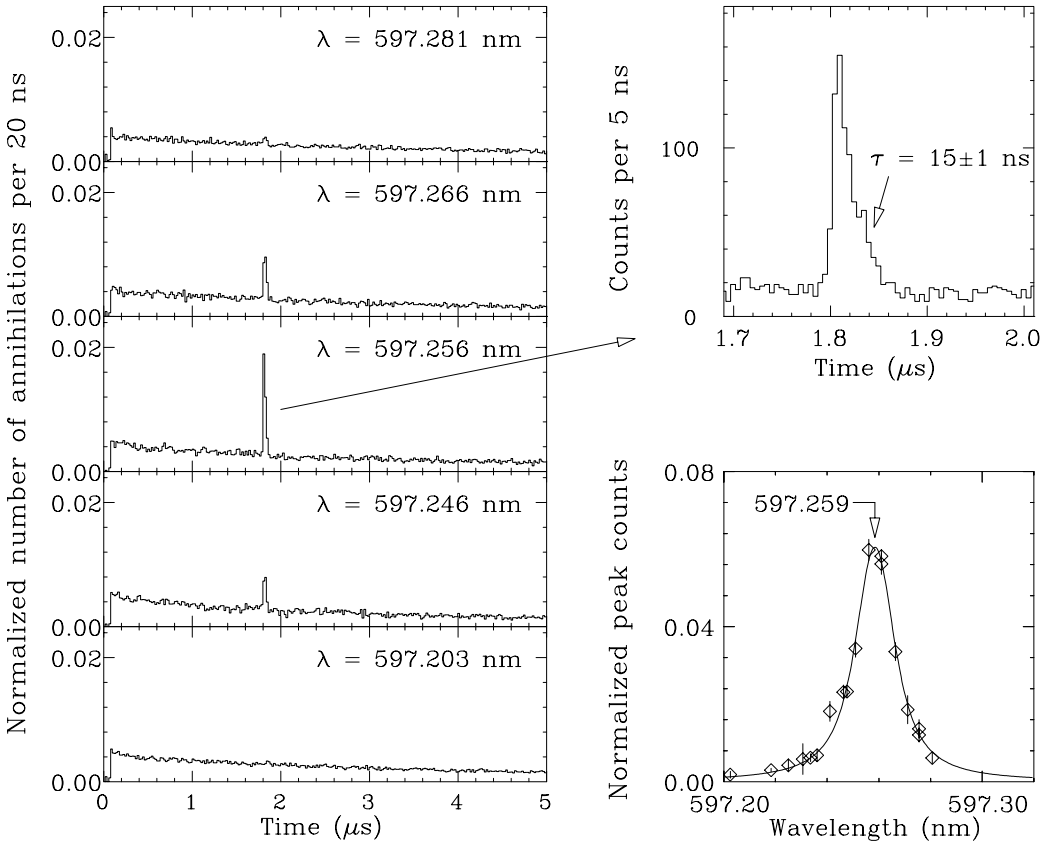

Figure 4.1: The first observation of the laser-induced annihilation signal. When the laser wavelength was tuned over the resonance line a sharp peak appeared in the $\overline{p}$ annihilation-time spectrum at the instant of arrival of the laser pulse (left and right top). The center of the resonance line, plotted as the peak area versus the wavelength, is at 597.259(2) nm (right bottom). This resonance has been assigned to the $(n,l) = (39,35) \Rightarrow (38,34)$ transition.

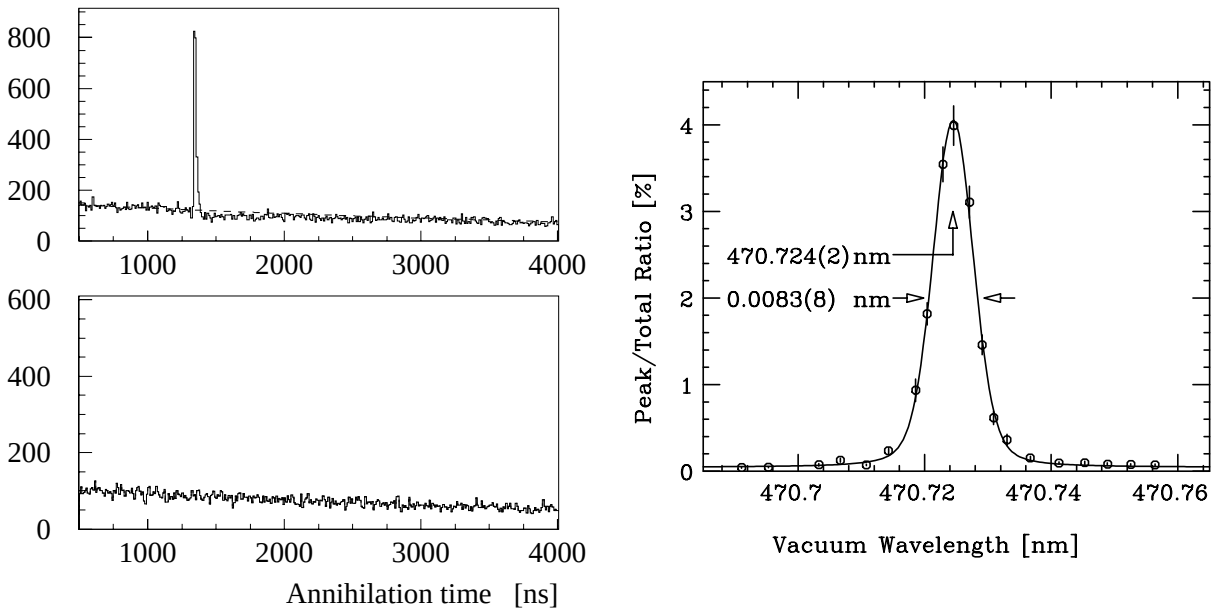

Figure 4.2: Observed delayed annihilation time spectrum of $\overline{p}\mathrm{He}^+$ atoms with laser irradiation at a vacuum wavelength of 470.724 ± 0.002 nm (left top) [49]. At the time of the irradiation (1.3 μs after the $\overline{p}$ stop), the laser has induced a resonant transition in the cascade series $v = n - l - 1 = 2$ from a metastable state $(n,l) = (37,34)$ to an Auger-dominated short-lived state (36,33), followed by an immediate annihilation and thus resulting in the sharp peak in the spectrum. The distinct depletion in the annihilation rate after the peak is also evidence for the depopulation of the metastable states. An off-resonance spectrum is shown in comparison (left bottom). (Right): The peak area normalized to the total number of metastable atoms plotted against the wavelength of the laser light, showing a typical resonance profile. The largest contribution to the line width is the saturation broadening due to the high laser power.

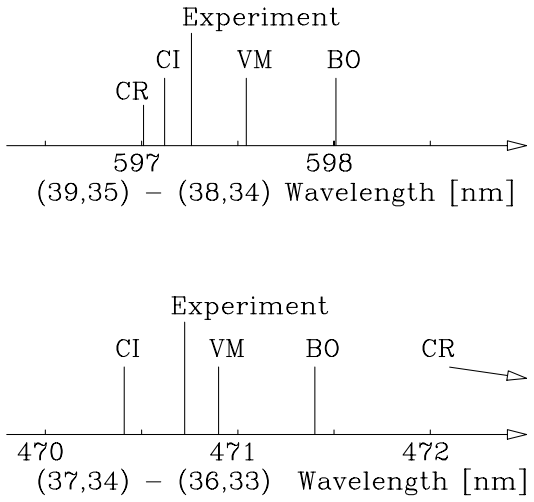

Figure 4.3: Experimentally determined vacuum wavelengths for the first two resonances found are compared with various calculations available at that time. The agreements are in the 10^{-3} order. See Section **2.2** for the full name of the different calculation methods.

i.e. the number of excess annihilations at the laser timing in the DATS was counted.* This peak count was then normalized to the total number of delayed annihilations and plotted against the wavelength. The obtained resonance curve was fitted with a Lorentzian function convoluted with a Gaussian of the laser bandwidth and the center of the resonance was determined.

Thus the first two discovered resonance lines had their central vacuum wavelengths† of 597.259 ± 0.002 nm [47] and 470.724 ± 0.002 nm [49], in agreement with the theoretical predictions. They were assigned to the transitions $(n,l) = (39,35) \Rightarrow (38,34)$ and $(37,34) \Rightarrow (36,33)$ at the ends of the radiative cascade series $v = n - l - 1 = 3$ and 2, based on the theoretical calculations [36, 45] of the Auger lifetimes discussed in Sections **2.1** and **2.3.2**. From the studies employing two successive laser shots to the atom as will be discussed in Appendix **B.2**, we could estimate the depopulation efficiency of the metastable states. Typically the value was as high as 80–90% [48, 49] due to the high power of the laser pulses, which produced a very distinct resonance signal. In fact, the laser power (2–5 mJ) turned out to be much higher for the "favored" transitions than was necessary to saturate the resonance (~ 0.1 mJ per pulse), causing thereby large power broadening of the resonance width.

*For the estimation of the non-resonant annihilation background below the resonance peak, the spectrum in a time window of 1 μs around the peak and excluding the peak itself was fitted by a linear line. Most of the DATS were fitted well enough by the linear functions, but DATS taken at high densities had a fast-decaying component with a lifetime of a few hundred nanoseconds (see Appendix **B.3**), and they had to be fitted instead by single-exponential curves. The number of resonant annihilations were then given as the number of total annihilation events within a 50–100 ns time window at the time of the laser irradiation, minus the estimated number of non-resonant annihilations.

†Throughout this thesis, all the wavelengths we refer to are "vacuum wavelengths", *i.e.* as measured in vacuum and not in the helium or any other media.

4.2 Other Resonances and Determination of Atomcular Structure

In 1995, Korobov calculated transition energies of the $\overline{p}\mathrm{He}^+$ atom [30] which agreed with our experimental value to a 50 ppm precision. His precise predictions helped us to reduce drastically the scanning time for search for new transitions (from one week to one hour), and we have subsequently found several more resonance lines.

In fact, in 1995, we found three more resonances at 529 nm [51], 713 nm and 726 nm [52, 53]. In 1996, the discoveries were for 5 more lines with the "HAIR" method explained in Appendix **B.4.3**. We also found 3 resonances in $\overline{p}\,^3\mathrm{He}^+$: two in 1995 as reported in Ref. [50], which corresponded to the first two in $\overline{p}\,^4\mathrm{He}^+$, and another one in the next year [58].

Table **4.1** and Figure **4.4** ($\triangleright$ Color figure V) summarizes all the resonances we have so far found, with their transition wavelengths in vacuum and state assignments. Detailed explanations on each resonance are to be mentioned in the following chapter and in Appendix **B**, as noted in the table.

With these many resonances, we have proven that the delayed annihilation is without doubt due to the formation of metastable $\overline{p}\mathrm{He}^+$ atomcules, as predicted by the early work of Condo [8] and Russell [9]. Recent theoretical calculations on the level energies of the three-body system has yielded good results which agrees with our experimental values to a 10^{-6} (or a ppm) level. Figure **4.5** compares our experimental vacuum wavelengths with those of Korobov's calculations [30, 31]. This precise agreement excludes the possibility of different assignments of the angular momentum l, which implies that the position of the theoretically-drawn distinct border between the metastable states and short-lived states has been experimentally settled. This gives a firm proof of the "$|\Delta l| \leq 3$ Auger dominance rule" (see Section **2.3.2**) and justifies the qualitative reliability of the calculations of the Auger transitions. A quantitative verification of the Auger rates is given in Appendix **B.2.3**.

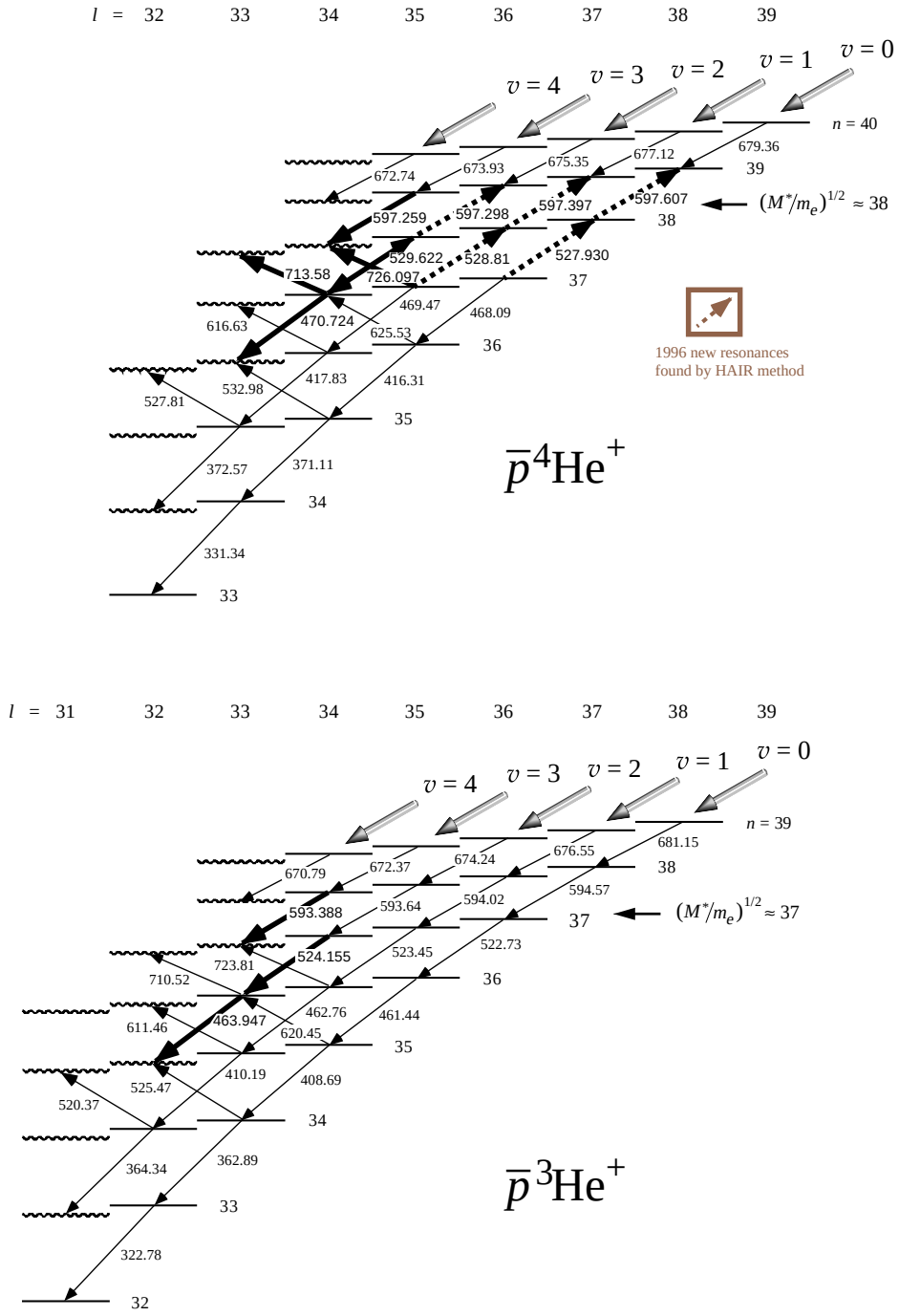

Figure 4.4: Level diagrams of the metastable states of the $\overline{p}\,^4\mathrm{He}^+$ and $\overline{p}\,^3\mathrm{He}^+$ atomcules are shown with so-far observed laser-induced resonant transitions in thick arrows. Unobserved lines are indicated with transition wavelengths calculated by Korobov [35, non-relativistic values].

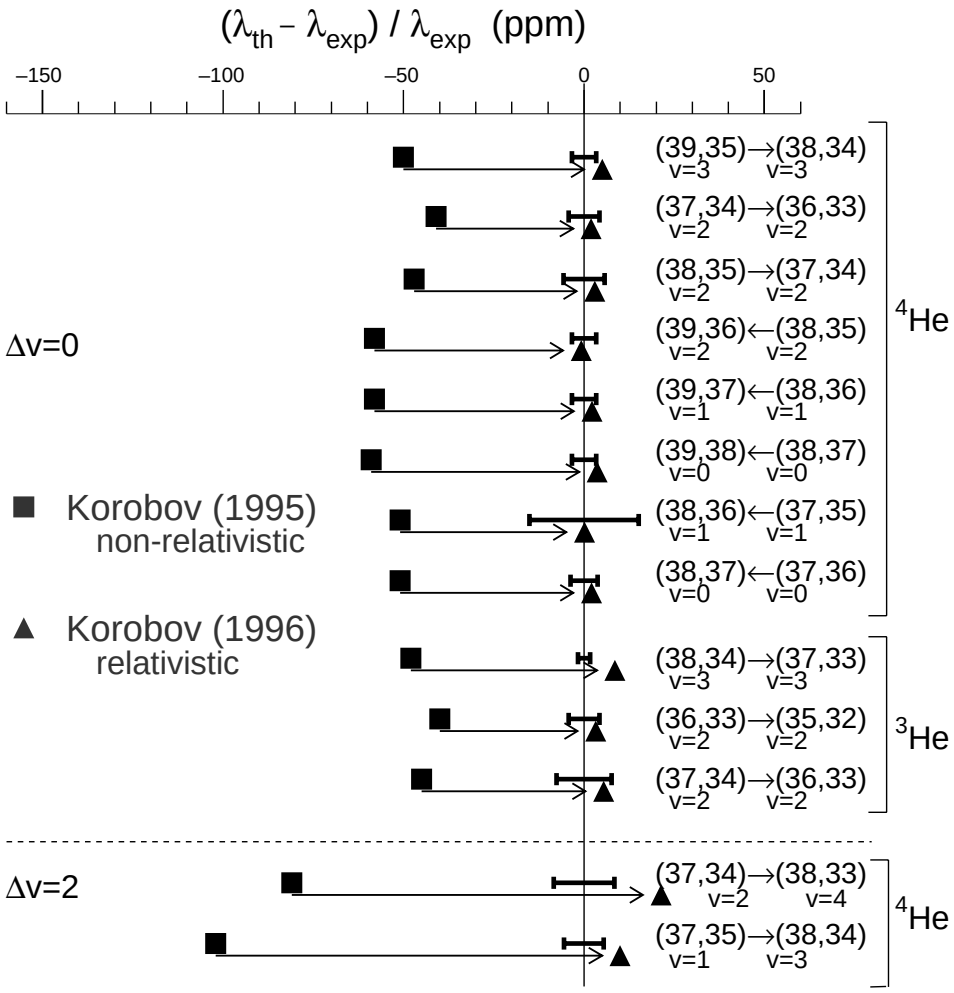

Figure 4.5: Comparison of the observed transition wavelengths λ_{exp} in vacuum and the calculated values λ_{th} from Refs. [30] and [31] (see Section **2.2.3**). The small discrepancies of typically 50 ppm (100 ppm for "unfavored" transitions) with non-relativistic calculations were further reduced to several ppm when relativistic effects (mainly correction to the kinetic energy of the electron) were taken into account. Note that the experimental values were obtained at different target conditions, typically at 6 K and 500 mb, and are or may be subject to a collisional shift, as explained in the following Chapter **5**.

Table 4.1: Transition wavelength and the assignments of the quantum numbers for the 13 discovered resonances are tabulated. The resonances are for $\overline{p}\,^4\mathrm{He}^+$ atomcules unless otherwise noted. Refer to each chapter for the different methods of observation.

Transition (n,l,v)	Wavelength [nm]	Comments	References	Chapter/Sections
$(39,35,3) \Rightarrow (38,34,3)$	597.259 ± 0.002		[47, 48]	**4.1, 5, B.2**
$(37,34,2) \Rightarrow (36,33,2)$	470.724 ± 0.002		[49]	**4.1, 5, B.2**
$(38,35,2) \Rightarrow (37,34,2)$	529.622 ± 0.003	Double reson.	[51]	**B.1.2**
$(37,35,1) \Rightarrow (38,34,3)$	726.097 ± 0.003	Unfavored	[52, 53]	**B.1.1, B.5**
$(37,34,2) \Rightarrow (38,33,4)$	713.578 ± 0.006	Unfavored	[52]	**B.1.1, B.2.4**
$(38,34,3) \Rightarrow (37,33,3)$	593.388 ± 0.001	$\overline{p}\,^3\mathrm{He}^+$	[50]	herein
$(36,33,2) \Rightarrow (35,32,2)$	463.946 ± 0.002	$\overline{p}\,^3\mathrm{He}^+$	[50]	herein
$(37,34,2) \Rightarrow (36,33,2)$	524.155 ± 0.004	$\overline{p}\,^3\mathrm{He}^+$	[58]	herein
$(38,35,2) \Rightarrow (39,36,2)$	597.298 ± 0.002	HAIR*	[55]	**B.4.3**
$(38,36,1) \Rightarrow (39,37,1)$	597.397 ± 0.002	HAIR*	[55]	**B.4.3**
$(38,37,0) \Rightarrow (39,38,0)$	597.607 ± 0.002	HAIR*	[55]	**B.4.3**
$(37,35,1) \Rightarrow (38,36,1)$	528.808 ± 0.008	HAIR*	[55]	**B.4.3**
$(37,36,1) \Rightarrow (38,37,1)$	527.930 ± 0.002	HAIR*	[55]	**B.4.3**

* HAIR stands for hydrogen-assisted inverse resonance which will be explained in Appendix **B.4.3** and in Ref. [55].

Chapter 5

Collisional Shift and Broadening of Resonance Lines

The measured transition energies for all the discovered lines showed good agreement with theoretical predictions as shown in Figure **4.5**. These theoretical calculations are based on a three-particle ($\overline{p}e^-\mathrm{He}^{++} = \overline{p}\mathrm{He}^+$) model in which the $\overline{p}\mathrm{He}^+$ atom is tacitly assumed to be isolated and in vacuum. Experimentally these exotic atoms were produced by stopping $\overline{p}$ particles in 0.5–1 bar helium gas, cooled down to 5–10 K (see Section **3.2**). In such relatively dense media the $\overline{p}\mathrm{He}^+$ atomcule is subject to frequent collisions with surrounding normal helium atoms so that the assumption of in vacuum isolation is by no means true. In fact, we will see in Appendix **B.3** that under this condition certain metastable level lifetimes are shortened drastically with increasing density [57]. Further effect of collisions are to shift the resonance frequencies away from their original values and to broaden the linewidths, generally known for normal atoms and molecules as the pressure shift and collisional broadening.* In fact, we did observe a certain shift of the central resonance frequencies at different target-density conditions, and systematically studied this phenomenon. The studies were important in determining precisely the unperturbed transition energies to be compared with the theoretical calculations. The shifts and widths themselves are an interesting subject, because they contain useful information on the collisional dynamics between $\overline{p}\mathrm{He}^+$ and helium atoms.

*We use in this paper, the terms "density shift" and "collisional broadening (width)" instead of "pressure shift" and "pressure broadening" as they are usually referred to. This is because the primary factor for the shift and broadening is the density of the media, which is not at all proportional to and should be strictly distinguished from the pressure at our low-temperature conditions.

5.1 Density Shift of the Resonance Lines

5.1.1 Experimental conditions

We have observed that the central resonance frequencies shift and broaden at different target conditions, and systematically studied this phenomenon for the resonance lines, $(n,l) = (39,35) \Rightarrow (38,34)$: 597.26 nm and $(37,34) \Rightarrow (36,33)$: 470.72 nm. These lie at the ends of metastable radiative cascade series $v = n - l - 1 = 3$ and 2, respectively. We measured resonance profiles by scanning the wavelength at different helium target conditions. Our data were taken at various laser powers. As expected, the laser power did not have any influence on the center of the resonance, while the width increased at high power on account of saturation broadening.

In the first series of experiments in 1995, our target pressure was limited to a maximum of 1 bar by the strength of the quartz window of the target vessel. The temperature was kept at 6.2 K, except for a few points taken at 15 K. In the next year, we improved the target system and took data at higher pressures up to 8 bar. We made use of the super-critical phase[†] of helium, where the density increases with pressure continuously without phase transition from gas to liquid. Refer to Figure **5.1** and Figure **5.2** for phase and density diagrams of ^{4}He.Thus we could achieve as high a density as that of liquid helium; helium of 8 bar at 5.8 K is denser than liquid helium under atmospheric pressure. Many data were taken at 5.8 K with different target pressures, but we avoided 3–5 bar region which is close to the critical point (5.2 K, 2.25 atm) where the density changes drastically with slight pressure fluctuations (see Figure **5.2**). Instead, we took one data-point at 6.3 K in order to do the measurement at well-defined density.

5.1.2 Observed shifts

Figure **5.3** shows resonance profiles taken for the 597.26 nm line at different pressures ranging from 530 mb to 8.0 bar at temperatures of 5.8–6.3 K. The graphs plot the normalized count of the resonance peak area in the DATS spectra, versus the calibrated vacuum wavelength. The center shifted toward longer wavelength and the width became broader for higher pressures. We determined the central vacuum wavelengths by fitting the profile data with a Lorentzian convoluted with a Gaussian of the laser bandwidth, and

[†]We first intended to increase the density by lowering the temperature and do the measurements in liquid helium. But in that case we would have had to use super-liquid phase of helium to avoid formation of gas bubbles due to the laser heat, and to be prepared for possible sudden burst of pressure on vaporization in case the temperature control failed. Instead, we decided to increase the pressure to achieve higher density, at a higher temperature than the critical temperature (5.2 K): the phase called "super-critical".

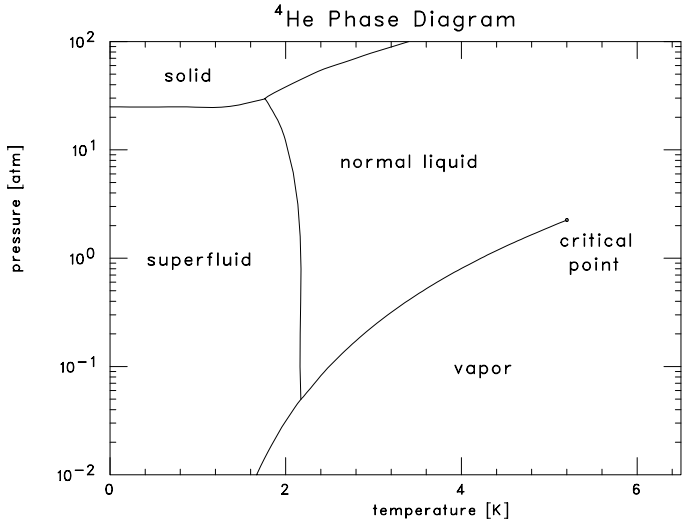

Figure 5.1: A phase diagram of ^{4}He. Experiments were performed mainly at around 6 K and 0.17–8.0 bar.

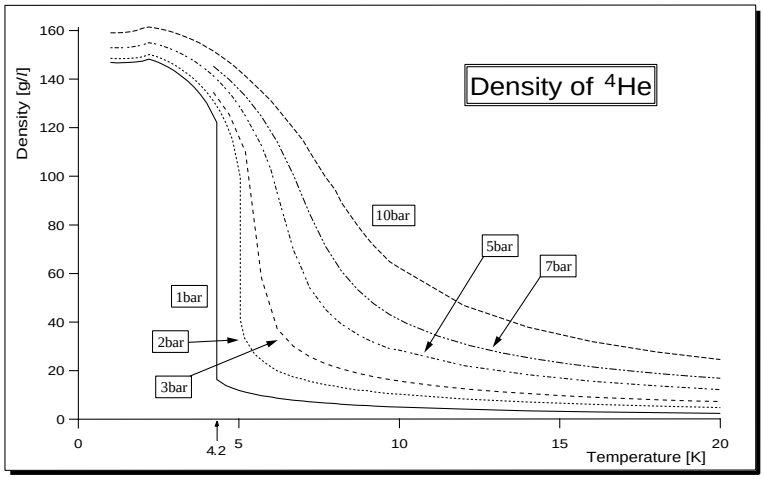

Figure 5.2: Density of ^{4}He is plotted as a function of the temperature and the pressure. Above the critical temperature of 5.2 K, no phase transition from gas to liquid is observed, but the density changes drastically near the critical pressure of 2.26 bar.

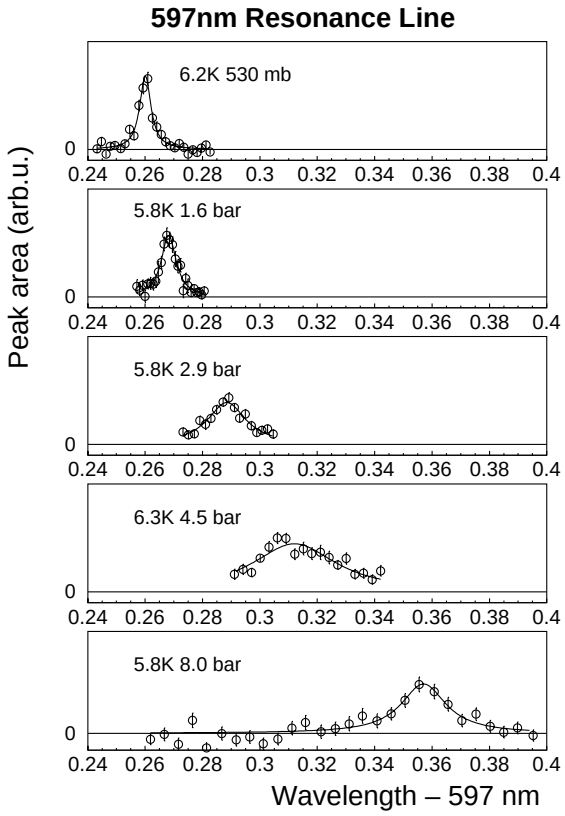

Figure 5.3: Resonance profiles of the 597.26 nm line showing red shifts of the center with helium density.

plotted them against the target density.[‡] The target temperature and pressure were always monitored and recorded on the data tape, and their calibrated values[§] were converted into the density using a program [76] based on the cryogenic helium database. It was essential to use this database, especially at the super-critical phase where the ideal-gas assumption is totally broken.

The results at different target conditions are summarized[¶] in Table **5.1**and in Figure **5.4** (for lower density conditions), which show both linear and "red" shifts for the two studied transitions. The data at 15 K fit well on the line if plotted against density, but not against pressure. This means that the shift is proportional to the density (ρ), with no, or small, dependence on the temperature. The vacuum wavelength λ is thus expressed in

[‡]The data in Table **5.1** are actually the results of hyperfine-doublet fit. See Section **5.3**.

[§]See Section **3.2.1** for the calibration of target temperatures.

[¶]Refer to Appendix **E.2**, p. 133, for a full set of data.

Table 5.1: Summary of the shift measurements. Calibrated values for the central vacuum wavelengths of the two resonances at different target conditions (temperature, pressure and corresponding density), obtained as results of hyperfine-doublet fits (597 nm lines, see Section **5.3.2**) or single-peak fits (470 nm lines), are shown with relative errors which include both statistical and systematic errors for the relative wavelengths. The data written in *italic style* were taken for the purpose of the absolute calibration of the wavelengths with respect to the standard reference lines, and the errors given are the absolute errors instead. A more detailed full set of data is listed in Appendix **E.2**.

T [K]	p [bar]	ρ [g/ℓ] $\pm$ $\delta\rho$	λ [nm] $\pm$ $\delta\lambda_{\mathrm{rel}}$
6.2	0.17	1.38 ± 0.03	597.2582 ± 0.0003
6.2	0.31	2.49 ± 0.05	597.2585 ± 0.0003
15.2	1.00	3.17 ± 0.03	597.2598 ± 0.0003
6.2	0.53	4.37 ± 0.09	597.2601 ± 0.0003
5.8	*0.54*	*4.78 ± 0.10*	*597.2606 ± 0.0002*
6.2	0.94	8.07 ± 0.18	597.2629 ± 0.0004
5.8	1.56	16.1 ± 0.6	597.2681 ± 0.0005
5.8	2.0	23.0 ± 1.1	597.2737 ± 0.0006
5.8	2.9	45 ± 5	597.2885 ± 0.0007
6.3	4.5	78 ± 6	597.3119 ± 0.0022
5.8	8.0	127 ± 2	597.3570 ± 0.0011
6.3	0.18	1.43 ± 0.02	470.7223 ± 0.0003
6.2	0.54	4.44 ± 0.08	470.7227 ± 0.0003
6.3	0.82	6.83 ± 0.14	470.7232 ± 0.0006
6.3	1.17	10.1 ± 0.2	470.7237 ± 0.0004
5.3	0.97	10.2 ± 0.3	470.7236 ± 0.0017
6.0	1.18	11.0 ± 0.3	470.7239 ± 0.0007
5.8	1.66	17.5 ± 0.6	470.7244 ± 0.0013
5.8	2.5	32 ± 2	470.728 ± 0.001

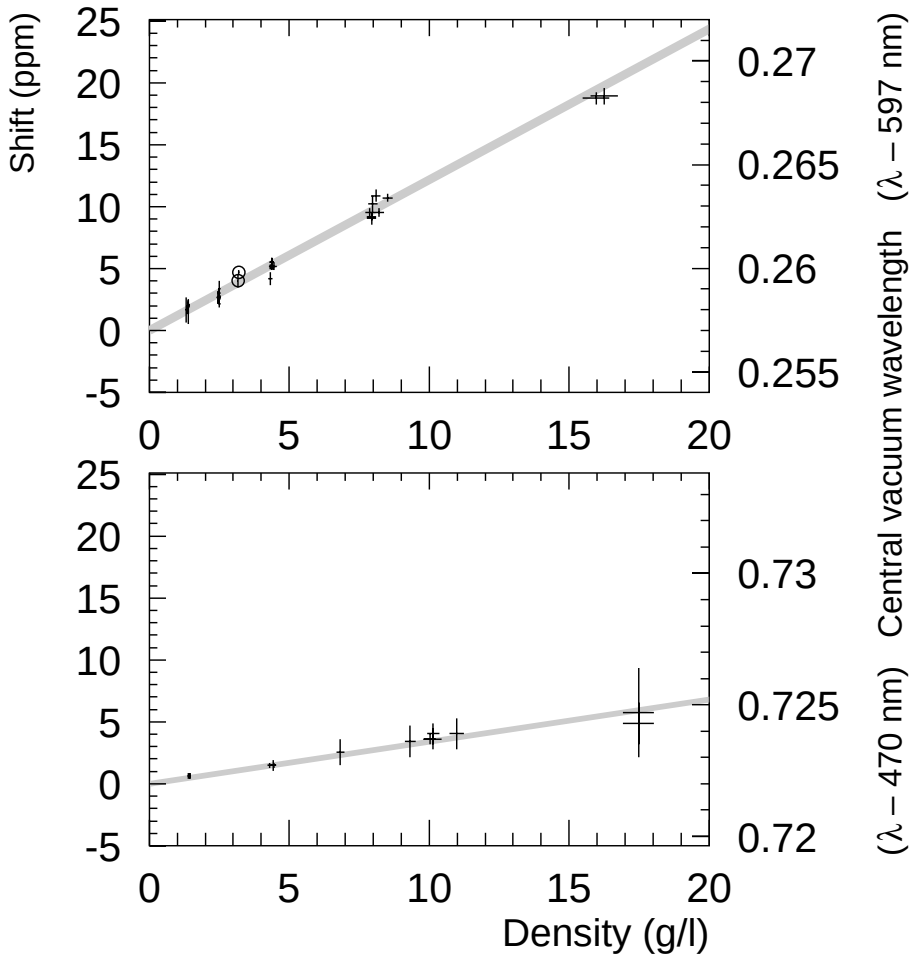

Figure 5.4: The central vacuum wavelength plotted against the density of the helium target at relatively low densities. The encircled data at 15 K falls roughly on the linear line. All the data within the plotted density-region are shown for the 570 nm line, while only selected data with relatively small statistical errors are plotted for the 470 nm line. The extrapolation to the zero-density limit gives the transition wavelengths of the $\overline{p}\mathrm{He}^+$ three-body system unperturbed by collisions. The line thickness covers the statistical error of the linear fit to the data.

the form

$$\lambda = \lambda_0 + s\rho\,, \tag{5.1}$$

where λ_0 is the extrapolated value at the zero-density limit.

For most of the data presented the $\overline{p}\mathrm{He}^+$ resonance data were taken with respect to a wavelength meter and this device was later calibrated against reference lines. In order to give a more reliable calibration for the absolute wavelength values, one set of resonance data for each transition in $\overline{p}\mathrm{He}^+$ atomcules was taken simultaneously with the standard molecular-absorption signals (see Appendix **E.1** for a detailed description). Figure **5.5** shows a resonance profile of the 597 nm line taken at our common target condition of 0.54 bar and 5.8 K, together with the absorption and transmission signals from a standard iodine cell and a spectrum analyzer (an etalon) with 3 GHz free spectral range. The central vacuum wavelength was obtained as 597.2606 ± 0.0002 nm for this condition and this value was used as a standard for the absolute wavelength calibration in determining the values for other data.

Table 5.2: Extrapolated vacuum wavelengths λ_0 at zero-density limit and shift parameters in various units.

Transition $(n,l)\Rightarrow(n',l')$	Wavelength $\lambda_0 \pm \delta\lambda_0$ [nm]	Density shift		
		$\Delta\nu/\rho$ [GHz/(g/ℓ)]	$\Delta\nu/N$ [10^{-21} GHz/cm^{-3}]	$(\Delta\lambda/\lambda)/\rho$ [ppm/(g/ℓ)]
(39,35)⇒(38,34)	597.2570±0.0003	-0.61 ± 0.01	-4.05 ± 0.07	1.22 ± 0.02
(37,34)⇒(36,33)	470.7220±0.0006	-0.22 ± 0.02	-1.5 ± 0.1	0.34 ± 0.03

Figure **5.6** (▷ Color figure VI) plots all the data at different target conditions, which show 0.61 ± 0.01 GHz and 0.22 ± 0.02 GHz red shifts per 1 g/ℓ for 597 nm and 470 nm lines (see Table **5.1**). The shifts are linear within the experimental error, except for one data-point at our maximum density of 127 g/ℓ = 32 mol/ℓ for the 597 nm line. In the case of the 470 nm transition, the density was limited to maximum 32 g/ℓ = 8 mol/ℓ, because the parent state $(n,l) = (37,34)$ was quenched by collisions at high density, reducing the height of the resonance peak and making measurements more and more difficult as the density increased (see Appendix **B.3** and Ref. [57]). One interesting fact is that the 597 nm transition is more sensitive to (elastic) collisions than the 470 nm transition, while its lifetime shortening effect is less marked.

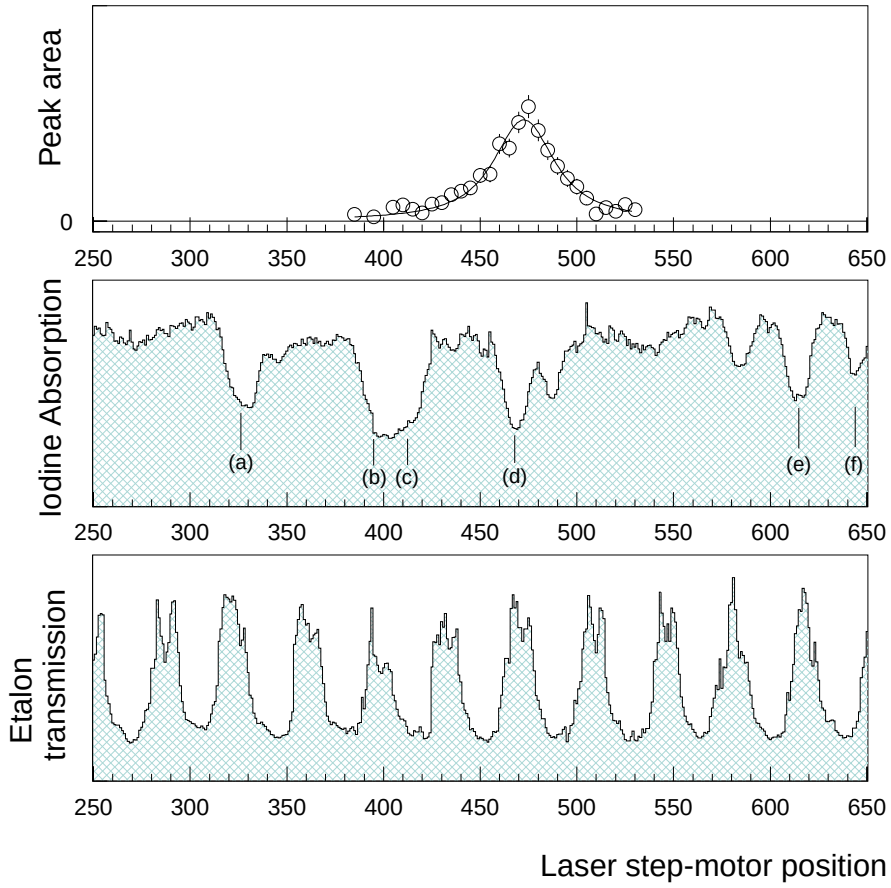

Figure 5.5: A 597 nm resonance profile was taken with a target of 0.54 bar at 5.8 K, together with standard iodine-absorption lines in order to give an absolute wavelength calibration. The resonance peak area is normalized to the number of delayed annihilation counts, and the iodine-absorption signal and the transmission signal of a spectrum analyzer are normalized to the incident laser-pulse energy. The symbols (a)–(f) correspond to reference lines listed in Table **E.1**, p. 131. The central vacuum wavelength was determined to be 597.2606 ± 0.0002 nm.

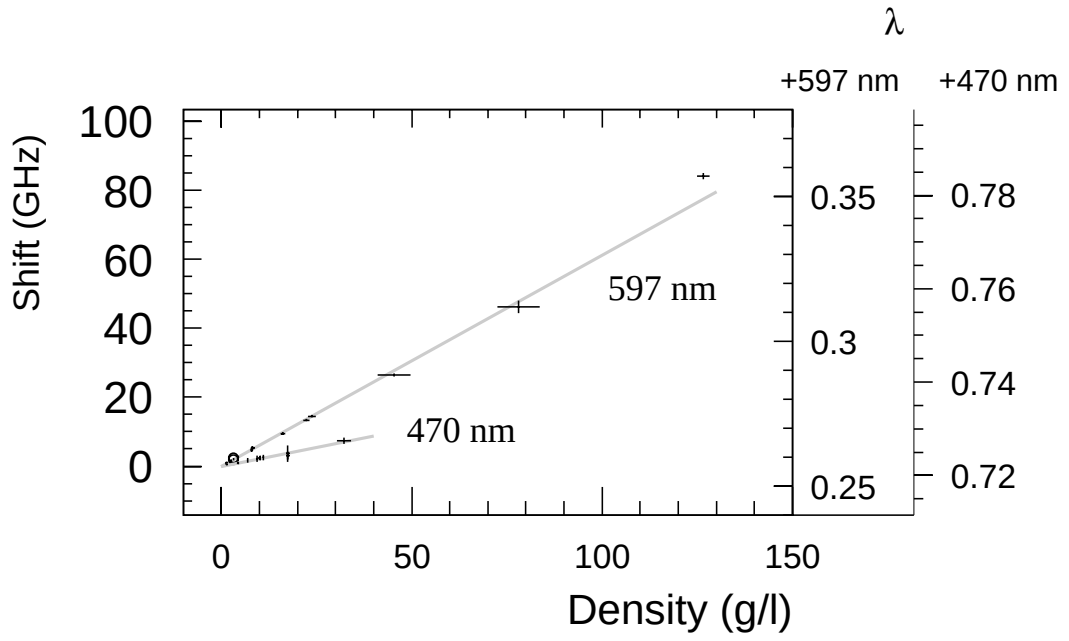

Figure 5.6: The central vacuum wavelength is plotted against the density of the target helium for the (n,l)=(39,35)⇒(38,34): 597 nm and (37,34)⇒(36,33): 470 nm resonance lines. No resonance was observed for the 470 nm line at higher density than 32 g/ℓ because of the quenched population of the parent state which is no longer metastable.

5.2 Precise Determination of Transition Wavelengths

5.2.1 Transition wavelengths at zero-density limits

The observation of the shifts has provided a more direct comparison between the experimental transition energies and the theoretical calculations. The wavelengths of the known 13 resonant transitions agree especially well with molecular-expansion variational calculations by Korobov [30]. The discrepancy found was generally about 50 ppm for the "favored" (n,l)⇒$(n-1,l-1)$ transitions and about 100 ppm for the "unfavored" (n,l)⇒$(n+1,l-1)$ transitions. These discrepancies were further reduced to a few ppm after taking into account the relativistic effect [31], as shown in Figure **4.5** and in Ref. [52]. In those figures, however, the experimental values compared were for our common condition of 0.5 bar at $\sim$ 6 K while the theory calculated values for an isolated three-body atomic system, *i.e.* at zero-density limit. Now that we know of the density shift, the extrapolated value λ of the observed vacuum wavelength at zero density should be compared with

the theoretical one. We determined this value taking a special care over the absolute wavelength calibration as explained in detail in Appendix **E.1**. Only the data at relatively low densities were used for the extrapolation. In this way we obtained $\lambda_0 = 597.2570 \pm 0.0003$ nm and 470.7220 ± 0.0006 for the two resonances. The errors include both statistical and systematic (calibration) errors and are still smaller than the laser bandwidth owing to our careful analysis. Thus the accuracies have improved by one order of magnitude compared with our first reports on the discovery of those resonances. These values were compared with the relativistic calculation by Korobov [31] and the discrepancies were

$$\begin{aligned}(\lambda_{\rm th} - \lambda_0)/\lambda_0 &\sim 8 \text{ ppm} \quad \text{for 597 nm} \\ &\sim 6 \text{ ppm} \quad \text{for 470 nm}\,,\end{aligned}$$

as indicated in Figure **5.7** (▷ Color figure VII).

Furthermore, most recently, Kino *et al.* [24, 25] and Elander *et al.* [32–34] have come up with new calculations including relativistic corrections and Lamb shifts.[‖] Korobov has also revised his calculation in the meantime [35]. All their values agree with each other to a precision of several ppm, and with all relativistic corrections taken into account, the discrepancies between theoretical and experimental values are only a few ppm or less, as shown in Figure **5.7**. Among these, the current best agreement is given by the non-relativistic value of Korobov which is now claimed to be accurate to 10 digits,[**] plus his relativistic corrections of order $\mathcal{O}(\alpha^4)$ [35] plus the Lamb shift values of Elander *et al.*,[††] with some corrections by Korobov. These theoreticians are currently working for more accurate values, and further results are anticipated.

The present precision of the theoretical calculations is certainly the best one in the history of calculation of Coulombic (or any other) three-body systems. It is therefore going to be a milestone in the development of theoretical calculation techniques.

5.2.2 Precise determination of antiproton's Rydberg constant

The excellent agreement has opened a possibility of measuring fundamental constants of the antiproton by means of high-resolution spectroscopy of the $\overline{p}\mathrm{He}^+$ atomcule. In

[‖] The relativistic corrections include a dominating correction to the kinetic energy of the bound electron, with smaller contributions from vacuum polarization effects and relativistic mass corrections to the kinetic energies of the two heavy particles. The Lamb shift derives from the radiative QED correction, mainly for the bound electron.

[**] It must be noted that the accuracy quoted here is for the binding energies, and since the transition energy is given by the small difference of binding energies between the two states, the effective accuracy for the transition energy is smaller by nearly 2 digits.

[††] Note that his publication contains a mistake of by a factor 2 too large values for the calculated Lamb shifts, as will be corrected in a forthcoming Erratum.

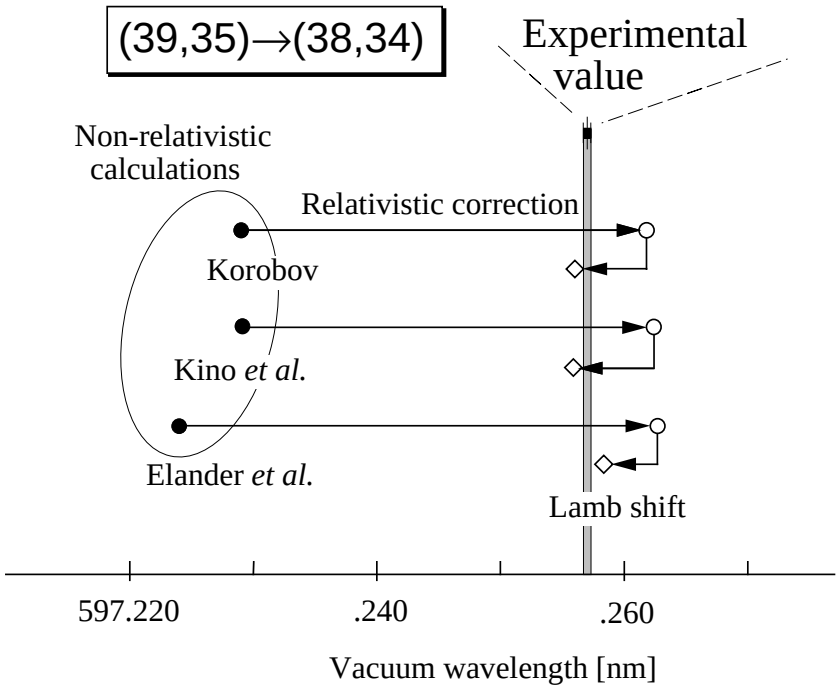

Figure 5.7: The experimental value of the (39,35)⇒(38,34) wavelength is compared with recent theoretical values [25, 33, 35] which agree within precisions of a few ppm. Korobov has not yet calculated the Lamb shift, so that Elander's value, with some correction by Korobov himself, is added to his relativistic value. This gives the currently available best agreement of 2 ppm with our experimental value. The so-far known precision of the antiproton Rydberg constant (50 ppm) is comparable to the discrepancy in the figure between the non-relativistic calculations and our experimental value, while the error of the present measurement of only 0.5 ppm is by far better than that.

a limited context, we can say that the current work has achieved the best precision in the determination of the Rydberg constant ($\mathrm{Ry}(\overline{p})^{\infty}$) of antiproton. The charge-to-mass ratio ($Q_{\overline{p}}/M_{\overline{p}}$) of antiproton[‡‡] is known with a high precision of 10^{-9} to be the same as that of proton, from a measurement of the cyclotron frequency at a trap experiment at LEAR [77]. This does not mean, however, that the charge and the mass respectively were measured with that high precision. In fact, the $\overline{p}$ charge is known only to such a precision that $|\,Q_p + Q_{\overline{p}}\,|/e < 2\times 10^{-5}$ [78], from an x-ray measurement of antiprotonic atoms[♯] [79]. This means that the current precision of antiproton's Rydberg constant is only 5×10^{-5}, since

$$\mathrm{Ry}(\overline{p})^{\infty} \equiv \frac{M_{\overline{p}}\, e^2 {Q_{\overline{p}}}^2}{2(4\pi\varepsilon_0)^2\hbar^2} \propto {Q_{\overline{p}}}^3 \left(\frac{Q_{\overline{p}}}{M_{\overline{p}}}\right)^{-1}, \qquad \frac{\delta \mathrm{Ry}(\overline{p})^{\infty}}{\mathrm{Ry}(p)^{\infty}} = 3\,\frac{\delta Q_{\overline{p}}}{e}\,. \tag{5.2}$$

We have determined the transition energy of the $\overline{p}\mathrm{He}^+$ atomcule to a precision of 5×10^{-7}. If we roughly assume that the half of the binding energy is carried by the antiproton (as expected from arguments in Appendix **A.2**), the achieved precision for the $\overline{p}$ Rydberg constant is about 10^{-6} — surpassing nearly two orders of magnitude by the currently known value. More precisely speaking, the binding energy of $\overline{p}\mathrm{He}^+$ is expressed using effective nuclear charges for $\overline{p}$ and e^-, as

$$\begin{aligned} E_{\mathrm{B}} = E_{\mathrm{B}}^{e} + E_{\mathrm{B}}^{\overline{p}} &\propto m_e (Z_{\mathrm{eff}}^{e})^2 e^4 + \frac{M^*}{n^2}(Z_{\mathrm{eff}}^{\overline{p}})^2 e^2 Q_{\overline{p}}^2 \\ E_{\mathrm{B}}^{e} &\sim E_{\mathrm{B}}^{\overline{p}}\,, \end{aligned} \tag{5.3}$$

where

$$M^* = \frac{M_{\overline{p}}\, M_{\mathrm{He}}}{M_{\overline{p}} + M_{\mathrm{He}}} \tag{5.4}$$

is the reduced mass between the antiproton and the helium nucleus. Under an assumption that the both effective charges $Z_{\mathrm{eff}}^{e}, Z_{\mathrm{eff}}^{\overline{p}}$ are independent of $Q_{\overline{p}}$, It can be deduced in the same manner as in Ref. [78], that[♭]

$$2\,\frac{\delta E_{\mathrm{B}}}{E_{\mathrm{B}}} = \frac{\delta E_{\mathrm{B}}^{\overline{p}}}{E_{\mathrm{B}}^{\overline{p}}} = \left(3 - \frac{1}{1 + M_{\mathrm{He}}/M_p}\right)\frac{\delta Q_{\overline{p}}}{e} = \frac{14}{5}\frac{\delta Q_{\overline{p}}}{e} \tag{5.5}$$

[‡‡] We define here the charges of antiproton and electron to be equal to $-Q_{\overline{p}}$ and $-e$, respectively, so that both $Q_{\overline{p}}$ and e are positive.

[♯] Robertson *et al.* have measured x-ray transition energies of antiprotonic atoms formed in targets of ^{6}Li, ^{7}Li, C, Si, P, Fe, Y, Zr, Cs, and Yb. They have only used those transitions un-shifted by the strong interaction.

[♭] The known precision of the mass of the helium atom is of the order of 10^{-10}, and this uncertainty can be neglected compared to the uncertainty of the antiproton mass or its charge. Also, the uncertainty in the charge-to-mass ratio of the antiproton is neglected, so that $\delta Q_{\overline{p}}/e = \delta M_{\overline{p}}/M_p$.

for the $\overline{p}\,^4\mathrm{He}^+$ atomcule. But in fact, if the (absolute value of) the antiproton charge and correspondingly the antiproton mass were slightly larger than those of electron, then the antiproton would be more attracted by and come closer to the helium nucleus, while the electron would feel less effective nuclear charge Z^e_{eff} and stronger repulsion from the $\overline{p}$, and its wavefunction would be slightly pushed outside. This means that the effective nuclear charges $Z^e_{\mathrm{eff}}, Z^{\overline{p}}_{\mathrm{eff}}$ would depend on the antiproton charge, and Eq. (5.5) above no more holds. Moreover, the expression in Eq. (5.3) using effective charges may not be suitable from the beginning for the detailed arguments. In order to know the actual relationship between the uncertainty in the $\overline{p}\mathrm{He}^+$ transition wavelength and that of the $\overline{p}$ Rydberg constant (or the $\overline{p}$ charge), theoretical comparison to an additional energy calculation with slightly deviated antiproton mass and charge may be required.

Therefore, currently we cannot give a fixed limit on the precise value, but as long as we believe in the theoretical calculations, we can state that we have determined the antiproton's Rydberg constant with a world's best precision of the order of 10^{-6}, from the comparison of our results with theoretical relativistic calculations.

5.3 Widths of the Resonance Lines

So far, we have cared about the center of the resonance which shifted with density. In this section we will discuss the observed broadening of the resonance lines and deduce collisional parameters.

5.3.1 Different types of widths

We are aiming at extracting collisional information from the observed width which seems to depend on target conditions as indicated in Figure **5.3**, p. 52. Before considering collisional widths, however, let us summarize other important origins of line broadening.

Natural width, observation time

Every line has a natural width as a consequence of the principle of uncertainty between the time and the energy. A level with a finite lifetime τ results in a Lorentzian with a *full* width at half maximum (FWHM) of $\Gamma \equiv \Delta\nu = \tau^{-1}/2\pi$. In our case, the width is dominated by the short lifetime of the daughter state. For a typical value of 10 ns, the natural width is $\Gamma = 16$ MHz which is much smaller than the laser bandwidth of 1.0 GHz. The natural width is therefore not usually observable, unless the lifetime of the

daughter state is much shorter than this.[♮] The laser pulse has a width of 30–40 ns and the broadening due to this observation time window[♢] is even smaller than the natural width.

Doppler width

The thermal motion of the atomcule causes an inhomogeneous broadening called the Doppler width. At a temperature of T [K] the velocity v of the atomcule distributes according to the Maxwell-Boltzmann distribution:

$$f(\boldsymbol{v})\,\mathrm{d}\boldsymbol{v} = \left(\frac{M}{2\pi kT}\right)^{\frac{3}{2}} \exp\left\{-\frac{M\boldsymbol{v}^2}{2kT}\right\}\mathrm{d}\boldsymbol{v}\ , \tag{5.6a}$$

$$f(v_x)\,\mathrm{d}v_x = \left(\frac{M}{2\pi kT}\right)^{\frac{3}{2}} \exp\left\{-\frac{M{v_x}^2}{2kT}\right\}\mathrm{d}v_x\ , \tag{5.6b}$$

$$f(v)\,\mathrm{d}v = \left(\frac{M}{2\pi kT}\right)^{\frac{3}{2}} 4\pi v^2 \exp\left\{-\frac{Mv^2}{2kT}\right\}\mathrm{d}v\ , \tag{5.6c}$$

where M is the mass of the atomcule, and the laser beam is introduced along the x axis. Since the Doppler shift is given by $\Delta\nu = \nu v_x/c$, the resultant shape of the resonance is a Gaussian with a FWHM

$$\Delta\nu_{\mathrm{D}} = 2\sqrt{2\ln 2}\times\sigma = 2.35\times\nu\sqrt{\frac{kT}{M}}\ . \tag{5.7}$$

At our typical temperature of 6 K, $\Delta\nu_{\mathrm{D}} = 390$ MHz at 597 nm and 500 MHz at 470 nm for $\overline{p}\,{}^4\mathrm{He}^+$ atomcules.

Power broadening

A troublesome fact in the measurement of the width is that it depends heavily on the laser power. When the power is low enough, the signal is always proportional to the intensity of the laser, independent of the frequency detuning around the resonance, so that the linearity of the signal and the same resonance width are retained. At a high power, however, the resonant transition signal saturates near the center while the the linearity is still valid in the wings, so that the overall resonance shape broadens. This effect is called the power broadening or the saturation broadening, and had a sizable influence on our measurements. The typical energy was 2–5 mJ per pulse for most of the

[♮] Only for an "unfavored" transition at 713 nm, a very large width was observed and a corresponding short daughter-state lifetime of 4.1 ps was deduced. See Appendix **B.2.4**.

[♢] This additional broadening is automatically included in the simulation of Rabi oscillation in the following Section **5.3.3**.

measurements (except for those presented in this chapter), which aimed mainly at the studies of state lifetimes and populations and we did not care so much about the resonance shape itself. In those measurements, rather, the saturation condition was favored because it assured a constant high depopulation efficiency of ca. 80%. The cross section of the beam was of the order of 1 cm^2 and the pulse duration was typically 20 ns, corresponding to power densities of 0.1–0.2 MW/cm^2 and Rabi frequencies $\Omega/2\pi \sim$ 1–2 GHz for the "favored" transitions. We measured the resonance intensity at different pulse energies and found that the saturation occurred already at 0.1 mJ. This means that the width was considerably broadened due to the surplus laser power. Generally, the broadened width is of the order of the Rabi frequency. It was therefore essential to reduce the power significantly and do the measurements under the condition of unsaturated responses.

Collisional broadening

It is well known and has been studied for a century that atoms and molecules colliding frequently with each other have broadened (and shifted) transition lines which depend on the type and frequency of the collision [80–82]. Intuitively, the broadening occurs because of the phase shifts due to slight changes in the transition energies during collisions. There are many successful theoretical formulations which link the collisional interactions with the observed broadened lines. In other words, some information about the interatomic/ intermolecular interaction can be provided by studying the "collisional broadening" effect. Experimentally, the residual width under the no-saturation condition *i.e.* the zero-power limit usually gives the collisional width.

5.3.2 Measurement of resonance widths

The reduction of the power to suppress saturation broadening was made with ND (neutral density) filters and not by the laser output itself, so as to keep stability and quality of the beam. In order to observe intrinsic widths free from power broadening, the resonance widths measured at several decreasing powers should be plotted and extrapolated to the zero-power limit. The precision of the measurements, however, was restricted by the statistical difficulty. Lower power naturally meant smaller resonance peak, and the peak height decreased by half when the power density was halved in the linear-response region. This worsened the statistical errors and it took four times longer measurement time to keep the same relative errors. It was practically impossible to do the measurements at a pulse energy lower than 0.01 mJ, so that our resonance profile data were taken at several different energies ranging 0.01–0.25 mJ$^{\heartsuit}$ for each target condition.

$^{\heartsuit}$The value is the corrected laser-pulse energy at the entrance of the quartz window of the target. See comments in the caption of Figure **5.12**, p. 69.

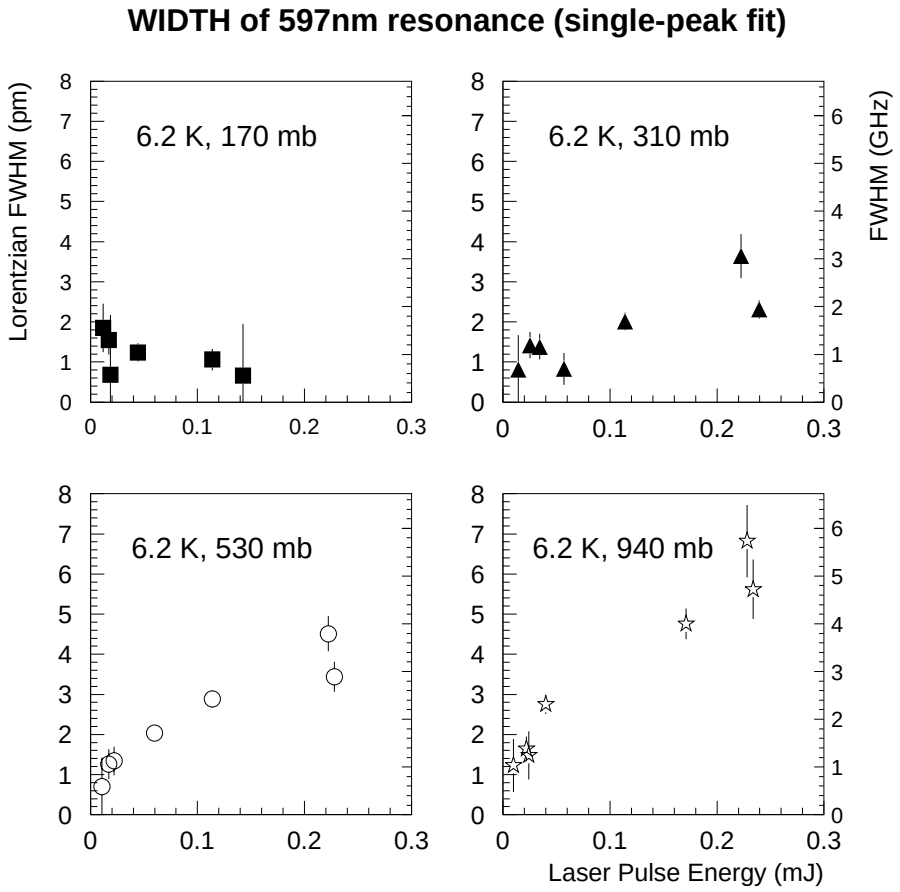

Figure 5.8: The Lorentzian full width of the 597 nm resonance obtained by single-peak fits is plotted against the laser-pulse energy. The width is greater at higher energy, and this dependence of power broadening is more dramatic for higher density. The residual width at the zero-energy limit is small and about 0.5 GHz for all conditions, and was ascribed to an unresolved hyperfine splitting. Note that the error bars in the figures include only the statistical errors, and that the absolute values for the widths, especially those which are small, are subject to systematic errors arising from possible misestimation of the laser bandwidth and the Doppler width. The values are listed in Appendix **E.2**.

The resonance profile data were fitted with a Lorentzian convoluted with a Gaussian of 0.96/1.3 GHz (= 1.14/0.95 pm♣) FWHM for the 597/470 nm lines, the Gaussian representing the laser bandwidth plus the Doppler width. The deduced Lorentzian widths of the 597 nm resonance are plotted in Figure **5.8** against the laser-pulse energy for different target pressures ranging from 170 mb to 940 mb at 6.2 K. The figure shows different dependence of power broadening for different target conditions. The width increases more rapidly with the power for higher pressure *i.e.* higher gas density, while the extrapolation at zero-power limit gives similar residual intrinsic widths of about 0.5 GHz. Since the natural width was negligibly small, this value was first identified as the collisional width. However, our simulations of the Rabi oscillation and the resonance profile explained in the next section did not support this interpretation. If the value of the collisional width depended only slightly, if at all, on the target condition, there was no reason for the behavior of the power broadening to vary so much at high laser powers.

After a while, we noticed that the observed 0.5 GHz width can be ascribed to the "hyperfine" (HF) splitting caused by the interaction between the large $\overline{p}$ angular momentum and the electron spin. The readers are referred to Appendix **B.5** for the explanation of "hyperfine" structure (HFS) specific to the $\overline{p}\mathrm{He}^+$ atomcule, and here we only mention that the interaction splits the levels into doublets. According to Bakalov and Korobov who have calculated the splitting energies [83, 84], the *difference* in the HF splitting between the parent and the daughter states is 0.2–0.6 GHz for the "favored" transitions $(n,l) \Rightarrow (n-1, l-1)$ with $35 \leq n \leq 39$, while the "unfavored" transitions $(n,l) \Rightarrow (n+1, l-1)$ generally have larger difference, and in fact we did observe a clear doublet splitting of 1.7 GHz in an "unfavored" resonance at 726 nm as shown in Appendix **B.5**, p. 106. The calculated value for the 597 nm resonance in question was 0.507 GHz, as listed in Table **B.2**, p. 107, coinciding with the observed residual width.

We then re-fitted the resonance profile with two identical♠ Voigt functions *i.e.* the Gaussian-convoluted Lorentzians, whose central wavelengths were separated by the theoretical value 0.507 GHz = 0.604 pm. This doublet-fit left the values of the central wavelength almost unchanged and reduced the width by roughly 0.5 GHz as was naturally expected. The obtained Lorentzian widths are plotted in Figure **5.9**, this time against the square root of the laser energy, which is proportional to the Rabi frequency. It can be seen that the power broadening is fairly proportional to the Rabi frequency and that its slope increases with the target density. The collisional widths at zero-power limit are too small to be determined and are identical with zero within errors of a few hundred megahertz.

♣pm: picometer = 10^{-12} m = 10^{-3} nm, see Appendix F.1.

♠The statistical weight of $(2l+2)/2l$ in the intensities of the two peaks can be well approximated by unity.

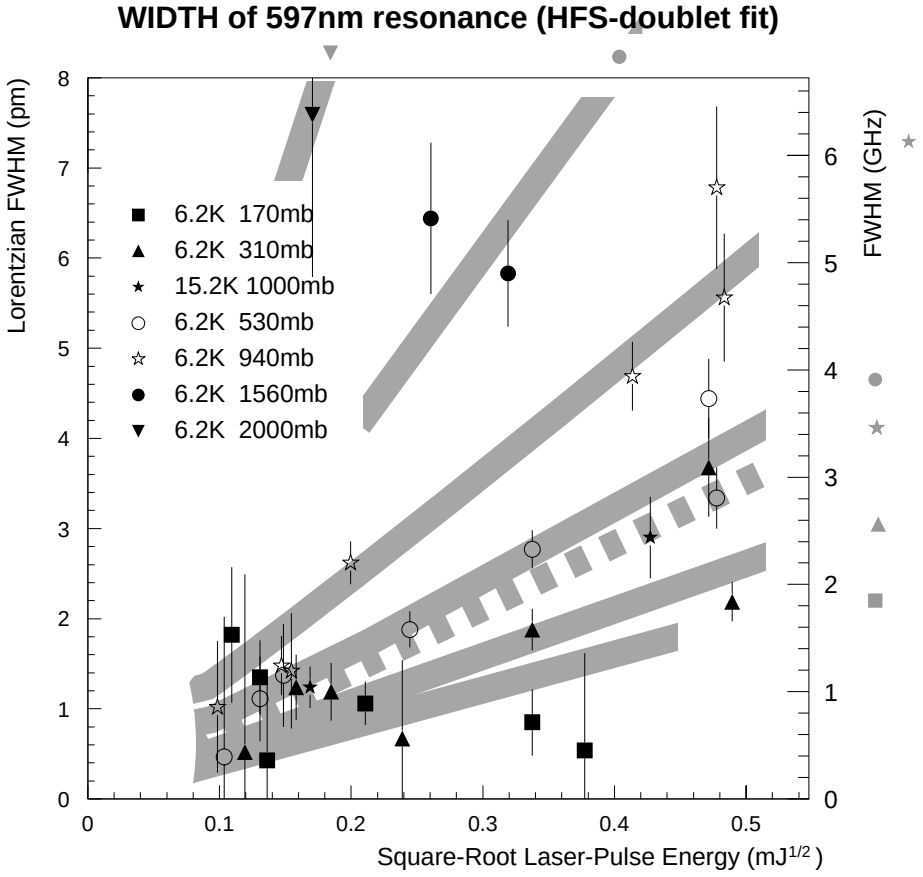

Figure 5.9: The Lorentzian full width of the 597 nm resonance obtained by a hyperfine-doublet fit is plotted against the square-root of the laser-pulse energy ($\sqrt{\mathcal{E}}$). It shows a roughly linear dependence of the width on $\sqrt{\mathcal{E}}$, which is proportional to the Rabi frequency. The values are listed in Appendix **E.2**.

In the case of the 470 nm line, the situation is a little different (see Figure **5.10**). The widths at low power are very small even for the fit results without the HFS taken into account. Also, no systematic dependence of power broadening on the density is visible. The theoretically calculated HFS is 0.370 GHz = 0.274 pm, and is too small to be recognized in the data obtained with large errors. So for this resonance, we can only set an upper limit on the collisional width (at zero-power limit) of $\gamma < 0.6$ GHz at 540 mb.

We limit the arguments in the following two sections only to the 597 nm resonance line.

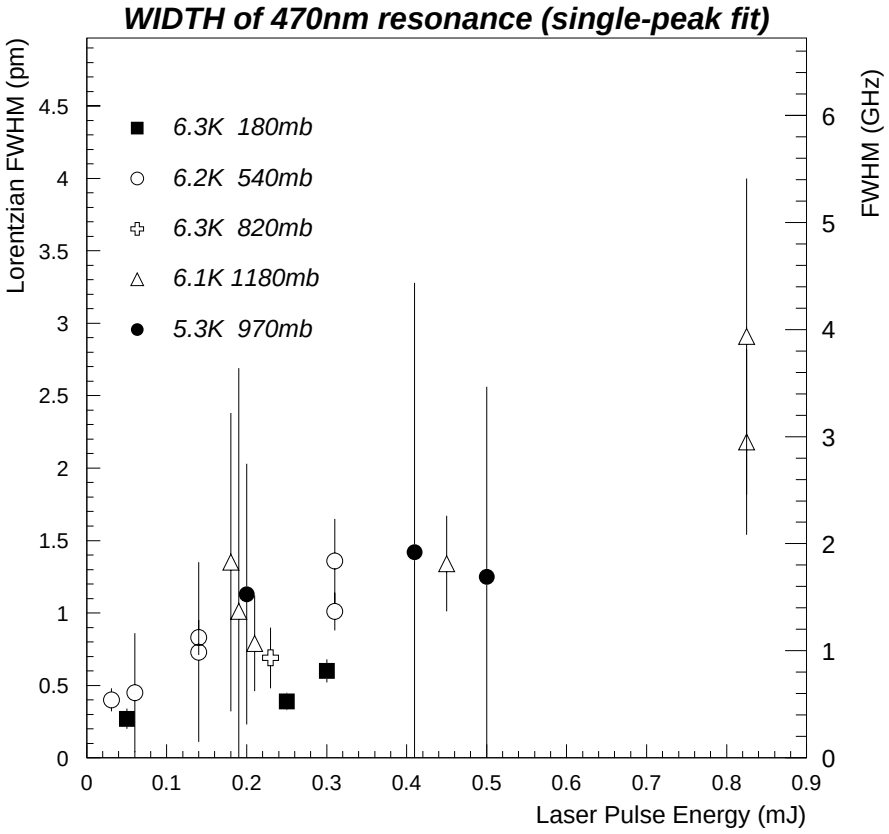

Figure 5.10: The Lorentzian full width of the 470 nm resonance obtained by single-peak fits is plotted against the laser-pulse energy. In contrast to the 597 nm resonance, no clear dependence of power broadening on the target density is observed. The values are listed in Appendix **E.2**.

5.3.3 Simulation of Rabi oscillation

We are interested in the collisional width, because, as mentioned before, the width contains information on the $\overline{p}\mathrm{He}^+$–He interaction potential at small distances, while the shift is related to soft collisions with large impact parameters. Although the remnant width at zero-power-broadening limit is too small to be determined, the collision rate may be deduced from the observed broader width at higher power densities. We performed a simulation of the Rabi oscillation under the condition of collisional relaxation and power broadening, and plotted the depopulation efficiency versus the frequency detuning. Then the collisional width in question can be determined implicitly by comparing the width of the simulated resonance profile with the observed one.

We wrote a simulation program as explained in Appendix **D.4**. The optical Bloch

differential equation was numerically solved for each of the magnetic subcomponents of the resonating states (m states; $-l \leq m \leq l$) using the finite difference method.

The laser pulse had an complex temporal shape with typically two peaks$^{\oplus}$ as shown in Figure **5.11-a**, which was included in the simulation program. The spatial profile of the laser spot was measured by a CCD camera, and is shown in Figure **5.12**. The distribution of the light intensity had an effective spot area of about $A = 4$ cm^2. The Rabi frequency can then be calculated, with the known dipole moment μ, according to Eq. (D.54), p. 128 and Eq. (F.15), p. 138.

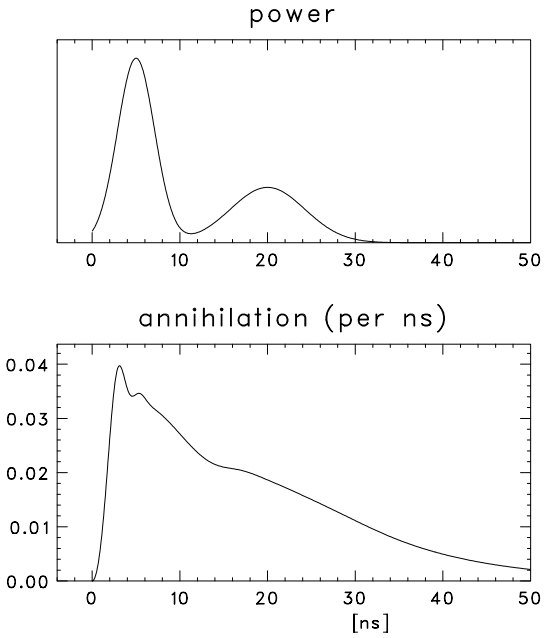

Figure 5.11-a: A typical temporal profile of the dye-laser pulses. It had two peaks of about 5 ns width and 10 ns apart, and the total duration was about 30 ns until the decaying tail faded out.

Figure 5.11-b: A simulated laser-induced annihilation peak under a typical condition of $\gamma_p/2\pi = 0.20$ GHz and $I^{(s)} = 0.04$ mJ/cm^2 (in the target) for the 597 nm transition ((39,35)⇒(38,34); $\mu_{tot} = 0.649$ debye and $\Gamma_A = 0.0845$ ns^{-1}).

Figure 5.11: Temporal profile of the dye-laser pulse and a simulated laser-induced annihilation peak.

One example of the simulated temporal profile of the laser-induced annihilation peak is given in Figure **5.11-b**. The shape bears a remote resemblance to the original profile of the laser pulse, with a tail due to the finite decay time of the daughter state.

The depopulation efficiency ϵ is defined as the number of $\overline{p}$'s which decayed resonantly with the laser pulse divided by the initial population of the parent state of the resonance. From the simulation, it can be calculated as $\epsilon = 1 - \rho_{11}(t)$ for a time t after the peak has diminished$^{\ominus}$, while experimentally, it is known from the resonance peak area and from the laser-time variant method mentioned in Appendix **B.2.1**. As long as the state-population at the time of the laser pulse is the same, the resonance peak area is proportional to ϵ.

$^{\oplus}$Refer also to comments in Section **3.3.1**.

$^{\ominus}$The total population is normalized to unity. The initial condition is ρ_{11}=1, ρ_{22}=0, ρ_{12}=ρ_{21}=0, with $|1\rangle$ representing the parent state and $|2\rangle$ the daughter state.

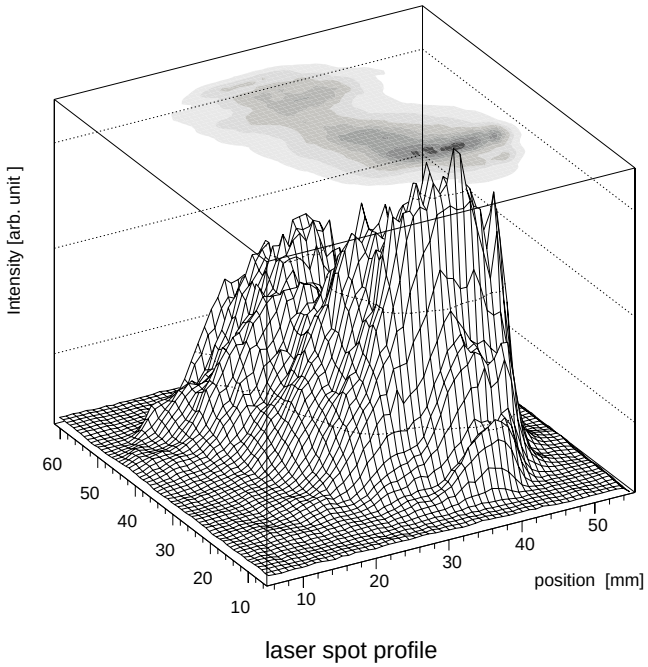

Figure 5.12: A spatial profile of the laser spot. The light intensity observed by a CCD camera is plotted in arbitrary units as a function of the position in the beam cross section expressed in millimeters. The effective cross section is about 4 cm^2. The profile has two peaks, but it must be noted that the area of the smaller peak was cut out halfway in the beam path and only the main peak, which had 60% of the total energy, was guided into the target.

We plotted the depopulation efficiency as a result of the simulation, against the frequency detuning $\Delta\nu = (\omega - \omega_0)/2\pi$, as shown in Figure **5.13**. It shows larger power-broadened widths, even at the same energy density (*i.e.* the time integral of the power density), for larger collision rates γ_p. This is in accordance with our measurements which showed larger broadening for denser targets, and with our expectation that denser condition means more frequent collisions. It was thus possible to deduce the dephasing collision rates γ_p, from comparison of the simulated broadening to the observed widths.

5.3.4 Deduction of collisional widths

Figure **5.14** plots the simulated width against the square-root of the laser's energy density I with variable collisional widths γ_p. The broadening seems linear with $\sqrt{I}$ at large enough energy densities, and the slope is almost proportional to $\sqrt{\gamma_p}$. This dependence is the same as the theoretically deduced broadening for a simple two-level atom in thermal

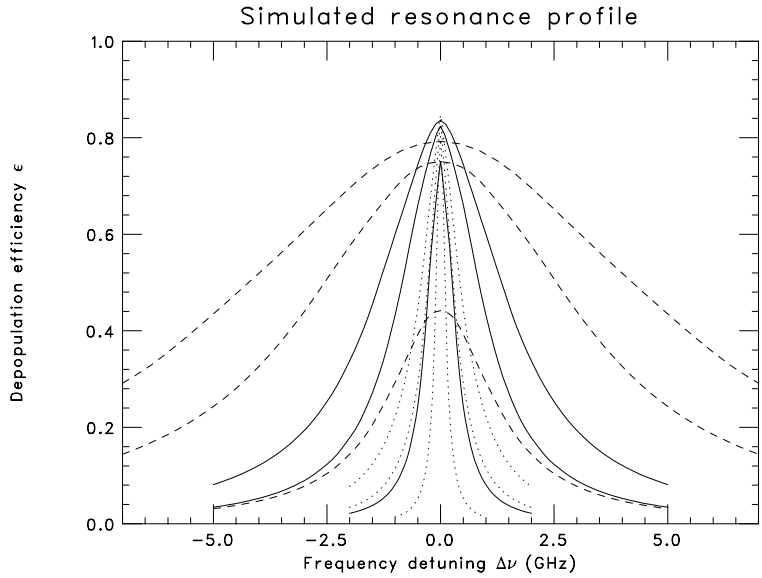

Figure 5.13: The simulated depopulation efficiency ϵ is plotted as a function of the frequency detuning $\Delta\nu = (\omega - \omega_0)/2\pi$, at different collisional widths $\gamma_\mathrm{p}/2\pi = 0.01$ GHz (dotted lines), 0.1 GHz (solid lines), and 1.0 GHz (dashed lines). Results for three different energy densities of 0.01, 0.1, and 0.25 mJ/cm^2 are plotted, showing broader resonances for larger energy densities. The graph indicates larger power-broadened widths at the same power density for larger collision rates γ_p. The maximum efficiency at saturation is 80–90%, which is in accordance with observation (see Section **4.1**).

equilibrium and interacting with the light field; in that case the stationary solution has a half width of

$$\gamma = \gamma_\mathrm{T} \sqrt{1 + \frac{\Omega^2}{\Gamma_\mathrm{L}\gamma_\mathrm{T}}}\,, \tag{5.8}$$

where Γ_L and $\gamma_\mathrm{T} = \gamma_\mathrm{p} + \Gamma_\mathrm{L}/2$ are the transverse and the longitudinal relaxation rates [85, 86]. The equation is reduced to

$$\gamma = \sqrt{\frac{\gamma_\mathrm{T}}{\Gamma_\mathrm{L}}}\,\Omega \tag{5.9}$$

for a large Rabi frequency $\Omega \gg \Omega_\mathrm{s} \equiv \sqrt{\Gamma_\mathrm{L}\gamma_\mathrm{T}}$, where Ω_s is the saturation frequency. In our case, it will soon turn out that inequalities $\Gamma_\mathrm{L} \sim \Gamma_\mathrm{A} \ll \gamma_\mathrm{T}$ and $\Omega \gg \Omega_\mathrm{s}$ are satisfied, and the result of the simulation matches well with Eq. (5.9).

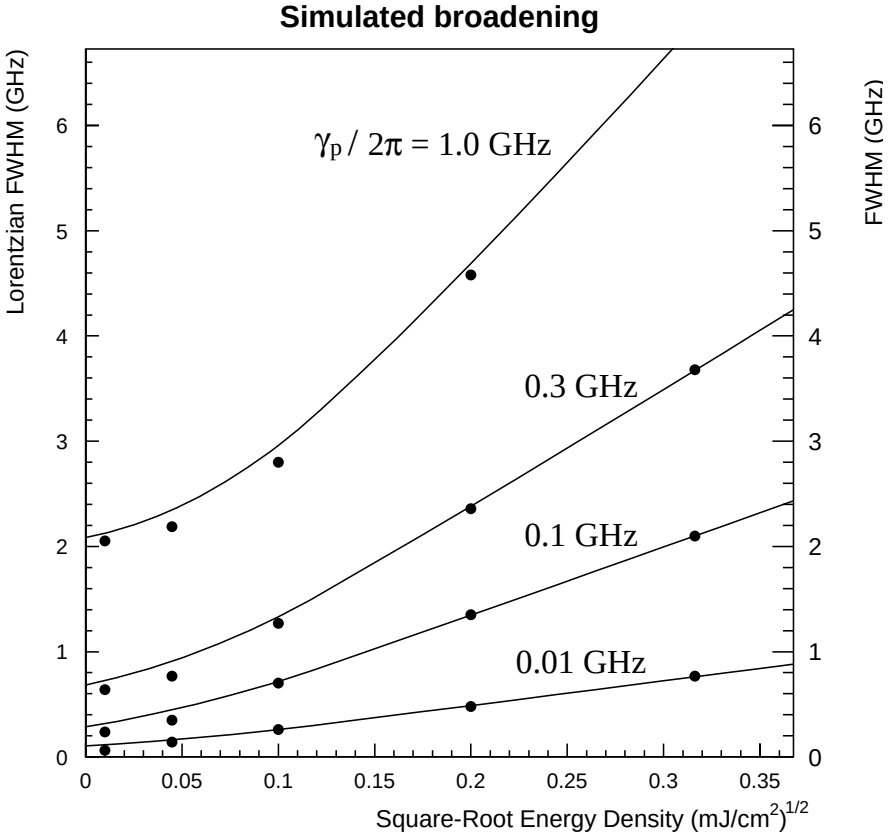

Figure 5.14: The simulated power-broadening for the 597 nm resonance is plotted against the square-root of the energy density ($\sqrt{I^{(s)}}$), for different values of the collisional width $\gamma_{\rm p}$. The solid lines shows the theoretical function Eq. (5.8) with $\Gamma_{\rm L} = \Gamma_{\rm A} = 0.0845$ ns^{-1} and $\overline{P} = I/\tau_{\rm l}^{*}$, where the effective laser-pulse length $\tau_{\rm l}^{*}$ was determined to give the best fit to the simulated points. (Thus the values for $\tau_{\rm l}^{*}$ were 9, 10, 12.5 and 35 ns for $\gamma_{\rm p}/2\pi$ = 1.0, 0.3, 0.1 and 0.01 GHz, respectively. Longer effective pulse-length under conditions with less frequent collisions corresponds to lower power density required for saturation and means that the small tail of the decaying laser pulse has more significant effect.) The dephasing collision rates $\gamma_{\rm p}$ were deduced from comparison between this figure and Figure **5.9** which are shown in the same size. The scale of the axes are taken to be the same when the conversion $I^{(s)}$ [mJ/cm^2] = 0.45 $\mathcal{E}$ [mJ] is used.

Now we compare this graph with Figure **5.9**. The average energy density was calculated using the $\overline{p}$'s stopping distribution of Figure **3.5**, p. 21 and the conversion relation

$$I\,[\mathrm{mJ/cm^2}] = (0.25 \pm 0.01)\,\mathcal{E}\,[\mathrm{mJ}]$$

was obtained between the pulse energy $\mathcal{E}$ and the energy density, at a typical target condition of 6 K and 500–600 mb.[⊗] This gave an effective cross section of the laser beam of $A = 4.0 \pm 0.2$ cm^2.

The argument above, however, does not consider the light beam retroreflected by the highly polished stainless-steel window. In the target, the incident and the reflected beams must have interfered to form a stationary-wave pattern in the spatial distribution of the energy density. This should have increased the effective power-density by a factor 2, because $E_0^{(s)}(x) = 2E_0^{(t)}\cos(2\pi x/\lambda)$, $I \propto E_0$ and $\langle\cos^2(2\pi x/\lambda)\rangle = 1/2$, where $E_0^{(s)}$ and $E_0^{(t)}$ are the amplitudes of oscillating electric field strength for the stationary wave and the incident traveling wave, and the x axis is taken along the beam path. This effect was taken into account with a measured reflection efficiency in power of 80%, in which case the increase factor is 1.8 instead of 2. The conversion relation is then re-written as

$$I^{(s)}\,[\mathrm{mJ/cm^2}] = 0.45\,\mathcal{E}\,[\mathrm{mJ}]\,,$$

where $\mathcal{E}$ is the energy of the laser beam and $I^{(s)}$ is the energy density of the total light field.

The collisional-width parameters γ_p were determined by comparing Figure **5.14** and Figure **5.9**, p. 66, which are shown in the same scale for the target condition of 6 K and 500–600 mb. The results are summarized in Tables **5.3** and **5.4**, and plotted in Figure **5.15** against the density. The obtained collisional width is roughly proportional to the density, and the deviation from the linearity may be ascribed to the different average energy densities: since the $\overline{p}$'s have a smaller stopping area in a denser target, the annihilated $\overline{p}$'s should have felt on average stronger electric fields near the center of the laser beam spot (even if the total energy of the laser pulse is the same) and the apparent width will be broader. The estimated deviation in the average energy density is about 30%[⊘] between the minimum and the maximum densities in the target conditions listed

[⊗]The $\overline{p}$ stopping distribution $g(\boldsymbol{r})$ of 2-dimensional Gaussian shape with a $\pi \times (1.0\ \mathrm{cm})^2$ (FWHM) cross section was assumed and the average energy density was defined as $\langle I\rangle = \int I(\boldsymbol{r})\,\epsilon(I(\boldsymbol{r}))g(\boldsymbol{r})\mathrm{d}\boldsymbol{r} / \int \epsilon(I(\boldsymbol{r}))g(\boldsymbol{r})\mathrm{d}\boldsymbol{r}$. Note that the average was taken with a weight on the number density of resonantly annihilated $\overline{p}$'s (not all the $\overline{p}$'s), which is given by $\epsilon(I(\boldsymbol{r}))g(\boldsymbol{r})\mathrm{d}\boldsymbol{r}$. The depopulation efficiency ϵ was assumed to be proportional to the energy density $I(\boldsymbol{r})$ at a position $\boldsymbol{r}$ in the laser spot. This assumption is rather reasonable because the width of the resonance is mainly determined by the frequency detuning that gives the half maximum of the resonance, where the linearity is barely conserved. Thus the equation was reduced to $\langle I\rangle = \int I(\boldsymbol{r})^2 g(\boldsymbol{r})\mathrm{d}\boldsymbol{r} / \int I(\boldsymbol{r})g(\boldsymbol{r})\mathrm{d}\boldsymbol{r}$.

[⊘]The deviation can be larger if saturation is considered, *i.e.* the linearity assumption $\epsilon(I) \propto I$ (see footnote of p. 72) is replaced by a more elaborate function.

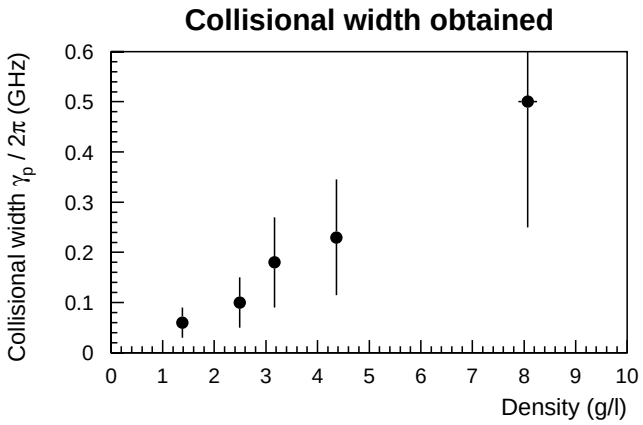

Figure 5.15: The collisional widths obtained are plotted against the target density. It shows a roughly linear dependence. Note that the systematic error can be as large as ±50%.

Table 5.3: Collisional shifts $\Delta = s\rho$ and half widths $\gamma = \gamma_p/2\pi$ are compared for the 597 nm resonance. The widths are one order of magnitude smaller than the shifts.

T [K]	p [bar]	ρ [g/ℓ]	Δ [GHz]	γ [GHz]
6.2	0.17	1.38	0.84	0.06
6.2	0.31	2.49	1.52	0.10
15.2	1.00	3.17	1.93	0.18
6.2	0.53	4.37	2.67	0.23
6.2	0.94	8.07	4.92	0.50

Table 5.4: Collisional-width parameters γ/ρ are shown for the 597 and 470 nm resonances. Only an upper limit is given for the latter transition.

Transition $(n,l)\Rightarrow(n',l')$	Wavelength λ [nm]	Collisional width	
		γ/ρ [GHz/(g/ℓ)]	γ/N [10^{-21} GHz/cm^{-3}]
(39,35)⇒(38,34)	597	0.05 ± 0.02	0.3 ± 0.15
(37,34)⇒(36,33)	470	< 0.14	< 1

in Figure **5.9**, and the correction is expected to push the points in Figure **5.15** toward a linear line.

It must be noted that the values of collisional width listed in Table **5.3** are not so reliable and the systematic errors are large. The comparison between the simulation and the experimental results required accurate estimation of not only the laser power density, which involved the measurement of pulse energy, spatial and temporal profile of the laser pulse, reflection at the end mirror in the target, etc., but also the stopping distribution of antiprotons which differed with target conditions. The simulation assumed perfect linear polarization of the laser beam and neglected collisions which may mix different m states. Wrongly estimated values of all these elements will lead to different results. Therefore, it may be possible that the real value is different from what we have deduced, by a factor 1.5 or ½ (*i.e.* an error of ±50%). But it may not be a factor 2 or more, because then the FWHM $= 2 \times \gamma_{\rm T}/2\pi$ ($\gamma_{\rm T} = \gamma + \Gamma_{\rm A}/2$, see Appendix **D.1.5**) would no longer be so small and could instead be directly observed as the residual width at the zero-power limit.

5.4 Theoretical Interpretation and Considerations

5.4.1 Microscopic target conditions

Let us now take a microscopic view of the $\overline{p}\mathrm{He}^+$ atomcule surrounded by the sea of helium atoms, which becomes important in the further discussions of collisional effects.

Both $\overline{p}\mathrm{He}^+$ atomcule and helium atoms have a mean radius $a \sim \langle r \rangle \approx 0.3$ Å $= 0.6$ a.u. Under the target condition of 1 bar at 6 K, the nearest helium atom is found in $R =$ 10 Å distance on an average from the $\overline{p}\mathrm{He}^+$ atomcule. The thermal velocity of a $\overline{p}\,{}^4\mathrm{He}^+$ atomcule is

$$\sqrt{\left\langle v^2_{\overline{p}\mathrm{He}^+} \right\rangle} = \sqrt{\frac{3kT}{M}} = 170 \text{ m/s}\,,$$

while that of the helium atom is 190 m/s. The average relative velocity is then $v = \sqrt{3kT/\mu} = 260$ m/s, where μ is the reduced mass between $\overline{p}\,^4\mathrm{He}^+$ and He. It should be noted that the temperature is so low that the de Broglie wavelength is already as long as $\lambda = h/Mv \sim 5$ Å, which is much longer than the actual size of the atomcule and nearly the average atomic distance.

If we assume the cross section σ of elastic collision to be a geometrical one, the mean free path is calculated as $\ell = 1/n\sigma \sim$ 100–1000 nm and the interval between subsequent collisions is $\nu_{\mathrm{c}}^{-1} = \ell/v \sim 0.5$–5 ns $= 0.5$–5×10^{-9} s, or the rate of collision is $\nu_{\mathrm{c}} \sim 0.2$–2 GHz. The duration of the collision is roughly given as $\tau_{\mathrm{c}} \sim 4a/v = 4 \times 10^{-13}$ s, and is 3–4 orders of magnitude shorter than the interval ν_{c}^{-1}.

It is interesting to compare the collision duration τ_{c} with the rotational time constant of $\overline{p}\mathrm{He}^+$. The atomcule is rotating rapidly due to its large angular momentum $l \sim 35$. Since the energy spacing between different rotational quantum numbers is $h\nu_{\mathrm{rot}} \sim 2$ eV or $\nu_{\mathrm{rot}} \sim 0.5$ PHz$^{\odot}$, one cycle of rotation takes only 2 fs $= 2 \times 10^{-15}$ s. This means that the atomcule rotates 200 times during the collision duration τ_{c}, so that there should be no orientation dependence between the $\overline{p}\mathrm{He}^+$ dipole moment and the radial vector ($\boldsymbol{R}$) connecting $\overline{p}\mathrm{He}^+$–He. Therefore, the only interatomic interaction at a large distance is the dispersion force — one type of the van der Waals interactions [87].

5.4.2 Theoretical description

Recently, Korenman has calculated possible shifts of the $\overline{p}\mathrm{He}^+$ resonances due to collisions with helium atoms, assuming a van der Waals interaction between the two atoms (atom and atomcule). By integrating the phase shift along rectilinear trajectories at different impact parameters, the shift and the width of the resonances are calculated simultaneously. Although this model is too rough to represent $\overline{p}\mathrm{He}^+$–He collisions, his calculation is not only qualitatively indicative, but also quantitatively, and gives results of the same order of red shift as our data [88].

His calculation is based on the widely-applied impact approximation (see Appendices **D.1.5** and **D.2.1**), which assumes that the collision occurs so instantaneously that the effect appears only as a phase shift between before and after the atomic collision, and does not depend on intermediate processes. If the collision is strong and the phase shift is greater than a typical value of π, the oscillation is totally interrupted and causes the line broadening.$^{\triangle}$ If on the other hand, the collision is weak enough for the phase shift

$^{\odot}$PHz: petahertz $= 10^{15}$ Hz, see Appendix F.1.

$^{\triangle}$Noting that phase shifts which defer by integral multiples of 2π ($\eta_1 - \eta_2 = 2n\pi$, $n = \pm1, \pm2, ...$) give exactly the same effect to the line shape, integration over different impact parameters (which give different phase shifts) results in cancellation of line shifts and loss of memory of the phase, and the latter

to be less than 1 radian, the main effect is the shift of the line center.

Another quite opposite approach in atomic collision theories is the quasi-static approximation, which assumes that the interatomic distance changes so slowly that transitions at certain fixed interatomic distances, whose energies are shifted from their original values, are directly observable. The intensity at a shifted frequency $\Delta\nu$ is then related to the probability of finding the nearest perturbing atom at a distance R which gives the energy difference of $V(R) = h\Delta\nu$.

Our experimental conditions as mentioned in the previous section are better approximated by the impact approach. The collisions take place randomly in a much shorter instance than the intervals between collisions, and the observation times limited by the laser-pulse duration and the daughter-state lifetime are even longer than the interval. The Rabi oscillation is fast due to the high power density of the laser and its period is as short as a few nanoseconds, but it is much longer than the instantaneous collision time. Therefore the conditions for impact approximation, $\tau_c \ll \nu_c^{-1} < \Delta t$ and $\tau_c \ll \Omega^{-1}$ in Appendix **D.1.5**, p. 121, are satisfied.

Furthermore, effects of collisions in which three or more atoms are involved can be neglected under these conditions; the interatomic interaction becomes significant when the atoms come close enough to a distance of a few atomic units, and at a density of $(10\ \text{Å})^{-3}$ the probability of finding two helium atoms simultaneously in this vicinity of the $\overline{p}\text{He}^+$ atomcule is very small.

Assuming that both the impact approximation and the binary-collision condition really hold, the observed shift is given by the sum of the small shifts associated with single collisions. It should then naturally be proportional to the rate of collisions and hence the density, apart from some possible dependence on the temperature. If, instead, three-body collisions have dominant effects, the shift should be proportional to the probability of finding two helium atoms at the same time in the vicinity of the atomcule, which is quadratic with the helium density.

In a case where the quasi-static approximation is applied and yet the binary-collision approximation is valid, we can easily derive the quadratic dependence of the shift on the density, from a naïve consideration. The mean interatomic distance R is inversely proportional to the cubic root of the number density N. Since the van der Waals interaction potential $V(R)$ shows a minus-6th-power dependence on the distance, and the potential is directly related to the shift, we obtain a quadratic dependence of the shift on the density:

$$R \propto \frac{1}{N^{1/3}}\,, \quad V_j(R) = -\frac{C_6^{(j)}}{R^6}\,, \quad \Delta\nu = \frac{|V_i(R) - V_f(R)|}{h} \propto N^2\,. \tag{5.10}$$

Our experimental results that the shift and the width depend linearly on the density,

is observed as the line broadening.

thus support the assumption of binary and impact collisions, and confirms the validity of the calculation.

However, it may be astonishing that the observed shift remains linear even at very high densities. At 8 bar and 5.8 K, the $\overline{p}\mathrm{He}^+$ atom will find the nearest helium atom at a distance of only 4 Å while the de Broglie wavelength is 5 Å; already much larger than the atomic diameter of $2a \sim 0.6$ Å. In such a dense medium, the $\overline{p}\mathrm{He}^+$ atom may well be always subject to interaction with several helium atoms. There the impact approximation may not be fully valid any more, although the quasi-static approximation is too extreme at the opposite limit to be applied. For a better comprehension, we should consider a more general approach that will mediate between the two limits. Nevertheless, our densest condition is expected to be at a boundary of the binary-collision approximation, with small effects coming from many-body interactions. Of course, the perfect theory should make a quantum mechanical approach to account for the long de Broglie wavelength, and include *ab initio* calculations of the interaction potential, but it is far beyond the current scope.

5.4.3 Theoretical calculation and considerations

In the calculation of Korenman which is explained in detail in Appendix **D.2**, three approximations are assumed in the model for simplicity of the calculation, apart from the binary-collision and the impact approximations:

(i) A hard-core repulsive potential at $R = R_1$, and therefore neglect of contributions from impact parameters $b < R_1$ (which are estimated as small in such a case),

(ii) semiclassical approximations for phase shifts as in Eq. (D.34), p. 124,

(iii) the rectilinear trajectory approximation for $R(t)$ after Eq. (D.34).

The repulsion between $\overline{p}\mathrm{He}^+$ and He is caused by the Pauli exchange of electrons. Therefore, we can expect that the repulsion will occur when the electrons of two subsystems are in the same space region, *i.e.* we can estimate R_1 as a sum of average electron radii for the two atoms, each being ~ 1 a.u., and then $R_1 \sim 2$ a.u. Old estimations of the interaction of kaonic helium with the helium atom show that the repulsion take place up to $R_1 \lesssim 3$ a.u. [9, (b)]. So the $R_1 \sim 2$–3 a.u. are among the appropriate values.

In Korenman's estimation, the $\overline{p}\mathrm{He}^+$ atomcule is approximated by a hydrogen-like atom with effective charges Z_{eff} (cf. Appendix **A.2**). For the Z_{eff} values obtained from different wavefunctions out of three different calculations, he came up with the values of shift and width listed in Table **5.5**. In spite of the simple model and the basic approximations, his calculation (except II in the table) succeeded in reproducing qualitatively the

experimental observation that (i) the shifts are toward longer wavelength (red shifts), (ii) the absolute value of the shift is larger for the 597 nm transition than the 470 nm, and (iii) the collisional widths are *smaller* than the shifts. Quantitatively, his estimation gives the same order of shifts, but the widths are too large. This means that a more elaborate treatment in the repulsive potential at small distances $R \lesssim 3$ a.u. are important.

Table 5.5: Theoretically calculated collisional shift and broadening for a target at 6 K by Korenman are compared with experimental results at 5.8–6.3 K. Calculations I–III use different values for the effective nuclear charges obtained from different theoreticians' energy-level calculations. The shifts and widths are expressed in units of $[10^{-6}$ a.u./10^{21} cm$^{-3}]$.

Transition		597 nm	470 nm
Theory I	Δ	-0.71	-0.55
	γ (R_1=2 a.u.)	0.78	0.55
	γ (R_1=3 a.u.)	0.53	0.29
Theory II	Δ	-0.37	$+0.67$
	γ (R_1=2 a.u.)	0.31	0.71
	γ (R_1=3 a.u.)	0.05	0.46
Theory III	Δ	-0.70	-0.63
	γ (R_1=2 a.u.)	0.76	0.66
	γ (R_1=3 a.u.)	0.51	0.41
Experiment	Δ	-0.62	-0.23
	γ	0.05	< 0.15

According to Eq. (D.40), the shift should have a temperature dependence of

$$\Delta \propto v_T^{3/5} \propto T^{\frac{3}{10}} . \tag{5.11}$$

We have ignored the possible temperature dependence of the observed shift for the 597 nm resonance in Section **5.1.2**, but here we modify Eq. (5.1), p. 55 to be:

$$\lambda = \lambda_0 + s(T)\,\rho . \tag{5.12}$$

From our data, $s(T) = (1.22 \pm 0.02) \times 597.26$ nm/(g/ℓ) at $T = 6.2$ K while the data at 15.2 K shows slightly larger shift:

$$\left.\frac{s(15.2\text{ K})}{s(6.2\text{ K})}\right|_{\text{exp}} = 1.22 \pm 0.15 .$$

This is in accordance with the theoretically deduced temperature dependence of

$$\left.\frac{s(15.2\ \mathrm{K})}{s(6.2\ \mathrm{K})}\right|_{\mathrm{th}} = \left(\frac{15.2}{6.2}\right)^{\frac{3}{10}} = 1.31\ ,$$

although the observation does not exclude the possibility of no temperature dependence of the shift parameter s.

From our experimental data of the shift (Δ) and width (γ), corresponding cross sections as defined in Eq. (D.29)* in Appendix **D.2.1**, p. 123 can be calculated to be

$$|\sigma_\Delta| = 1.38 \pm 0.02\ \text{Å}^2 = 4.9 \pm 0.1\ \text{a.u.}\ , \quad |\sigma_\gamma| = 0.12 \pm 0.06\ \text{Å}^2 = 0.4 \pm 0.2\ \text{a.u.} \quad (597\ \text{nm})$$
$$|\sigma_\Delta| = 0.51 \pm 0.05\ \text{Å}^2 = 1.8 \pm 0.2\ \text{a.u.}\ , \quad |\sigma_\gamma| < 0.3\ \text{Å}^2 = 1.1\ \text{a.u.} \quad (470\ \text{nm})\ ,$$

at 5.8–6.3 K. These cross sections for the elastic collisions are, as naturally expected, of geometrical size. In contrast to this, the cross sections for inelastic quenching collisions as observed by the lifetime shortening of the parent (37,34) state of the 470 nm resonance at high density, which is discussed in Appendix **B.3**, has a much smaller cross section of typically $(2.6\text{–}9.6) \times 10^{-4}$ Å^2. On the other hand, the quenching cross section by collision with hydrogen or oxygen molecules, as presented in Appendix **B.4**, turned out to be of the geometrical size. These results mean that for collisions with helium atoms, only one hard collision out of several thousand collisions is inelastic and results in the quenching of the state, while when $\overline{p}\mathrm{He}^+$ atomcules collide with active molecules, most of the collision will result in the quenching of the metastable state.

5.4.4 Comparison with ordinary atoms

Collisional shifts and widths for ordinary atoms and molecules have been studied both experimentally and theoretically for a century already [80–82]. In the case of collisions of normal atoms, especially for alkali and alkali-earth atoms, usually the observed width is larger than the shift, and sometimes the shift is even ignored in the discussion [81], [85, (a), Sect. 3.3]. This tendency is also true for microwave-transition lines in ordinary molecules [86, 89]. The typical shift and width parameters (Δ, γ) are of the order of 10^{-20} cm^{-1}/cm^{-3} $\sim 10^{-18\sim-19}$ GHz/cm^{-3} ($\sim$ 10 MHz/Torr at room temperature), and compared to this, our measured shift and width parameters are 2–3 and 3–4 orders of magnitude smaller. Also, the observed width is one order of magnitude smaller than the shift, which is a rare case under the condition of impact dominance.$^\times$

*We use an average value for the velocity $v \approx \langle v \rangle = \sqrt{8kT/\pi\mu} = \sqrt{4/\pi}\, v_T = 290$ m/s at 6 K.

$^\times$Larger shifts than the widths are also observed in high Rydberg states of alkali atoms [90–92]. But in that case, the energy was measured with respect to the ground state and not the energy difference

This situation can be understood by noting the weak interaction potential in the $\overline{p}\mathrm{He}^+$–He collision. Alkali atoms have a single weakly-bound valence electron, and therefore have a very large polarizability of 100–300 a.u. whilst that of helium is only 1.4 a.u. Also, what we have observed is the laser transition between very highly excited states of the atomcule, and therefore the main part of the potential changes are canceled and only a *small difference* in the possible energy shift and broadening is observable. Therefore, the difference in the phase shift is much smaller compared with collisions of normal atoms, and hence a small Weisskopf radius b_T (see Appendix **D.2**). Since the main contribution to the collisional width γ comes from hard collisions with impact parameters $R_1 < b < b_T$ and this region is small because $R_1 \sim 2$–3 a.u. and $b_T \sim 4$ a.u., γ will be very small; while the shift which is related with larger impact parameters $b > b_T$ is *relatively* large. The interaction itself is weak (c_{if} is small), however, and also the velocity v_T is small due to the low temperature[bb] (thus the collision is less frequent), the shift given in Eq. (D.40a), p. 125, should be naturally smaller in our case compared with normal atomic collisions.

Quite in contrast, in the usual cases of alkali atoms colliding with rare gas atoms, the interaction is much stronger and accordingly b_T is larger, therefore the second term in Eq. (D.40b) can be neglected. Then the ratio between the shift and the width is $\Delta/\gamma \approx \tan(\pi/5) = 0.73$ and $\Delta < \gamma$ is obtained.

between highly excited states. The observed large shifts ($\Delta \sim 10^{-18\sim-20}$ cm^{-1}/cm^{-3}) are due to the large cross sections (10^2–10^4 Å^2) of soft collisions with dilutely wide-spread wavefunction of the valence electron. So the situation is different from our case.

[bb] Our measurement was at 6 K, while normally the measurements in the literature were performed at room temperature or higher temperatures.

Chapter 6

Conclusions and Future Scope

6.1 Conclusions

In summary, we have observed density shifts of the laser resonance lines of antiprotonic helium atoms in dense helium medium. The central frequency showed linear red shifts of 0.61 ± 0.01 GHz and 0.22 ± 0.02 GHz per 1 g/ℓ for the 597 nm and 470 nm transitions, respectively. These phenomena were quantitatively explained by a simple theoretical model, and revealed the unusually small van der Waals interaction of $\overline{p}\mathrm{He}^+$ atomcule with helium atoms. We have also observed selective quenching of specific metastable states in dense helium media or by a small admixture of foreign molecules, and theoretical explanations to these effects are awaited. This requires calculation of collisional processes at near distances, which would also be necessary for further qualitative interpretation of the observed broadening.

With these measured shift parameters, we have determined the vacuum wavelengths at the zero-density limit. The values were compared with very recent theoretical calculations on the energy levels of the $\overline{p}\mathrm{He}^+$ "atomcule", and they showed excellent agreement at a level of 10^{-6} when the relativistic and QED corrections were taken into account. This is not only a breakthrough in the precise calculation of the Coulomb three-body systems from the theoretical point of view, but experimentally, our measurements surpass the currently known precision of the $\overline{p}$ Rydberg constant. This means that high-resolution spectroscopy of $\overline{p}\mathrm{He}^+$ atom now offers new possibilities for measuring fundamental properties of the antiproton.

6.2 Future Scope

The study of $\overline{p}\mathrm{He}^+$ atomcule was made possible by the use of the excellent $\overline{p}$ beam from the LEAR ring at CERN; indeed this antiproton source was the only one in the world capable of supplying a beam of suitable purity and quality. Although the LEAR facility was shut down at the end of 1996, we can now look forward to continue these experiments at the new AD (antiproton decelerator) ring currently being constructed at CERN [93]. The start of these new studies of the $\overline{p}\mathrm{He}^+$ atomcule is anticipated in the first year of the AD machine period [94].

We have measured the density shifts and broadenings in transitions between highly excited states of the $\overline{p}\,^4\mathrm{He}^+$ atomcule. These observations were made for only two of the many resonances discovered, and corresponding measurements for more lines are expected in the near future.

In spite of the high density of helium at the super-critical phase, the observed shifts were linear with density. What will happen if we perform spectroscopy of $\overline{p}\mathrm{He}^+$ at different target conditions? Spectroscopy of alkali and alkali-earth atoms in superfluid liquid helium has revealed very large shifts of resonances up to several nanometers in wavelength [95, 96]. This is well understood by means of a "bubble model", which assumes that the each alkali(-earth) atom is encaged in a bubble which is maintained by the Pauli repulsion between the atom and several surrounding helium atoms. The transition from ground (s) to an excited (p) state will change the shape of the wavefunction of the valence election, and accordingly the shape and volume of the bubble. This will shift and broaden the resonance line of the atom significantly, because the interaction at distances of the order of the atomic size is quite strong. The fact that similar situations may be realized for the $\overline{p}\mathrm{He}^+$ atomcule raises interesting possibilities for probing the $\overline{p}\mathrm{He}^+$–He interactions at near distances via the spectroscopic techniques described herein.

The above mentioned studies will be only a small part of the anticipated $\overline{p}\mathrm{He}^+$ work in the AD era. Among other subjects following on to our experiments at LEAR, we may especially mention an attempt to observe a microwave-laser double resonance which will directly measure the "hyperfine" splitting. This subject will be discussed in Appendix **B.6**.

Appendix A

Formation and Level Structure of Antiprotonic Helium Atomcules

A.1 Formation of $\overline{p}\mathrm{He}^+$ Atomcules

Experimentally, the $\overline{p}$ beams were extracted from the LEAR facility at an energy of 21 MeV and slowed down to hundreds of kiloelectronvolts (keV) after passing through degrader foils and windows before reaching the helium target. The $\overline{p}$ further lost its energy by ionizing helium atoms along the trajectory, until the energy became of the order of one hartree. Note that the annihilation cross section of $\overline{p}$ in flight is negligibly small. The first ionization potential of helium atom is $I_0 = 24.6$ eV, which corresponds to the $\overline{p}$ energy of 30.7 eV for ^{4}He target and 32.8 eV for ^{3}He in the laboratory frame. The formation of the $\overline{p}\mathrm{He}^+$ atomcule was theoretically studied by employing a classical trajectory Monte Carlo simulation (CTMC) [97] or a coupled-channels semiclassical approximation (CCSA) with adiabatic basis [98] and others [36]. The calculated capture cross section increases drastically at the border energy $E = I_0$ (in the center-of-mass frame) as shown in Figure **A.1**, which is in accordance with the general knowledge for atomic capture (cf. Refs. [99, 100] for the cross sections of $\overline{p}p$ formation in $\overline{p}$ + H/H_2 collisions).

In the process of $\overline{p}$ capture, one of the two electrons of the helium atom will be removed out, but according to the calculations, the electron does not carry out much more energy than its initial binding energy [94, (Appendix B.1)]. This means that the $\overline{p}$ is captured in an orbit with similar binding energy to that of the electron. In other words, the $\overline{p}$ orbit has a similar radius to that of the electron, and this condition automatically gives a very large principal quantum number $n \sim n_0 \equiv \sqrt{M^*/m_e} \approx 38$ for the heavy antiproton.

The neutral $\overline{p}\mathrm{He}^+$ atomcule formed has a large translational energy of several electron volts. This energy is lost quickly by collisions with low-temperature helium atoms with less than a millielectronvolt (meV) energy at 6 K. From a naïve idea with a hard elastic sphere collision model, we find that roughly half of the energy is taken away from the

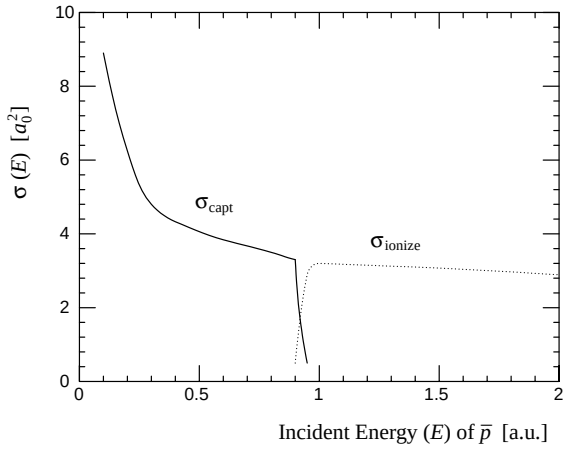

Figure A.1: Formation and ionization cross sections of $\overline{p}\mathrm{He}^+$ as a function of incident $\overline{p}$ energy E (in the center-of-mass frame), calculated by Ohtsuki [36]. The capture cross section σ_{capt} increases drastically while the ionization cross section σ_{ionize} drops as the energy decreases, at the ionization potential I_0 of the helium atom. The cross sections are of the order of the geometrical size.

$\overline{p}\mathrm{He}^+$ in each collision, so that the atomcule is expected to be thermalized after 10–20 collisions.* This means that the thermalization of the $\overline{p}\mathrm{He}^+$ atomcule is achieved within the order of 10 ns under our experimental conditions. It is not possible to judge the idea above from our experimental data, but we can confirm from the width of the observed laser resonances, that the atomcule is well thermalized at the timing of the laser roughly 1 μs after the $\overline{p}\mathrm{He}^+$ formation; otherwise the resonance would have a much larger Doppler width.

A.2 Intuitive Picture of the Level Structure

In this section, an intuitive level scheme of $\overline{p}\mathrm{He}^+$ atomcule in a simple atomic model is presented for a naïve understanding of its level structure.

In the vicinity of $n \approx n_0 = \sqrt{M^*/m_e}$ (≈ 38 for $\overline{p}\,^4\mathrm{He}^+$ and 37 for $\overline{p}\,^3\mathrm{He}^+$), the total binding energy E_{B} of $\overline{p}\mathrm{He}^+$ atomcule is similar to that of the helium atom, and it is shared nearly equally by the e^- and the $\overline{p}$:

$$\begin{aligned} E_{\mathrm{B}} = E_{\mathrm{B}}^{e} + E_{\mathrm{B}}^{\overline{p}} &= \frac{1}{2}(Z_{\mathrm{eff}}^{e})^2 m_e c^2 \alpha^2 + \frac{1}{2}(Z_{\mathrm{eff}}^{\overline{p}})^2 \frac{M^*}{n^2} c^2 \alpha^2 \\ &\sim 4\mathrm{Ry} + I_0 = 79.0 \text{ eV} = 2.90 \text{ a.u.}\,, \end{aligned} \tag{A.1}$$

where Z_{eff}^{e} and $Z_{\mathrm{eff}}^{\overline{p}}$ are the effective nuclear charges seen by the electron and the antiproton, respectively. The mean radii of e^- and $\overline{p}$ are almost the same for the states with $n \approx n_0$, so that $Z_{\mathrm{eff}}^{e} \approx Z_{\mathrm{eff}}^{\overline{p}}$ and $E_{\mathrm{B}}^{e} \approx E_{\mathrm{B}}^{\overline{p}}$. This gives $Z_{\mathrm{eff}} \approx \sqrt{2.90} = 1.7$.

*During these high-energy collisions (high energy in terms of atomic collisions), some of them may undergo inelastic processes and annihilate. Korenman has suggested [101] that primordially the $\overline{p}\mathrm{He}^+$ atomcules are also formed on metastable states with $41 \leq n \lesssim 50$ and as much as 20% of the $\overline{p}$ are initially captured in metastable states, but that most of those extremely highly excited states are weak against collisions and have been quenched by this thermalization processes. Evaluation of this hypothesis has to wait for future experiments with ultra-slow $\overline{p}$ beams crossed with helium beams.

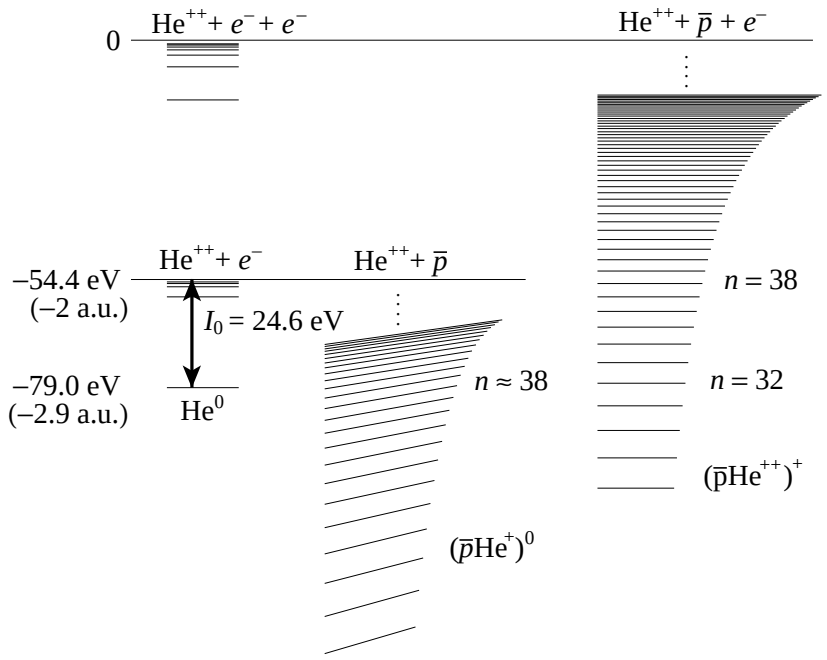

Figure A.2: Intuitive level scheme of the He atom, the $\overline{p}\mathrm{He}^{+}$ atomcule and the $\overline{p}\mathrm{He}^{++}$ ion. The energy level of neutral helium corresponds to $n \approx 38$ for $\overline{p}\,^{4}\mathrm{He}^{+}$ and 32 for $\overline{p}\,^{4}\mathrm{He}^{++}$ (the quantum numbers are smaller by 1 in the case of ^{3}He), and the large difference in the maximum angular-momentum quantum number ($\max(l) = n-1$, $\Delta(\max(l)) \approx 6$), together with the "$|\Delta l| \leq 3$ Auger dominance rule" is the key to the metastability.

The Rydberg series of the $\overline{p}\mathrm{He}^{+}$ atomcule with highly excited antiproton converges to the energy level of singly charged helium ion, that is $-E_{\mathrm{B}} = -2$ a.u. $= -54.4$ eV ($(\overline{p}\mathrm{He}^{+})^{0}_{n} \overset{n\to\infty}{\longrightarrow} \mathrm{He}^{+} + \overline{p}$). See Figure **A.2**.

On the other hand, the $\overline{p}\mathrm{He}^{++}$ ion is a hydrogen-like system and its binding energies are exactly given by the following equation (within the classical treatments):

$$E_{\mathrm{B}} = \frac{1}{2} Z \frac{M^{*}}{n^{2}} c^{2}\alpha^{2} \quad (Z = 2)\,. \tag{A.2}$$

The Rydberg series of this ion converges to zero energy ($(\overline{p}\mathrm{He}^{++})^{+}_{n} \overset{n\to\infty}{\longrightarrow} \mathrm{He}^{++} + \overline{p}$), while the binding energy of the He^{+} ion (2.0 a.u.) corresponds to $n \approx 38$ (for $\overline{p}\,^{4}\mathrm{He}^{++}$and 37 for $\overline{p}\,^{3}\mathrm{He}^{++}$) and that of the He^{0} atom (2.9 a.u.) corresponds to $n \approx 32$ (31) for the $\overline{p}\mathrm{He}^{++}$ ion

This means that the $\overline{p}\mathrm{He}^{+}$ atomcule with $n \approx 38$ having a binding energy of ca. 2.9 a.u. will find a $\overline{p}\mathrm{He}^{++}$ ionic state with $n \approx 32$ at a similar energy. This difference in

the principal quantum number is the key to the existence of metastable states. For the "most circular" state with $l = n - 1 \approx 37$, the atomcule has to release a large difference in the angular momenta, $37 - (32 - 1) = 6$. According to the "$|\Delta l| \leq 3$ Auger dominance rule" (Section **2.3.2**) based on the calculations of Auger-transition rates, a transition with $\Delta l = 6$ is by far too weak to compete with the slow radiative decay, and therefore the $\overline{p}\mathrm{He}^+$ state becomes metastable.

A.3 Non Metastability Except for Helium

The anomalous longevity of antiproton (or more generally, negative hadrons) in matter has been observed only in helium. Early works including our former group have disproven the existence of metastability in hydrogen (H_2 target) [102, 103], lithium and lithium hydride [3, 12], beryllium [3], carbon [3], nitrogen [6], neon [5, 11, 46], argon [6], calcium [3], krypton and xenon [46].

There are also some theoretical work to account for these results. In the case of the hydrogen, the antiproton may form a protonium atom ($\overline{p}p$) [99, 100]. However, it is a two-body system without an electron, so that it is very weak against external perturbations and will immediately annihilate [1, 2] after any collisions with surrounding hydrogen molecules which can easily penetrate through the protonium atom (because no Pauli repulsion exists) and cause Stark mixing of the degenerate l states (just like for $\overline{p}\mathrm{He}^{++}$) [104]. Or they may be destroyed even at the formation stage in the case of a molecular hydrogen target, by the weak electric field produced by the outgoing spectator hydrogen atom. Nevertheless, the protonium atom should have long-lived states if it is isolated in vacuum, and an experiment has been proposed, aiming at the production and spectroscopy of $\overline{p}p$ using cold antiproton and atomic hydrogen beams [94, (Sect. 4.2)].

In the case of lithium, no theoretical work has yet been done, except for a primitive argument [105] which stated that multiple Auger process is too fast for the two-electron system $\overline{p}\mathrm{Li}^+$ to have metastable lifetime. Some people have different opinions and think that $\overline{p}\mathrm{Li}^+$ atoms may be metastable when isolated in vacuum, but all agree that this atom can not have a long life when formed in lithium metal or lithium compounds, as was the case with the experiment.

As for the neon atom, Ohtsuki has pointed out that metastable states are indeed expected to exist around $n_{\overline{p}\mathrm{Ne}^+} \sim n_{\mathrm{Ne}}\sqrt{M^*_{\overline{p}-\mathrm{Ne}^{++}}/m_e} \approx 83$ and $l \lesssim n - 1$, but that the relatively small ionization potential $I_0 = 10.8$ eV prohibits large-l states to be populated, because even the maximum $\overline{p}$ energy is not enough to bring the necessary angular momentum into the system at a typical impact parameter which is the radius a of the neon atom; *i.e.* $n - 1 \gg l_{\max} = a\sqrt{2M^*I_0}/\hbar$ [106].

After these thoughts, helium seems to be the only gentle host to the antiproton, and the exotic $\overline{p}\mathrm{He}^+$ atomcule is a miraculous system where all the factors harmonize to allow longevity of $\overline{p}$ in matter.

Appendix B

Summary of Achievements of Laser Spectroscopy Experiments

In this chapter, some fruitful results not explained in the main text will be discussed. The so-far discovered 13 resonance lines not only clarified the structure of $\overline{p}\mathrm{He}^+$ atomcule but also made it possible for the first time to measure the lifetimes and populations of individual states. We also found that certain levels are quenched in high density media or by a small amount of foreign gases, and systematically studied these phenomena. These data provide interesting information on collisional and chemical aspects of the exotic atomcule, together with the data on resonance shifts and widths presented in Chapter **5**. The following discussions focus on the $\overline{p}\,^4\mathrm{He}^+$ atomcules.

B.1 Discovery of Resonances

B.1.1 Unfavored transitions

Most of the resonances we discovered are "favored" transitions which do not change the vibrational quantum number v. These transitions are strong due to relatively large dipole moments of 0.2–0.3 debye*, because the wavefunction of $\overline{p}$ overlaps very well between the initial (parent) and the final (daughter) states (refer to Section **2.3.1**). In 1995, however, we found two "unfavored" transitions $(n, l, v) \Rightarrow (n+1, l-1, v+2)$ with 10 times smaller dipole moments which change v by $\Delta v = 2$ [52]. These resonances at 726.10 nm and 713.58 nm were ascribed to $(n, l, v) = (37, 35, 1) \Rightarrow (38, 34, 3)$ and $(37, 34, 2) \Rightarrow (38, 33, 4)$, respectively, and were the first touch of the $v = 1$ and 2 metastable states (see Figure **4.4**, p. 46). Since the laser power density required to saturate these weak transitions was 100 times higher than for the strong "favored" transitions for which over 80% of the population were "shot" by the powerful laser pulses, the depopulation efficiencies for the unfavored

* 1 debye $\approx 0.4\, ea_0$, see Appendix **F.1**

transitions were supposed to be low and were not known. No systematic study has yet been performed to determine the populations and the lifetimes of these "circular" ($v = 0, 1$) metastable states.

The discovery of those two resonances were made with a different experimental setup than for other resonances, namely the "analog" method explained in Section **3.5** and in Ref. [75].

B.1.2 Double resonance

The laser-induced resonances so-far mentioned were observed only between pairs of metastable states and short-lived states. Resonances between metastable states are hardly visible because they do not create any distinct peak but only modify the DATS (delayed annihilation time spectra) slightly. We attempted, however, to observe a resonant transition (38,35) $\Rightarrow$ (37,34) at 529 nm which lied one-step upstream of the 470 nm resonance in the $v = 2$ decay chain, in the following "double resonance" technique: the idea was to take advantage of having two identical laser systems, and to shoot down the population at the parent (38,35) state through two resonant transitions at 529 nm and 470 nm. We always tuned the "blue" laser light on resonance to the 470 nm transition while sweeping the the other "green" light around the other transition. The timings of the two lasers were adjusted so that the two pulses overlapped in time. With this setting, we would always observe the 470 nm resonance peak, and the "green" resonance would be observed as an enhancement of the peak height, as the population of the (38,35) state as well as that of the (37,34) state would be depopulated simultaneously and contribute to the resonant annihilation of antiprotons. In fact, we succeeded in observing this double resonance at 529.622 ± 0.003 nm [51] in 1995.

This "green" resonance could also be observed without the aid of the "blue" light at 470 nm. We have observed a strong density-dependence of the lifetime of the (37,34) state, as will be discussed in Appendix **B.3**, and that the lifetime is shortened to a few hundred nanoseconds for a target of ca. 1 bar and ca. 6 K. This much shorter lifetime than the typical decay time of the DATS spectra enabled us to directly observe a "single resonance" of the 529 nm transition. The observed resonance peak decayed with the lifetime of the daughter (37,34) state, which was long enough compared with the laser-pulse duration for the accurate lifetime measurement mentioned in Appendix **B.2.3**.

B.1.3 Resonances so far undiscovered

Although we have observed many resonances, some transitions remain unobserved in spite of our long search for them. Soon after the discovery of the first resonance at 597 nm,

we tried to find a $v = 4$ transition $(40, 35) \Rightarrow (39, 34)$ expected at 673 nm. Although we searched with a step of 0.020 nm for a wide region between 671.56 and 674.44 nm,[†] this search was fruitless. The (40,35) state may not be populated or may be quenched under the target condition used, but it may also be possible that we simply missed the resonance in the gaps of the steps.[‡]

We also applied the double resonance method to search for the transition $(40, 36) \Rightarrow (39, 35)$ in the $v = 3$ series which feeds the parent state of the 597 nm resonance. The wavelength ranges scanned were 672.70–674.30 and 674.39–674.59 nm; again we found no resonance, which is inconsistent with our conclusion from the laser-time variant measurements explained in Appendix **B.2.1**, that the upper feeding state does exist and is populated. We attribute the reason for this failure, simply to imperfections in our double-resonance technique at that time (1993).[§]

In 1996, we searched for two unfavored transitions at 528 nm and 533 nm both from $n = 35$ to 36 without finding any significant resonance peaks.[¶] We used the analog data aquisition method explained in Section **3.5**, which might not have been sensitive enough to detect a small resonance peak,[‖] so that we can not yet conclude that the parent states at $n = 35$ of these transitions are not populated.

Nevertheless, this fact that we did not observe these transitions *from* these $n = 35$ states tempted us to look for the favored transitions *to* these states. Inferring from the fact that the (37,34) state was quenched by high density of the helium target while the (39,35) state was not (see Appendix **B.3**), we presumed that low-lying states are generally subject to quenching including the states (35,33) and (35,34). Then the resonant deexcitation to these daughter states would be observed at 417 and 416 nm, respectively (see the level diagram in Figure **4.4**, p. 46 or in Color figure V). We therefore scanned

[†]The target condition was unstable and fluctuated between 4.2–13 K and 460–850 mb.

[‡]The scanning step of 0.020 nm was larger than the laser bandwidth of 0.008 nm, so if the resonance was weak and/or the resonance width was small, we could easily miss it.

[§]This resonance was actually difficult to observed. In the case of the $(38, 35) \Rightarrow (37, 34) \Rightarrow (36, 33)$ double resonance mentioned in the previous section, we observed a large (more than 5 times) enhancement of the 470 nm resonance peak when we reached the upper resonance at 529 nm, because the state (37,34) was moderately quenched by the dense helium target (see Appendix **B.3**) while the upper state (38,35) was not, resulting in a much larger population in the (38,35) state than that in the (37,34) state. In the case of the $(40, 35) \Rightarrow (39, 34) \Rightarrow (38, 33)$ resonance, however, the population in the (40,35) state was expected to be smaller than that in the (39,34) state, and the estimated enhancement of the peak height was only 20%.

[¶]We scanned repeatedly for 527.601–528.002 nm and for 532.412–533.265 nm, both with a step of 0.005 nm. The target condition was 6.1 K and 550 mb.

[‖]But note that we did observe the 713 nm and 726 nm unfavored resonances with this analog method (see Appendix **B.1.1**), almost immediately after we started scanning around the values predicted by Korobov.

the laser wavelengths with a step of 0.002 nm, around the values theoretically predicted by Korobov [30].** We investigated different target pressures ranging from 120 mb to 800 mb, in order to deal with possibly differing degrees of quenching. We also searched for the resonant transition $(37, 35) \Rightarrow (36, 34)$ at 469 nm which lies one step upstream of the 417 nm transition in the $v = 1$ cascade sequence, under the hypothesis that the state (36,34) might be already quenched.†† In spite of these searches, we did not find any resonances, which may indicate that both the states (36,34) and (35,33) are not quenched by collisions with helium atoms under the target conditions examined.‡‡ In this case we may need to search for a lower-lying transition $(35, 33) \Rightarrow (34, 32)$ at 372 nm in order to investigate the "favored" transitions in the $v = 1$ cascade series. As for the states (36,35) and (35,34) in the $v = 0$ series, the scanned regions and conditions are so limited that we cannot draw any conclusion as to whether these states are populated or quenched.

B.2 Lifetime Measurements

The successful observation of the resonant transitions offered for the first time a unique opportunity to measure directly not only the transition energies but also the initial population and the individual level lifetimes of an exotic atom. There are four different types of measurements we used to deduce the lifetimes of individual states, which are to be explained in this section.

B.2.1 Laser-timing variant method

When the depopulation efficiency of the laser pulse is known, the area of the resonance peak reveals the population of the parent metastable state of the laser-induced transition, at the time of the laser irradiation. By varying the timing of the laser pulse and calculating the decay time of the resonance peak as in Figure **B.1-a**, the overall lifetime of the states in the cascade series can be determined [48, 49].

Taking advantage of having two identical laser systems, we also applied two laser

**The regions scanned were 416.319–416.328 nm and 417.830–417.865 nm at 120 mb, 417.823–417.885 nm at 350 mb, 417.809–417.873 nm at 550 mb, and 417.839–417.854 nm at 800 mb; the temperature being 5.8 K for all the targets.

††The wavelengths were scanned with a 0.003 nm step for 469.464–469.527 nm at 120 mb, 469.454–469.527 nm at 350 mb, and 469.478–469.502 nm at 800 mb; the temperature being 5.8 K for all the targets.

‡‡An alternative idea that the both states might be already quenched and are short-lived, can not be sustained, because it disagrees with our conclusion from the "DATS" measurements that the overall lifetime of the metastable $\overline{p}\mathrm{He}^+$ atomcule is longer than 3 μs under the target conditions examined (see Figure **1.2**, p. 4).

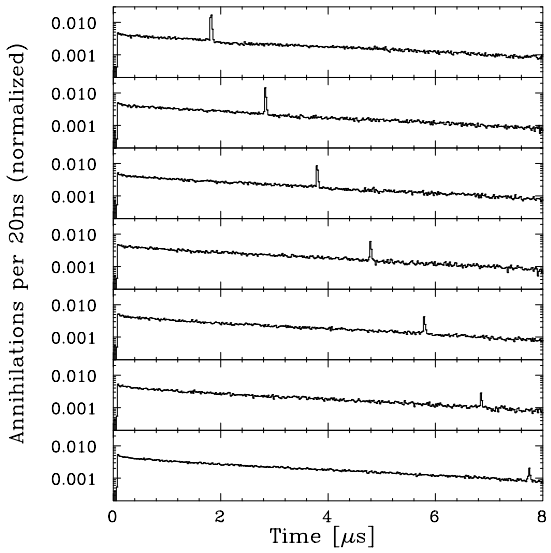

Figure B.1-a: Spectra of the time-variant one-laser measurement. The peak decays exponentially with the time of the laser irradiation (t_1). The observed lifetime of 2.0 μs reveals an overall lifetime of the $v = 3$ cascade series including possible feedings to the parent state (39,35) from upper states.

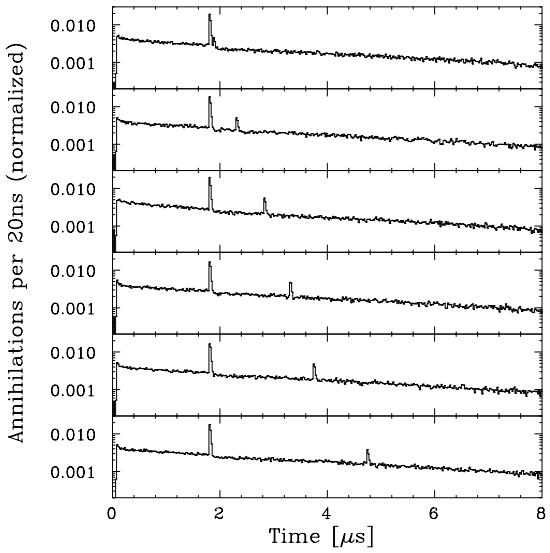

Figure B.1-b: Spectra of time-variant two-laser measurement. The peak at the timing of the second laser (t_2) shows for early timings the feeding from upper states and at later times the decay of the population.

Figure B.1: Observed time dependence of the peak height on the laser timing for the 597 nm resonant transition $(n, l) = (39, 35) \Rightarrow (38, 34)$.

pulses on resonance at different timings. As shown in Figure **B.1-b**, the second peak is small when its time difference relative to the first one is short, since the first laser shot has already depopulated most of the population in the parent state. As the second pulse is delayed, the second signal grows, indicating some population feeding from upper states. The peak then decays when the pulse is further delayed, as the population in the cascade series has already been exhausted.

Knowing that the radiative dipole transitions occur mostly along one of the constant-v series[♯] (because the branching ratios for other possible transitions are small by at least one order of magnitude due to the small dipole moment as explained in Section **2.3.1**), we used a chain-decay model neglecting the side paths as depicted in Figure **B.2** to simulate

[♯] $v = 3$ series: $(41, 37) \rightarrow (40, 36) \rightarrow (39, 35) \overset{597\ \mathrm{nm}}{\Longrightarrow} (38, 34)$,
$v = 2$ series: $(39, 36) \rightarrow (38, 35) \rightarrow (37, 34) \overset{470\ \mathrm{nm}}{\Longrightarrow} (36, 33)$.

the time development of the population.

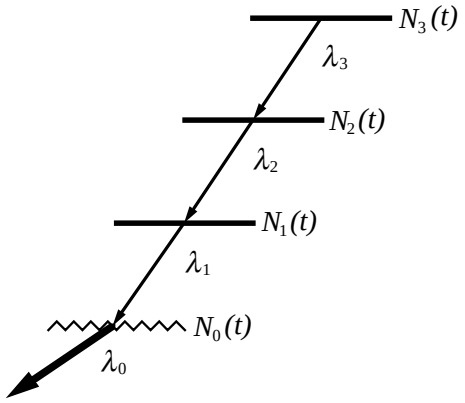

Figure B.2: A schema of the one-ladder cascade model used to fit the data of the time-variant lifetime measurements.

The rate equations of the level population involving 3 metastable levels as in the figure, are described as:

$$\frac{\mathrm{d}N_3(t)}{\mathrm{d}t} = -\lambda_3 N_3(t), \tag{B.1a}$$

$$\frac{\mathrm{d}N_2(t)}{\mathrm{d}t} = +\lambda_3 N_3(t) - \lambda_2 N_2(t)\,, \tag{B.1b}$$

$$\frac{\mathrm{d}N_1(t)}{\mathrm{d}t} = +\lambda_2 N_2(t) - \lambda_1 N_1(t)\,, \tag{B.1c}$$

$$\frac{\mathrm{d}N_0(t)}{\mathrm{d}t} = +\lambda_1 N_1(t) - \lambda_0 N_0(t)\,. \tag{B.1d}$$

Noting that the decay rate of the last state is very fast ($\lambda_0 \sim 100\ \mu\mathrm{s}^{-1}$) compared with the others ($\lambda \sim 1\ \mu\mathrm{s}^{-1}$), the population $N_0(t)$ can be neglected, so that the annihilation rate can be given by $\lambda_0 N_0(t) = \lambda_1 N_1(t)$. The resonance peak is then proportional to the population $N_1(t)$ of the parent state of the laser transition, at the time of the laser irradiation. When two lasers are applied, the second peak area can be simulated by solving the rate equations for $\tilde{N}_1$ instead of N_1, with an initial condition $\tilde{N}_1(t_1) = (1 - \epsilon)N_1(t_1)$ at the time t_1 of the first laser pulse, where ϵ is its depopulation efficiency. The solutions for these rate equations are displayed in Appendix **C.1**. We obtained a set of delayed laser-resonance measurements with different timings t_1 and t_2 of the two lasers. Figure **B.3** summarizes our data for the 597 nm resonance, with $t_1 = 1.8\ \mu$s (b), 2.8 μs (c) and 3.8 μs (d) and various further delayed t_2 timings. All these data together with the single-laser measurements (a) were fitted simultaneously to the solutions of the rate equations and the initial populations $N_1(0), N_2(0), N_3(0)$ and the decay rates $\lambda_1, \lambda_2, \lambda_3$, together with the depopulation efficiency ϵ, were obtained as fit parameters, as are listed in Table **B.1-a** for the 597 nm.Our results for the transition rates agreed well with those of the theoretical calculations (see Section **2.3.1** and Refs. [14, 15, 19–21, 30, 37]), which proved that these states are dominated by radiative transitions. As for the 470 nm

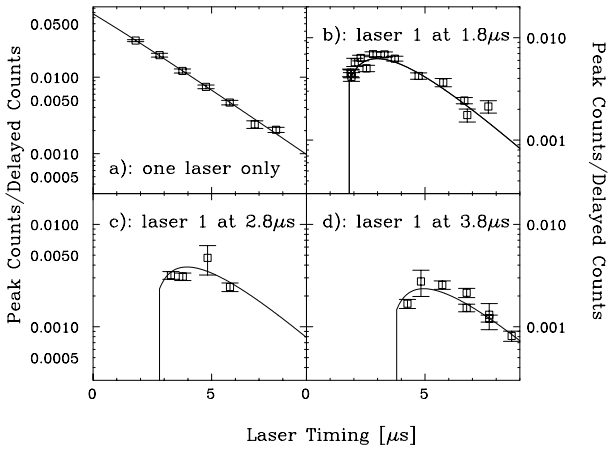

Figure B.3: The data points summarize the results of the one/two-laser timing measurements. Simultaneous fits to all these data revealed the initial populations and the lifetimes of the states in the $v=3$ decay chain.

resonance (Table **B.1-b**), the fit results had large ambiguities and did not give a unique good result. Nevertheless, it indicated that the measured lifetimes were nearly 40% shorter than calculated theoretically, which later turned out to be due to the collisional quenching with normal helium atoms at high density, as will be discussed in Appendix **B.3**.

With both measurements for the 597 nm and 470 nm resonant transitions, we have identified in total 30% of the metastable population in the $v = 3$ and 2 cascade series, and the rest are expected in the more "circular" $v = 1$ and 0 states. This has been the first direct measurement on the initial population of an individual state in any exotic atom, and contributes to the clarification of the not yet well-understood formation mechanism of these atoms.

B.2.2 Depletion and recovery measurement

The sharp resonance peak reveals the deexcited population of the parent metastable state. This population would have decayed gradually had it not been for the laser pulse. It is then obvious that the distinct dip observed after the peak is caused by the lack of this population, and that the area of this dip should be the same as that of the peak. Figure **B.4** compares the DATS (b) with and (a) without the laser-induced peak, and (c) the subtracted spectrum shows, right after the peak, a clear depletion which recovers after a few microseconds. The only difference between the two spectra (a) and (b) are whether the same fraction of the population on the parent state has gradually decayed

Table B.1: Populations and lifetimes of individual states obtained as a fit result of the chain-decay model to the laser-time variant measurements. The levels are indicated as the indices by their principal quantum numbers n. The theoretical calculation refers to [36].

Table B.1-a: Populations and lifetimes for the $v = 3$ cascade series observed with the 597 nm resonance.

N_n, λ_n	Experiment	Calculation
N_{39}	6.7 ± 0.7 %	
N_{40}	4.0 ± 0.3 %	
N_{41}	$< 1\%$	
λ_{39}	0.72 ± 0.02 μs^{-1}	0.61 μs^{-1}
λ_{40}	0.49 ± 0.02 μs^{-1}	0.54 μs^{-1}
λ_{42}	—	

Table B.1-b: Populations and lifetimes for the $v = 2$ cascade series observed with the 470 nm resonance. The values with "*" were intentionally fixed at the theoretical ones in the fitting.

N_n, λ_n	Two-level fit	Three-level fit	Calculation
N_{37}	$11 \pm 2\%$	$16 \pm 2\%$	
N_{38}	$12 \pm 1\%$	$4 \pm 2\%$	
N_{39}		$6 \pm 1\%$	
λ_{37}	1.17 ± 0.06 μs^{-1}	1.16 ± 0.05 μs^{-1}	0.73 μs^{-1}
λ_{38}	0.42 ± 0.06 μs^{-1}	*0.67 μs^{-1}	0.67 μs^{-1}
λ_{39}		*0.60 μs^{-1}	0.60 μs^{-1}

or got deexcited instantaneously by the laser pulse. Then this simple consideration leads to a correct conclusion that the time constant of this recovery tells directly and exactly the lifetime of the parent state of the resonance. It must be noted that this conclusion is always true regardless of any cascade models. A mathematical deduction is given in Appendix **C.3**.

The fact that the lifetime of a single state can be directly observed made this "depletion and recovery" measurement very useful [57]. With this method the lifetime of the parent state (39,35) for the 597 nm resonance was measured at 0.55 bar and 6.3 K, to be $\tau = 1.5 \pm 0.1$ μs (or $\lambda = \tau^{-1} = 0.69 \pm 0.05$ μs^{-1}), which agrees with the "laser-timing variant method" discussed in the previous section. A wider application of this method will be presented in Appendix **B.3**.

B.2.3 Decay rates of the daughter states

The decay rate of the short-lived daughter state of a laser-induced transition manifests

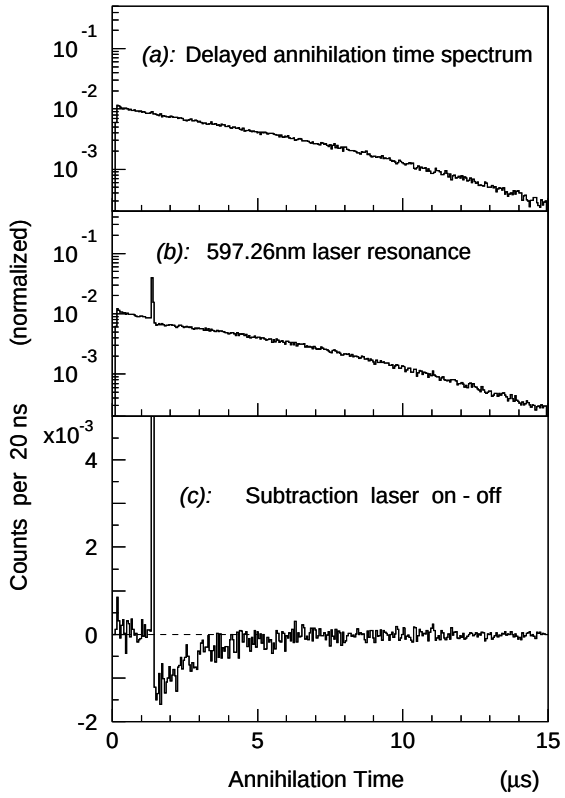

Figure B.4: Comparison of the DATS (b) with (a) and without the laser-induced peak. The subtracted spectrum (c) shows a clear depletion, and the recovery time directly gives the lifetime of the parent state of the resonant transition. The graphs are shown for a ^{4}He gas target of 550 mb and 6.3 K.

itself as the decay time of the resonance peak in the time spectra. The shape of the peak, however, is related with the complicated interaction of the laser with the atomcular states for the duration of the laser pulse. Under our experimental conditions, the temporal profile of the dye laser pulses typically had two peaks; the first main peak was roughly 5 ns wide and the second peak a little broader, and they were about 10 ns apart (see Figure **5.11-a**, p. 68 for a typical temporal profile of the dye laser pulses). This complicated structure was inherited from the pulse shape of the excimer laser with three peaks due to the characteristic of the discharge of the high voltage of the laser. For the duration of the laser pulse, the populations of the two resonating states were continuously mixed while some of them decayed via Auger transition from the daughter state. This resulted in longer decay time than the lifetime of the daughter state by a factor of 2 or more[♭], but it is not easy to analyze the complicated resonance shape.Instead, the lifetime of the daughter state was deduced from the decay constant of the resonance peak after the laser pulse terminated. Due to the fading shape of the laser pulse lasting up to 30–40 ns and the fact that even the small power at the tail can cause a significant amount of transitions (because

[♭]If the laser is very powerful and the Rabi oscillation is fast enough, the two (parent and daughter) states will always have the same population. The Auger decay then occurs for the half of the population, so that the apparent lifetime will be twice as long as if there were no light. If the laser power is weaker than is enough for saturation, the fraction of the population on the daughter state averaged over the duration of the laser pulse will be even smaller, therefore longer lifetime.

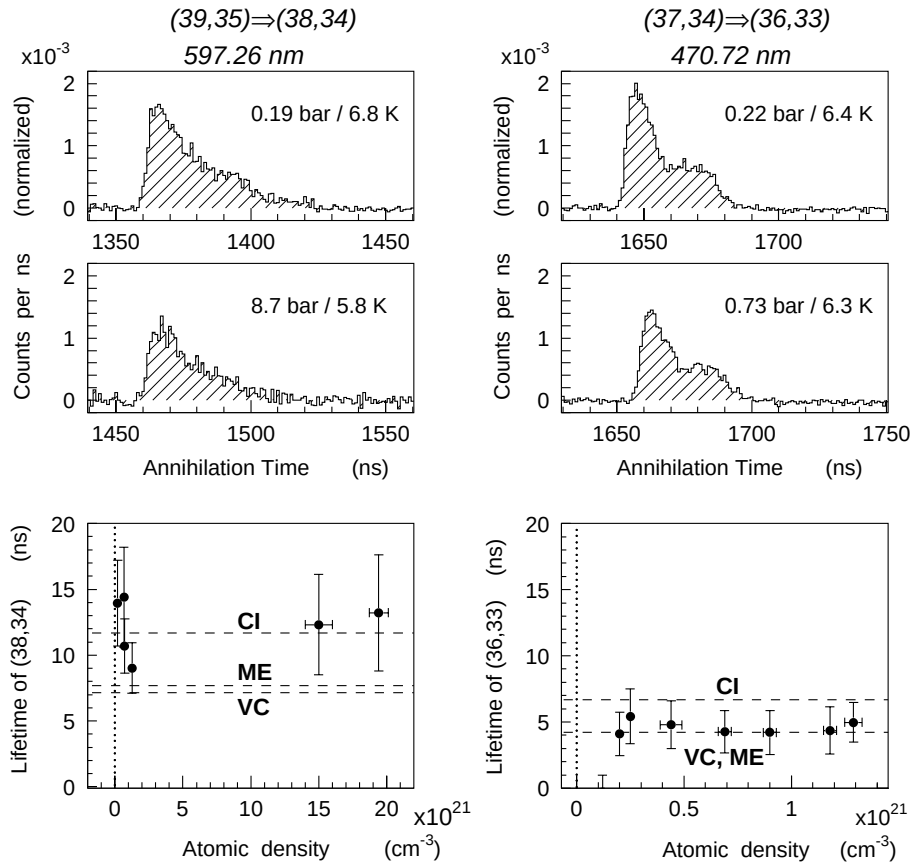

Figure B.5: Top: Temporal shape of the resonance peak for the 597 nm (left) and 470 nm (right) lines at different densities. Bottom: The lifetimes of the daughter states were obtained from the exponentially decaying tail of the peaks after the laser pulse terminated. The obtained values [57] (which do not exhibit any significant density-dependence) agree with what was estimated by theoretical calculations of the Auger-decay rates (CI: Ref. [36], VC: Refs. [37, 38], ME: Ref. [39]).

the total power was much more than enough for saturation), only the very last part of the resonance peak could be used for the fitting, and therefore the statistical error was large. Figure **B.5** shows the temporal shapes of the resonance peaks for the 597 nm and 470 nm lines, and the lifetimes obtained of the daughter states are presented [57], which agree with the theoretical estimations of Refs. [36–39] explained in Section **2.3.2**. Note that the shape of the laser-induced annihilation peak for the 597 nm resonance resembles that of the simulation in Figure **5.11-b**, p. 68 (although the collisional parameters and the power density are not the same).

This method was more useful for the determination of longer or intermediate (ca. 100 ns)

lifetimes of the daughter states for which we could neglect the first 40 ns without losing much statistics. This was the case when the daughter state was one of the metastable states, whose original lifetime of ca. 1 μs was shortened due to the quenching effect either by high-density or by the foreign gases (see Appendices **B.1.2**, **B.3** and **B.4**).

B.2.4 Natural linewidth measurement

If the lifetime of a state is very short, it can be observed as a broad natural width of the resonance line. Such is the case for the "unfavored" resonance observed at 713 nm. The transition is assigned as $(n, l, v) = (37, 34, 2) \Rightarrow (38, 33, 4)$ and the daughter state can decay via Auger transition to a $\overline{p}\mathrm{He}^{++}$ ionic state of $(n, l) = (32, 31)$ with a multipolarity $|\Delta l| = 2$. According to Section **2.3.2**, the Auger process is 3 orders of magnitude faster than for the daughter states of other laser transitions for which $|\Delta l| = 3$, and the rate is of the order of 10^{11} s^{-1}. In fact, the observed resonance width was as wide as 67 ± 6 pm$^{\natural}$ = 40 ± 4 GHz. From the equation based on the uncertainly principle (note that Γ is the *full* width at half maximum of the Lorentzian),

$$\Delta\nu\,\tau = \frac{1}{2\pi} \qquad (\Delta W \Delta t \lesssim \hbar)\,, \tag{B.2}$$

the lifetime of the daughter (38,33,4) state was deduced to be 4.1 ± 0.2 ps.$^{\diamondsuit}$ This result was consistent with recent calculations of the Auger transition rates by Korobov (3.2 ps) [39], Kartavtsev (5 ps) [37], Révai (3.7 ps) [40], and Kino (4.8 ps) [25], in spite of theoretical difficulties in the treatment of coupling between the states with the continuum.

B.3 Lifetime Shortening by Collisions with Helium Atoms

We have seen in Chapter **5** that the resonance frequencies of $\overline{p}\mathrm{He}^{+}$ atomcules shifted and broadened at high-density conditions. Another effect of frequent collisions with surrounding helium atoms was the quenching of metastable states observed as shortening of lifetimes. The first indication of this quenching effect due to high density of the helium target was the fact that the lifetime obtained of the (37,34) state — the parent state of the 470 nm transition at the bottom of the $v = 2$ radiative-cascade chain — was significantly shorter than expected from the theoretical calculations (as shown in Table **B.1-b**) and that it fluctuated and seemed to depend on the target conditions.

$^{\natural}$pm: picometer = 10^{-12} m = 10^{-3} nm, see Appendix F.1.

$^{\diamondsuit}$ps: picosecond = 10^{-12} s, see Appendix F.1

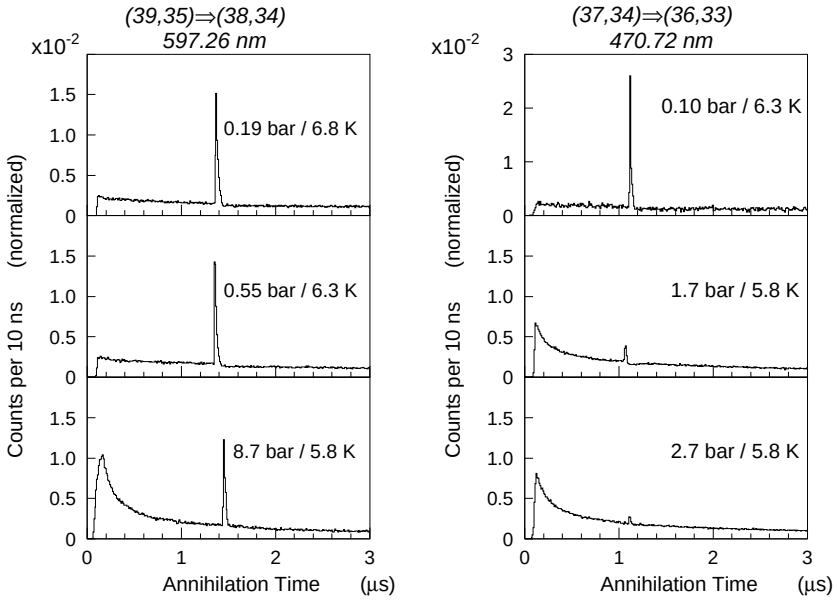

Figure B.6: DATS (delayed annihilation time spectra) with resonance peaks for 597 and 470 nm transitions, taken at different target densities. The height of the induced-resonance peak shrinks drastically for the 470 nm resonance at high densities due to collisional quenching of the parent state, while the 597 nm peak is not affected. The fast-decaying component at early times apparent at high-density conditions also implies shortening of certain metastable states.

Figure **B.6** shows DATS taken at different target densities with laser pulses on resonance for the 597 and 470 nm transitions. The height of the induced-resonance peak becomes drastically short for the 470 nm resonance at high densities above 1 bar at ca. 6 K, while no significant change is observable for the 597 nm peak. The shrinkage of the peak can be ascribed to the shortened lifetime of the parent (and upper) state(s) of the 470 nm transition; by the time the laser is fired, the parent state is already almost emptied as the fast-decaying component at early times may imply.

We studied this phenomenon more systematically in later years [57], directly measuring the parent-state lifetimes with the new and more reliable "depletion and recovery" method explained in one of the previous sections (**B.2.2**).

The results are summarized in Figure **B.7**. The graphs plot the decay rate (λ), or the inverse lifetime ($= \tau^{-1}$), against the number density of the helium target. The parent state (37,34) of the 470 nm resonance is subject to strong quenching due to frequent collisions with helium atoms at high densities. The decay rate first increases linearly with density N

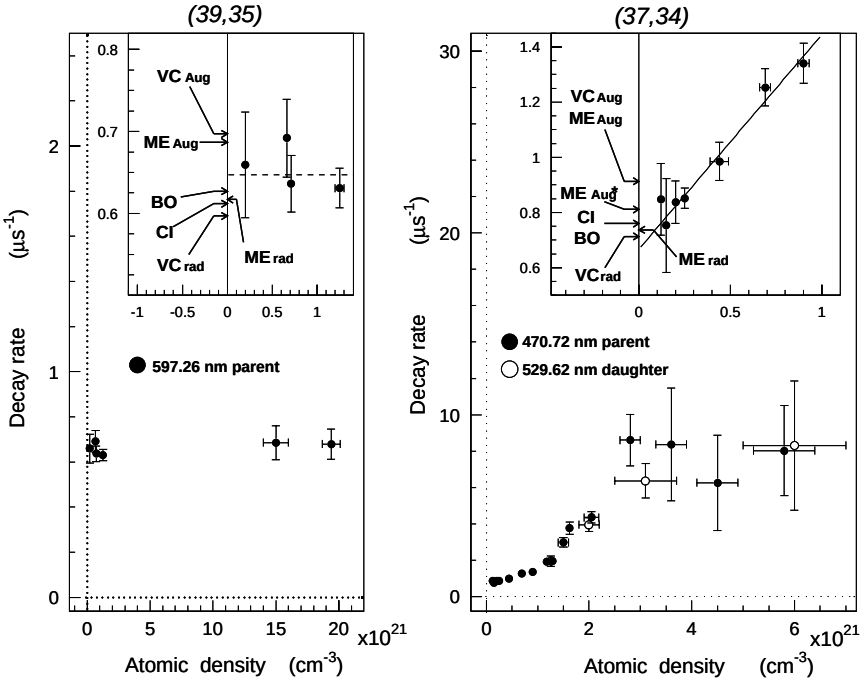

Figure B.7: The decay rates, *i.e.* the inverse of the lifetime, of the (39,35) and (37,34) states are plotted as a function of the target density. The former state, that is the parent state of the 597 nm "orange" resonance, has a constant lifetime, while the latter, that is the parent of the 470 nm "blue" resonance and also the daughter state of the 529 nm "green" resonance, is subject to collisional quenching and its lifetime shows a strong density-dependence. The extracted decay rates at the zero-density limit agree with values from theoretical calculations on the radiative transitions (BO: Refs. [19, 20], VC_{rad}: Ref. [37], ME_{rad}: Ref. [31]) and the sum of the radiative and Auger transition rates (CI: Ref. [36], VC_{Aug}: Refs. [37, 38], ME_{Aug}: Ref. [39], ME_{Aug^*}: Ref. [40]).

in the relatively low density region, and then increases more dramatically at around $N \sim 2 \times 10^{21}$ cm^{-3}, corresponding to 1–2 bar at ca. 6 K. Since the (37,34) state is the daughter state of the 529 nm resonance, its lifetime could be obtained by measuring the decay time of the 529 nm resonance peak (see Appendix **B.2.3**), although the measurements were possible only for relatively high densities for which the state-lifetime is shortened to several hundred microseconds (see Appendix **B.1.2**). This measurement gave consistent results with the ones obtained by the "depletion and recovery" measurements for the 470 nm resonance.

In sharp contrast to the drastic quenching effect for the (37,34) state, the lifetime of the parent state (39,35) of the 597 nm resonance was not at all affected. The observed lifetime was constant independent of the target density and was in accordance with theoretically calculated values. Also for the (37,34) state, the extrapolated decay rate $\tau^{(0)} = (\lambda^{(0)})^{-1}$ at the zero-density limit agreed very well with theoretical values of the radiative transition rate, with or without the small but not negligible Auger transition rate being added.

From the observed shortening of the state-lifetime (λ^{-1}), the collisional quenching cross section can be calculated by applying the following equation

$$\lambda = \lambda^{(0)} + N v \sigma \,, \tag{B.3}$$

where the thermal velocity is given by[♡]

$$v \approx \langle v \rangle = \sqrt{\frac{8kT}{\pi\mu}} = \sqrt{\frac{4}{\pi}}\, v_T \,. \tag{B.4}$$

Thus we obtained $\sigma = (2.6\text{–}9.6) \times 10^{-20}$ cm^2 for the (37,34) state. The lower value is for the relatively low density region where the decay rate λ shows a linear dependence on the density, while higher values are for denser conditions. This quenching cross section is more than three orders of magnitude smaller than that for the shift of the resonance frequency (see Section **5.4.3**, p. 79).[♣] This means that only one hard collision out of several thousand collisions is inelastic and results in the quenching of the parent state.

We observed that the parent state (37,34) of the 470 nm transition in the $v = 2$ radiative-cascade series was subject to quenching while the parent state of (39,35) of the 597 nm transition in the $v = 3$ series was not affected by the high density of helium. Together with an experimental indication that an upper state (38,35) in the $v = 2$ ladder is also quenched at 2–5 bar at ca. 6 K, we can assume either an n-dependence or a v-dependence of the quenching by helium atoms. It is interesting that this tendency is opposite for the observed density-shifts, which was larger for the 597 nm transition than

[♡] Refer also to Eq. (5.6c), p. 62, Section **5.4.1**, and the footnote on p. 79.

[♣] This difference in magnitude originates in the different typical units used: 10^{-21} GHz/cm^{-3} for the density shift whilst 10^{-21} μs^{-1}/cm^{-3} for the quenching and GHz $= 10^3$ μs^{-1}.

for 470 nm. Also, the quenching effect by aggressive hydrogen molecules was stronger for high-n states.

Figure **B.8** shows the radial probability densities of the $\overline{p}\mathrm{He}^+$ atomcule for the two states under discussion, which were reconstructed using effective nuclear charges obtained with an intuitive model (as in Appendix **A.2**) applied to the calculated energy-levels by Korobov [30]. The $\overline{p}$'s wave packet is more to the outside for higher n, while the electron wavefunction is slightly shrunken inside. This fact may give some hint to the observed collisional effects with different state-dependences, but we will have to wait for some theoretical works in order to account for these interesting results.

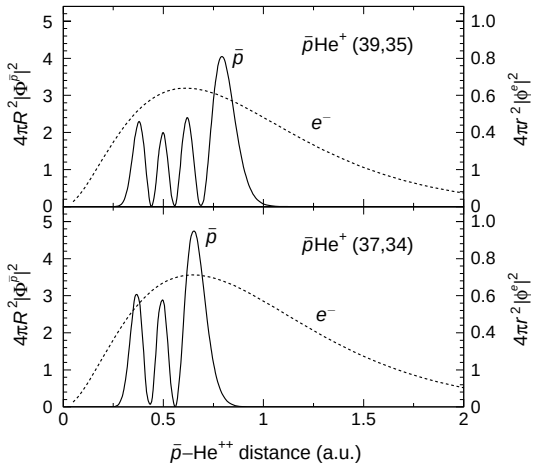

Figure B.8: Radial probability densities of the $\overline{p}\mathrm{He}^+$ atomcule for the (39,35) and (37,34) states are drawn. Wavefunctions were reconstructed from effective nuclear charges obtained from the energy calculations by Korobov [30]. Generally, the $\overline{p}$'s wave packet ($\Phi^{\overline{p}}(R)$) is more to the outside for higher-n states while electron wavefunction ($\phi^e(r)$) is shifted inward. This fact should be somehow connected with the observed different state-dependences of the quenching (lifetime-shortening) by helium and by foreign gases, and of the collisional shift and broadening of the resonances, although no good explanations are yet given from the theoretical side.

B.4 Quenching Effect by Foreign Gases

In the previous section, we have seen the effect of inelastic collisions of a $\overline{p}\mathrm{He}^+$ atomcule with helium atoms at high-density conditions. In this section, we will discuss collisional

quenching effects due to foreign atoms and molecules. We observed larger cross sections for rare-gas atoms than for helium, and much stronger quenching by even a tiny admixture of molecular gases. These studies open a new field of chemistry for the exotic atomcules.

B.4.1 Quenching by rare gases

In a series of extensive studies in 1992, our group (excluding the author) examined the effects of additive rare gases by measuring the decay-time constants of the "DATS" [46]. They observed significant shortening of $\overline{p}\mathrm{He}^+$ lifetime at a concentration of typically 10% for the admixed neon, argon and krypton gases. Xenon, however, acted as a stronger quencher of metastable $\overline{p}\mathrm{He}^+$ atomcules, and less than 10^{-3} admixing ratio was enough to quench the major fraction of the atomcules.

The quenching cross sections were deduced from these measurements, to be $\sigma_\mathrm{q} = 1\text{–}2\times10^{-20}$ cm^2 for Ne, $3\text{–}5\times10^{-20}$ cm^2 for Ar, $1\text{–}5\times10^{-19}$ cm^2 for Kr and $2\text{–}4\times10^{-18}$ cm^2 for Xe. The lifetimes were obtained by fitting the DATS to cascade-chain models explained in Appendix **C.2** and the values for the cross section vary depending on the models used. All values above are for measurements at room temperature (RT). They made one measurement at 470°C for Ar, and observed a large cross section of $1\text{–}2\times10^{-19}$ cm^2. In order to account for the factor 3–4 difference compared with the value at RT, an Arrhenius-type temperature dependence $\sigma_\mathrm{q} \propto \mathrm{e}^{-E_\mathrm{a}/kT}$ was assumed and an activation energy E_a of ~ 0.1 eV was extracted [46].

B.4.2 Quenching by hydrogen gases

Molecular gases act as strong quenchers of metastable $\overline{p}\mathrm{He}^+$ molecules, and even ppm-order impurities distorted the DATS shape drastically. For this reason, special care was taken about the purity of the helium gas target when we studied the metastability, as mentioned in Section **3.2**, but at the same time, systematic studies with intentionally admixed molecular gases provided much interesting information on the "chemistry" of $\overline{p}\mathrm{He}^+$ atomcules.

Especially, we studied intensively the effect of hydrogen gases (H_2), including deuterium (D_2), at a typical temperature of 30 K♠ [46, 54–56].

Figure **B.9** shows the time spectra (DATS) at different hydrogen concentrations. It shows, for higher concentrations, a more pronounced fast-decaying component with

♠This temperature was chosen so that hydrogen has large enough vapor pressure while other impurity gases have much too small vapor pressure. Especially it was important to assure that the lowest temperature in the target vessel and in the transfer tube was higher than the temperature which allows the vapor pressure of admixed hydrogen. The temperature of 30 K was chosen because it is higher than the liquefying temperature of 21 K for hydrogen at 1 atm, and the required condition above is well satisfied.

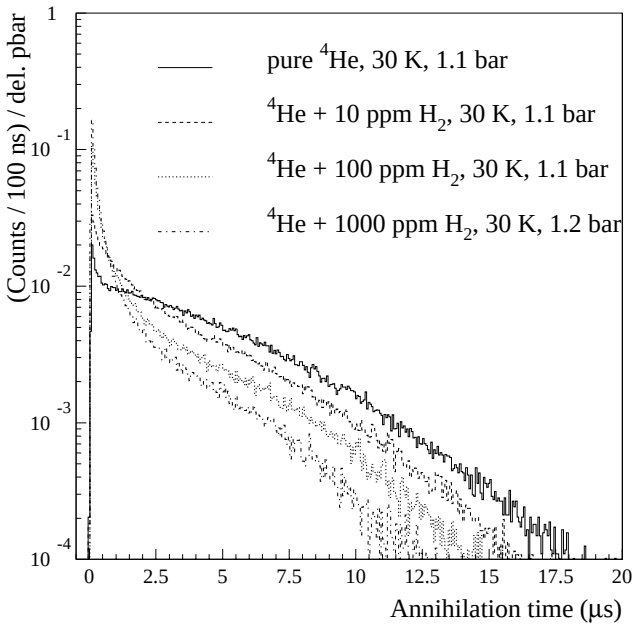

Figure B.9: DATS for hydrogen-admixed helium gas targets at 30 K with different hydrogen concentrations. The fast-decaying component at early timings becomes more pronounced and shorter-lived as the concentration is increased from 0 to 1000 ppm, while the spectra at later times are not affected. This suggests state-dependent quenching mechanisms of $\overline{p}\mathrm{He}^+$ atomcules by collisions with hydrogen molecules.

shorter lifetimes at early times of the spectra; while the spectra at later times does not change so much. This indicates that certain metastable states get quenched strongly, while others are persistent against collisions and remain metastable. This speculation was confirmed by further studies using laser resonances, which revealed stronger quenching effects for higher-lying (*i.e.* larger n-) states. Data also showed that the quenching is stronger for smaller angular momentum l. Quenching cross sections were deduced to be 5–28 $\times$ 10^{-16} cm^2 for $n = 39$ ($35 \leq l \leq 38$) states, 1–7 $\times$ 10^{-16} cm^2 for $n = 38$ ($35 \leq l \leq 37$) states, and 1 $\times$ 10^{-16} cm^2 for the (37,34) state [56], and are in accordance with values of 2–10 $\times$ 10^{-16} cm^2 obtained from the DATS measurements [46]. These are of the geometrical size, which means that the metastable $\overline{p}\mathrm{He}^+$ is totally quenched when it collides with a hydrogen molecule, in marked contrast to the case when it collides with rare gas atoms including helium.

B.4.3 Hydrogen-assisted inverse resonance

The fact that our annihilation-spectroscopy technique is applicable only to pairs of metastable–short-lived states, limited the observable transitions to the ones at (or near) the border between the metastable and the Auger-fast domains in the (n,l)-state diagram. We have seen in Appendix **B.1.2** that a transition between normally metastable states can be observed if the lifetime of one of the states is shortened by some quenching effect.

This condition is exactly met by making use of the state-dependent quenching effect with a small amount of hydrogen gas. By controlling the concentration of admixed hydrogen in the helium gas target, we could selectively shorten the lifetimes of states with higher principal quantum number n as compared to those of lower n'. Then the excitation of the population on a n'-state to a n-state would result in a visible resonance peak in the DATS. This method, named the "hydrogen-assisted inverse resonance"[⊕] (HAIR) method, opened access to transitions between extremely "circular" states with higher angular momenta l and vibrational quantum numbers $v = 0, 1, 2$ [55]. Thus we observed 5 new resonances between $n = 39$ and $n' = 38$, and between 38 and 37 (see the level diagram, Figure **4.4**, p. 46), in the very last minutes of our beamtime in 1996. The observed resonances were not observed as sharp peaks, but rather, as long-tailed humps, due to intermediate (~ 100 ns) lifetimes of the daughter n-state and small differences in the lifetimes between the two resonating states.

B.4.4 Effect of other molecular gases

Our former studies in 1992 included measurements for nitrogen and oxygen gases at room temperature [46]. The obtained cross sections were $\sigma_q = 3\text{–}9 \times 10^{-18}$ cm^2 for N_2 and $1\text{–}2 \times 10^{-15}$ cm^2 for O_2. The value for N_2 is comparable to that of Xe and smaller than for H_2, while the value for O_2 is even larger than for H_2.

In 1996 we studied both DATS and laser resonances in a more controlled condition at 100 K[⊖] [59]. An interesting characteristic of the DATS with oxygen admixture is that the overall shape corresponds to a single exponential. In all other spectra, from pure helium targets at low or high density to rare-gas and other molecular admixtures, the DATS had downward-bent shapes when plotted in semi-logarithmic scales, with or without a fast-decaying exponential component of typically hundreds of nanoseconds. These snaky shapes were an indirect evidence of the cascade-chain models and of state-dependence of quenching influence, but for the case of oxygen-admixed targets, the simple triangle shape

[⊕] The name "inverse" resonance was adopted because the $\bar{p}He^+$ was excited up in this method, instead of deexcited down in our normal cases.

[⊖] Cf.: the temperatures which give the vapor pressures of oxygen of 1 atm and 1 Torr are 90 K and 54 K, respectively.

suggested (almost) equal quenching to *all* the metastable states. Observed DATS were fitted to a four-level cascade-chain model with side branches which had equal quenching rates, and the resultant quenching rates showed a linear dependence on the number density of the oxygen molecules (not the relative mixing ratio but the absolute concentration). An overall quenching cross section of 1.1×10^{-15} cm^2 was obtained.

Laser studies (time variant method) for the well-known 597 nm and 470 nm resonances clarified the quenching cross sections for those individual parent states. Thus we obtained $\sigma = 1.6$ and 1.1×10^{-15} cm^2 for the (39,35) and (37,34) states, respectively. Therefore the cross section was only slightly higher for the higher-n state.

To conclude, studies on quenching effects by abundant helium atoms at high-density targets, or by admixed foreign rare gases and (diatomic) molecular gases, have provided a lot of interesting information on the collisional interaction of $\overline{p}\mathrm{He}^+$ with atoms and molecules. Unfortunately, there has been almost no theoretical work on this subject so far, but we hope that many theorists are interested and will perform some calculations or give some explanations in the near future.

So far we have only examined rare-gas atoms and non-polar molecules. Our future plan would include measurements with targets containing molecules with finite dipole moments. Certainly more drastic quenching effects can be expected, and some more interesting phenomena are awaited.

B.5 Hyperfine Splitting

The $\overline{p}\mathrm{He}^+$ atomcule has three angular momenta; an orbital angular momentum l which is mainly carried by $\overline{p}$, the spin $s_{\overline{p}}$ of the antiproton and the electron spin s_e. These angular momenta couple together to form:

$$\boldsymbol{F} = \boldsymbol{l} + \boldsymbol{s}_{\overline{p}} \tag{B.5a}$$

$$\boldsymbol{J} = \boldsymbol{F} + \boldsymbol{s}_{\mathrm{e}}. \tag{B.5b}$$

The dominant effect is splitting of the energy levels into a doublet ($F^+ = l + 1/2$ and $F^- = l - 1/2$) separated by a frequency ν_{HF} caused by the interaction of the large $\overline{p}$ orbital momentum with the electron spin. This splitting is called "hyperfine" (HF) structure[⊗]. The $\overline{p}$ spin causes an additional smaller splitting for each of the HF states, which is called here the "super-hyperfine" (SHF) structure.

[⊗]Some people may call it a fine structure (FS), but we use the terminology HFS because normally the word FS is used for self-interaction while HFS is for interactions between an electron and the nucleus, and our case corresponds to the latter.

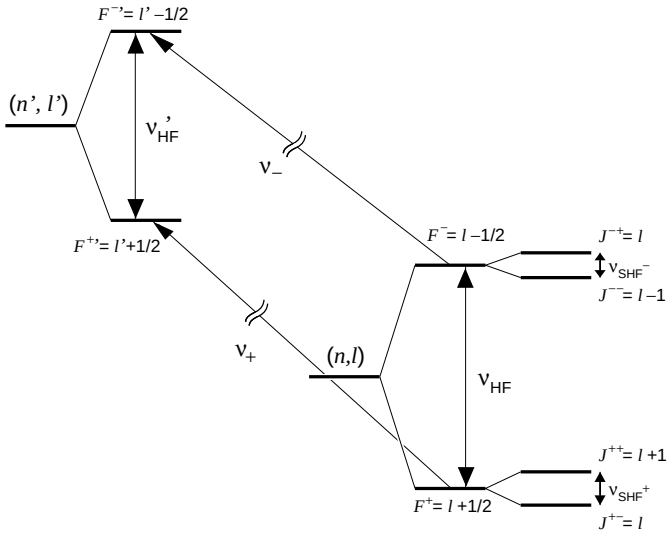

Figure B.10: Hyperfine (HF) and super-hyperfine (SHF) structures of the levels and the transition scheme for an unfavored transition. The SHF structures are shown only for the (n,l) state. The splitting observed by laser spectroscopy is the difference of the HF energies ($h\Delta\nu_{\rm HF} = |\, h\nu_{\rm HF} - h\nu_{\rm HF'}|$) between the parent and the daughter states.

Table B.2: Hyperfine splitting of levels calculated by Bakalov and Korobov [84] for $\overline{p}\,^4{\rm He}^+$. The values are in GHz. Although the splittings themselves are large, the *difference* between the levels, which are observable by laser transitions, are small. In general, "unfavored" transitions have larger splitting (difference) than the "favored" ones.

$(n,l,v)\Rightarrow(n',l',v')$	λ [nm]	type	$\nu_{\rm HF}$ [GHz]	$\nu_{\rm HF'}$ [GHz]	$\Delta\nu_{\rm HF}$ [GHz]
(39,35,3)⇒(38,34,3)	597.26	favored	10.632	11.138	0.507
(38,35,2)⇒(37,34,2)	529.62	favored	11.753	12.216	0.462
(37,34,2)⇒(36,33,2)	470.72	favored	12.216	12.586	0.370
(37,35,1)⇒(38,34,3)	726.10	unfavored	12.906	11.138	1.767
(37,34,2)⇒(38,33,4)	713.58	unfavored	12.216	10.483	1.732

The HF and SHF structures have been calculated[⊘] by Bakalov and Korobov [83, 84] using the best three-body wavefunctions of Korobov [30]. The level and transition scheme is shown in Figure **B.10** and the values are presented in Table **B.2**.Because of the large l, the electric-dipole laser transitions are subject to the selection rule $\Delta s_e = \Delta s_{\overline{p}} = 0^{\odot}$. This means that, although the level splittings are large, the splittings in the laser transition frequencies are small. In 1996, we observed a HF splitting in the $(n, l, v) = (37, 35, 1) \Rightarrow (38, 34, 3)$ "unfavored" transition at 726 nm [53]. Figure **B.11** (upper figure) shows the observed resonance profile[△] with a clear doublet splitting of 1.70 ± 0.05 GHz, in good agreement with the theoretical prediction of 1.77 GHz [84]. In the figure, λ_{A} corresponds to the transition ν_+ in Figure **B.10** and λ_{B} the ν_-. The much smaller SHF structure is beyond the reach of our current observation.

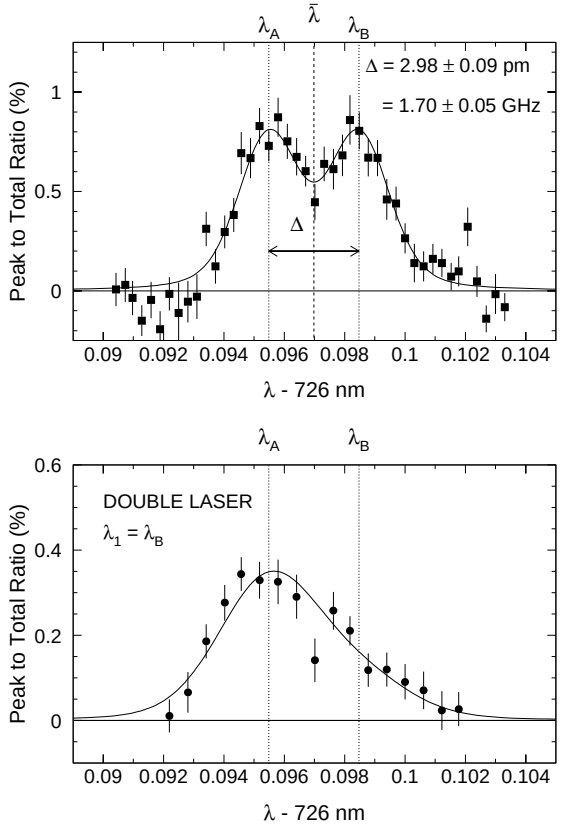

Figure B.11: Top: An "unfavored" transition $(n, l) = (37, 35) \Rightarrow (38, 34)$ was observed at 726.10 nm with a hyperfine splitting of 1.7 GHz [53], the value matching with theoretical predictions [83, 84]. The experimental data were fitted with two Lorentzian peaks convoluted each with a Gaussian with a fixed laser bandwidth of 1.2 GHz. Bottom: An asymmetric profile of the doublet due to the alignment of the population in the hyperfine sublevels caused by the first laser at λ_{B}.

We also observed an asymmetric profile of the doublet by making an alignment in

[⊘] Kartavtsev also calculated the HF splitting but obtained a different value [41].

[⊙] This selection rule is also applicable to the magnetic dipole transitions whose experimental achievement is expected in the near future (refer to Appendix **B.6**). Note that the transition which flips the electron spin is weaker by 3 orders of magnitude and therefore cannot be observed.

[△] The data were fitted, as shown in the figure, to a sum of two Lorentzians convoluted with a measured laser bandwidth of 1.2 GHz. The statistical factor $(2l+2)/2l \sim 1$ in the intensities of the two peaks were set to unity for simplification.

the population: we used two laser light beams in succession, one being fixed on one of the resonance wavelengths (λ_B) while stepping the wavelength of the second laser (λ). The lower graph of Figure **B.11** plots the resonance intensity (or the resonance peak area) against λ of the second laser. It is evident that the first laser has depopulated a considerable fraction of the population from the sublevel B of the parent state* and caused a population difference between the two sublevels. This measurement ensures that the observed doublet is related to two different sublevels which are not mixed together. This technique of inducing population asymmetries becomes important when we perform microwave resonance spectroscopy directly between the hyperfine sublevels in the near future (refer to Appendix **B.6**).

Note that the laser bandwidth was 1.2 GHz (in narrow-band mode), which was the narrowest possible for this "red" light, but still was comparable to the observed splitting. Therefore, special care was taken to optimize the power and the size of the laser beams in order to minimize power broadening while retaining enough depopulation efficiency. Actually, a different power density was used for the two observations in Figure **B.11**, resulting in the different power-broadened widths of the resonances.

According to the theoretical calculations, the differences of the HF splitting between the parent and the daughter states are larger in the "unfavored" transitions than in the "favored" ones. The splitting in the latter which is smaller than our laser bandwidth could hardly be observed, except for one indication mentioned in Section **5.3**.

B.6 Future Experiments

Apart from continuation of many sorts of experiments, we will attempt observation of microwave–laser double resonance in the new AD facility now under construction at CERN. The idea is to use a kilowatt-class high-power microwave at a frequency of 12.9 MHz to resonate the atomcules between the hyperfine sublevels of the (37,35) state and to observe the resonance using the "unfavored" laser transition at 726 nm. Actually, two laser pulses will be used; the first pulse will make an alignment in the population by selectively depopulating one of the doublet states, while the second pulse will be used to probe the state-population. The microwave will be applied for the period between the two laser pulses, and the oscillating magnetic field will either inverse or equalize the population of the two substates. The microwave resonance is expected to measure the hyperfine splitting directly, with a much better resolution than the observation by lasers mentioned in the previous section. A more detailed explanation on the experimental planning is

*The other sublevel A is also affected because of the overlap of the two resonances, and part of its population has been lost. (Compare the resonance intensities in the two figures.)

given in Ref. [94, (Sect. 2.5)].

Appendix C

Cascade Models and Their Solutions

C.1 Laser-Timing Variant Method

Here are presented the rate equations and their solutions used to fit the data of the laser-time variant method mentioned in Appendix **B.2.1**.

Two-level model

In a two-level model where only one upper state (#2) feeding the metastable parent state (#1) of the laser transition is considered, the rate equations for the state populations are written as

$$\frac{\mathrm{d}N_2(t)}{\mathrm{d}t} = -\lambda_2 N_2(t) \tag{C.1a}$$

$$\frac{\mathrm{d}N_1(t)}{\mathrm{d}t} = +\lambda_2 N_2(t) - \lambda_1 N_1(t)\,, \tag{C.1b}$$

where N_1 and N_2 denote the population of the lower and upper metastable states, respectively, and λ_1 and λ_2 the radiative transition rates from these states. The solution of the rate equations is given in the following:

$$N_2(t) = N_2(0)\,\mathrm{e}^{-\lambda_2 t} \tag{C.2a}$$

$$N_1(t) = N_2(0)\frac{\lambda_2}{\lambda_1 - \lambda_2}\,\mathrm{e}^{-\lambda_2 t} + \left(N_1(0) - N_2(0)\frac{\lambda_2}{\lambda_1 - \lambda_2}\right)\mathrm{e}^{-\lambda_1 t}\,. \tag{C.2b}$$

The intensity of the first laser $I_1(t_1)$ is directly connected with the population of the parent state at the time t_1 of the laser shot, while that of the second laser $I_2(t_2)$ at time $t_2\,(> t_1)$ reflects a part of the population which has escaped deexcitation by the first laser pulse, plus some feeding from the upper metastable state during the pulse interval. The fit functions for the first and the second peak intensity (or the area) are given by the

following equations with fit parameters $N_1(0), N_2(0)$ as initial populations, λ_1, λ_2 as the radiative transition rates, and ϵ the depopulation efficiency of each laser pulse:

$$I_1(t_1) = \epsilon N_1(t_1) \tag{C.3a}$$

$$I_2(t_2) = \epsilon \tilde{N}_1(t_2 - t_1) \tag{C.3b}$$

$$\begin{aligned}\tilde{N}_1(t_2 - t_1) = {} & N_2(t_1)\frac{\lambda_2}{\lambda_1 - \lambda_2}\,\mathrm{e}^{-\lambda_2(t_2-t_1)} \\ & + \left((1-\epsilon)N_1(t_1) - N_2(t_1)\frac{\lambda_2}{\lambda_1 - \lambda_2}\right)\mathrm{e}^{-\lambda_1(t_2-t_1)}\,.\end{aligned} \tag{C.3c}$$

Three-level model

Similarly, in the three-level model where one more metastable state (#3) upstream in the single cascade chain is taken into account as shown in Figure **B.2**, p. 93, the rate equation is given as

$$\frac{\mathrm{d}N_3(t)}{\mathrm{d}t} = -\lambda_3 N_3(t) \tag{C.4a}$$

$$\frac{\mathrm{d}N_2(t)}{\mathrm{d}t} = +\lambda_3 N_3(t) - \lambda_2 N_2(t) \tag{C.4b}$$

$$\frac{\mathrm{d}N_1(t)}{\mathrm{d}t} = +\lambda_2 N_2(t) - \lambda_1 N_1(t) \tag{C.4c}$$

and their solutions are

$$N_3(t) = N_3(0)\,\mathrm{e}^{-\lambda_3 t} \tag{C.5a}$$

$$N_2(t) = N_3(0)\frac{\lambda_3}{\lambda_2 - \lambda_3}\,\mathrm{e}^{-\lambda_3 t} + \left(N_2(0) - N_3(0)\frac{\lambda_3}{\lambda_2 - \lambda_3}\right)\mathrm{e}^{-\lambda_2 t} \tag{C.5b}$$

$$\begin{aligned}N_1(t) = {} & N_3(0)\frac{\lambda_2}{\lambda_1 - \lambda_3}\frac{\lambda_3}{\lambda_2 - \lambda_3}\,\mathrm{e}^{-\lambda_3 t} + \frac{\lambda_2}{\lambda_1 - \lambda_2}\left(N_2(0) - N_3(0)\frac{\lambda_3}{\lambda_2 - \lambda_3}\right)\mathrm{e}^{-\lambda_2 t} \\ & + \left(N_1(0) - N_3(0)\frac{\lambda_2}{\lambda_1 - \lambda_3}\frac{\lambda_3}{\lambda_2 - \lambda_3} - \frac{\lambda_2}{\lambda_1 - \lambda_2}\right. \\ & \left.\left[N_2(0) - N_3(0)\frac{\lambda_3}{\lambda_2 - \lambda_3}\right]\right)\mathrm{e}^{-\lambda_1 t}\,.\end{aligned} \tag{C.5c}$$

The fit functions are written in the form

$$I_1(t_1) = \epsilon N_1(t_1) \tag{C.6a}$$

$$I_2(t_2) = \epsilon \tilde{N}_1(t_2 - t_1) \tag{C.6b}$$

$$\begin{aligned}\tilde{N}_1(t_2 - t_1) = {} & N_3(t_1)\frac{\lambda_2}{\lambda_1 - \lambda_3}\frac{\lambda_3}{\lambda_2 - \lambda_3}\,\mathrm{e}^{-\lambda_3(t_2-t_1)} \\ & + \frac{\lambda_2}{\lambda_1 - \lambda_2}\left(N_2(t_1) - N_3(t_1)\frac{\lambda_3}{\lambda_2 - \lambda_3}\right)\mathrm{e}^{-\lambda_2(t_2-t_1)}\end{aligned}$$

$$+\left((1-\epsilon)N_1(t_1) - N_3(t_1)\frac{\lambda_2}{\lambda_1-\lambda_3}\frac{\lambda_3}{\lambda_2-\lambda_3} - \frac{\lambda_2}{\lambda_1-\lambda_2}\right. \tag{C.6c}$$
$$\left.\left[N_2(t_1) - N_3(t_1)\frac{\lambda_3}{\lambda_2-\lambda_3}\right]\right)\mathrm{e}^{-\lambda_1(t_2-t_1)}\,.$$

More levels

It is possible to extend the model with more levels in one ladder or to add side levels or side decaying branches. Here we will not exhibit any of these models in detail, but it should be straightforward to formulate the rate equations and their solutions. These models as well as the first two were used in the fitting of laser-resonance peaks [48, 49], and also the shape of the DATS [12, 13, 46, 59], as in the following section.

C.2 Downward-Bent Shape of the DATS

The cascade model in the previous section is not only useful for fitting the laser-resonance peaks but also is capable of expressing the DATS (delayed annihilation time spectra) which have downward-bent shape when plotted in semi-logarithmic scales, as mentioned in Section **1.2**.

In order to intuitively comprehend the property of the solutions Eq. (C.5) to the three-level decay-chain model, one may assume that all the metastable states have the same lifetime, *i.e.* $\lambda_1 = \lambda_2 = \lambda_3 \equiv \lambda$, which is a realistic approximation. Then it can be shown that the population at a later time t consists of three components: each contribution from the initial population on each of the three metastable states. Eq. (C.5c) is reduced to

$$N_1(t) = N_1(0)\,\mathrm{e}^{-\lambda t} + N_2(0)\,t\,\mathrm{e}^{-\lambda t} + N_3(0)\,\frac{t^2}{2}\,\mathrm{e}^{-\lambda t}\,. \tag{C.7}$$

The first term derives from the initial population on the last metastable state and contributes to the decaying component of the early times, while the second and third terms originating from the populations on upper states grow first before they decay, and contribute to the spectra at later times.

C.3 Depletion and Recovery Measurements

In this section, the shape of the depletion and recovery spectra discussed in Appendices **B.2.2** and **B.3** will be mathematically deduced.

We remark only on the parent and the daughter states of the resonance, and number them as #1 and #0, respectively, to be consistent with the previous sections. Assuming

a population flow scheme in Figure **C.1**, which includes all possible flow paths and thus is a general expression, the rate equations can be written as

$$\frac{\mathrm{d}N_1(t)}{\mathrm{d}t} = -\lambda_1 N_1(t) + V_1(t) \tag{C.8a}$$

$$(\lambda_1 = \lambda_1^{\mathrm{rad}} + \lambda_1^{\mathrm{others}})$$

$$\frac{\mathrm{d}N_0(t)}{\mathrm{d}t} = -\lambda_0 N_0(t) + \lambda_1^{\mathrm{rad}} N_1(t) + V_0(t)\ . \tag{C.8b}$$

Here $V_1(t)$ contains feeding from the upper state (#2) in the v-constant ladder, but also includes other possible side feedings from different states. Similarly, the daughter state may also receive population flow $V_0(t)$ from side branches. Moreover, the parent (#1) does not necessarily have to cascade into the daughter state (#0), but a fraction may decay to other states ($\lambda_1^{\mathrm{others}}$).

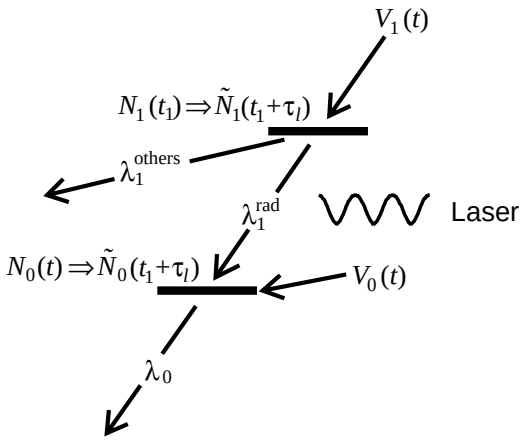

Figure C.1: A general population flow scheme showing all possible flow and decay paths of the parent and daughter states of a resonant transition. The laser on resonance modifies the populations $N_1(t_1)$ and $N_0(t_1)$ to $\tilde{N}_1(t_1 + \tau_l)$ and $\tilde{N}_0(t_1 + \tau_l)$.

Now we consider the effect of the laser resonance. Part of the population at the time (t_1) of the laser pulse on the parent state (#1) gets deexcited to the daughter state (#0) and annihilates, with an depopulation efficiency ϵ'.* If the duration of the laser pulse is much shorter than the typical state lifetimes (which is true: 30–40 ns versus 1 μs), the

*The definition of the depopulation efficiency ϵ' is different from that of ϵ in the previous Appendix **C.1** and in **D.1.1**. Here only the populations which annihilate within the duration of the laser pulse are counted while previously the deexcited population which stays at the daughter state and annihilates after the end of the pulse is also included.

parent population right after the end of the pulse is $\tilde{N}_1\left(t_1+\tau_1\right)=\left(1-\epsilon'\right)N_1(t_1)$ and then follows the same equation as Eq. (C.8a). The population of the daughter state $\tilde{N}_0\left(t_1+\tau_1\right)$ is not easy to calculate because it involves a complicated interaction between the laser and the atomcule (cf. Appendix **D.4**), but we know that the population $\tilde{N}_0(t)$ evolves according to the rate equation as in Eq. (C.8b) after the laser pulse is over ($t \geq t_1+\tau_1$).

Now we compare the time spectra with and without the laser resonance peak. The differences in the populations between the two cases are

$$\frac{\mathrm{d}\left(\tilde{N}_1(t)-N_1(t)\right)}{\mathrm{d}t}=-\lambda_1\left(\tilde{N}_1(t)-N_1(t)\right) \tag{C.9a}$$

$$\frac{\mathrm{d}\left(\tilde{N}_0(t)-N_0(t)\right)}{\mathrm{d}t}=-\lambda_0\left(\tilde{N}_0(t)-N_0(t)\right)+\lambda_1^{\mathrm{rad}}\left(\tilde{N}_1(t)-N_1(t)\right). \tag{C.9b}$$

An important point is that since the feedings (V_0, V_1) from upper states or side levels are not affected by the laser resonance, those terms cancel by subtraction between the two cases. The solutions for the population differences can be expressed analytically as

$$\tilde{N}_1(t)-N_1(t)=\left(\tilde{N}_1(t_1')-N_1(t_1')\right)\mathrm{e}^{-\lambda_1(t-t_1')} \tag{C.10a}$$

$$\begin{aligned}\tilde{N}_0(t)-N_0(t)=&\frac{\lambda_1^{\mathrm{rad}}\left(\tilde{N}_1(t_1')-N_1(t_1')\right)}{\lambda_0-\lambda_1}\mathrm{e}^{-\lambda_1(t-t_1')}\\&+\left(\tilde{N}_2(t_1')-N_2(t_1')-\frac{\lambda_1^{\mathrm{rad}}\left(\tilde{N}_1(t_1')-N_1(t_1')\right)}{\lambda_0-\lambda_1}\right)\mathrm{e}^{-\lambda_0(t-t_1')},\end{aligned} \tag{C.10b}$$

where $t_1' \equiv t_1+\tau_1$ is the time at the end of the laser pulse. The difference in the $\overline{p}$ annihilation rate is given by $\lambda_0\left(\tilde{N}_0(t)-N_0(t)\right)$, which decays first with the fast Auger-decay rate λ_0 of the daughter state (as explained in Appendix **B.2.3**) and then recovers with that of the parent state (λ_1). Therefore, the lifetime of the parent state (#1) can be directly measured to be $\tau_1=\lambda_1^{-1}$ without any ambiguities, if the lifetime of the daughter state is much shorter than that ($\lambda_1 \ll \lambda_0$). Since we have started with a generalized flow scheme, this result is always true, independent of whatever cascade model may be used.

Appendix D

Interaction of Light with Atoms and Effect of Collisions

D.1 Quantum Mechanics of Light-Atom Interaction

In the following sections a general quantum-mechanical treatment of the interaction between atoms and the light field is summarized.

D.1.1 Rabi oscillation

Generally, the Schrödinger equation is expressed as

$$\mathrm{i}\hbar\frac{\partial\psi}{\partial t} = \mathcal{H}\psi\,, \tag{D.1}$$

where $\mathcal{H} = \mathcal{H}_0 + \mathcal{H}'$ is the total Hamiltonian of the system and ψ the wavefunction. Let us now consider two quantum-mechanical states $|\psi_1\rangle$ and $|\psi_2\rangle$, which resonate with an external light field polarized in the z direction (see Figure **D.1**):

$$\mathcal{H}'(t) = -\boldsymbol{\mu}\cdot\boldsymbol{E}(t) = -\mu\,E_0\cos\omega t = -\mu\,\frac{E_0}{2}\,(\mathrm{e}^{\mathrm{i}\omega t} + \mathrm{e}^{-\mathrm{i}\omega t})\,. \tag{D.2}$$

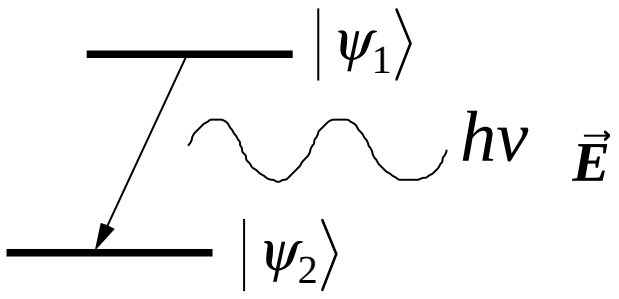

Figure D.1: Two-level atom interacting with an external field.

We define eigenstates

$$\psi_n = u_n \mathrm{e}^{-\mathrm{i}W_n t/\hbar} , \qquad n = 1, 2 \tag{D.3}$$

of the unperturbed Hamiltonian $\mathcal{H}_0$, with their eigen-energies W_n. The wavefunction of the two-level atom can be written as a linear sum of the two states:

$$\psi(t) = a_1(t)\psi_1 + a_2(t)\psi_2 . \tag{D.4}$$

Substituting this into the Schrödinger equation (D.1) gives the following differential equation for the probability amplitudes

$$\begin{cases} \mathrm{i}\hbar \dfrac{\mathrm{d}a_1}{\mathrm{d}t} = a_2 \mathcal{H}'_{12} \, \mathrm{e}^{-\mathrm{i}\omega_0 t} & \text{(D.5a)} \\ \mathrm{i}\hbar \dfrac{\mathrm{d}a_2}{\mathrm{d}t} = a_1 \mathcal{H}'_{21} \, \mathrm{e}^{\mathrm{i}\omega_0 t} , & \text{(D.5b)} \end{cases}$$

where

$$\mathcal{H}'_{12} = \langle u_1 \, | \mathcal{H}' | u_2 \rangle \quad \text{and} \quad \omega_0 = \frac{W_2 - W_1}{\hbar} . \tag{D.6}$$

Substituting Eq. (D.2) into Eq. (D.5) and by neglecting the quickly oscillating term $\mathrm{e}^{\pm \mathrm{i}\,(\omega+\omega_0)\,t}$ (rotating-wave approximation) we obtain

$$\begin{cases} \mathrm{i}\hbar \dfrac{\mathrm{d}a_1}{\mathrm{d}t} = \dfrac{\mathrm{i}\Omega}{2} \, a_2 \, \mathrm{e}^{\mathrm{i}\,(\omega-\omega_0)\,t} & \text{(D.7a)} \\ \mathrm{i}\hbar \dfrac{\mathrm{d}a_2}{\mathrm{d}t} = \dfrac{\mathrm{i}\Omega}{2} \, a_1 \, \mathrm{e}^{-\mathrm{i}\,(\omega-\omega_0)\,t} , & \text{(D.7b)} \end{cases}$$

where

$$\Omega = \frac{\mu E_0}{\hbar} \tag{D.8}$$

is called the Rabi (angular) frequency. Substitution of Eq. (D.7b) into the time differential of Eq. (D.7a) gives

$$\frac{\mathrm{d}^2 a_1}{\mathrm{d}t^2} - \mathrm{i}\,(\omega - \omega_0) \frac{\mathrm{d}a_1}{\mathrm{d}t} + \frac{\Omega}{4} a_1 = 0 . \tag{D.9}$$

The transition probability is calculated by solving the equation above under the initial condition $a_1 = 1$, $a_2 = 0$ $(t = 0)$:

$$|a_2(t)|^2 = \frac{\Omega^2}{\Omega^2 + (\omega - \omega_0)^2} \, \sin^2 \frac{\sqrt{\Omega^2 + (\omega - \omega_0)^2} \, t}{2} , \tag{D.10}$$

and is plotted in Figure **D.2**.

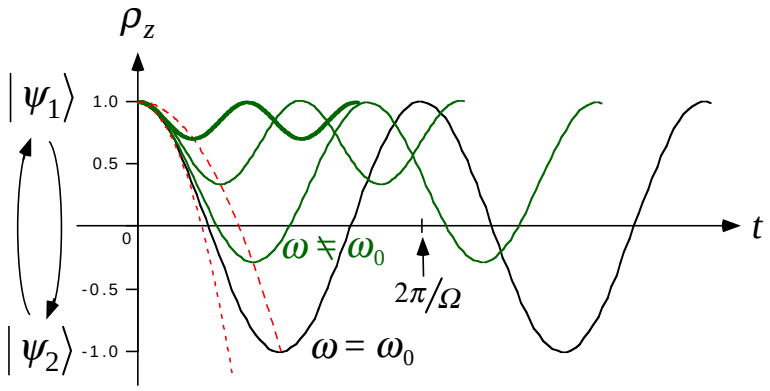

Figure D.2: A plot of the Rabi oscillation. When the frequency ω of the external field matches the transition frequency ω_0 (on-resonance), full conversion of the population between the two states occurs after $t = 2\pi/\Omega$, where $\Omega = \mu E_0/\hbar$ is the Rabi (angular) frequency.

D.1.2 Density matrix

We now introduce the density matrix ρ whose elements are defined in the following equation:

$$\rho_{nm} = a_n a_m^* \mathrm{e}^{-\mathrm{i}\,(W_n - W_m)\,t/\hbar}\,. \tag{D.11}$$

The density matrix is very useful because it describes not only a single atom but also the statistical average of an ensemble of many atoms. It can be shown that the density matrix obeys the Schrödinger equation expressed in the form

$$\mathrm{i}\hbar \frac{\mathrm{d}\rho}{\mathrm{d}t} = [\mathcal{H}, \rho\,] \tag{D.12}$$

or equivalently,

$$\mathrm{i}\hbar \frac{\mathrm{d}\rho_{nm}}{\mathrm{d}t} = \sum_k (\mathcal{H}'_{nk}\rho_{km} - \rho_{nk}\mathcal{H}'_{km}) - \mathrm{i}\,\frac{W_n - W_m}{\hbar}\rho_{nm}\,. \tag{D.13}$$

When we consider only two states, the diagonal elements of the density matrix

$$\rho_{11} = |a_1|^2, \quad \rho_{22} = |a_2|^2 = 1 - \rho_{11} \tag{D.14}$$

represent the population of each state while the non-diagonal elements

$$\rho_{12} = a_1 a_2^*\, \mathrm{e}^{\mathrm{i}\omega_0 t} = \rho_{21}^* \tag{D.15}$$

represent induced oscillating dipole moment, or the complex polarization.

D.1.3 Optical Bloch vector

If we consider a vector $\boldsymbol{\rho}$ with its components

$$\begin{cases} \rho_x \equiv \rho_{21} + \rho_{12} = 2\,\mathrm{Re}\{\rho_{12}\} & \text{(D.16a)} \\ \rho_y \equiv \mathrm{i}\,(\rho_{21} - \rho_{12}) = 2\,\mathrm{Im}\{\rho_{12}\} & \text{(D.16b)} \\ \rho_z \equiv \rho_{11} - \rho_{22} & \text{(D.16c)} \end{cases}$$

and a virtual force vector $\boldsymbol{G}$ with

$$\begin{cases} G_x \equiv -\dfrac{1}{\hbar}\,(\mathcal{H}'_{21} + \mathcal{H}'_{12}) = \Omega\,\cos\omega t & \text{(D.17a)} \\ G_y \equiv -\dfrac{\mathrm{i}}{\hbar}\,(\mathcal{H}'_{21} - \mathcal{H}'_{12}) = 0 & \text{(D.17b)} \\ G_z \equiv \omega_0\ , & \text{(D.17c)} \end{cases}$$

then the vector $\boldsymbol{\rho}$ precesses around the vector $\boldsymbol{G}$, *i.e.*

$$\frac{\mathrm{d}}{\mathrm{d}t}\boldsymbol{\rho} = \boldsymbol{G} \times \boldsymbol{\rho}. \tag{D.18}$$

Note that $\boldsymbol{\rho}$ is a unit vector since

$$|\boldsymbol{\rho}| = \sqrt{\rho_x^2 + \rho_y^2 + \rho_z^2} = \sqrt{|a_1|^2 + |a_2|^2} = 1\ . \tag{D.19}$$

When we look at this vector $\boldsymbol{\rho}$ in a frame rotating around the z axis with the laser (angular) frequency ω, the vector is expressed as $\tilde{\boldsymbol{\rho}}$ in the new frame coordinates:

$$\rho_{11} = \tilde{\rho}_{11}, \quad \rho_{22} = \tilde{\rho}_{22}, \quad \rho_{21} = \tilde{\rho}_{21}\mathrm{e}^{-\mathrm{i}\omega t} \tag{D.20}$$

and

$$\begin{cases} \tilde{\rho}_x = \tilde{\rho}_{21} + \tilde{\rho}_{12} & \text{(D.21a)} \\ \tilde{\rho}_y = \mathrm{i}\,(\tilde{\rho}_{21} - \tilde{\rho}_{12}) & \text{(D.21b)} \\ \tilde{\rho}_z = \tilde{\rho}_{11} - \tilde{\rho}_{22} = \rho_z\ . & \text{(D.21c)} \end{cases}$$

The vector $\tilde{\boldsymbol{\rho}} = (\tilde{\rho}_x, \tilde{\rho}_y, \rho_z)$ is called the "optical Bloch vector", and when the rotating-wave approximation is applied, it precesses around a fixed vector $\tilde{\boldsymbol{G}} = (\Omega, 0, -\Delta\omega)$ with a nutation (angular) frequency $\Omega' = \sqrt{\Omega^2 + \Delta\omega^2}$ ($\Delta\omega \equiv \omega - \omega_0$), according to the following "optical Bloch equations":

$$\begin{cases} \dfrac{\mathrm{d}\tilde{\rho}_x}{\mathrm{d}t} = \Delta\omega\tilde{\rho}_y & \text{(D.22a)} \\ \dfrac{\mathrm{d}\tilde{\rho}_y}{\mathrm{d}t} = -\Omega\rho_z - \Delta\omega\tilde{\rho}_x & \text{(D.22b)} \\ \dfrac{\mathrm{d}\rho_z}{\mathrm{d}t} = \Omega\tilde{\rho}_y\ , & \text{(D.22c)} \end{cases}$$

as illustrated in Figure **D.3**. The projection of $\boldsymbol{\rho}$ vector is exactly what is shown in Figure **D.2**.

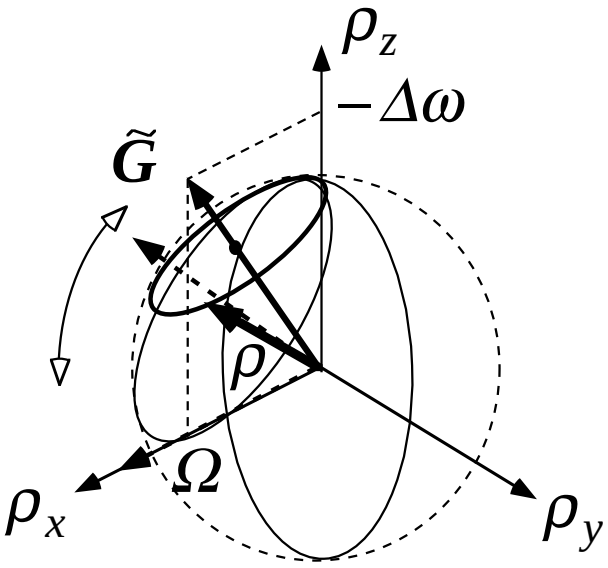

Figure D.3: A scheme of the optical Bloch vector precessing around a vector $\boldsymbol{G}$. Full conversion of the population is achieved when $\boldsymbol{G}$ is along the ρ_x axis, *i.e.* $\omega = \omega_0$.

D.1.4 Power broadening

Generally, the resonance width broadens at a higher laser intensity I than a value sufficient to cause saturation. This "power broadening" can be explained easily from Eq. (D.10). The resonance signal is proportional to $|a_2|^2$ which is expressed in the form of a Lorentzian having a half width of the Rabi frequency $\Omega \propto \sqrt{I}$. Pictorially, the situation is understood by considering the direction of the vector $\tilde{\boldsymbol{G}}$. The higher the laser power, the more tilted the vector is toward the horizontal plane for the same detuning $\Delta\omega$, and the $\boldsymbol{\rho}$ vector precesses with a larger amplitude. This means that the same resonance intensity is achieved for larger detuning; therefore the resonance width is broader.

D.1.5 Relaxation effects

Frequent collisions which change the phase of the oscillating atoms can be treated as relaxations of the states, under certain reasonable approximations below. There are two different types of collisions: one is elastic or adiabatic, which does not change the state of the atom and the other is inelastic or diabatic, for which the atomic state and its energy are subject to change. Figure **D.4** shows two states under the influence of inelastic relaxation (Γ_A and Γ_B for each state), resonating with the light field. Apart

from these relaxations, the atom is subject to elastic collisions with a rate γ_{p}. Here we assume the following conditions (impact approximation) which are applicable in most cases to low-density conditions.

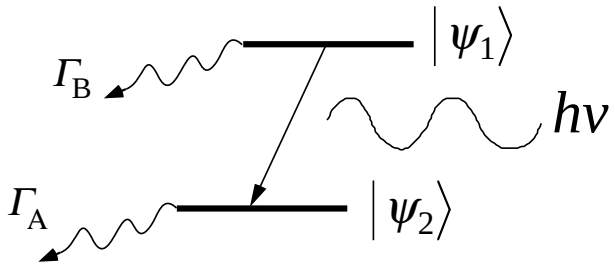

Figure D.4: A model of a two-level atom which is subject to relaxation and is interacting with an external light field.

(i) the collisional relaxation is a random and stationary process;

(ii) strong collisions change the phase randomly in a short time interval (the sudden approximation), so that the phase memory is totally lost after each collision;

(iii) the duration of the collision (τ_{c}) is much shorter then the interval between collisions (ν_{c}^{-1}), and the observation time (Δt) must be even longer ($\tau_{\mathrm{c}} \ll \nu_{\mathrm{c}}^{-1} < \Delta t$);

(iv) the duration of the collision is so short that the collisional processes can not be traced by the light field; that is, the period of the Rabi oscillation is much longer than the duration of the collision ($\tau_{\mathrm{c}} \ll \Omega^{-1}$).

In the assumption above, the possible shift of the resonance line is not treated, because the second assumption of complete randomness in the phase shift does not allow any resonance shift, so that the effect of collisions appears only as a broadening of the line. The modified optical Bloch equation is then given as the following [45, 85]:

$$\begin{cases} \dfrac{\mathrm{d}\tilde{\rho}_x}{\mathrm{d}t} = \Delta\omega\tilde{\rho}_y - \gamma_{\mathrm{T}}\tilde{\rho}_x & \text{(D.23a)} \\ \dfrac{\mathrm{d}\tilde{\rho}_y}{\mathrm{d}t} = -\Omega\rho_z - \gamma_{\mathrm{T}}\tilde{\rho}_y - \Delta\omega\tilde{\rho}_x & \text{(D.23b)} \\ \dfrac{\mathrm{d}\rho_z}{\mathrm{d}t} = \Omega\tilde{\rho}_y - \Gamma_{\mathrm{B}}\rho_{11} + \Gamma_{\mathrm{A}}\rho_{22}\ , & \text{(D.23c)} \end{cases}$$

where

$$\gamma_{\mathrm{T}} = \gamma_{\mathrm{p}} + \frac{\Gamma_{\mathrm{A}} + \Gamma_{\mathrm{B}}}{2} \tag{D.24}$$

is the total relaxation rate. Here γ_{T} is called the transverse relaxation rate, and Γ_{A} and Γ_{B} the longitudinal relaxation rates. Note the half-contribution (*i.e.* the factor $1/2$) of inelastic relaxation to the transverse relaxation.

D.2 Studies on Collisional Effects

Throughout this section the atomic units are used. Refer to Appendix **F.1**.

D.2.1 Theoretical treatments

The collisional effects on the form of spectral lines of ordinary atomic systems is a subject of extensive investigations, especially in plasmas. The theory of these effects has a long history (see, *e.g.* [80–82]). One successful approach was the impact approximation that we are going to discuss here, which assumes the collisions to take place instantaneously. The following discussions consider only adiabatic perturbations, and do not include transitions between different states of the atom.

Let us consider an atomic oscillator which is perturbed by collisions with surrounding atoms so that consequently the frequency of oscillations varies in time. Let $V(R)$ be the interaction potential, the oscillation can be described in the form

$$f(t) = \exp\Big\{\mathrm{i}\omega_0 t + \mathrm{i}\eta(t)\Big\}\,, \tag{D.25a}$$

$$\eta(t) = \int_{-\infty}^{t} \kappa(t')\,\mathrm{d}t'\,, \tag{D.25b}$$

$$\kappa(t) = V(R(t))\,, \tag{D.25c}$$

where ω_0 is the unperturbed frequency, $\kappa(t)$ is the frequency shift and $\eta(t)$ the phase of the oscillation caused by the interaction. Since we neglect here inelastic (diabatic) channels ($\Gamma_{\mathrm{A}} = \Gamma_{\mathrm{B}} = 0$ in Figure **D.4**, p. 121), the phase is a real number. The line shape is given by the Fourier transformation of the function $f(t)$:

$$I(\omega) = \lim_{\Delta t\to\infty} \left| \frac{1}{\sqrt{2\pi\,\Delta t}} \int_{-\Delta t/2}^{\Delta t/2} f(t)\,\mathrm{e}^{-\mathrm{i}\omega t}\,\mathrm{d}t \right|^2 . \tag{D.26}$$

Usually, the macroscopic target conditions such as gas pressure and temperature do not vary with time, and the functions $f(t)$ are stationary random processes. Then the power spectrum $I(\omega)$ can be rewritten as a Fourier transformation of the correlation function $\Phi(\tau)$ (Wiener-Khinchin Theorem):

$$I(\omega) = \frac{1}{\pi}\mathrm{Re}\left\{\int_0^\infty \Phi(\tau)\,\mathrm{e}^{-\mathrm{i}\omega\tau}\mathrm{d}\tau\right\}\,, \tag{D.27a}$$

$$\Phi(\tau) = \lim_{\Delta t\to\infty}\frac{1}{\Delta t}\int_{-\Delta t/2}^{\Delta t/2} f^*(t)\,f(t+\tau)\,\mathrm{d}t = \langle f^*(0)f(\tau)\rangle\,. \tag{D.27b}$$

In the last equation above, the time averaging was replaced by averaging over the statistical assembly as denoted by angle brackets.

It can be derived that

$$\Delta\Phi(\tau) = -\Phi(\tau)\left\langle 1-\mathrm{e}^{-\mathrm{i}\Delta\eta}\right\rangle \equiv -\Phi(\tau)\,(\Delta-\mathrm{i}\gamma)\,\Delta\tau \tag{D.28}$$

and the complex shift of spectral line due to elastic collisions at impact parameter $b \geq b_1$ is given by the equation

$$\Delta-\mathrm{i}\gamma = -\mathrm{i}Nv\int_{b_1}^\infty (1-\mathrm{e}^{-\mathrm{i}\eta(b)})\,2\pi b\,\mathrm{d}b \equiv -\mathrm{i}Nv\,(\sigma_\Delta - \mathrm{i}\sigma_\gamma)\,, \tag{D.29}$$

where N is the number density of the medium, v is relative velocity of colliding atoms, $\eta(b) = \eta_i(b) - \eta_f(b)$ is the difference of the phase shifts between the two states of the resonance.

From Eq. (D.28) it follows that

$$\frac{\mathrm{d}\Phi}{\mathrm{d}\tau} = -\left(\Delta-\mathrm{i}\gamma\right)\Phi\,, \qquad \Phi = \mathrm{e}^{-(\Delta-\mathrm{i}\gamma)\tau} \tag{D.30}$$

and by substituting Eq. (D.30) into Eq. (D.27), we obtain a Lorentzian resonance shape:

$$I(\omega) = \frac{\gamma}{2\pi}\cdot\frac{1}{(\omega-\Delta)^2+\gamma^2}\,. \tag{D.31}$$

At large impact parameters the phase shift is determined by the van der Waals potential

$$V_j(R) = -\frac{C_6}{R^6} = -\frac{\alpha G_j}{R^6}\,, \tag{D.32}$$

where $\alpha = 1.383$ a.u.* is the static polarizability of helium atoms and

$$G_j = \left\langle j\left|\boldsymbol{\mu}^2\right|j\right\rangle \tag{D.33a}$$

$$-\boldsymbol{\mu} = \boldsymbol{r}_{\overline{p}} + \boldsymbol{r}_{\mathrm{e}} - 2\boldsymbol{r}_{\mathrm{He}^{++}} = (1+\xi)\,\tilde{\boldsymbol{r}}_{\overline{p}} + \tilde{\boldsymbol{r}}_{\mathrm{e}} \tag{D.33b}$$

$$\tilde{\boldsymbol{r}}_{\overline{p}} = \boldsymbol{r}_{\overline{p}} - \boldsymbol{r}_{\mathrm{He}^{++}} \tag{D.33c}$$

$$\tilde{\boldsymbol{r}}_{\mathrm{e}} = \boldsymbol{r}_e - \left\{\xi\boldsymbol{r}_{\overline{p}} + (1-\xi)\,\boldsymbol{r}_{\mathrm{He}^{++}}\right\} \tag{D.33d}$$

$$\xi = \frac{M_{\overline{p}}}{M_{\overline{p}} + M_{\mathrm{He}^{++}}}\,, \tag{D.33e}$$

in which $\boldsymbol{\mu}$ is the dipole operator of the $\overline{p}\mathrm{He}^+$ atomcule. The potential $V_j(R)$ corresponds to the dispersion force [87], and the contribution from dipole–induced dipole interaction

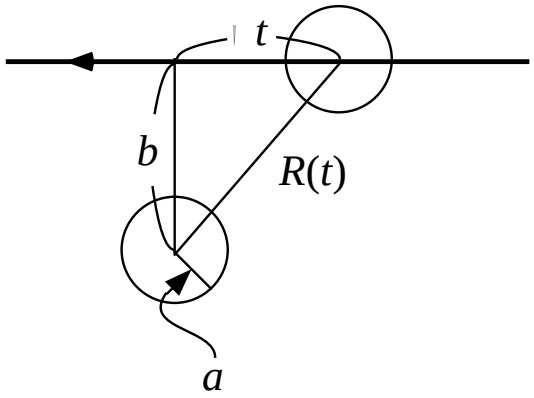

Figure D.5: A classical rectilinear trajectory was used for the calculation of phase shifts. The interatomic distance is given by the equation $R(t) = \sqrt{b^2 + (vt)^2}$.

is averaged out due to the fast rotation of the atomcule (see Section **5.4.1**). Using the simplest approximation for the phase

$$\eta_j(b) = \int_{-\infty}^{\infty} V_j(R(t))\mathrm{d}t \tag{D.34}$$

and the rectilinear trajectory shown in Figure **D.5** ($R(t)^2 = b^2 + (vt)^2$) at $b \geq R_1$, we obtain

$$\eta(b) = -\frac{3\pi\alpha}{8vb^5}\left(G_i - G_f\right) \tag{D.35}$$

and

$$\Delta - \mathrm{i}\gamma = -\frac{2\pi}{5} N {c_{if}}^2 v^{3/5} \left\{ I_1(x_0) + \mathrm{i} I_2(x_0) \right\}, \tag{D.36}$$

where

$$x_0 = \frac{{c_{if}}^5}{v{R_1}^5} \left(= \left(\frac{R_1}{b_T}\right)^{-5} \right), \quad c_{if} = \left(\frac{3\pi}{8} \alpha \left(G_i - G_f\right) \right)^{\frac{1}{5}}, \tag{D.37}$$

and

$$\begin{cases} I_1(x_0) = \displaystyle\int_0^{x_0} x^{-7/5} \sin x \, \mathrm{d}x \,, & \text{(D.38a)} \\ I_2(x_0) = \displaystyle\int_0^{x_0} x^{-7/5} \left(1 - \cos x\right) \mathrm{d}x \,. & \text{(D.38b)} \end{cases}$$

The integrals above can be expressed in terms of incomplete gamma-functions. At thermal velocity $v \sim v_T \equiv \sqrt{2T/\mu}$ (μ being the reduced mass between the $\overline{p}\mathrm{He}^+$ atomcule and a helium atom) and $R_1 \sim 1$ a.u., the parameter x_0 is large (~ 300 at $T = 6$ K; see next section), and the integrals are reduced to

$$\begin{cases} I_1 = \dfrac{25}{6} \Gamma\left(\dfrac{8}{5}\right) \sin\dfrac{\pi}{5} - x_0^{-7/5} \left\{ \cos x_0 + \mathcal{O}(x_0^{-1}) \right\}, & \text{(D.39a)} \\ I_2 = \dfrac{25}{6} \Gamma\left(\dfrac{8}{5}\right) \cos\dfrac{\pi}{5} - \dfrac{x_0^{-2/5}}{2} - x_0^{-7/5} \left\{ \sin x_0 + \mathcal{O}(x_0^{-1}) \right\}. & \text{(D.39b)} \end{cases}$$

*The atomic unit of polarizability is $4\pi\varepsilon_0 (a_0)^3$.

The terms of order $x_0^{-7/5}$ can be omitted, but the term $\sim x_0^{-2/5}$ in the second integral must be retained. Figure **D.6** plots functions I_1 and I_2, together with the approximated expansion to the $x_0^{-2/5}$ order. It shows that the approximation is good enough even for a small value of $x_0 \sim 2$ and hence for $R_1 \sim 3$ a.u.

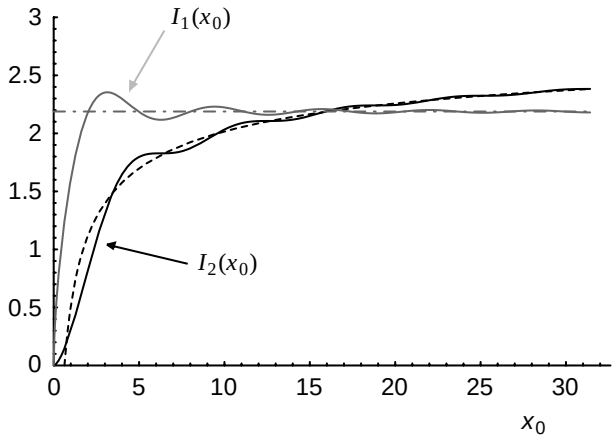

Figure D.6: The integral functions $I_1(x_0)$ and $I_2(x_0)$ are plotted (solid lines). The approximated expansion to the $x_0^{-2/5}$ order reproduces the original function well enough, even for small values of x_0 (dotted and dotdash lines). There, the oscillation is not described by the approximated expansion, but this discrepancy can be neglected, since the positive and negative discrepancies cancel out in the process of integration over the velocity distribution.

Averaging Eq. (D.36) over velocities with Maxwell-Boltzmann distribution (Eq. (5.6c), p. 62), we obtain

$$\Delta = -N{c_{if}}^2 v_T^{3/5}\, A \sin\frac{\pi}{5}\,, \tag{D.40a}$$

$$\gamma = N{c_{if}}^2 v_T^{3/5}\left\{A\cos\frac{\pi}{5} - 2\sqrt{\pi}\left(\frac{R_1}{b_T}\right)^2\right\}, \tag{D.40b}$$

where

$$v_T = \sqrt{2T/\mu}\,, \tag{D.40c}$$

$$A = \frac{10}{3}\sqrt{\pi}\,\Gamma\left(\frac{9}{5}\right)\Gamma\left(\frac{8}{5}\right) \approx 4.917\,, \tag{D.40d}$$

$$b_T = \frac{c_{if}}{v_T^{1/5}}\,. \tag{D.40e}$$

The impact parameter b_T is usually called the Weisskopf radius and is defined by the condition

$$\eta(b_T) = 1\,. \tag{D.41}$$

Therefore to an order of magnitude,

$$\sigma_\gamma \approx \pi {b_T}^2 \tag{D.42}$$

while the shift cross section σ_Δ is determined by more distant collisions $b \lesssim b_T$.

Coming back to Eq. (D.40), to calculate the shift and the broadening, it is necessary to know the values of G_j and, for the broadening, the repulsion radius R_1. In the framework of a hydrogen-like model with effective charges $Z^{\overline{p}}_{\text{eff}}(j)$ and $Z^{\text{e}}_{\text{eff}}(j)$,

$$\left\langle j \left| \boldsymbol{\mu}^2 \right| j \right\rangle = \left(\frac{1+\xi}{M^* Z^{\overline{p}}_{\text{eff}}(j)} \right)^2 \left\langle r^2 \right\rangle_j + \frac{3}{\left(Z^{\text{e}}_{\text{eff}}(j) \right)^2} \,, \tag{D.43}$$

where

$$\left\langle r^2 \right\rangle_j = \frac{1}{2}\, n^2 \left\{ 5n^2 + 1 - 3\, l\,(l+1) \right\} \tag{D.44}$$

is the mean radius of the excited hydrogen-like state.

D.2.2 Collision parameters for the $\overline{p}\text{He}^+$ atomcule

For the metastable states of $\overline{p}\text{He}^+$ where $n \approx 39$, $l \approx 35$, and $\sqrt{M^*/m_e} = n_0 \approx 38$; and $Z^{\overline{p}}_{\text{eff}} \approx 1.7$, $Z^{\text{e}}_{\text{eff}} \approx 1.6$, $-\Delta Z^{\overline{p}}_{\text{eff}} \sim \Delta Z^{\text{e}}_{\text{eff}} \sim 1/n$,

$$\left\langle r^2 \right\rangle_{(n,l)} - \left\langle r^2 \right\rangle_{(n-1,l-1)} \approx 4\, n^3 \tag{D.45a}$$

$$G_{(n,l)} - G_{(n-1,l-1)} \sim (1+2\xi) \left\{ \frac{4}{n \left(Z^{\overline{p}}_{\text{eff}} \right)^2} + \frac{2\, \Delta Z^{\overline{p}}_{\text{eff}}}{\left(Z^{\overline{p}}_{\text{eff}} \right)^3} \right\} + \frac{6\, \Delta Z^{\text{e}}_{\text{eff}}}{\left(Z^{\text{e}}_{\text{eff}} \right)^3} \tag{D.45b}$$

$$\sim \frac{1}{10}$$

$$c^5_{if} = \frac{3\pi}{8} \alpha \left(G_i - G_f \right) \sim \frac{1}{6} \text{ a.u.} \tag{D.45c}$$

At 6 K, the thermal velocity is

$$v_T = 210 \text{ m/s} \sim 10^{-4} \text{ a.u.} \,, \tag{D.46}$$

so that

$$b_T \approx 4 \text{ a.u.} \,, \tag{D.47a}$$

$$x_0 = \left(\frac{R_1}{b_T} \right)^{-5} \approx 10^3 \qquad \text{at } R_1 = 1 \text{ a.u.} \tag{D.47b}$$

D.3 Calculation of Dipole Moments

According to Wigner-Eckard theorem, tensor operators can be divided into a geometrical part and a physical part. The dipole moment $\boldsymbol{\mu}$ is a tensor operator of first rank and is expressed as

$$\langle \beta, L, M \,|\mu|\, \beta', L', M' \rangle = (-1)^{L-M} \begin{pmatrix} L & 1 & L' \\ -M & q & M' \end{pmatrix} \langle \beta, L || \mu || \beta', L' \rangle \,, \tag{D.48}$$

where β, β' represent indices of states apart from the quantum numbers L and M, and q is the polarization of the photon. The reduced dipole matrix element $\langle \beta, L||\mu||\beta', L'\rangle$ does not depend on the magnetic quantum numbers M, M', and the Wigner's $3j$ symbol is related with the Clebsch-Gordan coefficient:

$$\begin{pmatrix} l_1 & l_2 & L \\ m_1 & m_2 & -M \end{pmatrix} = \frac{(-1)^{l_1 - l_2 + M}}{\sqrt{2L+1}} \langle l_1 l_2 m_1 m_2 \,|LM\rangle \,. \tag{D.49}$$

From the equations above, the dependence of the dipole moments on the direction of the angular momentum and the (laser) photon polarization is derived.

$$\sigma^+ : \quad \begin{pmatrix} l & 1 & l+1 \\ m & 1 & -(m+1) \end{pmatrix} = (-1)^{l+m} \sqrt{\frac{(l+m+2)\,(l+m+1)}{(2l+3)\,(2l+2)\,(2l+1)}} \tag{D.50a}$$

$$\pi : \quad \begin{pmatrix} l & 1 & l+1 \\ m & 0 & -m \end{pmatrix} = (-1)^{l+m+1} \sqrt{\frac{2\,(l-m+1)\,(l+m+1)}{(2l+3)\,(2l+2)\,(2l+1)}} \tag{D.50b}$$

$$\sigma^- : \quad \begin{pmatrix} l & 1 & l+1 \\ m & -1 & -(m-1) \end{pmatrix} = (-1)^{-l-m} \sqrt{\frac{(l-m+2)\,(l-m+1)}{(2l+3)\,(2l+2)\,(2l+1)}} \tag{D.50c}$$

Now we consider the relation between the dipole moment and the lifetime of a spontaneous radiative transition. The Einstein's A coefficient is written as

$$A_{i \to f} = \frac{4}{3} \frac{\omega_{if}^3}{\hbar c^3} \sum_{m_f, q} \left| \langle l_i m_i \,|\mu_q\,|\, l_f m_f \rangle \right|^2 , \tag{D.51}$$

where the sum is taken over all allowed transitions with different photon polarization. It can be shown that the sum does not depend on m_i since

$$\sum_{m_f, q} \left| \begin{pmatrix} l_i & 1 & l_f \\ m_i & q & -m_f \end{pmatrix} \right|^2 = \frac{1}{2\,l_i + 1} \,, \tag{D.52}$$

so that the transition rate is expressed using the reduced matrix element as

$$\tau^{-1} = A_{i \to f} = \frac{4}{3} \frac{\omega_{if}^3 \, \mu_{\mathrm{tot}}^2}{\hbar c^3} \,, \tag{D.53a}$$

$$\mu_{\mathrm{tot}}^2 \equiv \frac{\left| \langle l_i || \mu || l_f \rangle \right|^2}{2\,l_i + 1} \,. \tag{D.53b}$$

D.4 Simulation of Laser-Induced Resonant Transitions

The optical Bloch equation (D.23a) under the condition of relaxation can not be solved analytically. We therefore wrote a computer program which simulated the Rabi oscillation and calculated the depopulation efficiency, to be compared with the observed resonances.

The laser light was about 80% polarized linearly, according to the specification of the dye laser. If we take the z axis along the polarized electric field $\boldsymbol{E}$, the resonances between two sets of $2\,l+1 \approx 70$ magnetic sublevels (denoted by the quantum number m) are treated as π transitions. We consider either a "favored" or "unfavored" transition, *i.e.* $l_i = l \Rightarrow l_f = l-1$ for the simulation. The Rabi (angular) frequency is calculated for different m states from Eq. (F.18), p. 139, and Eq. (D.50b):

$$\Omega_{\text{tot}}\ \ [\text{GHz}] = 2\pi \times 0.4370 \times \mu_{\text{tot}}\,[\text{debye}] \times \sqrt{P(t)\,[\text{kW/cm}^2]}\,, \tag{D.54a}$$

$$\Omega_\pi^{(m)} = \Omega_{\text{tot}} \times \sqrt{2\,l+1} \left| \begin{pmatrix} l-1 & 1 & l \\ m & 0 & -m \end{pmatrix} \right| . \tag{D.54b}$$

For the calculation of the power density $P(t)$ defined in Eq. (F.15), p. 138, a typical temporal shape of the laser pulse with two peaks (Figure **5.11-a**, p. 68) was used.

As for the relaxation rates, the elastic collision rate γ_{p} was the parameter whose value we wanted to determine by comparing the observed width and the simulation result. Γ_{A} was given by the Auger decay rate of the daughter state while the small Γ_{B} was neglected. The transverse relaxation rate γ_{T} was given by Eq. (D.24), p. 122.

With initial conditions $\rho_{11}^{(m)} = 1/(2\,l_i+1)$, $\rho_{22}^{(m)} = 0$, $\tilde{\rho}_x^{(m)} = 0$ and $\tilde{\rho}_y^{(m)} = 0$, the time-evolution of the $(2\,l+1)$ different optical Bloch vectors $\tilde{\boldsymbol{\rho}}^{(m)}$ is given by the following equations:[†]

$$\begin{cases} \dfrac{\Delta\tilde{\rho}_x^{(m)}}{\Delta t} = \Delta\omega\,\tilde{\rho}_y^{(m)} - \gamma_{\text{T}}\tilde{\rho}_x^{(m)} & \text{(D.55a)} \\ \dfrac{\Delta\tilde{\rho}_y^{(m)}}{\Delta t} = -\,\Omega_\pi \rho_z^{(m)} - \gamma_{\text{T}}\tilde{\rho}_y^{(m)} - \Delta\omega\,\tilde{\rho}_x^{(m)} & \text{(D.55b)} \\ \dfrac{\Delta\rho_{11}^{(m)}}{\Delta t} = \dfrac{\Omega_\pi}{2}\,\tilde{\rho}_y^{(m)} & \text{(D.55c)} \\ \dfrac{\Delta\rho_{22}^{(m)}}{\Delta t} = -\,\dfrac{\Omega_\pi}{2}\,\tilde{\rho}_y^{(m)} - \Gamma_{\text{A}}\rho_{22}^{(m)} & \text{(D.55d)} \\ \rho_z^{(m)} = \rho_{11}^{(m)} - \rho_{22}^{(m)}\,. & \text{(D.55e)} \end{cases}$$

[†] We must consider $(2\,l_i+1)$ initial states and $(2\,l_f+1)$ final states, but in fact, the $-m$ state and the m state follow the same equation since $\Omega_\pi^{(-m)} = \Omega_\pi^{(m)}$, so that only half the number of states needed to be considered in the actual computation.

The total populations in the parent (initial) state and the daughter (final) state are given by the sum of the diagonal components of the density matrix:

$$\begin{cases} N_i(t) = N_i(t_1) \sum\limits_{-l_i \le m \le l_i} \rho_{11}^{(m)}(t) & \text{(D.56a)} \\ N_f(t) = N_i(t_1) \sum\limits_{-l_f \le m \le l_f} \rho_{22}^{(m)}(t)\,, & \text{(D.56b)} \end{cases}$$

and the depopulation efficiency of the laser pulse and the resonance peak area are given as

$$\epsilon = 1 - \frac{N_i(t_1 + \tau_l)}{N_i(t_1)}\,, \qquad \text{(D.57a)}$$

$$\epsilon N_i(t_1) = N_i(t_1) - N_i(t_1 + \tau_l)\,, \qquad \text{(D.57b)}$$

where t_1 is the starting time of the laser pulse and $t_1 + \tau_l$ is the end of the pulse.

The multiple m states oscillate at different nutation frequencies $\Omega_\pi'^{(m)} = \sqrt{(\Omega_\pi^{(m)})^2 + (\Delta\omega)^2}$. By summing up these oscillations, the resultant effect was the average frequency $\overline{\Omega_\pi'}$ and an additional relaxation with a typical time constant of $\pi \big/ \overline{\Omega_\pi'}$. No collisional mixing between different m states was taken into account, which would not have much effect anyway.

We consider below the case of the (39,35)⇒(38,34) resonance at 597 nm. The dipole moment $\mu_{\rm tot}$ was determined from the lifetime of the parent (39,35) state, which reflects the transition rate by spontaneous emission. A value $\tau^{-1} = 0.620\ \mu\text{s}^{-1}$ was adopted to give $\mu_{\rm tot} = 0.649$ debye from Eq. (D.53a), by comparing the measured lifetime and the theoretically calculated dipole moment discussed in Appendices **B.2.1**, **B.2.2** and **B.3**. The Auger decay rate $\Gamma_{\rm A}$ was known by measuring the decay constant of the resonance peak after the laser pulse terminated (see Appendix **B.2.3**). We took a value $\Gamma_{\rm A} = 0.0845\ \text{ns}^{-1}$ [57].

Appendix E

Precise Measurement of Transition Wavelengths

This appendix supplements the shift and width measurements presented in Chapter **5**. The wavelength calibration method which was critical for the arguments in the main text is explained in more detail in the first section, and the obtained full experimental results on the shift and width are tabulated in the latter section here.

E.1 Calibration of the Wavelength

E.1.1 Reference cells

For a fine calibration of the wavelength in the case of the narrow-band mode, absorption spectra of the standard molecular lines were taken and referred to. Iodine ($^{128}I_2$) vapor was used for the 597 nm resonance while tellurium ($^{130}Te_2$) was used for the blue 470 nm line. An enclosed cylindrical glass cell of 2.5 cm diameter and 10 cm length containing a small amount of iodine/tellurium solid was put in a heating oven and heated to 260/650°C, respectively, in order to (i) have enough vapor pressure and (ii) to populate (ro-vibrationally) highly excited molecular levels. The iodine cell had a side-stem of 29 cm length so that its tip emerged from the oven. Since the vapor pressure inside the cell is determined by the temperature of the *coolest spot*, the tip was covered with a heating wire and its temperature was adjusted to about 80°C,* so as to minimize the pressure while retaining enough absorption intensity. With this condition the vapor pressure is some tens of Torr, and the possible shift of the reference frequency can be ignored whilst the lines are subject to Doppler broadening of the temperature at the hottest spot. In the case of tellurium, the boiling point is very high,† and such a procedure was not needed.

*Iodine: melting point at 114°C and boiling point at 185°C under the atmospheric pressure.

†Tellurium: melting point at 449°C and boiling point at 988°C under the atmospheric pressure.

Table **E.1** shows the reference molecular lines used for the calibration, quoted from Refs. [72, 73].

Table E.1: List of reference I_2 and Te_2 absorption lines used for the wavelength calibration. The identification number of the lines and the wave number values are taken from Refs. [72, 73] and listed, together with calculated corresponding vacuum wavelengths. Symbols a–f correspond to the lines in Figure **5.5**, p. 56.

$^{128}I_2$ reference lines [72]			
line	No. #	wave number [cm^{-1}]	vac. wavelen. [nm]
	4509	16742.0419	597.29871
	4510	16742.2272	597.29210
	4511	16742.3125	597.28905
	4512	16742.4869	597.28283
a	4513	16742.7148	597.27470
b	4514	16742.9009	597.26806
c	4515	16742.9484	597.26637
d	4516	16743.0984	597.26102
e	4517	16743.4965	597.24682
f	4518	16743.5754	597.24400
	4519	16743.8554	597.23402
	4520	16744.0762	597.22614

$^{130}Te_2$ reference lines [73]		
No. #	wave number [cm^{-1}]	vac. wavelen. [nm]
59	21242.6542	470.75097
60	21243.4691	470.73291
61	21245.9655	470.67760

E.1.2 Data acquisition

Since our spectroscopic method was to fire each laser pulse to a single atomcule and to count one by one each $\overline{p}$ annihilation, it took about 10 minutes to gain enough statistics for the resonance signal in the DATS spectrum at a fixed wavelength. Therefore, it took typically 1–3 hours to obtain a resonance curve, depending on the peak intensity *i.e.* the transition strength and the laser power. The heavy load to the laser, firing at more than 200 shots per second continuously, caused the dye solution to deteriorate rapidly. In fact, sometimes the output power even decreased within a few hours. We therefore did not let the laser stay at one wavelength for a long time, but instead, scanned the wavelength quickly over many cycles in order to average out the different laser powers.

For most of the data presented in Chapter **5**, the $\overline{p}\mathrm{He}^+$ resonance data were taken with respect to the wavelength meter and the device was later calibrated against the reference lines. In the analysis program, the recorded wavelength-meter values were selected into bunches and the peak area for each corresponding DATS spectrum was counted, normalized to the total delayed annihilation count, and plotted against the calibrated average wavelength of the bunch.

The laser bandwidth, which needed to be deconvoluted in fitting the resonance curve, was roughly known from the interference pattern of the wavelength meter, to be typically 1 GHz. More precisely, it was determined from the widths of the absorption lines in the iodine/tellurium cells and from the interference peaks measured by a spectrum analyzer, as FWHM $= 1000 \pm 100$ MHz for the 597 nm resonance and 1000 ± 150 MHz for the 470 nm line, after the Doppler width of the iodine (520 MHz FWHM) or the tellurium (860 MHz FWHM) was subtracted from the former widths.

The center and the width of the resonance were determined by fitting the resonance profile with one or two (representing hyperfine-splitting) Voigt functions, as explained in Sections **5.1.2** and **5.3.2**.

Aiming at a more precise determination of the transition wavelengths, we also took one set of $\overline{p}\mathrm{He}^+$ resonance data simultaneously with the signals of the calibration standard, as well as the interference pattern in the spectrum analyzer with a 3 GHz free spectral range and a finesse better than 125 (specified value). In this "on-line calibration" data acquisition, the hardware logic and the software program were both modified, so that the reference data should be taken alternately with the $\overline{p}\mathrm{He}^+$ data. It was not possible to synchronize the data-taking of the both signals, because the $\overline{p}\mathrm{He}^+$ required a large number ($> 10^4$) of laser shots per wavelength with a rough step and within a narrow range around the resonance, while the reference data required only tens of shots per wavelength but the sampling steps had to be small and the range wide. Therefore, the data-acquisition modes were switched automatically between the two, according to the following scheme: the scan for the reference data started from far outside the $\overline{p}\mathrm{He}^+$ resonance region, sweeping quickly with a small step of 0.10 pm. When the wavelength came close to the resonance, the $\overline{p}\mathrm{He}^+$ data were acquired, staying at one wavelength-point for a few minutes. Then the next four quick steps were only for the reference data, and at the fifth step again the $\overline{p}\mathrm{He}^+$ data were taken before the reference data, and thus the resonance signals were obtained every five steps until the wavelength came out of the resonance region. After that, again only the reference data were taken and the whole set of calibration data was accomplished. Part of the data so obtained is presented in Figure **5.5**, p. 56.

E.2 Full Data of the Density Shift and Width Measurements

Tables **E.2** and **E.3** list all the raw data of the shift and width measurements.

Table E.2: List of all raw data of the shift and width measurements for the 597 nm resonance. Listed are the run number of each measurement, the calibrated target temperature (T), the target pressure (p), the density (ρ) and its error ($\delta\rho$), the energy of the laser pulse ($\mathcal{E}$), the vacuum wavelength measured by the wavelength meter (λ_{WM}) and its statistical error ($\delta\lambda_{\mathrm{stat}}$), the calibration correction to be added to the measured value ($\Delta\lambda_{\mathrm{calib.}} = \lambda_{\mathrm{calib.}} - \lambda_{\mathrm{WM}}$) with its systematic error in parenthesis ($0.000x(y) \equiv 0.000x \pm 0.000y$), and the Lorentzian full width of the resonance (Γ, obtained by the hyperfine-doublet fit) and its statistical error ($\delta\Gamma$). The temperature sensor had an intrinsic error of ± 0.1 K, and the error of the density was dominantly given by this uncertainty. The last row in *italic style* shows data of the on-line calibration measurement, for which the wavelength value is a calibrated one ($\lambda_{\mathrm{calib.}}$) and its error includes both statistical and systematic (calibration) errors ($\delta\lambda_{\mathrm{abs}}$) for the absolute vacuum wavelength.

run #	T [K]	p [mb]	ρ [g/ℓ] $\pm$ $\delta\rho$	$\mathcal{E}$ [mJ]	$\lambda_{\mathrm{WM}} \pm \delta\lambda_{\mathrm{stat}}$ [nm]	$\Delta\lambda_{\mathrm{calib.}}$	$\Gamma \pm \delta\Gamma$ [nm]
220	6.2	533	4.34 ± 0.08	0.105	597.2595 ± 0.0001	$+0.0006(3)$	1.88 ± 0.20
222	6.2	536	4.37 ± 0.08	0.039	597.2597 ± 0.0002	$+0.0006(3)$	1.37 ± 0.57
223	6.2	536	4.37 ± 0.08	0.030	597.2597 ± 0.0002	$+0.0006(3)$	1.11 ± 0.47
225	6.3	537	4.38 ± 0.08	0.200	597.2595 ± 0.0001	$+0.0006(3)$	2.77 ± 0.21
226	6.2	535	4.37 ± 0.08	0.400	597.2594 ± 0.0001	$+0.0006(3)$	3.34 ± 0.34
227	6.2	530	4.33 ± 0.08	0.019	597.2589 ± 0.0003	$+0.0006(3)$	0.47 ± 1.55
228	6.2	994	8.52 ± 0.18	0.042	597.2628 ± 0.0002	$+0.0006(3)$	1.42 ± 0.64
229	6.3	966	8.21 ± 0.17	0.070	597.2621 ± 0.0002	$+0.0006(3)$	2.62 ± 0.24
231	6.2	927	7.88 ± 0.16	0.038	597.2621 ± 0.0002	$+0.0006(3)$	1.48 ± 0.33
232	6.2	934	7.94 ± 0.16	0.300	597.2619 ± 0.0002	$+0.0006(3)$	4.69 ± 0.38
233	6.2	932	7.94 ± 0.16	0.017	597.2618 ± 0.0003	$+0.0006(3)$	1.02 ± 0.73
235	6.2	314	2.51 ± 0.04	0.044	597.2577 ± 0.0002	$+0.0006(3)$	1.24 ± 0.36
236	6.2	314	2.51 ± 0.05	0.025	597.2584 ± 0.0004	$+0.0006(3)$	0.52 ± 1.97
237	6.2	316	2.52 ± 0.04	0.200	597.2580 ± 0.0001	$+0.0006(3)$	1.88 ± 0.23
238	6.2	314	2.50 ± 0.04	0.100	597.2582 ± 0.0002	$+0.0006(3)$	0.67 ± 0.87
239	6.3	314	2.49 ± 0.04	0.060	597.2580 ± 0.0002	$+0.0006(3)$	1.19 ± 0.32
240	6.2	311	2.48 ± 0.04	0.420	597.2578 ± 0.0001	$+0.0006(3)$	2.19 ± 0.22
241	6.2	177	1.40 ± 0.02	0.250	597.2573 ± 0.0006	$+0.0006(3)$	0.54 ± 1.08
242	6.2	177	1.40 ± 0.02	0.200	597.2577 ± 0.0002	$+0.0006(3)$	0.85 ± 0.37
402	6.2	180	1.42 ± 0.02	0.078	597.2576 ± 0.0001	$+0.0006(3)$	1.06 ± 0.24
404	6.1	163	1.31 ± 0.02	0.033	597.2574 ± 0.0006	$+0.0006(3)$	0.43 ± 0.92
405	6.1	168	1.34 ± 0.02	0.030	597.2574 ± 0.0002	$+0.0006(3)$	1.35 ± 0.41
406	6.2	177	1.40 ± 0.02	0.021	597.2575 ± 0.0003	$+0.0006(3)$	1.82 ± 0.75
407	6.2	949	8.10 ± 0.17	0.410	597.2629 ± 0.0003	$+0.0006(3)$	5.56 ± 0.71
408	6.2	937	7.99 ± 0.16	0.400	597.2625 ± 0.0004	$+0.0006(3)$	6.78 ± 0.90
409	6.2	547	4.46 ± 0.08	0.390	597.2595 ± 0.0002	$+0.0006(3)$	4.44 ± 0.44
410	6.2	306	2.44 ± 0.04	0.390	597.2580 ± 0.0003	$+0.0006(3)$	3.68 ± 0.55
411	15.3	997	3.16 ± 0.02	0.320	597.2588 ± 0.0003	$+0.0006(3)$	2.90 ± 0.45
412	15.2	1003	3.19 ± 0.02	0.050	597.2592 ± 0.0001	$+0.0006(3)$	1.24 ± 0.23
716	5.8	1552	16.0 ± 0.5	0.105	597.2681 ± 0.0003	$+0.0001(3)$	5.83 ± 0.59
717	5.8	1571	16.3 ± 0.5	0.070	597.2682 ± 0.0004	$+0.0001(3)$	6.44 ± 0.84
718	5.8	1984	22.3 ± 0.9	0.030	597.2728 ± 0.0005	$+0.0001(3)$	7.59 ± 1.80
719	5.8	2075	23.8 ± 1.0	0.023	597.2741 ± 0.0004	$+0.0001(3)$	7.79 ± 0.85
726	5.8	2912	45.4 ± 4.3	0.047	597.2884 ± 0.0005	$+0.0001(3)$	16.1 ± 1.65
728	6.3	4545	78.0 ± 5.6	0.065	597.3118 ± 0.0022	$+0.0001(3)$	33.7 ± 8.16
735	5.8	7964	126.6 ± 1.7	0.085	597.3569 ± 0.0011	$+0.0001(3)$	17.7 ± 2.70
768	*5.8*	*541*	*4.78 ± 0.10*	*0.035*	*597.2602 ± 0.0002*	*calib.*	*3.36 ± 0.28*
run #	T [K]	p [mb]	ρ [g/ℓ] $\pm$ $\delta\rho$	$\mathcal{E}$ [mJ]	$\lambda_{\mathrm{calib.}} \pm \delta\lambda_{\mathrm{abs}}$ [nm]	–	$\Gamma \pm \delta\Gamma$ [nm]

Table E.3: List of all raw data of the shift and width measurements for 470 nm resonance. See caption of the previous Table **E.2** for the explanation of listed items. The resonance width Γ was obtained from the single-peak fit, instead.

run #	T [K]	p [mb]	ρ [g/ℓ] $\pm$ $\delta\rho$	$\mathcal{E}$ [mJ]	$\lambda_{\mathrm{WM}} \pm \delta\lambda_{\mathrm{stat}}$ [nm]	$\Delta\lambda_{\mathrm{calib.}}$	$\Gamma \pm \delta\Gamma$ [nm]
801	5.3	962	10.32 ± 0.29	0.41	470.7238 ± 0.0017	$-0.0002(6)$	1.42 ± 1.86
802	5.4	971	10.10 ± 0.27	0.50	470.7237 ± 0.0016	$-0.0002(6)$	1.25 ± 1.31
803	5.4	990	10.36 ± 0.28	0.20	470.7239 ± 0.0012	$-0.0002(6)$	1.13 ± 0.90
804	6.3	1153	10.02 ± 0.22	0.45	470.7239 ± 0.0002	$-0.0002(6)$	1.34 ± 0.33
805	6.2	1169	10.23 ± 0.23	0.19	470.7236 ± 0.0011	$-0.0002(6)$	1.01 ± 1.68
814	6.4	1185	10.13 ± 0.32	0.83	470.7239 ± 0.0004	$-0.0002(6)$	2.18 ± 0.64
815	6.3	1167	10.14 ± 0.22	0.83	470.7241 ± 0.0004	$-0.0002(6)$	2.91 ± 1.09
820	6.3	546	4.42 ± 0.08	0.31	470.7228 ± 0.0012	$-0.0002(6)$	1.36 ± 0.29
821	6.2	545	4.45 ± 0.08	0.31	470.7229 ± 0.0001	$-0.0002(6)$	1.01 ± 0.13
822	6.2	544	4.46 ± 0.08	0.14	470.7229 ± 0.0007	$-0.0002(6)$	0.73 ± 0.62
823	6.2	529	4.31 ± 0.08	0.14	470.7229 ± 0.0001	$-0.0002(6)$	0.83 ± 0.12
824	6.2	543	4.44 ± 0.08	0.06	470.7229 ± 0.0002	$-0.0002(6)$	0.45 ± 0.41
825	6.2	546	4.47 ± 0.08	0.03	470.7230 ± 0.0011	$-0.0002(6)$	0.40 ± 0.08
826	6.5	190	1.44 ± 0.02	0.30	470.7225 ± 0.0001	$-0.0002(6)$	0.60 ± 0.08
827	6.2	183	1.44 ± 0.02	0.25	470.7225 ± 0.0001	$-0.0002(6)$	0.39 ± 0.06
828	6.3	180	1.40 ± 0.02	0.13	470.7225 ± 0.0001	$-0.0002(6)$	*** $\pm$ ***
830	6.5	1120	9.32 ± 0.19	0.21	470.7238 ± 0.0006	$-0.0002(6)$	0.79 ± 0.33
831	6.3	815	6.83 ± 0.14	0.23	470.7234 ± 0.0005	$-0.0002(6)$	0.69 ± 0.21
832	6.2	180	1.43 ± 0.02	0.05	470.7225 ± 0.0010	$-0.0002(6)$	0.27 ± 0.07
632	6.0	1177	10.99 ± 0.26	0.18	470.7241 ± 0.0006	$-0.0002(6)$	1.35 ± 1.03
634	5.8	1660	17.5 ± 0.6	0.26	470.7249 ± 0.0017	$-0.0002(6)$	1.17 ± 1.61
635	5.8	1660	17.5 ± 0.6	0.12	470.7245 ± 0.0008	$-0.0002(6)$	4.37 ± 2.42
652	5.8	2477	32.3 ± 1.9	0.30	470.7277 ± 0.0007	$-0.0002(6)$	1.38 ± 1.30
701	*5.8*	*587*	*5.21 ± 0.11*	*0.21*	*470.7224 ± 0.0002*	*calib.*	*2.47 ± 0.29*
704	*5.8*	*498*	*4.37 ± 0.09*	*0.16*	*470.7229 ± 0.0003*	*calib.*	*1.20 ± 0.15*
run #	T [K]	p [mb]	ρ [g/ℓ] $\pm$ $\delta\rho$	$\mathcal{E}$ [mJ]	$\lambda_{\mathrm{calib.}} \pm \delta\lambda_{\mathrm{abs}}$ [nm]	–	$\Gamma \pm \delta\Gamma$ [nm]

Appendix F

Units, Notation and Terminology

F.1 Conversion between Various Units

basic units

Units of length, time, frequency, and energy with prefixes used in this paper are summarized in the table in the next page.

It is noteworthy to list the following conversion equations:

$$\begin{cases} 1\ \text{Å} = 0.1\ \text{nm} = 10^{-8}\ \text{cm} & \text{(F.1a)} \\ 1\ \text{a.u.} = 0.5292\ \text{Å}\,, & \text{(F.1b)} \end{cases}$$

$$\begin{cases} 1\ \text{Å}^2 = 10^{-16}\ \text{cm}^2 & \text{(F.2a)} \\ 1\ \text{a.u.} = 0.2800\ \text{Å}^2\,, & \text{(F.2b)} \end{cases}$$

$$1\ \text{nm}^3 = 10^{-21}\ \text{cm}^3\,. \qquad \text{(F.3)}$$

dipole moment

$$\begin{aligned} 1\ \text{debye} &= 10^{-18}\ \text{esu} = \frac{10}{3^*} \times 10^{-30}\ \text{C/m} \\ &= 0.3934\, e\, a_0 \end{aligned} \qquad \text{(F.4)}$$

*In this section 3^* always means a defined number 2.99792458 (exact) $\equiv 10^{-8}\, c/[\text{m/s}]$.

10^{order}	prefix	length	time	frequency	energy
24	Y				
21	Z				
18	E				
15	P			PHz	
12	T			THz	
9	G			GHz, ns^{-1}	GeV
6	M			MHz, μs^{-1}	MeV
3	k				keV
2	h				
1	da				
0	–	m	s	Hz, s^{-1}	eV
−1	d				
−2	c	cm			
−3	m	mm	ms		meV
−6	μ	μm	μs		μeV
−9	n	nm	ns		
−10		Å			
−12	p	pm	ps		
−15	f	fm	fs		
−18	a				
−21	z				
−24	y				

pressure

$$1 \text{ bar} = 1000 \text{ mb (millibar)} = 10^5 \text{ Pa} = 1/1.013 \text{ atm} = 760/1.013 \text{ Torr} \qquad \text{(F.5)}$$

density

The density of the helium is given as follows:

$$N = 1 \text{ mol}/\ell = 6.022 \times 10^{20} \text{ cm}^{-3} \Leftrightarrow \rho = 4.0 \text{ g}/\ell \qquad \text{(F.6)}$$

F.1.1 Conversion of energy units

$$E = kT, \quad k = 0.8617 \times 10^{-4}\ \text{eV/K}, \quad 1\ \text{eV} = 11\,600\ \text{K} \tag{F.7}$$

$$e = 1.602 \times 10^{-19}\ \text{C}, \quad 1\ \text{eV} = 1.602 \times 10^{-19}\ \text{J} \tag{F.8}$$

$$c = 299\,792\,458\ \text{m/s} = 3^*0\ \text{GHz cm} \tag{F.9a}$$

$$1\ \text{cm}^{-1} = 3^*0\ \text{GHz} \tag{F.9b}$$

$$h = 4.136\ \text{eV/PHz} \tag{F.10a}$$

$$1\ \text{PHz} = 4.136\ \text{eV}, \quad 1\ \text{GHz} = 4.136\ \mu\text{eV} = 48.0\ \text{mK} \tag{F.10b}$$

F.1.2 Units frequently used in laser physics

$$c\ (= 3^*0\ [\text{GHz cm}]) = \nu\ [0.1\ \text{PHz}] \cdot \lambda\ [100\ \text{nm}] \tag{F.11}$$

$$c\ (= 10\,000) = \nu\ [\text{cm}^{-1}] \cdot \lambda\ [\mu\text{m}] \tag{F.12}$$

example:

$$600\ \text{nm} \Leftrightarrow 16\,667\ \text{cm}^{-1} = 0.500\ \text{PHz}\ (= 500\ \text{THz}) = 2.07\ \text{eV}$$

$$\Delta\nu\ [\text{GHz}] = -\frac{3^*0\ [\text{GHz cm}]}{(\lambda\ [100\ \text{nm}])^2}\Delta\lambda\ [\text{pm}] \tag{F.13}$$

example:

$$\lambda = 600\ \text{nm}\ : \quad \Delta\nu\ [\text{GHz}] = -\frac{3^*0}{6^2}\Delta\lambda\ [\text{pm}]$$

$$\mathcal{E}\ [\text{mJ}] = \int_S I(\boldsymbol{r})\ [\text{mJ/cm}^2]\,\mathrm{d}\boldsymbol{r}\ [\text{cm}^2] = IA \tag{F.14}$$

$$I\ [\text{mJ/cm}^2] = \int_{t_1}^{t_1+\tau_\text{l}} P(t)\ [\text{MW/cm}^2]\,\mathrm{d}t\ [\text{ns}] = P\tau_\text{l} \tag{F.15}$$

*In this section 3*0 always means a defined number 29.9792458 (exact) $\equiv 10^{-7}\,c/[\text{m/s}]$.

$$\begin{aligned} P &= \frac{1}{2}\, c \left\{ \varepsilon_0 \overline{|\boldsymbol{E}|^2} + \mu_0 \overline{|\boldsymbol{H}|^2} \right\} \\ &= c\, \varepsilon_0 \overline{|\boldsymbol{E}|^2} = \frac{1}{2}\, c\, \varepsilon_0 {E_0}^2 \end{aligned} \tag{F.16}$$

$$E_0\ [\mathrm{V/cm}] = \sqrt{0.75346\, P\ [\mathrm{mW/cm^2}]} = 0.8680 \sqrt{P\ [\mathrm{mW/cm^2}]} \tag{F.17}$$

$$\begin{aligned} \frac{\Omega}{2\pi}\ [\mathrm{GHz}] &= 0.5034\, \mu\ [\mathrm{debye}]\, E\ [\mathrm{V/m}] \\ &= 0.4370\, \mu\ [\mathrm{debye}] \sqrt{P\ [\mathrm{kW/cm^2}]} \end{aligned} \tag{F.18}$$

F.1.3 Atomic units

The atomic units are widely used in atomic physics and this paper is not an exception. The basic units are defined as the following:

$$\begin{cases} m_e = 1 \text{ a.u.} \quad [\, 9.109 \times 10^{-31} \text{ kg} \,] & \text{(F.19a)} \\ \hbar = 1 \text{ a.u.} \quad [\, 1.055 \times 10^{-34} \text{ J s} \,] & \text{(F.19b)} \\ e = 1 \text{ a.u.} \quad [\, 1.602 \times 10^{-19} \text{ C} \,] , & \text{(F.19c)} \end{cases}$$

and also implied are:

$$4\pi\varepsilon_0 = 1 \quad [\, 4\pi \times 8.854 \times 10^{-12} \text{ F/m} \,] \tag{F.20a}$$

$$k = 1 \quad [\, 1.381 \times 10^{-23} \text{ J/K} \,] \tag{F.20b}$$

$$\alpha = \frac{e^2}{4\pi\varepsilon_0 \hbar c} = \frac{1}{c}$$

$$\text{in other words,} \quad c = \frac{1}{\alpha} = 137.0 \quad [\, 2.998 \times 10^8 \text{ m/s} \,] , \tag{F.20c}$$

where the values and units in the MKSA system are also written in square brackets. The unit of lengths, velocity, time, and energy are the Bohr radius, electron velocity, one cycle of electron motion, and twice the Rydberg energy of hydrogen atom (at the limit of infinite nuclear mass):

$$a_0 = \frac{\hbar}{m_e c \alpha} = 1 \text{ a.u.} \quad [\, 0.5292 \times 10^{-10} \text{ m} \,] \tag{F.21a}$$

$$v = c\alpha = 1 \text{ a.u.} \quad [\, 2.188 \times 10^6 \text{ m/s} \,] \tag{F.21b}$$

$$t = \frac{a_0}{v} = 1 \text{ a.u.} \quad [\, 2.419 \times 10^{-17} \text{ s} \,] . \tag{F.21c}$$

$$2\,\mathrm{Ry} = m_e c^2 \alpha^2 = 1 \text{ a.u.} \quad [\, 27.21 \text{ eV} = 43.60 \times 10^{-19} \text{ J} \,] \tag{F.21d}$$

F.1.4 Natural units

In high-energy physics, the natural units are often used. This unit system is based on the following physics constants:

$$\begin{cases} m_e = 1 \ \text{ or } \ 0.5110 \text{ MeV} & \text{(F.22a)} \\ \hbar = 1 & \text{(F.22b)} \\ c = 1 & \text{(F.22c)} \end{cases}$$

with implicit assumptions

$$4\pi\varepsilon_0 = 1 \tag{F.23a}$$

$$\alpha = \frac{e^2}{4\pi\varepsilon_0\hbar c} = e^2$$

$$\text{in other words,} \quad e = \sqrt{\alpha} = 0.08542\,. \tag{F.23b}$$

A useful equation is

$$\hbar c = 1 = 197.3 \ [\,\text{MeV fm} = \text{eV nm}\,]\,. \tag{F.24}$$

In the convention which uses MeV as a unit for energy and mass (instead of setting the electron mass to unity), units of length and time are given by

$$\begin{cases} 1 \text{ MeV}^{-1} = 197.3 \text{ fm} & \text{(F.25a)} \\ 1 \text{ MeV}^{-1} = \dfrac{\hbar c/\text{MeV}}{c} = 6.582 \times 10^{-22} \text{ s}\,. & \text{(F.25b)} \end{cases}$$

F.2 Terminology

$|\Delta l| \leq 3$ Auger dominance rule The Auger transition rate has a dramatic dependence on the angular momentum change $|\Delta l|$, taken away by the outgoing electron. In the $\overline{p}\,^4\text{He}^+$ atomcule, the Auger transition dominates over the much slower radiative transition if $|\Delta l| \leq 3$ is achieved, while the opposite is true for states with $\min(|\Delta l|) \geq 4$.

propensity rule As for metastable states of $\overline{p}\text{He}^+$ atomcules, the radiative (electric dipole) transitions occur mainly along a decay chain which keeps the vibrational quantum number v constant. In the atomic picture, this is because the well-localized antiproton's wavefunctions overlap best between the states when $\Delta n = \Delta l = -1$.

favored transition We call the radiative transitions which obey the propensity rule above, by the name "favored". We have found 8 favored transition in $\overline{p}\,^4\text{He}^+$ atomcule and 3 in $\overline{p}\,^3\text{He}^+$.

unfavored transition A type of radiative transition with $\Delta n = -\Delta l = 1$ which changes v by $\Delta v = +2$. The transition rate is two orders of magnitude smaller than for the favored transition, but is larger than other allowed transitions $\Delta l = \pm 1$ with different Δn. Two resonant transitions of this type were observed in $\overline{p}\,^4\mathrm{He}^+$ atomcules.

DATS Delayed annihilation time spectra of antiprotons originating in the metastable $\overline{p}\mathrm{He}^+$ atomcules.

vacuum wavelength Wavelength of laser light, measured in vacuum. Symbol λ. We always refer to vacuum wavelengths throughout this thesis, and never to any wavelengths measured in media.

density shift The centers of the resonance lines shift by an amount depending primarily on the density of the target. The term "pressure shift" is usually used instead to mean the same phenomenon, but we will avoid using this term here.

power density Peak power (which may be a function of time) of the laser pulse, divided by the spot area. Denoted by P.

energy density Energy of one laser pulse (symbol $\mathcal{E}$), divided by the spot area (A). Denoted by I.

quantum numbers We use n, l, m, L, v, F, J, and Λ as quantum numbers. See the next section ("notation") for an explanation of each quantum number.

hyperfine (HF) and super-hyperfine (SHF) structures The word "hyperfine" is used in a slightly different context from the normal terminology. The hyperfine splittings of $\overline{p}\mathrm{He}^+$ states are caused by the interaction between the large angular momentum of the antiproton and the electron spin, while the SHF splitting is related with the antiproton's spin.

F.3 Notation

$\overline{\sim}$ mean value of a physical value

$\langle\sim\rangle$ mean value or statistical average of a physical value

a mean radius of an atom/atomcule

a_0 Bohr radius of hydrogen

a_1, a_2 probability amplitude

A cross-section area of the laser spot

$A_{i\to f}$ Eisntein's A coefficient

$\alpha = 1/137$ fine structure constant

α polarizability

$\alpha = {}^4\mathrm{He}^{++}$ alpha particle = nucleus of helium four.

b impact parameter

b_T Weisskopf radius

β, β' quantum numbers of the states

c speed of light

$c_{if} = b_T v_T^{1/5}$

C_6 coefficient in the representation of van der Waals potential

d dead time of the laser after one shot

Δ shift of central frequency

$\delta\sim$ error of a physical variable

$\Delta\sim$ difference of a physical variable

ΔE energy difference

Δt time window, observation time

$\Delta\omega = \omega - \omega_0$ difference or offset in angular frequency

$\Delta\nu = \Delta\omega/2\pi$ frequency detuning

$\Delta\nu_{\mathrm{D}}$ Doppler width (FWHM)

$|\Delta l|$ multipolarity

Δt observation time

$\mathrm{e} = 2.71828$ base of natural logarithm

$e\ (>0)$ electron charge

e^-, e^+ electron and positron (particles)

$\boldsymbol{E}, E$ electric field

E_0 amplitude of oscillating electric field

E_{a} activation energy in Arrhenius equation

E_{B} binding energy

$\mathcal{E}$ energy of laser pulse

$\sim_{\mathrm{exp}}$ index for experimental values

ϵ depletion efficiency of state population by a laser pulse

ε_0 dielectric constant in vacuum

f fraction of delayed annihilation

$F\ (\boldsymbol{F} = \boldsymbol{l} + \boldsymbol{s}_{\overline{p}})$ a quantum number

$\sim_f$ index for the final state

$\Phi(\tau)$ correlation function

ϕ, Φ, ψ, Ψ wavefunctions

$\boldsymbol{G}, G_{x,y,z}, \tilde{\boldsymbol{G}}, \tilde{G}_{x,y,z}$ virtual force vector acting on an optical Bloch vector

$G = \left\langle j \middle| \boldsymbol{\mu}^2 \middle| j \right\rangle$

γ gamma ray (high-energy photon)

γ Lorentzian half width

γ collisional broadening (half width)

γ_{T} transverse relaxation rate

γ_{P} rate of purely elastic collisions

Γ Full width

Γ_{L} longitudinal relaxation rate

$\Gamma_{\mathrm{A}}, \Gamma_{\mathrm{B}}$ decay rate from the daughter state (Auger rate), and from the parent state (including side branches)

$\Gamma(x)$ Gamma function

h Planck constant

$\hbar = h/2\pi$ reduced Planck constant

$\boldsymbol{H}$ magnetic field

$\mathcal{H}, \mathcal{H}_0, \mathcal{H}'$ Hamiltonian (total, unperturbed and perturbation)

η phase shift

$\mathrm{i} = \sqrt{-1}$ imaginary unit

I energy density of laser light

$I(\omega)$ power spectrum

I_0 first ionization potential

$I_1(x_0), I_2(x_0)$ an integral for calculation of shift and broadening

$\sim_i$ index for the initial state

j index for an unspecified state

J ($\boldsymbol{J} = \boldsymbol{F} + \boldsymbol{s}_{\overline{p}} = \boldsymbol{l} + \boldsymbol{s}_e + \boldsymbol{s}_{\overline{p}}$) total angular momentum

k Boltzmann constant

$K^{\pm}$ kaons (meson particles)

κ shift of angular frequency

l azimuthal quantum number, orbital angular momentum

$L = l$ rotational quantum number, angular momentum

ℓ mean free path (in [nm])

λ vacuum wavelength (in [nm])

λ_0 extrapolated vacuum wavelength at zero-density limit

$\lambda = \tau^{-1}$ transition rate

$\lambda^{(0)} = (\tau^{(0)})^{-1}$ extrapolated transition rate at zero-density limit

Λ angular momentum of electron along the molecular axis, a quantum number

m magnetic quantum number

$m_e = 0.511\ \mathrm{MeV}/c^2$ electron mass

M magnetic quantum number

M mass of $\overline{p}\mathrm{He}^+$ atomcule

$M_{\overline{p}}, M_p = 938\ \mathrm{MeV}/c^2$ antiproton/proton mass

$M_{\mathrm{He}^{++}}$ mass of helium nucleus

M^* reduced mass between antiproton and helium nucleus

$M, \overline{M}$ multiplicity: the number of "hit" counters, and its mean value

μ dipole moment

$\boldsymbol{\mu}$ dipole moment vector or operator

μ reduced mass between the $\overline{p}\mathrm{He}^+$ atomcule and a helium atom

μ_0 magnetic permeability of free space

$\mu^{\pm}$ muons (lepton particles)

n principal quantum number

$n_0 = \sqrt{M^*/m_e}$ typical value for n

N number density

$N, \tilde{N}$ state population, and population after the first laser irradiation

ν frequency

$\nu_{\rm c}$ collision rate

$\nu_{\rm c}^{-1}$ interval between collisions

p, p' rate of delayed annihilation and that free from pre-pile-up

P power density of laser light

$\overline{p}$ antiproton (particle)

$\overline{p}\mathrm{He}^+$, $(\overline{p}\mathrm{He}^+)^0$ antiprotonic helium atom-cule

$\overline{p}\mathrm{He}^{++}$, $(\overline{p}\mathrm{He}^{++})^+$ antiprotonic helium ion

$\pi = 3.14159$ ratio of the circumference of the circle to the diameter

$\pi^\pm$ laser transition with $\Delta m = \pm 1$

$\pi^\pm$, π^0 pions (meson particles)

q polarization of photon

$Q_p, Q_{\overline{p}}$ charge of proton/antiproton

r rate of incident $\overline{p}$ beam

r radius of an atom(cule)

$\boldsymbol{r}$ position vector

$\boldsymbol{R}, R$ internuclear distance, interatomic distance

R_1 interatomic repulsion radius

$R_{\rm l}, R_{\rm o}, R_{\rm tot}$ rates of useful delayed events (with and without laser, and the total)

$\mathrm{Ry} = 13.6\ \mathrm{eV} = {}^1\!/_2$ a.u. Rydberg energy

$\mathrm{Ry}(p)^\infty$, $\mathrm{Ry}(\overline{p})^\infty$ Rydberg energy of proton and antiproton (bound to a negative and positive particle, respectively, with a virtual infinite mass)

ρ density of helium target

ρ, ρ_{nm} density matrix

$\boldsymbol{\rho}, \rho_{x,y,z}, \tilde{\boldsymbol{\rho}}, \tilde{\rho}_{x,y}$ optical Bloch vector

s shift parameter

$s, s_e, s_{\overline{p}}$ spin (of electron, antiproton)

$s, p, d...; S, P, D...$ states with $l = 0, 1, 2...$

σ collisional cross section

$\sigma_{\rm q}$ collisional quenching cross section

$\sigma_\Delta, \sigma_\gamma$ collisional cross section for resonance shift and broadening

$\sigma = \Gamma\,/\,2\sqrt{2\ln 2}$ Gaussian sigma

σ laser transition with $\Delta m = 0$

$\sigma, \pi, \delta...$ electron states with $\Lambda = 0, 1, 2...$

t time

t_1, t_2 timing of the first and second laser irradiation after $\overline{p}$ capture

$t_1' = t_1 + \tau_{\rm l}$ time at the end of the (first) laser pulse

T temperature (in [K])

$\sim_{\rm th}$ index for theoretical values

τ lifetime

$\tau_{\rm l}$ duration of laser pulse

$\tau_{\rm c}$ duration of collision

u_n time-independent wavefunction

$v = n - l - 1$ vibrational quantum number

$\boldsymbol{v}, v$ velocity

$v_T = \sqrt{2kT/\mu}$ most probable velocity

$V(R)$ interatomic interaction potential

V_0, V_1 feeding to the daughter and parent states of the resonance

w width of the beam gate and the pile-up veto signals

W, W_1, W_2 energy (of each state)

$\omega = 2\pi\nu$ angular frequency

$\omega_0 = |\, W_1 - W_2 \,| \,/\, \hbar$ resonance angular frequency

$\Omega = \mu E/\hbar$ Rabi angular frequency (at $\omega = \omega_0$)

$\Omega' = \sqrt{{\Omega_0}^2 + (\omega - \omega_0)^2}$ nutation angular frequency

$\Omega_{\rm s} = \sqrt{\Gamma_{\rm L}\gamma_{\rm T}}$ Rabi angular frequency at saturation

$\sim_{x,y,z}$ index for the three coordinates

$x_0 = (R_1/b_T)^{-5}$

$\xi = M_{\overline{p}} \,/\, (M_{\overline{p}} + M_{\rm He^{++}})$ a mass ratio between two nuclei in $\overline{p}{\rm He}^+$ atomcule

Z nuclear charge

$Z^{\overline{p}}_{\rm eff}, Z^{\rm e}_{\rm eff}$ effective nuclear charge for $\overline{p}$ and e^-.

Acknowledgments

It is a great pleasure to express my gratitude to my supervisor Prof. Dr. R.S. Hayano*, who always gave me invaluable and insightful advice and encouraging comments in his dedicated guidance. I am very much stimulated by his enthusiasm and vigor toward physics. I would also like to pay my respect to Prof. Emeritus Dr. T. Yamazaki*† for his continuous encouragement and precious advice. It was a great honor for me that I was able to work under his supervision. And I am much obliged to Prof. Dr. N. Morita‡ for his private lectures on laser physics and handling of the laser system. He has also given me many important hints and much advice in our long discussions about the interpretation of the data obtained and presented in this thesis.

This experiment was done by the PS205 collaboration at the LEAR facility at CERN. This collaboration includes Tokyo*†, Okazaki‡, München§, Budapest¶ and CERN‖. I would like to thank all the collaborators with whom I spent months of interesting stays in the laboratory for this five years. Especially I am grateful to Dr. E. Widmann** who taught me all about the experiment from the beginning and often helped me with my problems. I would like to express my gratitude to Dr. F.E. Maas†† for his continuous advice, persevering guidance and kind help. I spent most of the days with him at CERN and in Tokyo for two years during my master-course period and I really learned a lot from him. I also thank Mr. B. Ketzer§ for frequent discussions about the electronics and analysis methods. He and I have started our studies at the same time from the beginning

*Department of Physics, Univ. of Tokyo, Tokyo, Japan.

†Institute for Nuclear Study (INS, *Genshikaku Kenkyuujo*), University of Tokyo (now part of KEK), Tokyo, Japan.

‡Institute for Molecular Science (*Bunshi Kagaku Kenkyuujo*), Okazaki, Aichi, Japan.

§Physik-Department, Technische Universität München (TUM), München, Germany.

¶KFKI (Központi Fizikai Kutató Intézete): Central Research Institute for Physics, Budapest, Hungary.

‖CERN: Organisation Européenne pour la Recherche Nucléaire, – European Laboratory for Particle Physics – , Geneva, Switzerland.

**Current affiliation is the Muon Science Laboratory, RIKEN (*RIkagaku KENkyuujo*), Wako, Saitama, Japan.

††Currently at University of Mainz, Mainz, Germany.

of the laser experiments of the $\overline{p}\mathrm{He}^+$ research in 1993 and share our experiences as two young physicists. Acknowledgments are due to the teachers of TUM: Prof. Dr. H. Daniel and Prof. Dr. T. von Egidy, and especially, I learned a lot from Dr. F.J. Hartmann, with whom I spent most of the time of the early-morning shift during the experiment. I also thank Prof. Dr. D. Horváth[¶] for valuable advice and discussions. And I would like to express my appreciation to Dr. J. Eades[‖] for his great help during my stay at CERN. He was a good consultant for me, especially on the brushing up of my English, and always gave me elaborate replies.

I appreciate Dr. H. Tamura[‡‡], Dr. T. Ishikawa[*] and Dr. M. Iwasaki[♯] for their helpful advice and guidance. Also I owe thanks to Dr. S.N. Nakamura[♭] and Dr. T.M. Ito[♮] for their kind help. I wish to give my special thanks to Dr. I. Sugai[†] who gave me a lot of useful lessons on the scientists' way of life, and I am so much obliged to Mr. M. Kumakura[‡] as my private teacher of laser physics and technical manipulation of the laser system. I also thank students at TUM: Mr. A. Niestroj, Mr. R. Pohl and Ms. C. Maierl.

In designing the shower counter system, Mr. T. Morimoto[†] helped us a great deal as a mechanical engineer. On behalf of the group, I wish to acknowledge his invaluable help in designing the experimental setup.

I give my special thanks, representing our experiment group, to all the theoreticians who have given so many great results and insights. Our achievement is a good example of cooperation and co-inspiration between the experimental and theoretical works toward a new physics goal.

Now I express my thanks to all the members of Ishihara-Hayano-Sakai group, and Nagamine group of the Meson Science Laboratory[◇], of the University of Tokyo. I thank all my senior colleagues, in particular to Dr. T. Wakasa who helped me a lot about the computers and to Dr. A. Kawachi for encouragement. I would like to say thank you to my close classmates, to Mr. M. Hirai, Mr. Y. Satou and Mr. N. Kawamura who gave valuable discussions and daily communications. Especially, Mr. K. Itahashi is a nice friend and a group- and cubicle-mate, and we both helped and stimulated each other. And I owe so much to Mr. M. Hori, a junior colleague and a collaborator, who worked very hard for the experiments and from whom I was given much help. I hope that the new younger students will actively participate in the successive new experiments and do good jobs in the near future.

[‡‡] Currently an Assistant Professor, Tohoku University, Sendai, Miyagi, Japan.

[♯] Currently an Assistant Professor, Tokyo Institute of Technology, Tokyo, Japan.

[♭] Current affiliation is the Muon Science Laboratory, RIKEN, Wako, Saitama, Japan.

[♮] Current affiliation is Istituto Nazionale di Fisica Nucleare, Laboratori Nazionale di Frascati, Frascati, Italy.

[◇] UT-MSL now belongs to KEK.

Although the first discovery of the metastable states in the $\overline{p}\mathrm{He}^+$ atomcule was made at KEK in Japan, the further successful investigation of these and the subsequent laser experiments which left us with an abundance of fruitful results were only possible at the LEAR facility with its excellent $\overline{p}$ beams. We are deeply indebted to the LEAR and PS staff at CERN for their tireless dedication, and hope for a bright future in the newly constructed AD facility at CERN. We are also much grateful to the cryogenics group at CERN, who gave us devoted help in building up and testing a new target system. Last but not least, I acknowledge financial support for these three years from the Japan Society for the Promotion of Science (JSPS).

In the last sentence, I would like to thank my parents, my sister and my grand parents who have always understood me and encouraged me, and all my friends who gave me love and friendship and whom I loved.

* * * * *

Thank you.

Vielen Dank.

Merci Beaucoup.

Köszönöm szépen!

Спасибо большое.

Благодаря.

ありがとう。

Bibliography

[1] T.B. Day, Nuovo Cimento **18** (1960) 381; T.B. Day, G.A. Snow, J. Sucher, Phys. Rev. Lett. **3** (1959) 61; T.B. Day, G.A. Snow, J. Sucher, Phys. Rev. **118** (1960) 864.

[2] M. Leon and H.A. Bethe, Phys. Rev. **127** (1962) 636.

[3] T. Yamazaki, M. Aoki, M. Iwasaki, R.S. Hayano, T. Ishikawa, H. Outa, E. Takada, H. Tamura and A. Sakaguchi, Phys. Rev. Lett **63** (1989) 1590.

[4] R.S. Hayano, T. Ishikawa, M. Iwasaki, H. Outa, E. Takada, H. Tamura, A. Sakaguchi, M. Aoki and T. Yamazaki, Phys. Lett. B **231** (1989) 355.

[5] S.N. Nakamura, M. Iwasaki, H. Outa, R.S. Hayano, Y. Watanabe, T. Nagae, T. Yamazaki, H. Tada, T. Numao, Y. Kuno and R. Kadono, Phys. Rev. A **45** (1992) 6202.

[6] M. Iwasaki, S.N. Nakamura, K. Shigaki, Y. Shimizu, H. Tamura, T. Ishikawa, R.S. Hayano, E. Takada, E. Widmann, H. Outa, M. Aoki, P. Kitching and T. Yamazaki, Phys. Rev. Lett. **67** (1991) 1246.

[7] T. Yamazaki, E. Widmann, R.S. Hayano, M. Iwasaki, S.N. Nakamura, K. Shigaki, F.J. Hartmann, H. Daniel, T. von Egidy, P. Hofmann, Y.-S. Kim and J. Eades, Nature **361** (1993) 238.

[8] G.T. Condo, Phys. Lett. **9** (1964) 65.

[9] J.E. Russell, (a) Phys. Rev. Lett. **23** (1969) 63; (b) Phys. Rev. **188** (1969) 187; (c) Phys. Rev. A **1** (1970) 721, 735, 742; (d) D.E. Wright and J.E. Russell, Phys. Rev. A **6** (1972) 2488.

[10] E. Fermi and E. Teller, Phys. Rev. **27** (1947) 399.

[11] S.N. Nakamura, R.S. Hayano, M. Iwasaki, K. Shigaki, E. Widmann, T. Yamazaki, H. Daniel, T. von Egidy, F.J. Hartmann, P. Hofmann, Y.-S. Kim and J. Eades, Phys. Rev. A **49** (1994) 4457.

[12] E. Widmann, I. Sugai, T. Yamazaki, R. S. Hayano, M. Iwasaki, S.N. Nakamura, H. Tamura, T.M. Ito, A. Kawachi, N. Nishida, W. Higemoto, Y. Ito, N. Morita, F.J. Hartmann, H. Daniel, T. von Egidy, W. Schmid, J. Hoffmann and J. Eades, Phys. Rev. A **51** (1995) 2870.

[13] B. Ketzer, F.J. Hartmann, H. Daniel, T. von Egidy, A. Niestroj, S. Schmid, W. Schmid, T. Yamazaki, I. Sugai, K. Nakayoshi, R.S. Hayano, F.E. Maas, H.A. Torii, T. Ishikawa, H. Tamura, N. Morita, D. Horváth, J. Eades, E. Widmann, Phys. Rev. A **53** (1996) 2108.

[14] T. Yamazaki and K. Ohtsuki, Phys. Rev. A **45** (1992) 7782; K. Ohtsuki, private communication (1993).

[15] R. Ahlrichs, O. Dumbrajs, H. Pilkuhn and H.G. Schlaile, Z. Phys. A **306** (1982) 297.

[16] T.P. Terada and R. S. Hayano, Phys. Rev. C **55** (1997) 73.

[17] see, a series of journal Muon Catalyzed Fusion, **1**– (1987–).

[18] T. Yamazaki and K. Ohtsuki, Phys. Rev. A **50** (1994) 5350.

[19] I. Shimamura, Phys. Rev. A **46** (1992) 3776, and private communication (1993).

[20] P.T. Greenland and R. Thürwächter, Hyperfine Interactions **76** (1993) 355.

[21] P.T. Greenland, J.S. Briggs, and R. Thürwächter, J. Phys. B **27** (1994) 1233.

[22] I.V. Puzynin, T.P. Puzynina, S.I. Vinitsky and V.I. Puzynin, Hyperfine Interactions **101/102** (1996) 493.

[23] Y. Kino, private communication (1993).

[24] Y. Kino, M. Kamimura and H. Kudo, Proc. XV. Int. Conf. on Few-Body Problems in Physics, Groningen, the Nederlands (1997).

[25] Y. Kino, M. Kamimura and H. Kudo, Proc. XVII RCNP Int. Symp. Conf. on Few-Body Problems in Physics, Groningen, the Nederlands (1997).

[26] O.I. Kartavtsev, Yad. Fiz. **59** (1996) R1541.

[27] O.I. Tolstikhin, S. Watanabe and M. Matsusawa, Phys. Rev. Lett. **74** (1995) 3573.

[28] O.I. Tolstikhin, S. Watanabe and M. Matsusawa, Phys. Rev. A **54** (1996) R3705.

[29] F. Benvenuto, G. Casati and D. L. Shepelyanski, Phys. Rev. A **53** (1996) 737.

[30] V.I. Korobov, Phys. Rev. A **54** (1996) R1749.

[31] V.I. Korobov, Phys. Rev. Lett., in print; V.I. Korobov, Proc. Int. Conf. on Low Energy Antiproton Physics (LEAP 96, Dinkelsbühl, Germany, Aug. 1996), Nuclear Physics B (Proc. Suppl.) **56A** (1997) 89

[32] E. Yarevsky and N. Elander, Europhys. Letters **37** (1997) 453.

[33] N. Elander and E. Yarevsky, Phys. Rev. A, **56** (1997) 1855; Erratum submitted.

[34] S. Andersson, N. Elander and E. Yarevsky, Phys. Rev. A, submitted.

[35] V.I. Korobov, D.D. Bakalov Phys. Rev. Lett., **79** (1997) 3379.

[36] K. Ohtsuki, private communication (1992–1997).

[37] O.I. Kartavtsev, At. Nucl. **59** (1996) 1483.

[38] S. I. Fedotov, O. I. Kartavtsev, and D.E. Monakhov, At. Nucl. **59** (1996) 1662.

[39] V.I. Korobov, I. Shimamura, Phys. Rev. A, **56** (1997) 4587.

[40] J. Révai and A.T. Kruppa, Phys. Rev. A, accepted.

[41] O.I. Kartavtsev Proc. Int. Symp. on Exotic Atoms and Nuclei (Hakone, Japan, 1995), Hyperfine Interactions **103** (1996) 369.

[42] M.S. Fee *et al.*, Phys. Rev. A **48** (1993) 192.

[43] F.G. Mariam *et al.*, Phys. Rev. Lett. **49** (1982) 993.

[44] F.E. Maas, B. Braun, H. Geerds, K. Jungmann, B.E. Matthias, G. zu Putlitz, I. Reinhard, W. Schwarz, L. Willmann, and L. Zhang, Phys. Lett. A **187** (1994) 247.

[45] N. Morita, K. Ohtsuki and T. Yamazaki, Nucl. Instrum. Methods A **330** (1993) 439.

[46] E. Widmann, I. Sugai, T. Yamazaki, R.S. Hayano, M. Iwasaki, S.N. Nakamura, H. Tamura, T.M. Ito, A. Kawachi, N. Nishida, W. Higemoto, Y. Ito, N. Morita, F.J. Hartmann, H. Daniel, T. von Egidy, W. Schmid, J. Hoffmann, J. Eades, Phys. Rev. A **53** (1996) 3129.

[47] N. Morita, M. Kumakura, T. Yamazaki, E. Widmann, H. Masuda, I. Sugai, R.S. Hayano, F.E. Maas, H.A. Torii, F.J. Hartmann, H. Daniel, T. von Egidy, B. Ketzer, W. Müller, W. Schmid, D. Horváth, J. Eades, Phys. Rev. Lett. **72** (1994) 1180.

[48] R.S. Hayano, F.E. Maas, H.A. Torii, N. Morita, M. Kumakura, T. Yamazaki, H. Masuda, I. Sugai, F.J. Hartmann, H. Daniel, T. von Egidy, B. Ketzer, W. Müller, W. Schmid, D. Horváth, J. Eades, E. Widmann, Phys. Rev. Lett. **73** (1994) 1485; **73** (1994) 3181(E).

[49] F.E. Maas, R.S. Hayano, T. Ishikawa, H. Tamura, H.A. Torii, N. Morita, T. Yamazaki, I. Sugai, K. Nakayoshi, F.J. Hartmann, H. Daniel, T. von Egidy, B. Ketzer, A. Niestroj, S. Schmid, W. Schmid D. Horváth, J. Eades, E. Widmann, Phys. Rev. A **52** (1995) 4266.

[50] H.A. Torii, M. Hori, T. Ishikawa, F.E. Maas, R.S. Hayano, N. Morita, M. Kumakura, I. Sugai, B. Ketzer, H. Daniel, F.J. Hartmann, R. Pohl, R. Schmidt, T. von Egidy, D. Horváth, J. Eades, E. Widmann, T. Yamazaki, Phys. Rev. A **53** (1996) R1931.

[51] R.S. Hayano, T. Ishikawa, H. Tamura, H.A. Torii, M. Hori, F.E. Maas N. Morita, M. Kumakura, I. Sugai, F.J. Hartmann, H. Daniel, T. von Egidy, B. Ketzer, R.Pohl, D. Horváth, J. Eades, E. Widmann, T. Yamazaki, Phys. Rev. A **55** (1997) 1.

[52] T. Yamazaki, E. Widmann, J. Eades, M. Kumakura, N. Morita, H.A. Torii, M. Hori, T. Ishikawa, F.E. Maas, H. Tamura, R.S. Hayano, I. Sugai, Y. Fujita, B. Ketzer, H. Daniel, F.J. Hartmann, M. Hasinoff, R. Pohl, R. Schmidt, T. von Egidy, D. Horváth, Phys. Rev. A, **55** (1997) R3295.

[53] E. Widmann, J. Eades, T. Yamazaki, H.A. Torii, R.S. Hayano, M. Hori, T. Ishikawa, M. Kumakura, N. Morita, I. Sugai, F.J. Hartmann, T. von Egidy, B. Ketzer, C. Maierl, R. Pohl, D. Horváth, Phys. Lett. B **404** (1997) 15.

[54] T. Yamazaki, B. Ketzer, E. Widmann, J. Eades, H. Daniel, F.J. Hartmann, M. Hasinoff, R. Pohl, R. Schmidt, T. von Egidy, D. Horváth, M. Kumakura, N. Morita, I. Sugai, Y. Fujita, H.A. Torii, M. Hori, T. Ishikawa, F.E. Maas, H. Tamura, R.S. Hayano, Chem. Phys. Lett. **265** (1997) 137.

[55] B. Ketzer, F.J. Hartmann, T. von Egidy, C. Maierl, R. Pohl, J. Eades, E. Widmann, T. Yamazaki, M. Kumakura, N. Morita, R.S. Hayano, M. Hori, T. Ishikawa, H.A. Torii, I. Sugai, D. Horváth, Phys. Rev. Lett. **78** (1997) 1671.

[56] B. Ketzer, F.J. Hartmann, T. von Egidy, C. Maierl, R. Pohl, J. Eades, E. Widmann, T. Yamazaki, M. Kumakura, N. Morita, R.S. Hayano, M. Hori, T. Ishikawa, H.A. Torii, I. Sugai, D. Horváth, J. Chem. Phys. accepted (1998).

[57] M. Hori, H.A. Torii, R.S. Hayano, T. Ishikawa, F.E. Maas, H. Tamura, B. Ketzer, F.J. Hartmann, R. Pohl, C. Maierl, T. von Egidy, M. Kumakura, N. Morita, I. Sugai, D. Horváth, E. Widmann, J. Eades, T. Yamazaki, Phys. Rev. A, **57** (1998) 1698.

[58] C. Maierl, Master thesis, Technische Universität München (1997), Germany, unpublished; C. Maierl, F.J. Hartmann, B. Ketzer, R. Pohl, T. von Egidy, R.S. Hayano, M. Hori, T. Ishikawa, H. Tamura, H.A. Torii, M. Kumakura, N. Morita, I. Sugai, D. Horváth, J. Eades, E. Widmann, T. Yamazaki, Phys. Rev. A, to be submitted (1998).

[59] R. Pohl, Master thesis, Technische Universität München (1997), Germany, unpublished; R. Pohl, et al., F.J. Hartmann, B. Ketzer, T. von Egidy, C. Maierl, J. Eades, E. Widmann, T. Yamazaki, M. Kumakura, N. Morita, R.S. Hayano, M. Hori, T. Ishikawa, H.A. Torii, I. Sugai, D. Horváth, J. Chem. Phys. to be submitted (1998).

[60] W.Müller, F.J. Hartmann, J. Eades, R.S. Hayano, B. Ketzer, F.E. Maas, Nucl. Instrum. Methods A **349** (1994) 307.

[61] M. Iwasaki, Program *Low-energy particle simulator*, unpublished; based on J.F. Ziegler, *The stopping and Range of Ions in Solid*, Pergamon Press (1985).

[62] G. Bendiscioli *et al.*, Nucl. Phys. A **518** (1990) 683–708.

[63] F. Balestra *et al.*, Nucl. Phys. A **465** (1987) 714–732.

[64] Application Software Group of CERN, *GEANT*, CERN Program Library Long Writeup W5013.

[65] Sukeyasu Yamamoto, *Kou-enerugī Butsurigaku* (*Shin Butshrugaku Series 14*), Baifūkan, Tokyo (1973), *in Japanese.*

[66] R. Hagedorn, Relativistic kinematics — A guide to the kinematic problems of high-energy physics — , W.A. Benjamin, inc. (1963).

[67] C. Ghesquière, Proc. Symposium on antinucleon-nucleon interactions, Liblice-Praga, 1974; CERN Report 74-18 (1974) p. 436.

[68] C.B. Dover, T. Gutsche, M. Maruyama and A. Faessler, Prog. Part. Nucl. Phys. **29** (1992) 87–173.

[69] H.A. Torii, R.S. Hayano, F.E. Maas, N. Morita, M. Kumakura, T. Yamazaki, H. Masuda, I. Sugai, B. Ketzer, F.J. Hartmann, H. Daniel, T. von Egidy, W. Müller, W. Schmid, A. Niestroj, D. Horváth, J. Eades, E. Widmann, Nucl. Instr. and Meth. A **396** (1997) 257.

[70] S. Iida *et al.*, *Shinban Butsuri Teisuu-hyou*, Asakura Shoten (1978) p 113 *in Japanese*.

[71] Edited by F.M. Phelps, *MIT Wavelength tables Vol.2, Wavelength by element*, the MIT press, Cambridge, Massachusetts (1983).

[72] S. Gerstenkorn, J. Verges and J. Chevillard, *Atlas du Spectre d'Absorption de la Molecule d'Iode*, Laboratoire Aimé Cotton CNRS II, France (1982).

[73] J. Cariou and P. Luc, *Atlas du Spectre d'Absorption de la Molecule de Tellure*, Laboratoire Aimé Cotton CNRS II, France (1980).

[74] H.A. Torii, Master thesis, Dept. of Physics, Graduate School of Science, University of Tokyo, (1995), unpublished.

[75] A. Niestroj, F.J. Hartmann, H. Daniel, B. Ketzer, T. von Egidy, F.E. Maas, R.S. Hayano, T. Ishikawa, H. Tamura, H.A. Torii, N. Morita, T. Yamazaki, I. Sugai, K. Nakayoshi, D. Horváth, J. Eades, E. Widmann, Nucl. Instrum. Methods A **373** (1996) 411.

[76] Cryodata Inc., Program *Helium thermophysical properties software HEPAK* version 3.30 (1992).

[77] G. Gabrielse *et al.*, Phys. Rev. Lett, **65** (1990) 1317.

[78] R.J. Hughes and B.I. Deutch, Phys. Rev. Lett, **69** (1992) 578.

[79] P. Robertson *et al.*, Phys. Rev. C, **16** (1977) 1945.

[80] I.I. Sobel'man, L.A. Vainshtein, E.A. Yukov, *Excitation of Atoms and Broadening of Spectral Lines, 2nd Ed.*, Springer-Verlag, Moscow (1995).

[81] N. Allard and J. Kielkopf, *"The Effect on Neutral Nonresonant Collisions on Atomic Spectral Lines"*, Rev. Mod. Phys. **54** (1982) 1103–1182.

[82] G. Peach, *"Theory of the pressure broadening and shift of spectral lines"*, Advances in Phys. **30** (1981) 367–474.

[83] D. Bakalov, I. V. Puzynin, T. P. Puzynina, S. I. Vinitsky, Phys. Lett. A **211** (1996) 223.

[84] D. Bakalov and V.I. Korobov, Phys. Rev. A, in print.

[85] see, *e.g.* (a) W. Demtröder, *Laser Spectroscopy, 2nd Enlarged Ed.*, Springer-Verlag, Berlin, (1996) Chap. 2 & 3; (b) R. Loudon, *The quantum Theory of Light, 2nd Ed.*, Oxford University Press, UK (1983) Chap. 2 & 3: Japanese translation is available as *Hikari no Ryoushiron, 2nd Ed.*, translation by T. Kojima and K. Kojima, Uchida Rōkakuho Publishing Co., Tokyo (1994); (c) L. Allen and J.H. Eberly, *Optical Resonance and Two-Level Atoms*, Dover Publications Inc., New York (1975); (d) Kouichi Shimoda, *Rēzā butsuri nyuumon*, Iwanami Shoten, Tokyo (1983) Chap. 7 & 8, *in Japanese*; (e) Kouichi Shimoda *et al.*, *Ryoushi Erekutoronikusu (Joukan) (Butsurigaku Sensho 13)*, Shōkabō, Tokyo (1972), Chap. 1, *in Japanese*.

[86] C.H. Towns and A.L. Schawlow, *Microwave Spectroscopy, 2nd Ed.*, Dover Publications Inc., New York (1975) Chap. 13.

[87] J.N. Israelachvili, *Intermolecular and Surface Forces*, Academic Press Ltd., London, (1985); Japanese translation is available as *Bunshikanryoku to Hyoumenryoku*, translation by T. Kondou and H. Ooshima, Revised Ed., Asakura Shoten, Tokyo (1995).

[88] G.Ya. Korenman, INP MSU Preprint 97-I/452, M.V. Lomonosov Moscow State University, D.V. Skobeltzyn Institute of Nuclear Physics, Moscow, (1997); G.Ya. Korenman, ITAMP Workshop "Exotic Atoms" (at Cambridge, USA) and the Workshop "Metastable Exotic Systems in Helium and Related Topics" (at Udine, Italy) (July 1996).

[89] Edited by K.N. Rao and A. Weber, *Spectroscopy of the Earth's Atmosphere and Interstellar Medium*, Academic Press, Inc., San Diego (1992).

[90] R. Kachru, T.W. Mossberg, and S.R. Hartmann, Phys. Rev. A **21** (1980) 1124.

[91] K.-H. Weber and K. Niemax, Z. Phys. A **307** (1982) 13

[92] H. Heinke, J. Lawrenz, K. Niemax, and K.-H. Weber, Z. Phys. A **312** (1983) 329; 339.

[93] T. Yamazaki, Proc. Int. Conf. on Low Energy Antiproton Physics (LEAP 96, Dinkelsbühl, Germany, Aug. 1996), Nuclear Physics B (Proc. Suppl.) **56A** (1997) 379.

[94] ASACUSA Collaboration (T. Azuma, *et al.*), A proposal of experiments *"Atomic Spectroscopy And Collisions Using Slow Antiprotons"*, submitted to and accepted by SPSC committee of CERN (1997).

[95] H.J. Reyher et al., Phys. Lett. A, **115**, (1986) 238

[96] S.I. Kanorsky et al., Phys. Rev. B, **50** (1994) 6296.

[97] W.A. Beck, L. Wilets and M.A. Alberg, Phys. Rev. A **48** (1993) 2779.

[98] G.Ya. Korenman, Hyperfine Interactions **101/102** (1996) 81.

[99] J.S. Cohen and N.T. Padial, Phys. Rev. A **41** (1990) 3460.

[100] J.S. Cohen, Phys. Rev. A, **56** (1997) 3583.

[101] G.Ya. Korenman, Hyperfine Interactions **101/102** (1996) 463; G.Ya. Korenman, Hyperfine Interactions **103** (1996) 341.

[102] J.H. Doede, R.H. Hildebrand, M.H. Israel, and M.P. Pyka, Phys. Rev. **129** (1963) 2808.

[103] R. Knop, R.A. Burnstein, and G.A. Snow, Phys. Rev. Lett. **14** (1965) 767.

[104] V. Markushin, *Electromagnetic Cascade and Chemistry of Exotic Atoms*, Edited by L.M. Simons, D. Horváth, and G. Torelli, Plenum Press, New York (1990) 73.

[105] O.D. Dalkarov and A.Yu. Voronin, Int. Conf. on Low Energy Antiproton Physics (LEAP 96, Dinkelsbühl, Germany) (Aug. 1996), unpublished.

[106] K. Ohtsuki, The third RIKEN symposium on the theoretical studies of dynamical processes in exotic atoms (at RIKEN, Wako, Japan) (Feb. 1995), unpublished.

Bibliography sorted by subject

Studies on exotic atoms

[3] [4] [5] ; [17] [42] [43] [44] ; [102] [103] [104] [105] [106]

Delayed annihilation of antiprotonic helium atomcules

[6] [7] [11] , [12] [13] [46]

Laser spectroscopy studies of antiprotonic helium atomcules

[45] ; [47] [48] [49] [50] [51] [52] [53] [58] ; [54] [55] [56] [57] [59]

Instrumentation for the $\overline{p}\mathrm{He}^+$ experiments

[60] [69] [74] [75]

Annihilation of antiproton

[62] [63] [64] [65] [66] [67] [68]

Theoretical calculations on the $\overline{p}\mathrm{He}^+$ atomcule and other exotic atoms

Early studies on exotic atoms [1] [2] [8] [9] [10] [15]
Energy calculation of $\overline{p}\mathrm{He}^+$ atomcule
[14] [18] [19] [20] [21] [22] [23] [26] [27] [28] [29] ; [30] [31] [35] , [32] [33] [34] , [24] [25]
Calculation of Auger rates of the $\overline{p}\mathrm{He}^+$ atomcule [36] [37] [38] [40] [39]
Calculation of hyperfine structures of the $\overline{p}\mathrm{He}^+$ atomcule [83] [84] [41]
Formation of exotic atoms [16] [97] [98] [99] [100] [101]

Studies on shift and broadening of spectral lines

[85] ; [80] [81] [82] [86] [89] , [90] [91] [92] , [88] ; [87]

Future experiments

[93] [94]

Others

[61] ; [70] [76] ; [71] [72] [73] ; [77] [78] [79] ; [95] [96]

List of Figures

List of Tables

Index

Curriculum vitae of the Author

Hiroyuki A. Torii

Nov 1970	Born at Ashiya City, Osaka region.
Apr 1989	Entered Science Course I, University of Tokyo.
Apr 1991	Proceeded to Physics Department.
Mar 1993	Graduated from the Department of Physics, Faculty of Science, University of Tokyo.
Apr 1993	Entered the Department of Physics, Graduate School of Science, University of Tokyo.
Mar 1995	Finished the Master Course with a Master's Degree of Science. Title of the Master's Thesis: "Development of a Laser-Induced Annihilation Spectrometer for Metastable Antiprotonic Helium Atoms"
Apr 1995	Proceed to the Doctor Course
Mar 1998	To graduate from the Doctor Course with a Doctor's degree of Science at the University of Tokyo. Title of the Doctoral Dissertation (this thesis): "Laser Spectroscopy of Antiprotonic Helium Atomcules — Collisional Shift and Broadening of Resonance Lines —"
1993–1996	Participated in a series of PS205 experiments at CERN, Geneva, Switzerland.
Oct 1994	Invited talk at "the Third International Symposium on Muon and Pion Interactions with Matter", Dubna, Russia.
Jan 1995	Attended a workshop on "Metastable Hadronic States in Helium (MHSH)" held at Balatonfüred, Hungary.
Aug 1996	Attended an international conference on "Low Energy Antiproton Physics (LEAP96)", Dinkelsbühl, Germany.
Sep 1996	Gave two talks at a workshop "Metastable Exotic Systems in Helium and Related Subjects (MESH)", Udine, Italy.